IMAGING ELEMENTAL DEFENCES IN METAL HYPERACCUMULATOR PLANTS

A thesis submitted for the degree of Doctor of Philosophy

Rose Bourdon



Linacre College

Department of Biology

University of Oxford

Michaelmas Term 2024

IMAGING ELEMENTAL DEFENCES IN METAL HYPERACCUMULATOR PLANTS

Rose E. Bourdon
Linacre College
Department of Biology
University of Oxford

Supervisors: Professor Gail M. Preston
Doctor Konstantin Ignatyev (Diamond Light Source)

Michaelmas Term 2024

Abstract

Metal hyperaccumulation is a relatively rare trait that has been observed in approximately 700 plant species to date and is characterised by the active uptake and storage of heavy metals in aerial tissues. There are a number of hypotheses to suggest why this trait has evolved but the one with the most support is commonly referred to as the "elemental defence" hypothesis. In this, hyperaccumulated metal confers a defence against herbivory and pathogens. Previous work has shown that increasing zinc in the leaves of the hyperaccumulator plant *Noccaea caerulescens* is associated with increased disease resistance to the bacterial pathogen *Pseudomonas syringae*. However, the mechanistic involvement of zinc, particularly its localisation relative to the pathogen, was unclear. In this thesis, the role of hyperaccumulated zinc in disease resistance in *N. caerulescens* was studied using synchrotron-based X-ray fluorescence and X-ray absorption spectroscopy to monitor the respective zinc distribution and speciation in untreated and infected leaf tissue. To achieve this, sample preparation and mounting pipelines were first developed to enable

the 2D and 3D imaging of sections of frozen-hydrated leaf tissue. Zinc was found to be highly localised to epidermal vacuoles but exhibited unexpected concentration-dependent heterogeneity in its distribution within the epidermis. Upon infection with *P. syringae*, zinc was observed to mobilise into the apoplastic space, the known site of *P. syringae* inhabitation within the plant. The potential consequences on the bacteria of zinc moving into the apoplast was also explored. It was previously established that reactive oxygen species (ROS) are generated in the apoplast during the immune response of *N. caerulescens* to *P. syringae*. Additionally, the leaves of the Prayon population of *N. caerulescens* used in this study exhibit high ROS levels, which further increase with increasing zinc concentration in the growth medium. A synergistic relationship between zinc and ROS was determined. Zinc was shown to increase the sensitivity of *P. syringae* to ROS, and zinc was additionally found to cause sustained oxidation of the bacteria when the stressors were applied in conjunction. Overall, this study has enhanced imaging capabilities of biological samples at the synchrotron facility Diamond Light Source, has provided insight into the mechanisms by which hyperaccumulated zinc provides a defence against the bacterial pathogen *P. syringae*, and presents evidence in support of the joint effects hypothesis of metal hyperaccumulation.

Acknowledgements

I am indebted to a great number of people for their knowledge, time, advice, and support. First and foremost I wish to acknowledge my supervisors, Gail Preston and Konstantin Ignatyev – I genuinely could not have wished for better supervisors. Gail has been a source of constant inspiration and invaluable support. It has been wonderful to unravel this project with mutual enthusiasm, bounce ideas off each other and I thank her for letting me try (and sometimes fail at) new ideas. And I thank Konstantin, firstly for sacrificing a not-insignificant number of weekends to work with me on the beamline! Your help and support have also been invaluable, particularly for helping me get to grips with the more physics side of the project.

I am grateful to have met some wonderful people and I am sure I have made life-long friendships throughout my PhD. I am particularly grateful to members of the Preston lab for making this whole experience a positive one. I wish to particularly thank a few members. Firstly, Alison, for being a one-woman hype train and incredibly generous with your time and energy (and brain!). Also, Ashleigh and Tee for being fonts of knowledge and helping me, an initially lost chemist, grasp new biological concepts and coding with R. No PhD student in the department would be half as productive if it was not for the amazing support staff. A sincere thanks goes to Sarah Rodgers, Caroline O'Brien, Patty Bowman, and Urszula Pyzio for all their help. I am grateful to have shared some great conversations with each of them.

I also wish to thank past and present staff of the I18 microfocus beamline at Diamond. Particular thanks to Tina Geraki and Sylvia Britto for their help and knowledge, especially with troubleshooting the many times during the method development stage of the project where things kept seeming to go wrong! Thank you to Steve Keylock for 3D-printing components and making various mounts and adjustments throughout the different iterations of sample preparation trials. Thank you to Rhiannon Boseley, for all her help and knowledge in the latter stages of the project. And thank you to Ann-Kathrin Geiger for her invaluable help throughout.

Thank you to Wei Wang and Jiabao Xu at Begbroke Science Park for their help with Raman spectroscopy and for allowing me to use their Raman instrument. Likewise, thank you to Andrew Dodson at Reading University for his help with ICP-MS and running the ICP-MS samples.

A massive thank you to my Mum, Dad, Adam, and Lauren, for their unceasing support, allowing me to vent various frustrations when things go wrong, celebrating with me when things go well, and, perhaps most importantly, plying me with food and coffee. Likewise to my wonderful friends, especially Howard, thank you for your support and encouragement.

Finally, I wish to thank the Biotechnology and Biological Sciences Research Council (BBSRC) for providing me with a studentship and Linacre College for awarding me a scholarship to carry out this work. I would additionally like to thank Linacre College and the British Society for Plant Pathology (BSPP) for providing additional funding which allowed for an extension of time due to COVID-19 disruption.

Statement of Collaboration

Custom 3D-printed components for the preparation and mounting of plant samples for synchrotron study were designed and made by Steve Keylock (mechanical technician, I18 beamline, Diamond Light Source).

Athira Menon (DPhil student in the Preston Lab) assisted with bioluminescence imaging discussed in Chapter 3.

Dr. Rhiannon Boseley (post-doctoral research associate, I18 beamline, Diamond Light Source and University of Oxford) assisted with aspects of Chapter 3. Specifically, Rhiannon made some of the zinc standards for XANES analysis, pre-processed XANES

standard and sample spectra, extracted spectra from XANES sample maps, and performed LCF fits.

Numerous members (particularly Alison Hochen and Morgan Wade) of the Preston lab assisted with apoplast extraction for ICP-MS in Chapter 3 due to the large volume of plants to process and time-sensitive nature of the experiment.

Carolin Artmann (visiting undergraduate student, Universität Bielefeld) assisted with aspects of Chapter 5. Carolin performed some of the replicates of plate reader-based tolerance and roGFP assays, though the experiments were designed and data was analysed by me.

Table of Contents

LIST OF ABBREVIATIONS AND DEFINITIONS 1

CHAPTER 1: INTRODUCTION AND LITERATURE REVIEW 2

1.1 Overview 2

1.2 Heavy metals 4

1.3 Metal hyperaccumulation 5

1.4 The "elemental defence" hypothesis 12

1.5 Metal and non-metal defences in *Noccaea caerulescens* 17

1.6 The *Noccaea caerulescens*-*Pseudomonas syringae* model system 20

..... 25

..... 25

1.7 Synchrotron-based X-ray imaging and spectroscopy 26

1.8 Research aims and rationale 32

CHAPTER 2: MATERIALS AND METHODS 34

2.1 Plant growth conditions 34

2.2 Bacterial strains, media, and culture conditions 35

2.3 Chemicals 37

2.4 Inoculation of plants 37

2.5 Mini-Tn7 delivery by four-parental mating conjugation 37

2.6 Bioluminescence imaging 38

2.7 Histology section preparation and imaging 39

2.8 2D-XRF data collection, image processing, and analysis 40

2.9 Apoplast extraction 42

2.10 ICP-MS sample preparation and analysis 44

2.11 XANES standards preparation 45

Zinc Phytate 46

Zinc Cysteine 46

Zinc Succinate *46*

Zinc Oxalate *47*

Zinc Citrate *47*

Zinc Phosphate *47*

Zinc Aspartate *47*

Zinc Histidine *47*

Zinc Malate *47*

Zinc Glutamate *47*

Zinc Nicotianamine *47*

2.12 XANES MEASUREMENTS AND ANALYSIS 48

2.13 3D-XRF TOMOGRAPHY DATA COLLECTION AND IMAGE ANALYSIS 49

2.14 PREPARATION OF ROGFP2 BACTERIAL TRANSFORMANTS AND CONTROL STRAINS 50

2.15 MEASUREMENT OF BACTERIAL INTERCELLULAR REDOX STATE WITH ROGFP 51

2.16 BACTERIA TOLERANCE ASSAYS 53

2.17 RAMAN MICROSPECTROSCOPY SAMPLE PREPARATION, DATA ACQUISITION, AND ANALYSIS 54

CHAPTER 3: MONITORING ZINC DISTRIBUTION AND SPECIATION IN HEALTHY AND INFECTED *NOCCAEA CAERULESCENS*..... 56

3.1 INTRODUCTION..... 56

3.2 RESULTS 59

3.2.1 Determining the pathogenicity of Pseudomonas syringae pv. maculicola NCPPB2038 in Noccaea caerulescens..... 59

3.2.2 Development of a pipeline to prepare and mount transverse sections of leaf on the I18 beamline at Diamond Light Source 60

3.2.3 XRF imaging of healthy and infected Noccaea caerulescens 69

3.2.4 ICP-MS analysis of healthy and infected Noccaea caerulescens apoplast 81

3.2.5 XANES analysis of healthy and infected Noccaea caerulescens 85

3.3 DISCUSSION 91

CHAPTER 4: CRYO-XRF TOMOGRAPHY OF *NOCCAEA CAERULESCENS* 99

4.1 INTRODUCTION 99

4.2 RESULTS 100

4.2.1 Mounting test with Arabidopsis thaliana 100

4.2.2 Comparison of metal distributions in seeds of Noccaea caerulescens and Arabidopsis thaliana 102

..... 105

4.2.3 3D-XRF tomography of young and mature Noccaea caerulescens leaves 105

4.3 DISCUSSION 114

CHAPTER 5: UNDERSTANDING THE EFFECT OF ZINC AND REACTIVE OXYGEN ON THE VIABILITY OF *PSEUDOMONAS SYRINGAE* 119

5.1 INTRODUCTION 119

5.2 RESULTS 123

5.2.1 Investigating the zinc and ROS tolerance of Pseudomonas syringae 123

..... 132

5.2.2 Investigating the cellular redox state of zinc and ROS stressed Pseudomonas syringae 133

5.2.3 In vitro Raman microspectroscopy of zinc stressed Pseudomonas syringae 138

5.3 DISCUSSION 147

CHAPTER 6: GENERAL DISCUSSION AND CONCLUSIONS 152

BIBLIOGRAPHY 158

APPENDIX 187

List of Abbreviations and Definitions

AWF	Apoplastic washing fluid
B11	*Pseudomonas syringae* pv. syringae SnB11
CFU	Colony forming units
DPI	Days post inoculation
eV	Electron volt
ICP-MS	Inductively coupled plasma mass spectrometry
Pca	*Pseudomonas cannabina* pv. alisalensis ES4326
Psm	*Pseudomonas syringae* pv. maculicola NCPPB2038
ROI	Region of interest
ROS	Reactive oxygen species
T3SS	Type III secretion system
XANES	X-ray absorption near-edge structure
XAS	X-ray absorption spectroscopy
XRF	X-ray Fluorescence

Extra low zinc	*Noccaea caerulescens* plants grown on 10 μM zinc
Low zinc	*Noccaea caerulescens* plants grown on 30 μM zinc
High zinc	*Noccaea caerulescens* plants grown on 300 μM zinc
Diamond	Diamond Light Source

Chapter 1: Introduction and literature review

1.1 Overview

Metal hyperaccumulation is an unusual trait that has been identified in approximately 700 plant species to date (1,2). Plants with this trait are not only hyper-tolerant to, but also actively sequester heavy metals in their aerial tissues (3). A number of hypotheses have been suggested to explain this phenomenon but the theory with the most support is commonly known as the “elemental defence” hypothesis. In this, accumulated heavy metal is said to be directly toxic to pathogens and herbivores, thereby imparting an adaptive advantage (4,5).

Work by Fones et al. has provided support for the elemental defence hypothesis using the model system of the metal hyperaccumulating plant *Noccaea* (formerly *Thlaspi*) *caerulescens* and bacterial pathogens belonging to the *Pseudomonas syringae* species complex (henceforth referred to as *P. syringae* when discussed in general terms), where it was shown that a greater degree of protection is conferred with increasing concentration of zinc in foliar tissue (6). However, the mechanistic involvement of hyperaccumulated metal in this elemental defence has yet to be fully demonstrated.

Previous reports have indicated that zinc is likely to be predominantly stored in the epidermal vacuoles of a hyperaccumulator’s leaves, theorised to be a strategy employed by the plant to reduce toxicity (7,8). However, it is also well established that *P. syringae* inhabits the extracellular apoplastic space of leaf tissue, where metal concentrations are elevated in metal hyperaccumulating plants relative to non-metal hyperaccumulating plants, but considerably lower than vacuolar concentrations (6). It is currently unknown whether this apoplastic metal concentration is sufficient for *in planta* inhibition or what happens upon infection to demonstrate the observed defensive effect. As the degree of metal toxicity will depend on the local concentration and chemistry of the metal at the specific areas of

pathogen localisation, however, bulk-measurements of plant extracts are not sufficient to study this interaction.

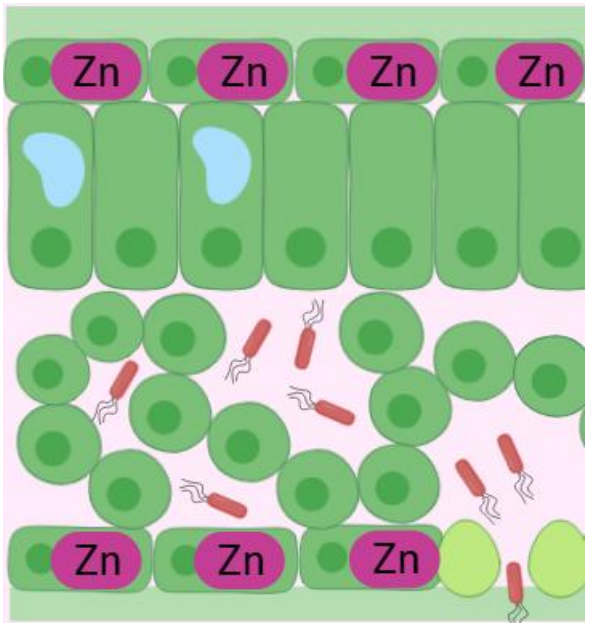


Figure 1: Cartoon of a transverse section of leaf tissue indicating the relative localisations of zinc in epidermal cells and *Pseudomonas syringae* in the extracellular spaces, after entering the leaf via natural openings. Created using BioRender, using, for example (6-8) to guide component location.

The primary aim of this work, therefore, is to investigate the mechanism by which hyperaccumulated zinc provides a defence against bacterial disease using multi-modal imaging techniques and spectroscopy; notably using high resolution synchrotron-based X-ray fluorescence microscopy to identify the distribution of zinc in healthy tissue, and to determine if and how this may change upon infection. Additionally, the potential synergistic role of zinc in combination with other plant defences, namely reactive oxygen, will be explored.

Much of this work was undertaken in partnership with Diamond Light Source, a synchrotron facility, where sample preparation and mounting pipelines were established for the high-resolution analysis of frozen-hydrated plant tissue. In this introductory chapter, the topics relevant to this work will be introduced.

1.2 Heavy metals

Heavy metals, often defined as those with a density greater than 5 g/cm^3, are necessary to plants in low concentration as they can, for example, act as cofactors in enzymatic processes or as catalysts (9,10). Due to their essential role in plant metabolic processes, many metals are considered micronutrients (11).

Many of these essential metals are first series transition metals and, as such, possess redox potential that facilitates their role as catalytically active cofactors (12,13). For example, the electron transfer function of iron is known to have a role in photosynthesis, nitrogen fixation and oxygen metabolism (14–16). However, not all of the essential metals are redox active. For example, the stability of the divalent zinc cation (Zn^{2+}) enables its use as a Lewis acid type catalyst (17). In this situation, Zn^{2+} can accept an electron pair and thus can be directly involved in bond making and breaking processes (17,18). Specifically, zinc has been shown to be necessary for normal RNA polymerase function, carbohydrate metabolism and protein synthesis and a deficiency of the metal leads to abnormalities in plants including stunted growth (18,19).

Many heavy metals exist naturally in the soil and some soils have naturally elevated levels of heavy metals; however, concentrations can also often increase dramatically due to anthropogenic activities, for example in areas of industrial activity or those surrounding mining sites (20). At elevated soil concentrations, heavy metals can easily become toxic to plants. Elevated concentrations of heavy metals in plant tissue may lead to competition and potential displacement at cofactor protein binding sites, resulting in a loss of activity (2,21). Additionally, elevated zinc concentrations may interfere with other metal transport processes (22). For example, increased extracellular zinc was found to competitively inhibit manganese transport in *Streptococcus pneumoniae* resulting in reduced superoxide dismutase activity and increased oxidative stress (23).

Toxicity from heavy metals is also likely to arise due to the to the overproduction of reactive oxygen species (ROS), inducing oxidative stress and cell death (24,25). Redox active metals such as iron and copper produce ROS directly as by-products of redox reactions. An example of this, outlined in Equation 1, is the Fenton reaction in which iron catalyses the formation of hydroxyl radicals from hydrogen peroxide (9,26).

Equation 1: Fenton Reaction

$$H_2O_2 + Fe^{2+} \rightarrow \cdot OH + OH^- + Fe^{3+}$$

Metals lacking redox activity, such as zinc, can cause elevated ROS production indirectly; for example this may occur via cofactor displacement at binding sites of ROS scavenging enzymes such as catalases and superoxide dismutase (26,27).

1.3 Metal hyperaccumulation

Some plants, known as metallophytes, are known to survive in areas of heavy metal contamination. Of these, some may be defined as hyperaccumulators; a term originally introduced in 1977 by Brooks et al to refer to “a group of highly unusual plants” with the ability to accumulate over 1000 μg/g nickel (dry weight), a metal which normally would induce toxicity at concentrations of 50 μg/g (28,29). Today, plants considered to be hyperaccumulators uptake and store exceptionally high concentrations of one or more of a range of heavy metals in their aerial tissues without showing signs of toxicity, the threshold values of which can be seen in Table 1 (1,3).

Table 1: Modified from Global Hyperaccumulator Database, Reeves et al, 2018. No longer funded/online – information obtained directly from corresponding author Antony van der Ent, February 2024. Threshold values for dry weight.

Metal Hyperaccumulation Thresholds and Occurance

Element	Threshold (µg/g)	Families	Genera	Species
Arsenic (As)	>1000	1	2	5
Cadmium (Cd)	>100	7	9	43
Cobalt (Co)	>300	18	33	43
Copper (Cu)	>300	20	44	53
Chromium (Cr)	>1000	1	1	1
Lead (Pb)	>1000	7	9	9
Manganese (Mn)	>10,000	16	24	42
Nickel (Ni)	>1000	54	131	532
Selenium (Se)	>100	7	15	41
Thallium (Tl)	>100	1	2	2
Zinc (Zn)	>3000	9	12	21

To date, over 700 plant species have been identified to possess this trait, with the majority belonging to the Brassicaceae and Phyllanthaceae families (1). Most hyperaccumulator plants accumulate a single metal specifically and approximately 75% of plants with this trait are nickel hyperaccumulators (2). This is likely to be in part due to the high and widespread availability of nickel in soils – with nickel-rich serpentine soils accounting for over 3% of the Earth's surface (30,31). Beside nickel, various other metals have been demonstrated to be hyperaccumulated by specific plants. Copper, cobalt, manganese, selenium, and zinc, for instance, have all individually been found to be hyperaccumulated by between 21-53 different plant species. Interestingly, cadmium, a non-essential and typically highly toxic metal, is also hyperaccumulated by a number of plant species including the brassica *Noccaea caerulescens* (1).

N. caerulescens (Figure 2) is often used as a model species expressing the hyperaccumulation trait as, unusually, it has the ability to hyperaccumulate three heavy metals: zinc, nickel, and cadmium (29). Likewise, its use as a model hyperaccumulator has benefitted from its close relationship to the extensively studied *Arabidopsis thaliana*, sharing approximately 88.5% nucleotide identity in coding regions (3,32). Particularly, the population originating from a site surrounding a zinc/cadmium smelter in Prayon, Belgium, is frequently studied and is notable for its high tolerance of zinc.



Figure 2: (A) *N. caerulescens* plants found at the Nenthead mining site in Cumbria, UK. Photo courtesy of R. Boseley. (B) *N. caerulescens* plants found at a former mining site in Snowdonia, UK. Photo courtesy of G. Preston. (C) Hydroponically cultivated Prayon ecotype of *N. caerulescens*.

However, *N. caerulescens* is a variable species where specific populations exhibit differences in their hyperaccumulation ability (33,34). As noted by Sterckeman et al, *N. caerulescens* is found in three edaphic environments throughout Europe: calamine, serpentine and non-metalliferous (35). Calamine populations are those typically found surrounding mining or smelting sites where the soil contains elevated concentrations of zinc, cadmium and lead. Examples of calamine populations include Ganges and Viviez (France), the former of which exhibits remarkably high accumulation and tolerance to cadmium, in addition to the aforementioned Prayon (34,35). Serpentine populations exist in areas of soil particularly rich in nickel, derived from ultramafic rock erosion, and include Monte Prinzera (Italy) noted for its high nickel accumulation (35–37). Finally, non-metalliferous populations

exist in areas of uncontaminated, or otherwise non-metalliferous, soil and include the Wilwerwiltz (Luxembourg) population (35).

Summarised in Figure 3, Fones et al noted that the capacity for zinc accumulation varied between four hydroponically cultivated populations of *N. caerulescens.* Using atomic absorption spectroscopy to measure whole-leaf zinc concentrations, the calamine population of Prayon was found to accumulate significantly more zinc than the remaining three populations in plants grown on both 30 µM and 300 µM of zinc. Included in these three remaining populations was the fellow-calamine population of Ganges in which reduced zinc accumulation relative to Prayon was observed in the plants grown on 300 µM of zinc. Interestingly, the non-metalliferous population, Wilwerwiltz, expressed a similar degree of metal accumulation compared to the three populations from metalliferous environments (38).

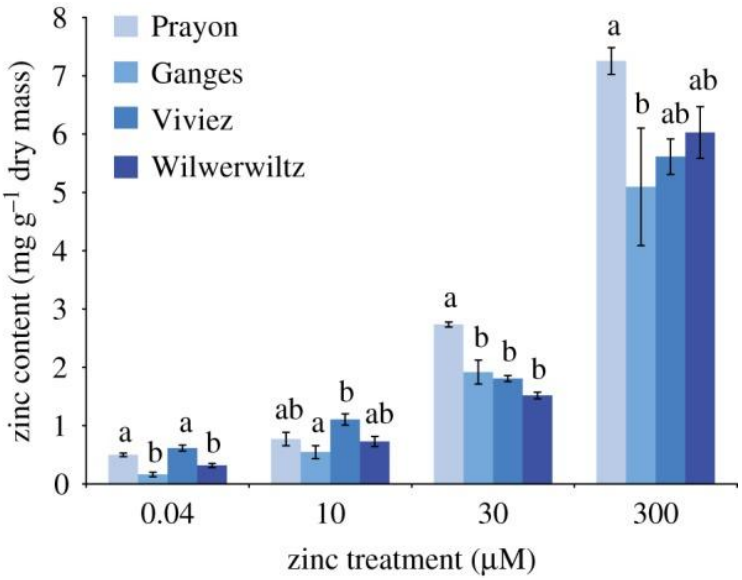


Figure 3: Zinc concentrations in *N. caerulescens* bulked leaf samples from four populations as measured by atomic absorption spectroscopy. Data are mean values of two independent experiments and error bars indicate standard error. Means that are not significantly different (Bonferroni simultaneous comparisons) are marked with the same letter; letters apply only within the group compared by each ANOVA, i.e. within zinc treatments. Taken from Fones et al, 2019.

The accumulation ability of different ecotypes may also vary depending on its environment. Escarré et al noted that the accumulation ability of the same populations of *N.*

caerulescens growing on culture soils (garden soil supplemented with metal) was closer to those in field soils than plants growing in hydroponics (39). However, Kozhevnikova et al found the opposite – that *N. caerulescens* grown in hydroponics are representative of those in nature (40). It is therefore unclear whether hydroponic cultivation completely accurately represents the field setting. However, the major benefit of being able to finely control the amount of metal a plant is exposed to in hydroponic cultivation warrants its use in the study of metal hyperaccumulating plants.

Heavy metals enter the plant *via* the root system and, in non-accumulating plants, are often excluded from the aerial tissue preventing phytotoxicity (41). However, in hyperaccumulators, heavy metals are actively transported and stored in the aboveground tissues. It has been suggested that, in *N. caerulescens,* enhanced uptake of zinc into the roots is facilitated due to an increased copy number and expression of the genes belonging to the *ZIP (*Zinc-regulated transporter Iron-regulated transporter Proteins) family (2,42). These genes encode for cation transporters that are located in the plasma membrane. Once the metal enters the root, it is transported through the symplast and loaded into the xylem via the ATPase *HMA4* (Heavy Metal transporting ATPase). As with the *ZIP* transporters, there appears to be a greater overexpression of the genes encoding these transporters in hyperaccumulator plants compared to related non-accumulators (2,43–45). In addition to possessing a greater number of these *HMA4* transporters, the root-to-shoot translocation of metals has been shown to occur at a faster rate in hyperaccumulators than in non-accumulators (42,46,47).

Metals are subsequently unloaded from the xylem and sequestered into the leaves. It has previously been suggested that the majority of accumulated zinc in *N. caerulescens* is transported via the apoplast and stored in the vacuoles of the epidermis (Figure 4) (18,48,49). This is likely a strategy employed by the plant to avoid disruption to important cellular processes by keeping the cytoplasmic concentration of metals to a minimum (8,49). Likewise, Monsant et al demonstrated using particle-induced X-ray emission (PIXE) that

approximately 88% of zinc was stored in the vacuoles of the upper and lower epidermis in the Prayon population (50). Though the majority of accumulated zinc is likely to be stored in the epidermal vacuoles of *N. caerulescens*, zinc has also been shown to be distributed in the vacuoles and cell walls of mesophyll cells (48,49). In plants that possess trichomes, these structures are also sites of metal accumulation both in hyperaccumulators and non-hyperaccumulators such as *Arabidopsis thaliana* (51–53).

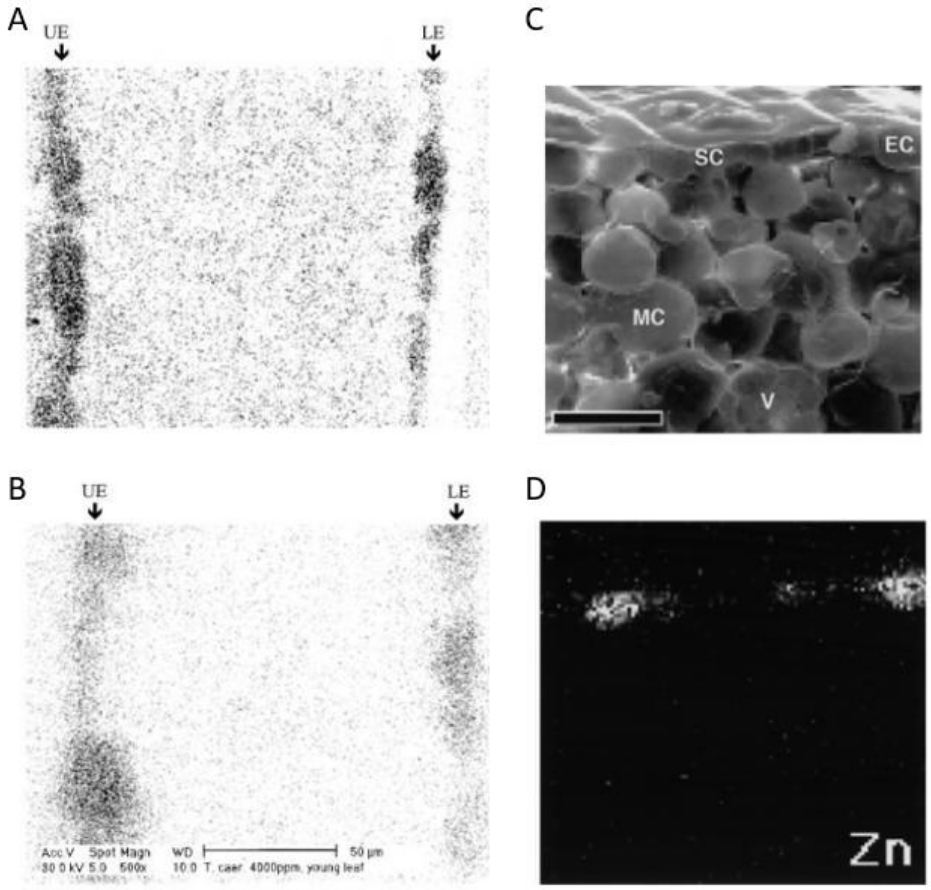


Figure 4: Elemental mapping of zinc in *N. caerulescens.* A and B taken from Küpper et al, 1999 and show energy dispersive X-ray microanalysis (EDXMA) scans from transverse sections of mature (A) and young (B) leaves. C and D taken from Frey et al, 2000 and show SEM (C) and EDXMA (D) from the same leaf of *N. caerulescens.* UE = upper epidermis, LE = lower epidermis, SC = stomatal complex, EC = epidermal cell, MC = mesophyll cell, V = vein.

Detoxification in hyperaccumulators is likely to be aided by chelation of the heavy metal in addition to the increased presence of ROS scavenging enzymes (54). However, the identity of the chelators zinc is complexed to in hyperaccumulating plants seems to vary between species. Sarret et al, studying the hyperaccumulator *Arabidopsis halleri,* used X-ray

absorption spectroscopy (XAS) to provide evidence that the majority of foliar zinc was complexed to malate (55). Conversely, Salt et al used the same methodology to suggest that 40% of zinc present in the leaves of *N. caerulescens* is complexed with citrate and observed no presence of malate (56). Amino acids, particularly histidine, are also thought to have an important role in metal detoxification. For example, Salt et al found that histidine has a major role in the detoxification of zinc in the roots of *N. caerulescens* (56).

In addition to these small organic and amino acids, a number of other compounds have been observed to be involved in the complexation of metals in hyperaccumulator and non-hyperaccumulator plants. Notably, compounds containing the thiol moiety are commonly found in plants and include glutathione, phytochelatins and metallothioneins (57). Phytochelatins are small cysteine-containing peptides and are thought to be of particular importance in the detoxification of the non-essential metal cadmium (57,58). This was demonstrated by Zhang et al in the cadmium hyperaccumulator *Sedum alfredii* (59). A "building block" of phytochelatins, glutathione, has additionally been shown to act as a monodentate ligand in plants (57). Specifically, it is thought to be involved in the detoxification of nickel in various hyperaccumulating species of *Noccaea* (60). Lastly, while the exact function of metallothioneins is not completely understood, it is thought that they are involved in metal, particularly copper, homeostasis and may have a more significant role in non-hyperaccumulating plants (58). While chelation is known to be involved in the detoxification of sequestered heavy metals, there is less understanding over the involvement of ligands in the various transport mechanisms. Nicotianamine, an ubiquitous metal chelator in plants, is believed to be involved in root-to-xylem loading mediated by YSL (Yellow Strip 1-Like protein) transporters (61).

As summarised by Rascio and Navari-Izzo, hyperaccumulator plants therefore have "a much greater capability of taking up heavy metals from the soil; a faster and effective root-to-shoot translocation of metals; and a much greater ability to detoxify and sequester huge amounts of heavy metals in the leaves" than non-accumulators (2).

1.4 The “elemental defence” hypothesis

In an early review by Boyd and Martens, several theories were proposed as to why hyperaccumulator plants may have evolved to possess the hyperaccumulation trait. These are: increased metal tolerance/disposal from plant body, interference and allelopathy, drought tolerance, and pathogen and herbivore defence (62).

The first of these theories suggests that hyperaccumulators may have simply evolved out of necessity to be hyper-tolerant to metals in order to survive in areas where there is high heavy metal concentration in the soil. Metals are thought to be sequestered in aerial tissues before the heavy-metal-containing leaf is shed from the plant and thus phytotoxicity is avoided. However, there is little evidence to support this theory and, in fact, it has been shown that the hyperaccumulation and hyper-tolerance traits are genetically independent (63–65).

The interference and allelopathy theory suggests that hyperaccumulator plants can cause local enrichment of heavy metal in surface soil from the recycling of element-rich decaying tissue (2). This local enrichment may prevent neighbouring plants, that lack heavy metal tolerance, from establishing and thus reducing competition for the hyperaccumulator plant (2,65). While not widely studied, there has been some support for this hypothesis. Elemental allelopathy by the arsenic hyperaccumulating fern *Pteris vittata* was studied by Jaffe et al. In this work, the authors discovered that the concentration of arsenic in the soil directly surrounding the base of a *P. vittata* plant was approximately twice that of soil three meters away from the plant, and additionally that the levels of arsenic surrounding the plant was high enough to be inhibitory to competitors (66). Likewise, Mehdawi et al, studying the selenium hyperaccumulators *Astragalus bisulcatus* and *Stanleya pinnata* found there to be elevated soil concentrations of selenium surrounding these hyperaccumulators compared to surrounding non-accumulators. It was also observed that there was reduced ground cover of plants surrounding the hyperaccumulator plants (65,67).

The third hypothesis suggests that the hyperaccumulation trait may have evolved to increase the plant's resistance to drought. It has been proposed that heavy metals may act as osmolytes or have a role in water-conservation (65,68). Again, however, there have been few studies on this hypothesis, but of those that do exist, the consensus is generally that there is not a correlation between hyperaccumulation and drought resistance. For example, a study by Statwick et al found no evidence that selenium improved drought tolerance in two hyperaccumulators of the *Astragalus* genus (69).

The final theory suggests that the hyperaccumulated heavy metals provides a defence against pathogens and/or herbivores and thus impart an adaptive advantage over non-accumulating plants (4). This theory is commonly known as the "elemental defence" hypothesis and, although it is generally the most supported of suggested theories, this support is not universal (70). These non-supporting studies, however, typically involve herbivores and viruses and may be confounded by co-evolution of hyperaccumulator plants with pests and pathogens that themselves have increased metal tolerance (70,71).

Nickel hyperaccumulation in the Brassicaceae *Streptanthus polygaloides* was found to provide an effective defence against insect herbivory in an early study by Martens and Boyd (72). Accumulated zinc and cadmium in the hyperaccumulator *Arabidopsis halleri* have additionally been shown to provide a defence against insect species with varying feeding styles (73). Likewise, defence against aphids has been demonstrated by Hanson et al in the selenium accumulator *Brassica juncea* (74).

Fewer studies have looked into defence against pathogens. However, work by Fones et al has provided further evidence for this theory, using the hyperaccumulator plant *N. caerulescens* and the bacterial pathogen *Pseudomonas cannabina* pv. alisalensis (Pca) (formerly *Pseudomonas syringae* pv. maculicola) as a model system (25). This system shall be described in greater detail in section 1.6, but, in brief, increasing concentrations of zinc, cadmium, and nickel were found to provide a greater degree of defence against the invading pathogen, with reduced disease symptoms and fewer colony forming units (CFU) produced

during colony count infection assays (6,25). However, the effectiveness of the metal in defence depends on the type of invading pathogen (65). As discussed earlier, hyperaccumulated metals are predominately stored in epidermal vacuoles, with additional sites of storage being cell walls and apoplast, and storage is avoided in the cytoplasm to prevent disruption to important cellular processes (7,40). Thus, intracellular pathogens such as viruses may be less sensitive to hyperaccumulated metals than apoplast-inhabiting biotrophic and necrotrophic bacteria or haustoria-forming fungi (65,71).

More recently, an additional two theories have been suggested, expanding on from the latter-described “elemental defence” hypothesis: the defensive enhancement and joint effects hypotheses (70,75). The first of these is based on the observation that even at levels below the hyperaccumulation threshold, a protective effect has been demonstrated (71). The theory thus states that plants that uptake a so-called “defensively effective” concentration of metal have increased fitness, which drives the hyperaccumulation trait to evolve in a stepwise fashion (70). This defensive enhancement theory has been suggested by Boyd to be linked to the joint effects theory, where the effect of reduced inorganic defence is counteracted by an additive or synergistic effect from the plants’ organic/innate defences in conjunction with the metal (70).

This enhanced “joint” defence has been demonstrated by Cheruiyot et al who fed an artificial diet of metal in combination with organic compounds to the model herbivore *Spodoptera exigua* (beet armyworm). The authors used pairwise combinations of cobalt, copper, nickel, and zinc with each other (metal/metal joint effect) and with nicotine, mustard seed powder, and tannic acid (metal/organic compound joint effect). As shown in Figure 5, each metal/metal and metal/organic compound combination provided either an additive or synergistic effect at lethal concentrations; the former being defined by the level of defence being equal to the sum of the two components and the latter meaning the defensive effect is enhanced above that of the additive effect (75,76). Likewise, as outlined in Figure 6, the same observation was found when sublethal concentrations were given, with the greatest

synergistic effects observed when zinc was given in combination with any of the organic compounds tested (76). As noted by the authors, these sublethal effects are of particular interest as, if they were to occur *in planta*, they would “extend the lower limits of elemental defences even further and show elemental defences to be defensively effective at relatively low concentrations in plants”, which would provide support for both the defensive enhancement and joint effects hypotheses for hyperaccumulation described by Boyd and would indicate that studies on the effect of metals in plant defence could be broadened to include non-hyperaccumulator plants (70,76).

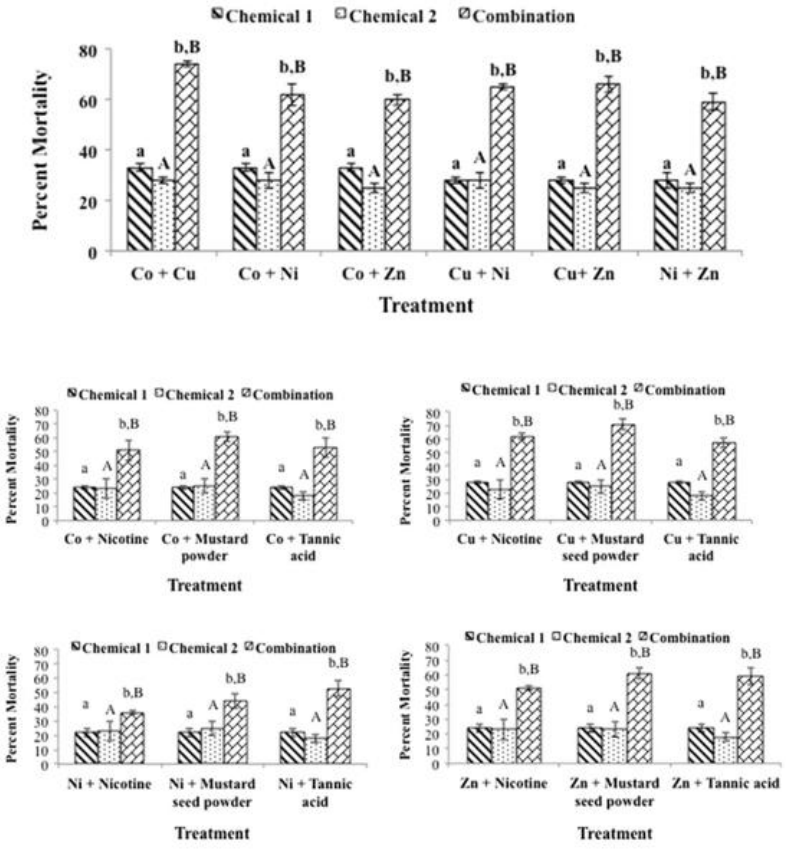


Figure 5: Additive and synergistic effects of metals in combination with either other metals (top) or organic compounds (below) given as artificial diets at lethal concentrations to the insect *Spodoptera exigua*. Standard error is shown (n=3 in all cases). Statistical analysis was performed by means of Mann-Whitney U tests, $P < 0.05$, where lower-case letters compare Chemical 1 against the combination treatment and upper-case letters compare Chemical 2 against the combination treatment. Taken from Cheruiyot et al, 2015.

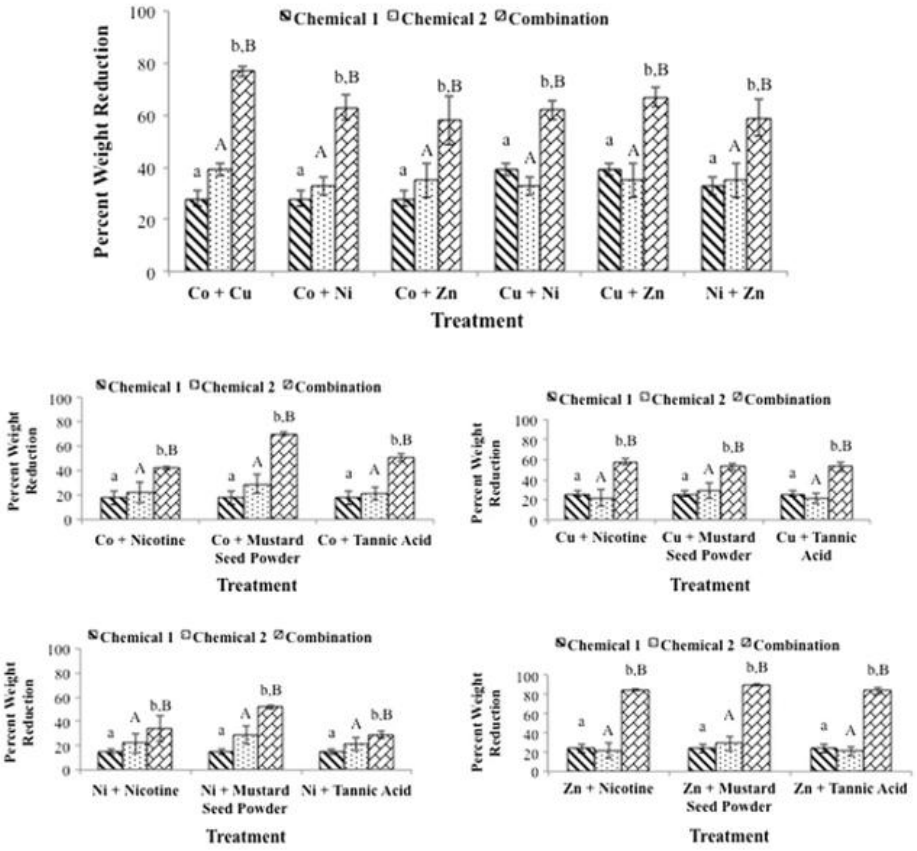


Figure 6: Additive and synergistic effects of metals in combination with either other metals (top) or organic compounds (below) given as artificial diets at sublethal concentrations to the insect *Spodoptera exigua.* Standard error is shown (n=3 in all cases). Statistical analysis was performed by means of Mann-Whitney U tests, $P < 0.05$, where lower-case letters compare Chemical 1 against the combination treatment and upper-case letters compare Chemical 2 against the combination treatment. Taken from Cheruiyot et al, 2015.

While there is evidence to suggest that hyperaccumulated metal may have a synergistic or additive effect in conjunction with innate plant defences, it is also reasonable to assume that there may be antagonistic interactions (75). Likewise, the evolution of the hyperaccumulation trait may have also led to these innate defences becoming dampened or altered.

1.5 Metal and non-metal defences in *Noccaea caerulescens*

In order to protect themselves against biotic stress, plants have developed a complex arsenal of defences that pathogens must evade in order to establish infection. Upon recognition of pathogen-associated molecular patterns (PAMPs) (also referred to as microbe-associated molecular patterns – MAMPs) by pattern recognition receptors (PRR), for example flagellin produced by *Pseudomonas syringae*, the plant's first line of defence is activated – a process known as PAMP-triggered immunity (PTI) (77). In response, pathogens that successfully evade PTI release virulence and effector proteins that further work to supress the plant's immune system. In some disease resistant plants these secreted effectors trigger a further layer of defence known as effector triggered immunity (ETI), through the direct or indirect recognition of effectors by resistance (*R*) genes, which is often associated with a form of localised, programmed cell death known as the hypersensitive response (HR) (78). Figure 7 provides an overview of some typical innate plant defence processes (79).

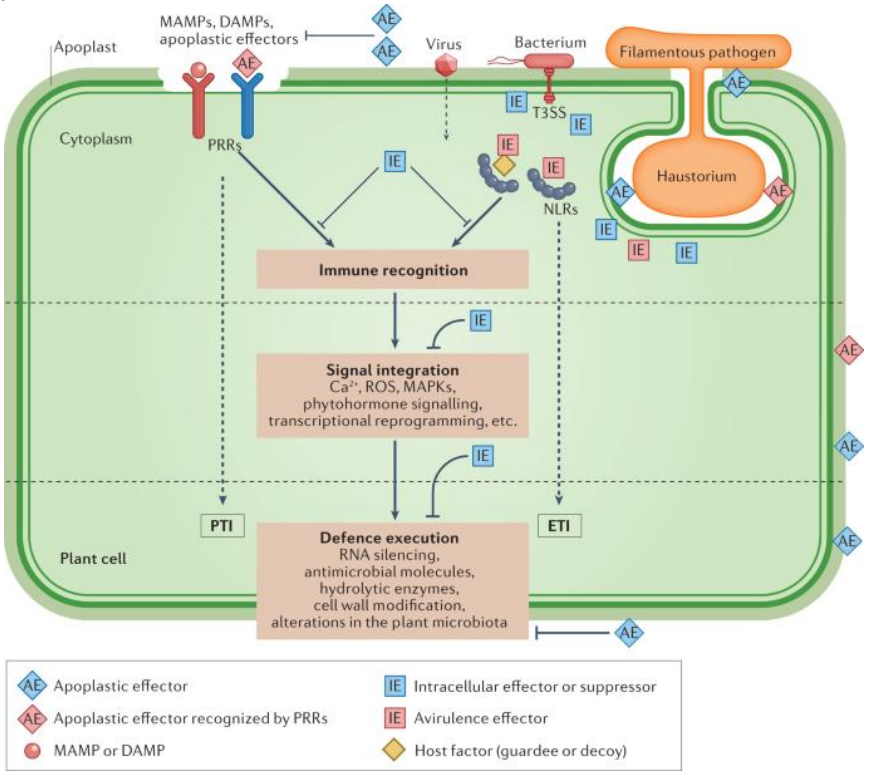


Figure 7: Overview of the plant innate immune system. Taken from Wang et al, 2022

One of the earliest immune responses to pathogens is initiation of the so-called oxidative burst which produces antimicrobial reactive oxygen species (ROS) and triggers a signalling cascade, leading to downstream effects including HR and callose deposition in the form of antimicrobial-enriched, cell wall appositions known as papillae, which act as physical and chemical barriers to limit pathogen spread (77,78,80–82). Another early response to pathogen infection is the initiation of the salicylic acid (SA) signalling pathway which mediates plant defence gene expression and may act synergistically with ROS to reinforce immunity (80,83).

In addition to these inducible defences, plants possess a series of constitutive defences. Notably, glucosinolates are sulfur containing compounds that are ubiquitous in Brassicaceae. Upon maceration by microbes or herbivores, myrosinase enzymes are released causing the hydrolysis of glucosinolate into metabolites containing the toxic isothiocyanate moiety (84,85). These metabolites have been found to inhibit growth of *P. syringae* in vitro (38).

Metal, or inorganic, defences in hyperaccumulator plants are not produced through typical plant metabolic processes and cannot be broken down by enzymes from pathogens or herbivores. As a result, invading organisms have fewer strategies to evade or detoxify these defences (75). Additionally, the presence of these elemental defences may be metabolically favourable to the plant by negating the requirement for “costly” inducible organic defences (86). However, as previously discussed, hyperaccumulation is a complex trait, where a number of adaptations are required to facilitate the enhanced transport, storage, and detoxification of the metals. Thus, this can be thought of as potentially resulting in a “trade-off” whereby there is an increased cost to obtain the hyperaccumulation trait, but a decrease in cost of inducible defences (70,86).

Evidence for this so-called trade-off in defences has been observed in the Prayon population of *N. caerulescens* inoculated with *Pseudomonas cannabina* pv. alisalensis ES4326 (formerly *Pseudomonas syringae* pv. maculicola ES4326), herein Pca, where

certain defences were modified or absent entirely (87). As discussed previously, one of the first defences usually triggered by the plant in response to a pathogen is the oxidative burst. In Figure 8, an increase in Nitroblue tetrazolium (NBT) staining can be observed when *Arabidopsis thaliana* is inoculated with Pca, consistent with an increase in superoxide, a ROS. However, with *N. caerulescens*, there is not a response to pathogen but rather increasing zinc concentrations, indicating an altered ROS response (38,87). More recently, and complicating matters further, it was determined that the earlier flg22-dependent NADPH ROS burst is present in *N. caerulescens* but the later peroxidase-dependent ROS burst is absent (Johnson, Bach-Pages and Preston, unpublished).

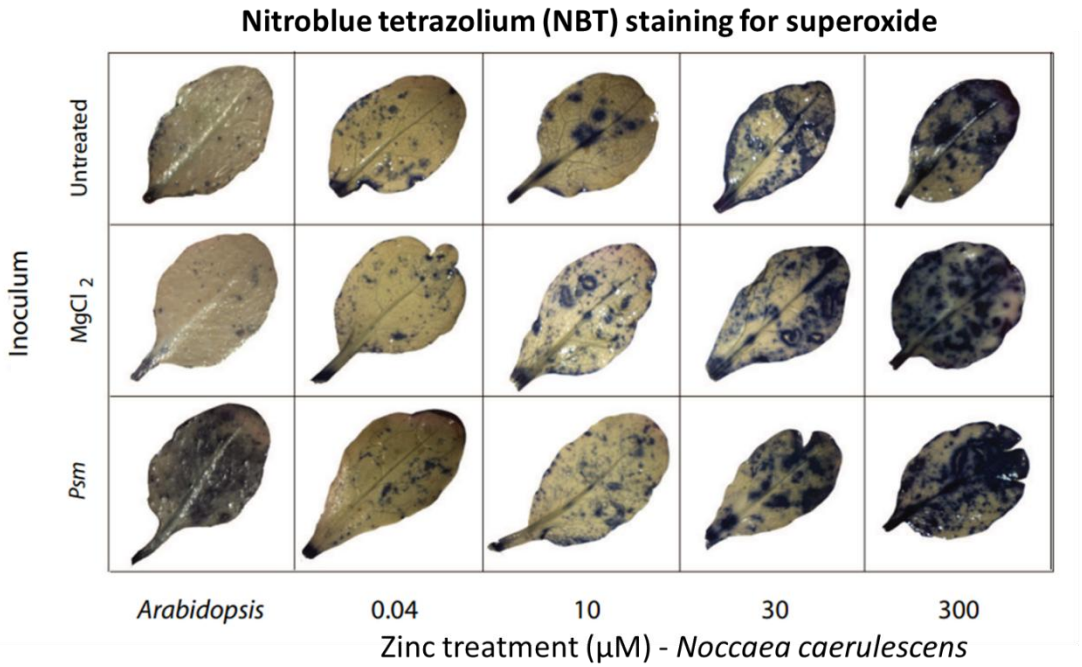


Figure 8: Nitroblue tetrazolium staining for superoxide in *A. thaliana* and *N. caerulescens* inoculated with *P. cannabina* pv alisalensis, MgCl2 (mock), or left untreated. At the time of this papers' publishing, Pca was known as *Pseudomonas syringae* pv maculicola (Psm). Adapted from Fones et al, 2013.

Furthermore, the downstream defences of callose deposition and *pathogenesis-related (PR)* gene expression were also found to be absent in *N. caerulescens* (87). It could therefore stand to reason that the constitutively high levels of ROS in *N. caerulescens*, and possibly other hyperaccumulators, may have "led to uncoupling of ROS-based defence

signalling, leaving the plants increasingly dependent on accumulated metals for defence" (87).

Additionally, production of the phytoalexin camalexin was found to be reduced in response to fungal infection in the hyperaccumulator *Arabidopsis halleri* grown on metalliferous soil indicating a negative interaction between organic and inorganic defences (53). Conflicting results, however, have been found with respect to glucosinolates. The concentrations of glucosinolates in the Prayon population of *N. caerulescens* was found to be inversely proportional to increasing zinc, with other populations – tested by the same authors – being the opposite with increasing zinc being paired with higher glucosinolate concentrations (38).

1.6 The *Noccaea caerulescens-Pseudomonas syringae* model system

As previously mentioned, *N. caerulescens* is often used as a model hyperaccumulator as it has the ability to hyperaccumulate three heavy metals: zinc, nickel and cadmium (29). Previous work has found that the Prayon population of *N. caerulescens* grown on 300 μM zinc accumulated 14000 μg/g (dry weight) zinc, well above the hyperaccumulation threshold of 3000 μg/g (6). It is also a facultative metallophyte, meaning *N. caerulescens* can survive on both metal rich and non-metalliferous soil (88,89). These traits make *N. caerulescens* an attractive model plant as they enable the effect of altering the concentration of different metals on bacterial viability to be studied.

Pseudomonas syringae is a common hemibiotroph that infects the phyllosphere of several plant species, including *N. caerulescens* (90). *P. syringae* enters through natural openings or wounds into the apoplastic space between plant cells. Once in the apoplast, it multiplies and eventually causes leaf speck disease or bleeding cankers on horse chestnut (91,92). Importantly, *P. syringae* is a known pathogen of multiple economically important

crop species (90). Typically, infection occurs via the type III secretion system (T3SS) where *P. syringae* secretes a series of effector proteins supressing the plant's immune defences and triggering the hypersensitive response in susceptible plants (90,91).

N. caerulescens has been observed to have increased resistance to Pca when grown on increasing concentrations of zinc. As shown in Figure 9A, the higher the concentration of zinc the plants are grown on, the less severe the disease symptoms. This was additionally quantified using infection assays, where significantly fewer bacteria were able to proliferate in higher zinc treated plants (Figure 9B) (6).

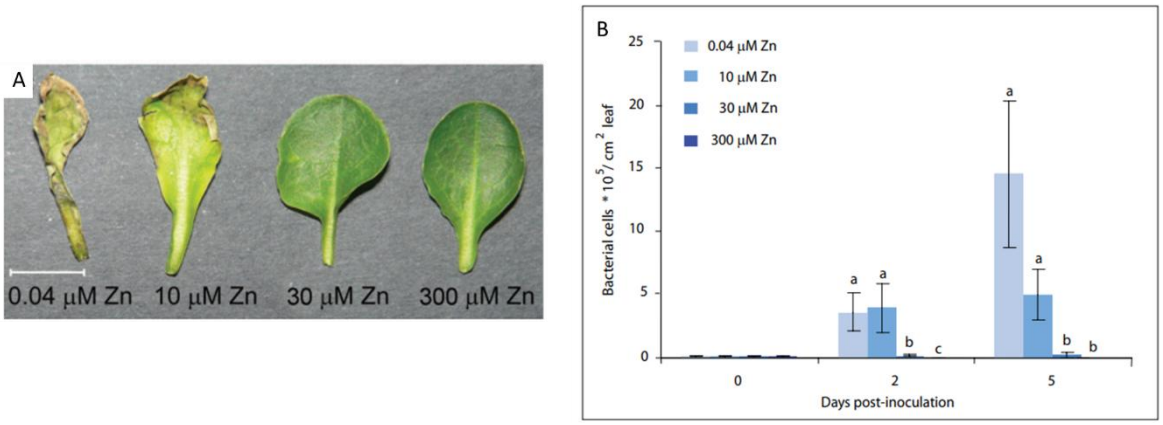


Figure 9: A) Disease symptoms in leaves of *N. caerulescens* hydroponically cultivated on different concentrations of zinc and infected with *P. cannabina* pv alisalensis. Photographs taken at 4 days post infection. B) Growth of *P. cannabina* pv alisalensis in *N. Caerulescens* hydroponically cultivated on different concentrations of zinc. Error bars indicate standard error. Taken from Fones, 2010.

The direct effect of zinc on bacterial fitness in *N. caerulescens* was demonstrated using mutants of Pca with reduced and increased metal tolerance. Bacteria with reduced metal tolerance were less able to grown in *N. caerulescens* than wildtype Pca. Conversely, mutants with increased metal tolerance were able to survive and grow more successfully than wildtype (6,25).

Due to the volume of work being carried out at Diamond Light Source, and the lack of an APHA plant health licence for work with licenced plant pathogens on the beamline and in associated laboratories, Pca was not able to be used for this work as it is not a UK-native

pathogen and was subject to licence at the time this project was undertaken. Instead, two other strains of UK-native *Pseudomonas syringae* were used throughout this work. The first, *Pseudomonas syringae* pv. maculicola NCPPB2038 (Psm), originally isolated by M.T. Dervish from *Brassica oleracea* var *Botrytis* (cauliflower; NCPPB), is from the same phylogroup as Pca (phylogroup 1) and the other, *Pseudomonas syringae* pv. syringae SnB11 (B11), is a natural endophyte of *N. caerulescens* isolated from plants growing in Snowdonia, UK, which belongs to phylogroup 2. A phylogenetic tree showing the relationship between the described strains, and others, can be seen in the Appendix, Figure 84.

Results obtained from comparative genomics analysis performed using OrthoFinder (Harper, Dodds, Emms, Preston, and Sanguankiattichai, unpublished) were used to understand the difference in effectors and toxins produced by Pca, Psm, and B11 (93). The T3SS has previously been found to be required for pathogenicity in *N. caerulescens*; two Pca mutants, *hrcN*$^{-}$ and *hrpS*$^{-}$, lacking aspects of the T3SS were not able to proliferate in *N. caerulescens* grown on any concentration of zinc (25). *Pseudomonas syringae*, like many gram-negative bacteria, rely on the T3SS to initiate disease – using needle-like apparatus to inject effector proteins into plant cells (94,95). A schematic representation of this is given in Figure 12 (96).

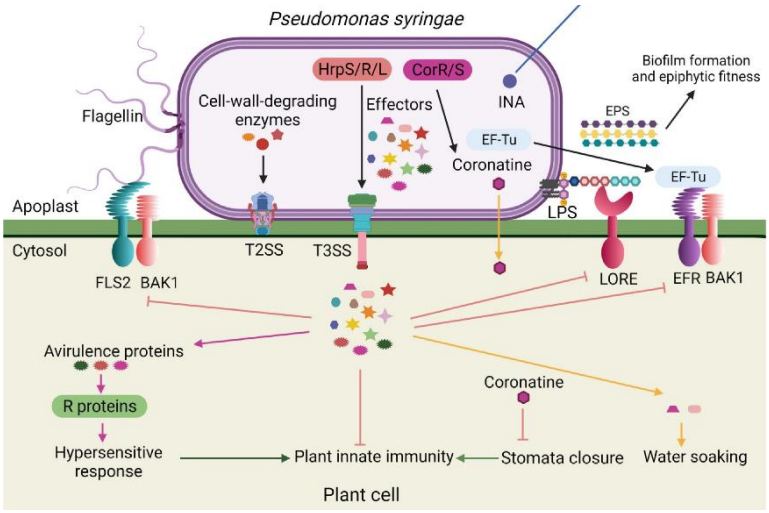


Figure 10: Cartoon schematic representation of *Pseudomonas syringae* interactions with a plant cell. The bacterium uses the type III secretion system to inject effector proteins into the plant cell to suppress host immune responses. Adapted from Chen et al, 2022.

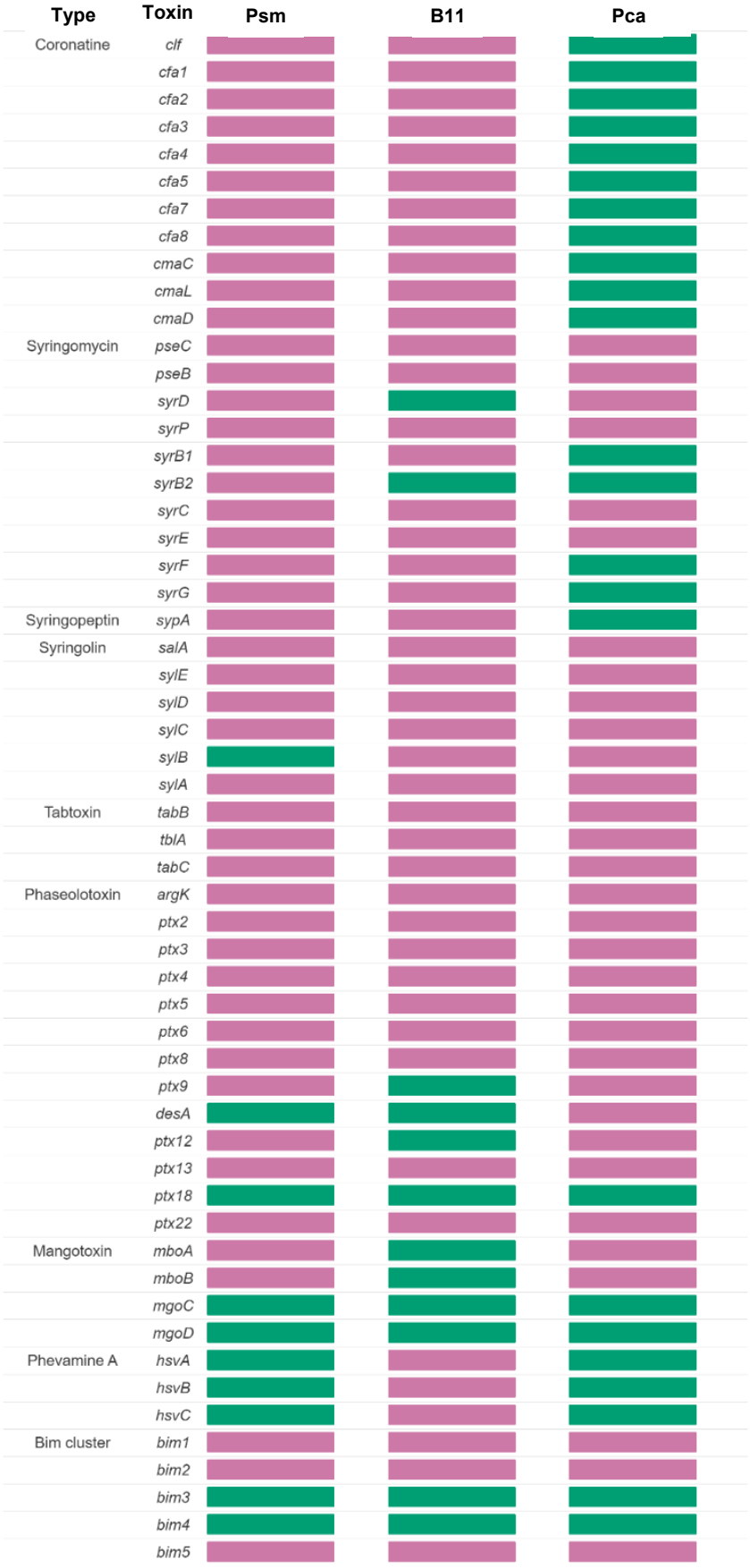
As seen in Table 2, B11 is predicted to produce comparatively few effector proteins, which perhaps contain the minimum number of effectors required for pathogenicity in *N. caerulescens.* Three of the eight effectors released by B11 are also present in Psm and Pca. These effectors, AvrE, HopM1, and HopAA1, are part of the defined so-called conserved effector locus (CEL) of *P. syringae* and are thought to be required for pathogenicity (90,97,98). AvrE contributes to bacterial virulence by suppressing SA-dependent defence responses, such as callose deposition, and also promotes water soaking in the apoplast by functioning as a channel in the plant cell plasma membrane (94,95,99). These water and solute-permeable channels aid pathogen establishment by creating a nutrient-rich and hydrated apoplast (90,94,99). As discussed previously, SA-dependent responses are altered in *N. caerulescens*, but water-soaking symptoms are apparent potentially indicating a role of AvrE in infection of the hyperaccumulator. HopM1 is a multifunctional effector that has been found to suppress the early NADPH-dependent ROS burst (100). Parallel deletion of AvrE and HopM1 was shown to significantly dampen virulence in both *Arabidopsis thaliana* and *Lycopersicon esculentum* (101,102). HopAA1 is implicated in chlorosis and necrotic lesion development (98).

In addition to effector proteins, *Pseudomonas syringae* also produce a range of phytotoxins that can contribute to pathogenicity (103). The toxins produced by the strains used in this study are outlined in Table 3. Unlike Psm and B11, Pca produces the phytotoxin coronatine, a mimic of the plant hormone methyl jasmonate that promotes stomatal opening for bacterial entry, induces chlorosis, and is thought to disrupt the plant's SA-induced defences (103–106). One possible explanation for the pathogenicity of B11 is that it produces the phytotoxin syringomycin. Syringomycin induces pore formation in the plasma membrane which allows for uncontrolled movement of cations, causing an ion imbalance and eventual cell death (103,107).

Table 2: T3SS effector proteins present in the bacterial strains used in this study. Green indicates presence and magenta indicates absence based on OrthoFinder analysis.

Effector	Psm	B11	Pca
AvrB2			
AvrE1			
AvrPto1			
AvrRPm1			
AvrRpt2			
HopA1			
HopB1			
HopC1			
HopD1			
HopD2			
HopE1			
HopF1			
HopF2			
HopG1			
HopH1			
HopI1			
HopJ			
HopL1			
HopM1			
HopN1			
HopO1			
HopQ1			
HopR1			
HopS1			
HopT1			
HopU1			
HopV1			
HopW1			
HopX1			
HopY1			
HopAA1			
HopAB1			
HopAD1			
HopAF1			
HopAH1			
HopAI1			
HopAK1			
HopAL1			
HopAM1			
HopAQ1			
HopAX1			
HopBE1			
HopBF1			

Table 3: Phytotoxins present in the bacterial strains used in this study. Green indicates presence and magenta indicates absence based on OrthoFinder analysis.



1.7 Synchrotron-based X-ray imaging and spectroscopy

Clearly, there is a correlation between the abundance of metal in the aerial tissue of the hyperaccumulator *N. caerulescens* and bacterial pathogen viability. However, as previously discussed, there is a heterogenous distribution of metal within the leaves of *N. caerulescens* and as such simple bulk leaf measurements are not representative of the concentrations that pathogens are exposed to during infection. Therefore, in order to study the mechanism of defence, an understanding of the cellular and subcellular distribution and speciation of metal and how this changes in response to infection is required.

There are a number of techniques that can be used for the quantitative measurement of metals; each varying in their sensitivity, availability, and the range of detectable metals (108). Atomic absorption spectroscopy (AAS) is a widely accessible technique that can facilitate high-specificity analysis of bulk samples and, as discussed in section 1.3 has been previously used to quantify the total zinc content in the leaf tissue of different ecotypes of *N. caerulescens* (38,109). A drawback of AAS is that only one element can be detected at a time. An alternative but more expensive technique is inductively coupled plasma - mass spectrometry (ICP-MS) which is capable of the simultaneous analysis of multiple elements and has greater sensitivity than AAS – down to parts per trillion (110,111). However, both AAS and ICP-MS are destructive and do not provide spatial information (108).

Laser ablation inductively coupled plasma – mass spectrometry (LA-ICP-MS) combines the high sensitivity of ICP-MS with the ability to measure the spatial distribution of metal across a sample through surface ablation (108,111). This technique is inherently destructive, however, and with its maximum spatial resolution typically being around 5 μm, offers limited utility for subcellular experiments (108,112). An alternative surface-based technique offering much greater (nanoscale) spatial resolution is secondary ion mass spectrometry (SIMS) (108). Additionally, with a few notable exceptions, NanoSIMS is capable of measuring almost all of the elements in the periodic table (113). Unfortunately for

this work, however, one of the elements NanoSIMS is less suited to measuring is zinc due to the metal's low secondary ion yield (113). Unlike the previously discussed techniques, particle-induced X-ray emission (PIXE) is non-destructive and enables high sensitivity mapping of a wide range of elements (sodium to uranium) at up to 1 μm spatial resolution. However, its use is limited by the need for a particle accelerator, reducing accessibility (108,114). Scanning electron microscopy coupled with energy-dispersive X-ray spectroscopy (SEM-EDS) enables high resolution imaging alongside the simultaneous mapping of a wide range of elements. However, long scan times are associated with this technique and the resolution achievable is element dependant (108,114).

The focus of this work, however, is synchrotron-based X-ray fluorescent (XRF) mapping which is a technique similar to PIXE (113). XRF mapping allows for visualisation of the spatial metal distribution *in planta* by exploiting the characteristic fluorescent emission observed from a sample excited with X-ray radiation (115). As outlined in Figure 11, if the energy of an incident X-ray photon is sufficient, it causes the ejection of an inner-shell electron leaving an unstable "core-hole" (116). To rectify this unstable state, an electron from an outer shell relaxes down and causes the release of a secondary, fluorescent X-ray photon which is then detected. The energy of this emitted X-ray photon is characteristic to each element as it depends on the difference between the atom shell energy levels which are unique for different elements (115). Depending on the incident beam size, as well as other sample-dependent parameters such as thickness, XRF can monitor the cellular and subcellular distributions of elements in a sample. Using XRF to measure a sample containing multiple metals, as is the case with biological samples, one can build up a hyperspectral image comprising both spatial and elemental information.

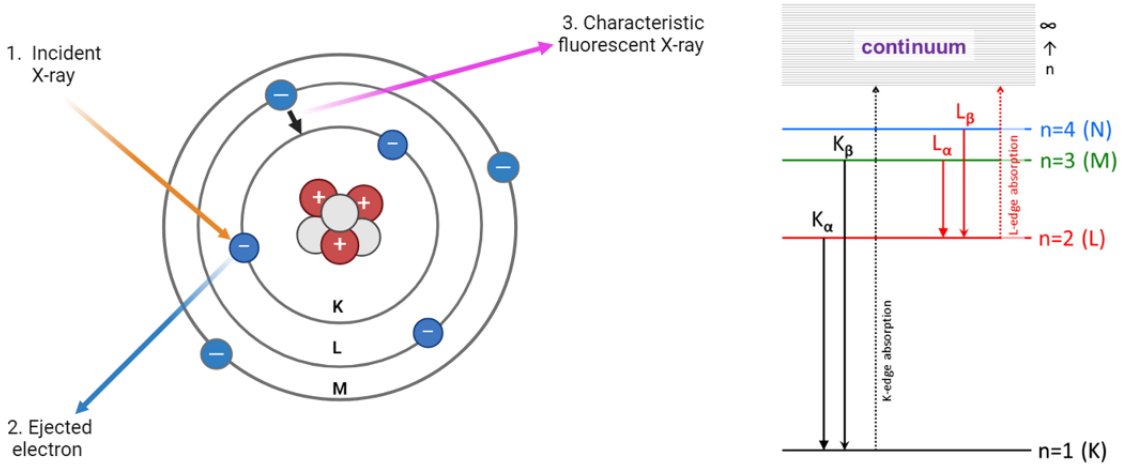


Figure 11: Principle of XRF spectroscopy. An incident X-ray ejects an electron leaving a so-called “core hole”. This unstable state is rectified by an electron from a higher energy level relaxing down and releasing a characteristic fluorescent X-ray in the process. Made in BioRender (left). X-ray emission lines (solid arrows) following the excitation of an electron from the K and L levels. Dashed arrows correspond to ionisation of a core electron. Taken from Kowalska and DeBeer, 2015 (right).

Complementary to XRF, X-ray absorption spectroscopy (XAS) is a technique which enables an understanding of the local chemical environment of an element of interest. For example, identifying its chelator(s) or speciation. Upon absorption of an X-ray photon, if of sufficient energy, a core electron will be ejected giving rise to the major peak in an XAS spectrum, an example of which can be seen in Figure 12 (117). This peak is known as the absorption edge which is characteristic for each element and will provide information on the oxidation state and coordination symmetry. The ejected electron interacts with neighbouring, non-excited atoms which act as point scatterers and results in interference patterns; destructive interference leading to troughs and constructive interference leading to peaks past the absorption edge (118–120).

XAS spectra can be split into two regions: X-ray absorption near-edge structure (XANES) and extended X-ray absorption fine structure (EXAFS), as outlined in Figure 12 (117). The latter, EXAFS, is what is described in the above section as interference patterns occurring after the edge and can be used to identify types of neighbouring atoms and bond lengths. The former, which will be the technique primarily used in this work, can provide

information on the oxidation state and coordination environments (118–120). Analysis of XANES data is typically done using a fingerprinting method - comparing sample data and matching spectral features to known, empirical standards. Thus, when conducting a XANES experiment, a spectral library needs to be produced or utilised for a given element in addition to the sample to be measured (118,121).

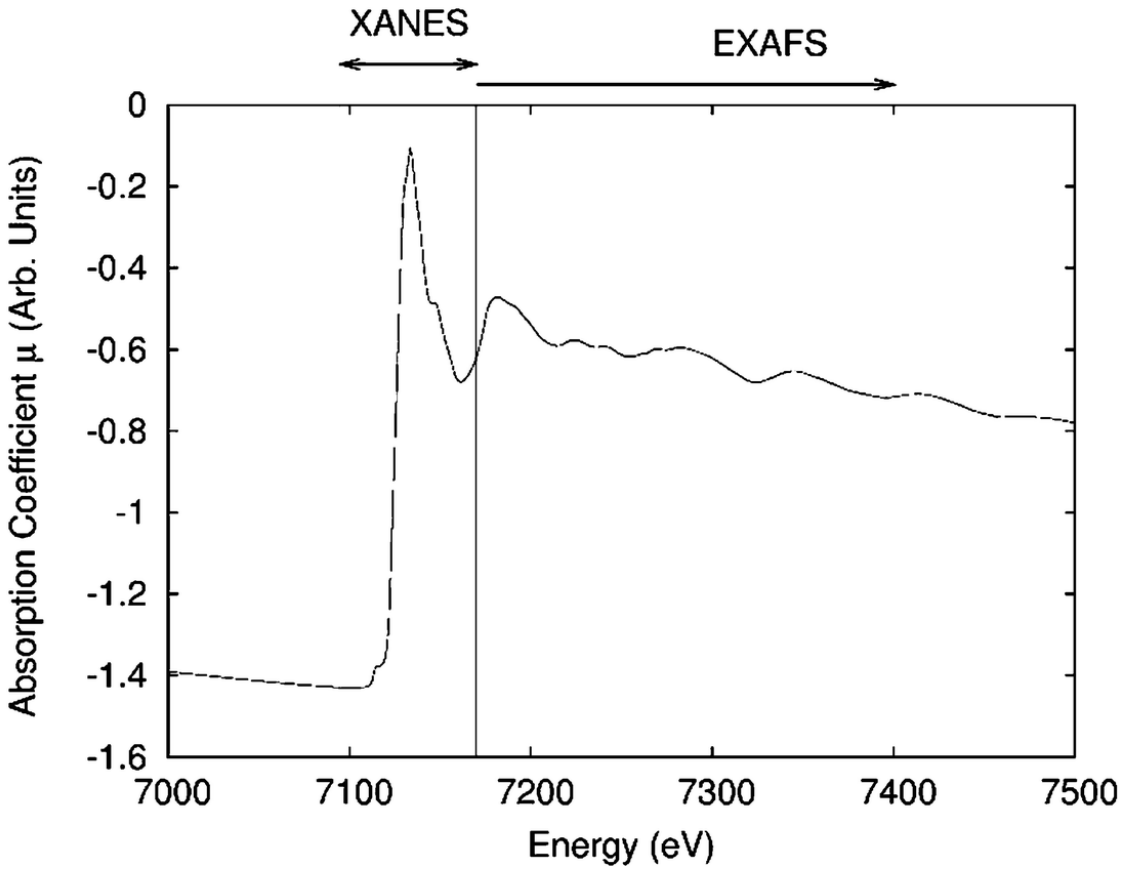


Figure 12: Example iron X-ray absorption scan of hematite (Fe2O3) with approximate XANES and EXAFS regions noted. It should be noted that for EXAFS, the energy usually extends further past the edge than indicated here. Taken from d'Acapito, 2018.

While bench-top XRF and XAS instrumentation are available, significantly higher brightness and sensitivity can be obtained using synchrotron radiation (122). This is particularly useful when working with samples with low concentrations of the analyte of interest. A synchrotron, like Diamond Light Source, is a circular particle accelerator (123). A full description of the physics behind a synchrotron is beyond the scope of this thesis, but briefly, electrons are released from an electron gun and accelerated to relativistic speeds,

that is nearing the speed of light, via a linear accelerator and booster ring. From the booster ring, the electrons enter the storage ring where their trajectory can be altered by bending magnets, resulting in the release of highly collimated, broad-spectrum light which is then transferred into a series of experimental stations, “beamlines”, each utilising different X-ray energies, techniques, sample environments, and sample types (119,121,122,124).

Synchrotron-based XRF has previously been used to successfully study metal distributions in both hyperaccumulating and non-hyperaccumulating plants. For example, in the non-accumulating *Helianthus annuus,* zinc was found to be preferentially stored in trichomes on both leaf surfaces (125). In the nickel and zinc hyperaccumulator *Noccaea tymphaea*, contrasting distribution patterns were observed; with nickel being preferentially stored in the epidermal vacuoles and zinc in the mesophyll tissue – as shown in Figure 13 (126). The relatively thick sample (200 μm), however, limits the spatial resolution making it difficult to observe finer details across the tissue.

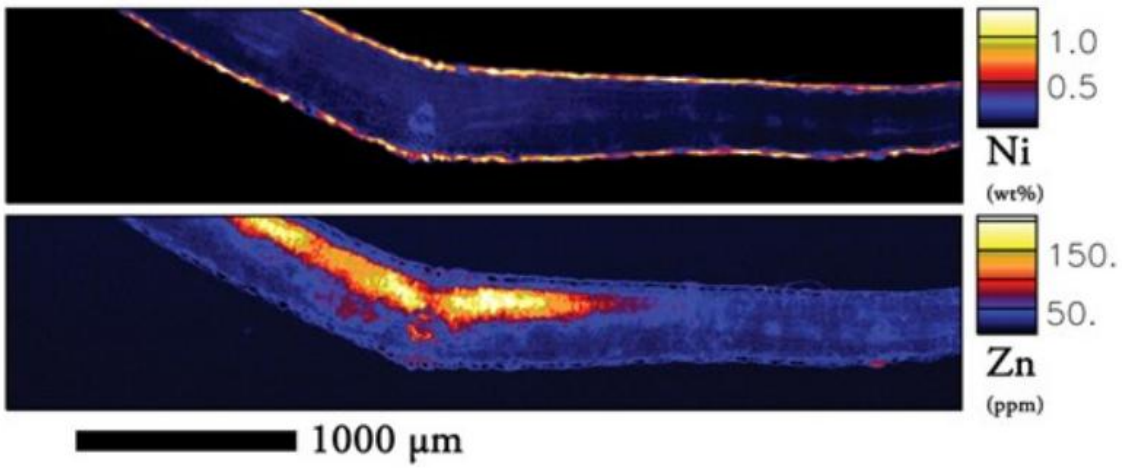


Figure 13: XRF map of Semi-thick (200 μm) transverse section of *Noccaea tymphaea* leaf showing differential nickel and zinc distribution. Taken from A van der Ent et al, 2019.

Few studies have measured metals in transverse sections of *N. caerulescens*, perhaps due to the inherent difficulty of sample preparation which will be discussed in more detail in section 3.1. Dinh et al, used SEM-EDS to study the distribution of zinc in the leaf

tissue of *N. caerulescens* grown hydroponically on different concentrations of zinc (127). While this study agrees with previous reports by identifying an epidermal localisation of zinc, the spatial resolution is quite low and there may have been issues with sample preparation. Firstly, the samples were cryofixed by submersion directly in liquid nitrogen which may lead to poor sample preservation due to the Leidenfrost effect. Secondly, the samples were stored at -30°C prior to analysis which is not sufficient to maintain ice in the amorphous state and, as will be discussed in section 3.1, may introduce artefacts and lead to metal redistribution (114).

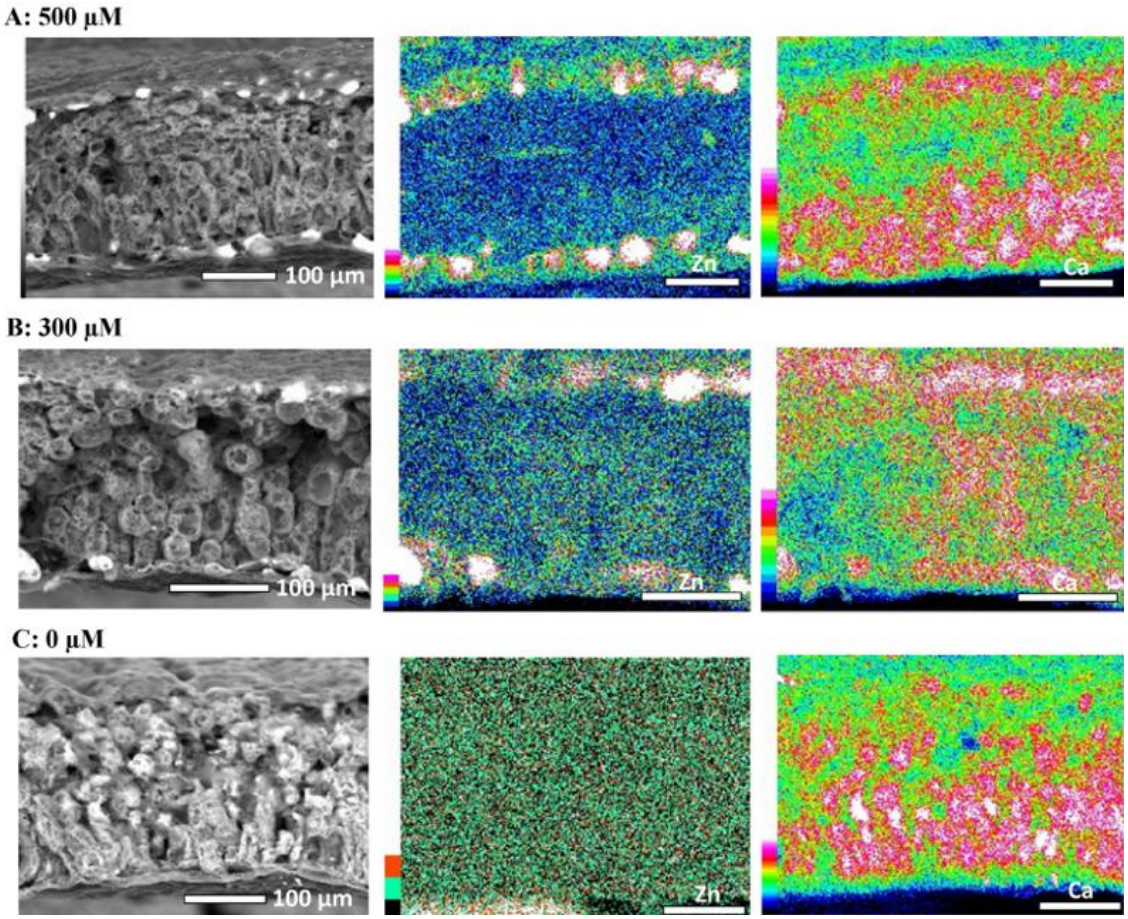


Figure 14: Scanning electron microscopy images (left) and zinc and calcium elemental maps (right) of transverse sections of *Noccaea caerulescens* grown on 0, 300, and 500 µM zinc for 16 weeks. Taken from Dinh et al, 2015.

A priority of this work, therefore, is to produce transverse sections of tissue that maintain elemental distributions to be as close to physiological as possible.

1.8 Research aims and rationale

The major aim of this work was to investigate the mechanisms by which accumulated zinc in the metal hyperaccumulator plant *Noccaea caerulescens* can provide a defence against the bacterial pathogen *Pseudomonas syringae.* Two UK-native pathovars are used in this work: *Pseudomonas syringae* pv. syringae SnB11 (B11) and *Pseudomonas syringae* pv. maculicola (Psm). Both strains are known to infect *N. caerulescens* and the related non-accumulating plant *Arabidopsis thaliana*, but have distinctive virulence mechanisms, which could affect plant immune responses and local concentrations of accumulated metal. The Prayon population of *Noccaea caerulescens* is used throughout this work, notable for particularly high zinc tolerance and accumulation, and plants were cultivated hydroponically on zinc concentrations of 10, 30 and 300 µm. In Chapter 2, the methods used throughout this work will be discussed.

This project was undertaken in partnership with Diamond Light Source, where another major aim was to develop sample preparation and mounting methods to improve and expand biological imaging capabilities at Diamond for the wider scientific community and, specifically in this work, to enable an understanding of zinc distribution and speciation in healthy and infected *N. caerulescens* tissue. Chapter 3 of this work will be focussed on developing these methods for 2D imaging and spectroscopy with the aim of building a spatially resolved picture of the local environment to which the pathogen is exposed and to identity if and how this changes in response to infection. In Chapter 4, this will be expanded to 3D imaging.

It has previously been established that *N. caerulescens* has evolved to possess an altered innate immune system potentially due to the development of the hyperaccumulation trait, but this altered immune system, specifically related to ROS, may provide a synergistic effect in combination with metal defences. Thus, the aim of Chapter 5 is to explore whether the trade-off and joint effects hypotheses could both be true in metal hyperaccumulator

plants in relation to the joint effects of metal and ROS. Additionally this chapter will explore potential mechanisms of zinc toxicity in *P. syringae*, and the effect of zinc on the metabolic activity of the bacteria.

Chapter 2: Materials and methods

2.1 Plant growth conditions

Seeds of *Noccaea caerulescens* from Prayon, Belgium (provided by Prof A. J. M. Baker and Prof C. Lefebvre) were grown on a 50:50 mixture of compost (Sinclair Modular Seed, UK) to vermiculite (Sinclair, fine grain, UK) in a temperature and light-controlled growth chamber. Light was provided for 16 hours, during which the temperature was maintained at 25ºC. During the dark hours the temperature was maintained at 15ºC. After between 2 and 3 weeks, seedlings were transferred to hydroponic tanks containing modified 0.5-strength Hoagland solution (Table 4).

Table 4: Modified 0.5-strength Hoagland solution for the hydroponic culture of *Noccaea caerulescens*.

Constituent	Final Concentration
KNO_3	2.5 mM
KH_2PO_4	0.5 mM
$Ca(NO_3)_2.4H_2O$	2.0 mM
$MgSO_4,7H_2O$	1.0 mM
FeEDDHA	50 µM
H_3BO_3	50 µM
$MnSO_4.H_2O$	10 µM
$ZnSO_4.7H_2O$	1 µM
$CuSO_4.5H_2O$	1 µM
$Na_2MoO_4.2H_2O$	0.5 µM

The hydroponic solution was supplemented with zinc to a final concentration of either 10 (“extra low”), 30 (“low”), or 300 µM (“high”) $ZnSO_4.7H_2O$ (128,129). These concentrations were chosen as a continuation of doctoral work by Helen Fones, as discussed in section 1.6.

The highest concentration was able to prevent bacterial proliferation with the lower concentrations of zinc leading to greater bacterial growth and more significant symptoms (25). The nutrient solution was refreshed weekly for between 9 and 12 further weeks. All *N. caerulescens* plants had additional zinc added (there was no 0-zinc treatment) to prevent zinc-deficiency symptoms such as stunted growth.

Arabidopsis thaliana (Col-0) seeds were sown in a mixture of 3:1 compost to vermiculite and maintained in a growth cabinet. The temperature was maintained at 21°C and light was provided for 16 hours. After 14 days seedlings were transferred to individual pots and maintained in the same conditions for 3-4 weeks.

2.2 Bacterial strains, media, and culture conditions

Bacterial strains used in this study are given in Table 5. All bacterial strains were stored in 25% glycerol at -80°C.

Lysogeny broth (LB; 10 g/L NaCl, 10 g/L tryptone, 5 g/L yeast extract) was used throughout this work (130). Other media were tested in combination with zinc but formation of a precipitate prevented their use. Agar was added at 2% (w/v) for solid media (LBA).

Bacteria were cultured onto LBA and incubated at 28°C for *Pseudomonas syringae* strains or 37°C for *Escherichia coli* for 1-2 days until single colonies formed. Single colonies were used to inoculate 10 mL LB which was incubated with shaking (220 RPM) at the appropriate temperature overnight (16-20 hours).

Table 5: Bacterial strains used in this work.

Strain/plasmid	Description	Antibiotic(s)	Source/Reference
E. coli DH5α (pRS-pnptII::lux)	*E. coli* DH5α with pRS-pnptII::lux	Gentamicin	Soldan et al, 2021 (131)
E. coli DH5α (pRS-pOXB20::lux)	*E. coli* DH5α with pRS-pOXB20::lux	Gentamicin	Soldan et al, 2021 (131)
E. coli DH5α (pRK2013)	*E. coli* DH5α with helper plasmid pRK2013	Kanamycin	Figurski and Helinski,1979 (132)
E. coli SM10/λ pir (pUX-BF13)	*E. coli* SM10/λ pir with miniTn7 helper plasmid pUX-BF13	Carbenicillin	Miller and Mekalanos, 1988 (133)
E. coli S17-1 λpir pDSK-roGFP	*E. coli* S17-1 λpir with pDSK-roGFP	Kanamycin	Solmi et al, 2023 (134)
E. coli pDSK519	*E. coli* with pDSK519	Kanamycin	Keen et al, 1988 (135)
P. syringae pv maculicola (Psm) NCPPB2038	Wildtype	Nitrofurantoin	NCPPB
P. cannabina pv alisalensis (Pca) ES4326	Wildtype	Nitrofurantoin	Dong et al, 1991 (136)
P. syringae pv syringae SnB11 (B11)	Wildtype	Nitrofurantoin	Fones et al, 2010 (6)
P. syringae pv maculicola (Psm) pnptII::lux	Psm expressing luxCDABE under the nptII promoter	Gentamycin, nitrofurantoin	This work
P. syringae pv maculicola (Psm) pOXB20::lux	Psm expressing luxCDABE under the OXB20 promoter	Gentamycin, nitrofurantoin	This work
P. syringae pv syringae SnB11 (B11) pDSK-roGFP	B11 expressing roGFP via pDSK-roGFP	Kanamycin	This work
P. syringae pv syringae SnB11 (B11) pDSK519	B11 with pDSK519 (roGFP control)	Kanamycin	This work

2.3 Chemicals

All chemicals were purchased from Sigma-Aldrich unless otherwise specified. Unless otherwise specified, zinc sulfate heptahydrate was used throughout this work.

Antibiotics were used at the following concentrations:

- Kanamycin = 20 μg/mL
- Nitrofurantoin = 25 μg/mL
- Gentamicin = 10 μg/mL
- Carbenicillin = 50 μg/mL

2.4 Inoculation of plants

For inoculation of *N. caerulescens*, an overnight culture of *Pseudomonas syringae* was first centrifuged for 10 minutes at 3500 xg and washed either once or twice in sterile water (twice if the bacteria were grown in the presence of antibiotics). Bacteria were then resuspended in 10 mM $MgCl_2$ and adjusted so the OD_{600nm} was 0.02, equivalent to approximately 10^7 cfu/mL.

Fully expanded leaves were syringe infiltrated with a 1 mL needleless syringe on the abaxial surface, approximately half-way up the length of the leaf and lateral to the midvein. Infiltration was performed until the entire leaf darkened in appearance. Mock infiltrations were prepared in the same manner with just the 10 mM $MgCl_2$ buffer.

2.5 Mini-Tn7 delivery by four-parental mating conjugation

The *luxCDABE* operon was inserted into *Pseudomonas syringae* pv. maculicola via four-parental mating conjugation in order to produce bioluminescent bacteria (131). Two donor strains (*E. coli* DH5α (pRS-p_{nptII}::lux) and *E. coli* DH5α (pRS-p_{OXB20}::lux)) introducing

two different promotors, nptII and OXB20 respectively, were used; the former has been shown to be a significantly stronger promoter (131).

2 x 1.5 mL per overnight cultures of the donor, helpers (*E. coli* SM10/λ pir (pUX-BF13) and *E. coli* DH5α (pRK2013)), and recipient (WT Psm) were centrifuged for 1 minute at 8000 xg, and washed with warm (50°C) LB. 750 μL of warm LB was added to one of each culture and resuspended. This suspension was added to the remaining pellet and resuspended, forming a more concentrated suspension. An additional 750 μL of warm LB was added to produce a final volume of 1.5 mL. 700 μL recipient, 300 μL donor, and 100 μL of each helper were combined, centrifuged for 1 minute at 8000 xg and resuspended with 50 μL warm LB. The 50 μL suspension was spotted onto an LBA and left to dry at room temperature before being incubated at 28°C for 24 hours. The spot was scraped from the agar plate and resuspended in 900 μL LB. 200 μL of this suspension was spread onto LBA containing gentamicin and nitrofurantoin to select against the *E. coli.* The plate was incubated at 28°C for 2 days.

Successful transformation was confirmed by screening the plates for luminescence using the NightOWL LB 983 NC100 in vivo imaging system (Berthold Technologies).

2.6 Bioluminescence imaging

After leaves were inoculated with bioluminescent bacteria, they were excised from the plant using a razor blade at the appropriate time points, surface sterilised with 70% ethanol and washed twice with sterile water. The petiole was wrapped in damp cotton to lessen dehydration and leaves were placed in a lidded square petri plate for imaging.

Leaves were incubated in the dark for 10 minutes before imaging with the NightOWL LB 983 NC100 in vivo imaging system. A luminescence (20-minute exposure time) and brightfield (0.1-second exposure time) image were collected and overlaid using IndiGO™

software (version 2.0.5.0, Berthold Technologies). Data is expressed as counts per second (cps).

2.7 Histology section preparation and imaging

For the histological study of *N. caerulescens*, leaves were first cut into 2-3 mm sections using a razor blade before being fixed with a 3:1 solution of 100% ethanol and glacial acetic acid. After 30 minutes, the fixative was removed and replaced with 70% ethanol. After 30 minutes, the ethanol was refreshed and leaf samples were stored at 4°C until use.

As paraffin is not miscible with water, the samples required dehydrating before wax embedding. This and further tissue processing was performed using a Tissue-Tek VIP system (Sakura Finetek, Japan) with the following programme as described by Hughes et al, 2019 (137). Samples were first dehydrated at 35°C through the following 1-hour steps: 70%, 80%, 90% (with 1% eosin), 95%, 100%, 100%, 100% ethanol. Samples were subsequently incubated at 35°C three times in Histo-Clear (National Diagnostics, USA) for 1 hour each step. Samples were then incubated four times at 65% in paraffin wax for 2 hours each step. The resulting wax blocks were trimmed and allowed to solidify before preparing 10 μm transverse sections with a Leica RM2135 rotary microtome.

Safranin O (1% in 50% ethanol) was used to stain lignified tissue, nuclei and chromosomes, and Fast Green (0.5% in 95% ethanol) was used to stain cytoplasm and cellulosic cell walls with the following timings: Histo-Clear 5 minutes, Histo-Clear 5 minutes, 100% ethanol 2 minutes, 100% ethanol 2 minutes, 70% ethanol 2 minutes, Safranin O 30 minutes, 70% ethanol 2 minutes, Fast Green 30 seconds, 100% ethanol 2 minutes, 100% ethanol 2 minutes, Histo-Clear 5 minutes. Sections were imaged using a Zeiss LSM 880 microscope in brightfield mode.

2.8 2D-XRF data collection, image processing, and analysis

All 2D-XRF imaging was performed on the I18 microfocus beamline at Diamond Light Source (138). Sample preparation and mounting will be discussed in detail in Chapter 3.

Measurements were taken with a monochromatic beam with energy of 10 KeV to encompass the zinc K shell electron binding energy. A Vortex®-ME4 Silicon Drift Detector (Hitachi High-Tech, Japan) was used in conjunction with Xspress3 X-ray fluorescence detector readout system (Quantum Detectors, UK). A MicrostatHiRes liquid nitrogen-cooled cryostat (Oxford Instruments, UK) was used as the sample environment, and was cooled to 80K (-193.15^{o}C) for measurements. To prevent a build-up of ice, the cryostat was brought to room temperature between sample changes and lowered to 150K for mounting the samples. Map step (pixel) sizes between 1 and 10 μm were used, and measurements were collected with exposure times of between 0.001 and 0.1s per point (pixel).

2D-XRF maps were processed using PyMca software (Version 5.5.4) (139). Data was first energy calibrated using the elastic scatter peak (equivalent to the incident X-ray energy) and the peaks relating to zinc and argon Kα1 emission lines – the energies of which can be seen in Figure 15. XRF spectra were fitted to resolve any overlapping peaks or more difficult to distinguish peaks, such as potassium (Figure 15). The fit range was limited to between 0 and 9 KeV to exclude the scatter peak. The quality of the fit was checked on the sum spectrum and on a single pixel from the XRF map and then applied to the data using the software's fast XRF stack fitting with average weight policy applied.

X-Ray Energies

Element	Kα1 (KeV)
Mg	1.254
Ar	2.958
K	3.314
Ca	3.692
Mn	5.899
Fe	6.404
Ni	7.478
Cu	8.048
Zn	8.639

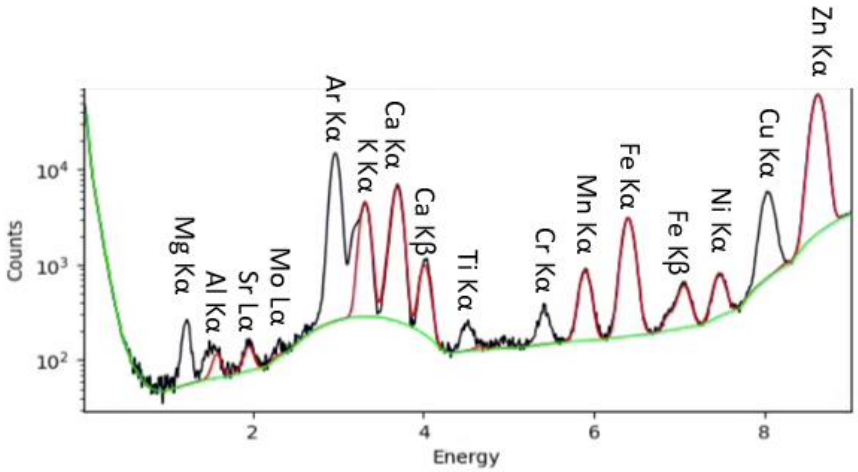


Figure 15: Select photon energies of Kα1 emission lines found in this study (left). 2nd derivative of an average/sum XRF spectrum from an extra low (10 μM) zinc leaf sample (right). The red line indicates the peaks fitted and the green line indicates the baseline fit. Taken from PyMca software.

Resulting element maps were analysed using Fiji software (version 2.3.0) (140). Background subtraction was performed by first selecting a region of interest (ROI) from above and below the sample, avoiding any artefacts or debris. The mean intensity values of these two regions were averaged, and this value was subtracted from the whole image. The same ROIs were used for the different element maps extracted from the same image. To show the difference in intensity in single element maps, the perceptually uniform lookup table mpl-inferno was used. A perceptually uniform colourmap ensures equal steps in data intensity value correspond to equal perceived changes in colour by the viewer (141).

In order to study the elemental distributions along the epidermal cells in Chapter 3, ROIs were approximated in Fiji using potassium maps (Figure 16) avoiding any debris or artefacts. These ROIs were approximated by hand, which may not completely accurately outline the cell and may introduce unintentional overlap of cells. The average intensity from each of these manually defined “cells” was measured and used in future analysis. The same

ROIs were used for the different element maps from the same image. For zinc in the mesophyll, between 30-50 single pixel spots were averaged. Plots using this data were produced using the R package ggplot2 (version 3.5.1) (142).

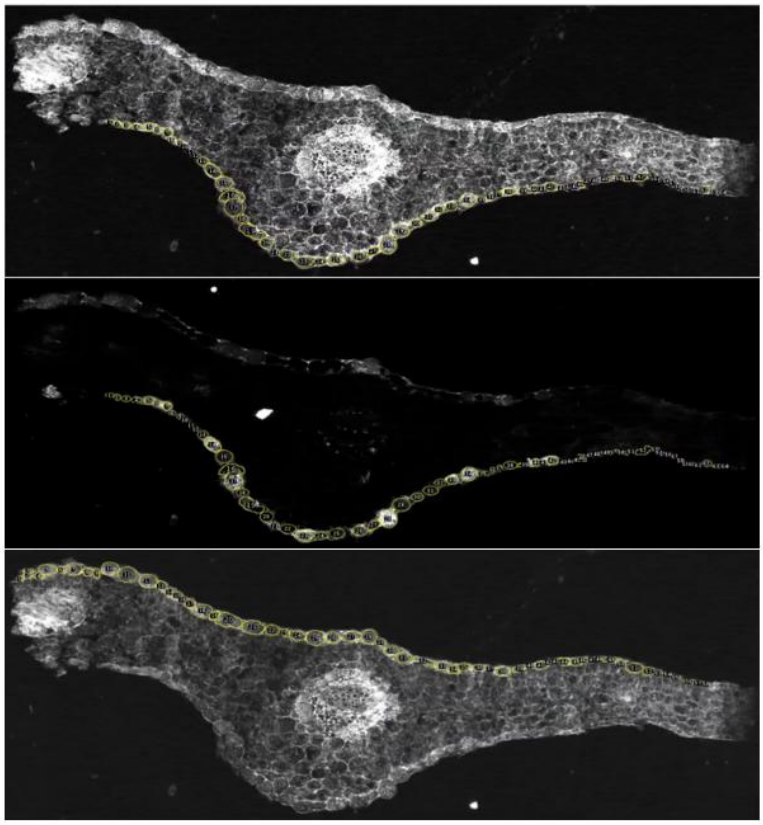


Figure 16: ROI selection in Fiji software for analysis of epidermal cells. A potassium map (top and bottom) and zinc map (centre) shown with approximated defining of epidermal cells.

2.9 Apoplast extraction

Apoplastic washing fluid (AWF) was isolated from *N. caerulescens* and *Arabidopsis thaliana* using the established infiltration-centrifugation technique by O'Leary et al with modifications in the centrifugation step as described by Chen et al (143,144). Briefly, damage-free leaves were excised from the plant using a razor blade and washed in sterile water to remove surface contaminants. Plants infected with bacterial pathogens were additionally surface sterilised with 70% ethanol before being washed in water. Infiltration was

carried out using a 60 mL syringe and sterile water, creating positive and negative pressure until the entire leaf surface had visibly darkened.

For recovery of AWF, an approximately 20 x 1.5-inch strip of Parafilm was laid flat and one end wrapped tightly around the larger end of a 1 mL syringe (plunger removed). Infiltrated leaves were laid onto the parafilm with the base of the leaves pointing towards the bottom of the syringe and more leaves were added as the Parafilm was wound around the syringe. Once the end of the Parafilm was reached, it was secured to the syringe using tape being careful not to touch the leaves or wrapping too tight to cause damage. See Figure 17 for a diagram of this procedure (taken from Chen et al (144)) and a photograph of the setup. The wrapped syringe was then placed in a 50 mL Falcon tube and centrifuged at 4°C, 1000 xg for 10 minutes. If the leaves still had dark patches, they were centrifuged in additional 5-minute increments until these were no longer observable. Recovered AWF was transferred into Eppendorf tubes on ice and centrifuged at 4°C for 10 minutes at 3214 xg (the maximum speed of centrifuge 5810R (Eppendorf, Germany)) to remove any cells or particulates. AWF was then transferred to fresh Eppendorf tubes and maintained on ice or at -80°C for long-term storage.

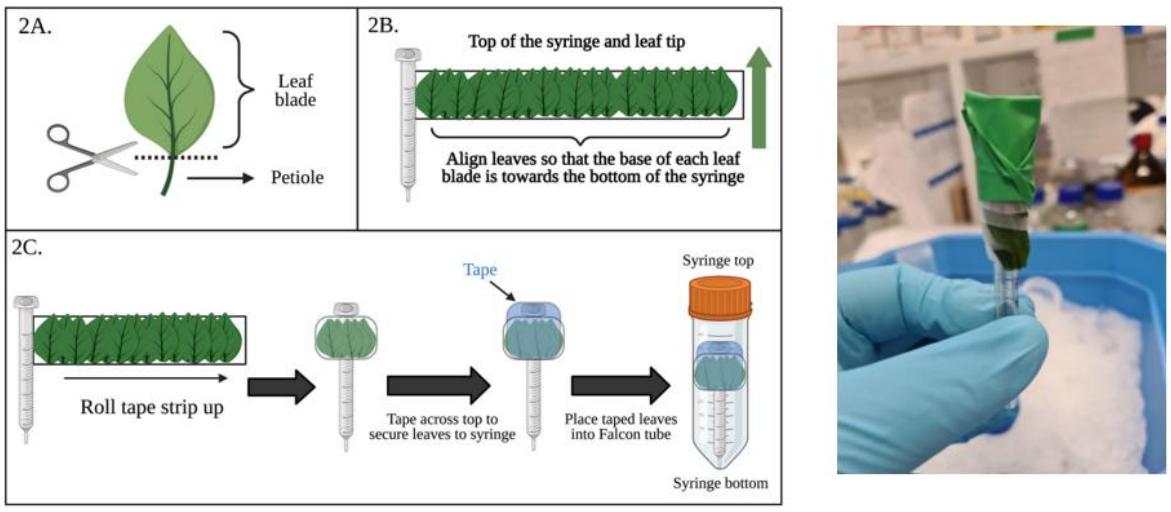


Figure 17: Diagram outlining the apoplast extraction step, taken from Chen et al, 2022 (left). Photograph of the apoplast washing fluid recovery setup, taken after centrifugation (right).

To account for any dilution effect during the infiltration step, dilution factors were calculated for each plant using indigo carmine, as described by O'Leary et al (143). Briefly, the absorbance at 610 nm (OD_{610}) of infiltration fluids (water or indigo carmine [50 μM]) were measured using an Infinite M200 plate reader (Tecan, Switzerland). Two to three replicate infiltrations and extractions were performed for each plant listed in Table 6 using each infiltration fluid, as described above. Averaged OD_{610} values from the replicates were used to calculate the dilution factor using the calculation described in the protocol. Again, due to low recovery volumes with *N. caerulescens* and *A. thaliana*, a modification to the protocol was that 100 μL of AWF was used per well instead of the described 200 μL.

Table 6: Dilution factors for *Arabidopsis thaliana* and *Noccaea caerulescens*.

	Dilution factors
A. thaliana	1.5968
Extra low Zn	1.5137
Low Zn	2.6477
High Zn	3.1743

2.10 ICP-MS sample preparation and analysis

To prepare apoplastic washing fluid (AWF) for inductively coupled plasma mass spectrometry (ICP-MS) analysis, the samples first needed to be digested to remove organic material. This was done by combining 75 μL AWF with 75 μL nitric acid (69%) and leaving samples to digest for approximately 16 hours. Samples were then heated for 30 minutes at 55°C. Blanks were produced in the same way, using 75 μL of sterile water instead of AWF. Each sample of AWF was extracted from one plant (approximately 15-25 leaves), and samples from different plants were not pooled.

A non-analyte internal standard of rhodium (10 μg/L final concentration) was added to all samples, blanks, and calibration standards to monitor instrument drift and to facilitate

correction of any matrix effects. ICP-MS required a minimum sample volume of 3 mL, so the samples plus washings and rhodium were made up to this volume with sterile water. All volume measurements were made by mass for increased precision, with the mass of each component per sample being noted down to allow for calculation of the dilution factor.

Samples were measured on a Thermo Fisher Scientific iCAP Q Inductively Coupled Plasma Mass Spectrometer by Andrew Dodson at the Chemical Analysis Facility, University of Reading. Two multielement external standards were prepared by Andrew Dodson. The first contained alkali, alkaline earth, and non-transition metals (CCS-4, Inorganic Ventures) and the second contained a mix of transition metals (Transition metal mix 1, *Trace*CERT®, Sigma-Aldrich). Both of these standard mixes contained 100 ppm of each metal and were diluted to concentrations of between 0 and 1200 ppb from which calibration curves were generated. These calibration curves were used to calculate the analyte concentrations in the diluted samples. Final concentrations were corrected with the dilution factors accounting for both the infiltration step (Table 6) and the dilution of the final samples prior to analysis.

Plots were produced using the R package ggplot2 (version 3.5.1) (142).

2.11 XANES standards preparation

Unless otherwise stated, all standard solutions were prepared using sterile water and adjusted to pH 7. Zinc sulfate was initially used as the zinc source in order to be consistent with the form used in the Hoagland's hydroponic media. Additionally, standards in this initial beamtime were measured at room temperature. However, in this beamtime some of the resulting compounds, particularly amino acid complexes, did not appear to go to completion as their spectra looked identical to that of zinc sulfate. Thus, in a subsequent beamtime, zinc nitrate or zinc chloride were used as described below, and the standards were measured frozen (145,146).

For samples that were measured at cryogenic temperatures, 1 mL (or 0.5 mL for zinc nicotianamine) of the resulting solution was pipetted into an Eppendorf tube, flash frozen in liquid nitrogen-cooled isopentane, and mounted upside down in a custom 3D-printed sample holder. This mount was placed under a liquid nitrogen cryostream (Oxford Instruments, UK) as shown in Figure 18.



Figure 18: Measurement of XANES standards at cryogenic temperatures. Flash frozen liquid standards in Eppendorfs are mounted upside down under a liquid nitrogen cryojet. Photo courtesy of Rhiannon Boseley.

Zinc Phytate

Equal volumes of zinc sulfate [1 g/mL] and phytic acid [20 mM] (147). 1 mL of the resulting solution was pipetted into an Eppendorf tube and measured at room temperature.

Zinc Cysteine

Equal volumes of zinc sulfate [7 mM] and cysteine solution [70 mM] (148,149). 1 mL of the resulting solution was pipetted into an Eppendorf tube and measured at room temperature.

Zinc Succinate

Equal volumes of zinc sulfate [7 mM] and succinate solution [70 mM] (148,149). 1 mL of the resulting solution was pipetted into an Eppendorf tube and measured at room temperature.

Zinc Oxalate

Equal volumes of zinc sulfate [7 mM] and oxalic acid solution [70 mM] (56). An insoluble precipitate formed which was washed via vacuum filtration and dried at 40^{o}C for 3 hours. The precipitate was measured at room temperature as a solid by applying to Kapton (polyimide) tape.

Zinc Citrate

Zinc citrate was purchased from Thermo Fisher and dissolved in water to make a 5 mM solution. Measured frozen.

Zinc Phosphate

Zinc phosphate was purchased from Sigma Aldrich and measured in suspension at 5 mM. Measured frozen.

Zinc Aspartate

Equal volumes of zinc nitrate [1 mM] and L-aspartic acid [10 mM]. Measured frozen.

Zinc Histidine

Equal volumes of zinc nitrate [1 mM] and L-histidine [10 mM]. Measured frozen (145).

Zinc Malate

Equal volumes of zinc nitrate [1 mM] and DL-malic acid [10 mM]. Measured frozen.

Zinc Glutamate

Equal volumes of zinc nitrate [1 mM] and L-glutamic acid monosodium salt [10 mM] (145). Measured frozen.

Zinc Nicotianamine

Equal volumes of zinc chloride [0.8 mM] and nicotianamine [1.2 mM] (146). Measured frozen. Nicotianamine was purchased from LGC Standards UK.

XANES standard spectra were pre-processed (normalised) in Larch software (version 0.9.81) and plots were produced using the R package ggplot2 (version 3.5.1) (142).

2.12 XANES measurements and analysis

All XANES measurements were collected on the I18 microfocus beamline at Diamond Light Source (138). Leaf samples were prepared in the same manner as for 2D-XRF spectroscopy, and this will be discussed in detail in Chapter 3. Apoplast samples were extracted using the method described in section 2.10 and were mounted onto the beamline as described for the frozen XANES standards in section 2.11.

X-ray absorption spectra were energy calibrated by measuring a zinc foil with the first derivative of its absorption edge matched to the tabulated value at 9659 eV. XANES mapping was used for leaf tissue at spatial resolutions of between 2 and 5 μm, with each pixel of the resulting image comprising a XANES spectrum. XANES point scans were taken for zinc standards and apoplast samples using a beam spot size of 90 x 200 μm. XANES measurements were recorded with scanning energies in the range 9500-9975 eV and varying collection intervals (energy step sizes).

ROIs were selected from XANES maps from the upper epidermis, lower epidermis, mesophyll, and the midrib vein, and XANES spectra were averaged from these regions using Quasar software (version 1.4.0) (150). XANES spectra from these averaged regions, as well as standard and point scan measurements were exported into Larch software (version 0.9.81) for preprocessing and linear combination fitting (LCF) (151). LCF analysis was used to fit standard spectra to sample data to identify individual zinc compound contributions.

Plots were produced using the R package ggplot2 (version 3.5.1) (142).

2.13 3D-XRF tomography data collection and image analysis

All 3D-XRF tomography was performed on the I18 microfocus beamline at Diamond Light Source (138). Sample preparation and mounting will be discussed in detail in Chapter 4.

Measurements were taken with a monochromatic beam with energy of 10 KeV to encompass the zinc K-edge. Two Vortex®-ME4 Silicon Drift Detectors (Hitachi High-Tech, Japan) were used in conjunction with Xspress3 X-ray fluorescence detector readout system (Quantum Detectors, UK).

For leaf samples, a Kapton polyimide capillary was affixed to a pin and mounted on a series of motors (Picomotor™ Piezo Linear Actuators, Newport Corporation, USA) to allow for rotation and tomography alignment. The mount was placed under a liquid nitrogen cryojet (Oxford Instruments, UK) which keeps a spot with diameter of approximately 5 mm frozen. For seed samples, the seed was simply affixed to the pin and the samples were measured at ambient room temperature.

Spatial resolutions of 5 or 10 μm were used, and measurements were collected in the range of 180^{o} sample rotations with 0.25 or 5^{o} step size with an exposure time of 0.003s per point in translation-rotation geometry. The sample was scanned horizontally, then rotated and the process repeated. Multiple single slice scans were collected along the vertical axis to form the resulting 3D image. XRF data was fit using windowing of the Kα energies of the elements of interest, notably 8.43 - 8.83 KeV to encompass the zinc peak. Due to self-absorption with elements of lower mass (particularly potassium and calcium), these were not used in tomography analysis of leaf tissue and instead analysis focussed on zinc distribution and its comparison to 2D-XRF samples. Self-absorption will be discussed in more detail in Chapter 4. Tomographic reconstructions were performed using the simultaneous iterative reconstruction technique (SIRT) algorithm. 3D-XRF renderings were made using Avizo software (version 2021.1, Thermo Fisher Scientific).

2.14 Preparation of roGFP2 bacterial transformants and control strains

The pDSK-roGFP and empty vector plasmid pDSK519 were introduced to *P. syringae* pv. syringae SnB11 via electroporation. The latter acts as a control and provides the background signal for roGFP experiments.

Plasmids were isolated from *E. coli* S17-1 λpir pDSK-roGFP and *E. coli* pDSK519 using the Nucleospin® plasmid miniprep kit (MACHEREY-NAGEL, Germany) according to the manufacturer's instructions for low-copy plasmids (version 12, revised 07/2021). DNA concentration was measured using a NanoDrop Microvolume Spectrophotometer (Thermo Fisher Scientific, USA) and adjusted to 100 ng/μL in sterile water. Plasmids were stored at -20°C until use.

Electrocompetent B11 cells were prepared by first centrifuging an overnight culture at 4°C for 8 minutes at 3214 xg (the maximum speed of centrifuge 5810R (Eppendorf, Germany)). The cells were washed twice in ice cold 10% glycerol : 1mM HEPES solution and resuspended in ice cold 10% glycerol : 1mM HEPES solution to 0.067 x the starting volume. Cells were maintained on ice until use.

80 μL of electrocompetent cells were combined with 2 μL of 100 ng/μL plasmid and incubated on ice for 10 minutes. The mixture was transferred to a pre-chilled Fisherbrand™ Electroporation Cuvette Plus™ with 2mm width gap (FisherScientific, USA) and maintained on ice until use. Electroporation was performed using a BTX™ ECM™ 630 Exponential Decay Wave Electroporation System (Harvard Bioscience, USA) with the following protocol: 2500 V, 200-ohm resistance, and 25 μF capacitance. B11 was recovered in 0.5 mL LB and incubated at 28°C for 2 hours with shaking (220 RPM). Cells were plated on kanamycin LBA and incubated at 28°C for 24 hours.

2.15 Measurement of bacterial intercellular redox state with roGFP

Overnight cultures of B11 pDSK-roGFP and B11 pDSK519 were centrifuged for 10 mins at 3000 xg, washed twice with 0.9% saline solution, and adjusted to have an optical density at 600nm (OD) of 2.0 in 2 mL saline. ODs were prepared to double the working value, as these will be halved when in the plate.

100 μL of B11 pDSK-roGFP and B11 pDSK519 were added to wells A-G of columns 1 and 2 respectively of a clear-bottomed black 96-well plate. This 96-well plate was then placed into a pre-warmed Infinite M200 plate reader (Tecan, Switzerland) at 28°C and continuous measurements were taken for 30 minutes with the following parameters: 405 and 480 nm excitation, 510 nm emission, gain 120, 2 second shaking after all filled cells were measured. While the plate was being measured, the treatment solutions were prepared; as hydrogen peroxide solutions are very unstable, they were prepared as close as possible to the time of their addition to the 96-well plate.

For experiments where hydrogen peroxide was the sole stressor, stock solutions were prepared from 30% hydrogen peroxide (9.8 M) and 0.9% saline to double the final concentration. 500 mM hydrogen peroxide was used to cause maximum oxidation and 5 mM dithiothreitol (DTT – Thermo Fisher scientific, UK) was used to cause reduction of bacteria.

After the 30-minute incubation period, the plate was quickly removed from the plate reader and a multichannel pipette was used to add 100 μL of each treatment to the 96-well plate as described in Table 7. After the treatments were applied, each well was thoroughly mixed with the multichannel pipette and the plate was put back in the plate reader for an additional 90 minutes under the same conditions as described previously.

Table 7: 96-well plate schematic for roGFP experiments showing the concentrations of hydrogen peroxide treatments.

	B11 pDSK-roGFP	B11 pDSK519
	1	**2**
A	Water	Water
B	5 mM	5 mM
C	50 mM	50 mM
D	100 mM	100 mM
E	150 mM	150 mM
F	500 mM	500 mM
G	DTT	DTT

[1]B11 pDSK-roGFP was added to cells A-G of column 1, and B11 pDSK519 (the control strain) was added to cells A-G of column 2.

For experiments where two stressors were applied (hydrogen peroxide plus zinc or nickel), these metal and hydrogen peroxide treatments were prepared to 4X the final concentration and 50 μL of each were added to 100 μL bacteria. Zinc and nickel treatments were prepared using 0.9% saline and zinc sulfate heptahydrate or nickel sulfate hexahydrate, respectively.

Analysis of roGFP data was performed in R (version 4.2.1) as described by van der Heijden and Finley, 2015 (152,153). Briefly, the 405 nm/480 nm ratio was calculated by subtracting the fluorescence intensity measured for the control B11 pDSK519 strain from the value obtained for B11 pDSK-roGFP for each time point and treatment. Then, for each time point and treatment, the values for 405 nm were divided by the values for 480 nm. The resulting 405/480 nm ratios could then be plotted against time to indicate the intracellular redox state of the bacteria, with peaks demonstrating oxidation. Plots were produced using the R package ggplot2 (version 3.5.1) (142).

2.16 Bacteria tolerance assays

Bacterial zinc and ROS tolerance was tested in vitro using clear 96 well plates and an Infinite M200 plate reader (Tecan, Switzerland). For zinc tolerance assays, an overnight bacterial culture was centrifuged for 10 mins at 3000 xg, washed twice with sterile water, resuspended with LB and adjusted to have an optical density at 600nm (OD) of 0.2. For ROS tolerance assays, an overnight culture was centrifuged for 10 mins at 3000 xg, washed twice with sterile water, resuspended with LB, and adjusted to have an optical density at 600nm (OD) of 0.1. The latter was used in conjunction with zinc stocks prepared in LB, and equal volumes of this and the bacteria were combined so the bacteria was prepared to double the working OD. The former was used in conjunction with H_2O_2 prepared with sterile water, where 145 μL bacteria and 5 μL H_2O_2 were combined. This distinction in preparation was to not introduce any other factor that could limit bacterial growth over the 24 hours, as adding equal volumes of bacteria and H_2O_2 prepared with water would dilute the LB media. Where both zinc and ROS were tested in conjunction with one another, bacteria were adjusted to have an OD of 0.2, and 75 μL of this was combined with 70 μL zinc stock and 5 μL H_2O_2 stock.

Zinc stocks were prepared from filtered zinc sulfate heptahydrate solution (50 mM) and LB. Hydrogen peroxide stocks were prepared from 30% hydrogen peroxide (9.8 M) and sterile water, and due to lability, were prepared as close as possible to the time of their addition to the 96-well plate. At least 3 replicate wells were assayed per treatment and at least 6 blank wells (containing no bacteria) were prepared. Wells showing significantly anomalous responses, for example resulting from an air bubble, were not used in analysis.

The 96-well plate was added to the plate reader (pre-warmed to 28°C) and the OD was measured every 30 minutes for 24 hours. The plate was shaken every 20 minutes. Growth curves and dose response plots were produced from this data using the R package

ggplot2 (version 3.5.1) (142). From these charts, stressor concentrations causing half-maximal inhibition (IC_{50}) could be determined (shown in the appendix).

2.17 Raman microspectroscopy sample preparation, data acquisition, and analysis

To determine whether zinc stress introduces a characteristic change in the biomolecular phenotype of *Pseudomonas syringae,* and whether this stress influences metabolic activity, Raman microspectroscopy was used. For the former, overnight cultures of B11 were prepared as previously described. For the latter, overnight cultures were prepared using 50% deuterated LB (D-LB), made by replacing 50% of the water in the standard LB recipe with D_2O. This concentration of deuterium was used as it has been shown to be sufficient to detect with Raman spectroscopy and higher concentrations were found to inhibit bacterial growth (154).

Bacterial cultures grown in LB were centrifuged for 10 mins at 3000 xg, washed twice with sterile water, resuspended with LB, and adjusted to have an optical density at 600nm (OD) of 0.2. Bacterial cultures grown in D-LB were centrifuged for 10 mins at 3000 xg, washed twice with D_2O, resuspended with “normal” LB, and adjusted to have an OD of 0.2. At this point, the protocol was followed as quickly as possible to minimise deuterium unlabelling.

Zinc stocks were prepared as previously described to concentrations of 0 mM, 0.8 mM, and 2 mM; representing no inhibition, sub-lethal inhibition, and complete inhibition (as determined in section 5.2.1). 75 μL each of bacteria and zinc stocks were pipetted into a clear 96-well plate and each well was mixed using a multi-channel pipette. Three replicate wells were prepared per treatment, and each treatment was replicated four times to facilitate sampling at four timepoints (0, 2, 4, and 6 hours).

Before incubating the plate, 100 μL from the 0-hour time points was transferred to sterile Eppendorf tubes. The plate was incubated using a pre-warmed Infinite M200 plate reader (Tecan, Switzerland) and shaken every 20 minutes. The bacteria-containing Eppendorf tubes were centrifuged for 1 minute at 17,000 xg, washed with PBS, and resuspended in 4% formaldehyde. The cells were left to fix for 30 minutes at room temperature before centrifuging for 1 minute at 17,000 xg, washing twice with sterile water, and resuspending in 100 μL sterile water. 2 μL of the suspended bacteria was spotted on an aluminium-coated microscope slide and allowed to air dry. This was repeated at each time point.

Raman spectra were collected using a confocal Raman microscope (LabRAM HR Evolution, Horiba Scientific, UK). Single bacteria were viewed through a dry 100x objective (MPLN, NA 0.9, Olympus) and Raman measurements of these were taken with a 532 nm laser (Ventus, Laser Quantum, UK) at a laser power of 80mW (with neutral density filter set to 25%). A diffraction grating of 300 lines/mm was used. The acquisition time for a single cell was 7 seconds and between approximately 30 to 100 cells were measured for each treatment and time point. The instrument was calibrated before each use using silicon which has a known peak at 520.6 cm^{-1}.

Raman spectra were baseline corrected and normalised by peak area using LabSpec6 software (version 6.4.3.35, HORIBA scientific, UK). The peak areas assigned to C-D (2050 - 2300 cm^{-1}) and C-H (2800 - 3100 cm^{-1}) were integrated and the ratio of C-D/(C-D + C-H) was used as a measure of bacterial metabolic activity. Plots showing Raman spectra and boxplots were produced using the R package ggplot2 (version 3.5.1) (142). Scree plots were produced using the R package factoextra (version 1.0.7) (155). PCA analysis and plots were produced using the R package ggfortify (version 0.4.17) (156).

Chapter 3: Monitoring zinc distribution and speciation in healthy and infected *Noccaea caerulescens*

3.1 Introduction

Zinc hyperaccumulation in the metal hyperaccumulator plant *Noccaea caerulescens* has been previously shown to confer defence against the bacterial pathogen *Pseudomonas syringae* (6,25). However, the mechanistic involvement of the metal has yet to be understood. As the degree of metal toxicity will depend on the local concentration and chemistry of the metal at the specific areas of pathogen localisation, this chapter will focus on the use of synchrotron-based X-ray fluorescence microscopy (XRF) and X-ray absorption near-edge structure (XANES) to study the respective distribution and speciation of zinc within healthy, untreated leaves and to understand whether this changes upon infection.

As discussed in Chapter 1, there have been a number of studies using XRF to study metal distribution in hyperaccumulator plants but, to the best of our knowledge, none have done so with respect to the elemental defence hypothesis. There have been a couple of studies, however, using XRF to visualise plant-pathogen interactions in non-accumulator plants but these studies typically look at surface lesions rather than internal structure (157). For example, Brouwer et al. looking at the interaction between *Solanum tuberosum* and the oomycete *Phytophthora infestans* found distinct distribution patterns of metals surrounding the inoculation site between susceptible and resistant plants (158).

In order to study any cellular or subcellular changes that occur as a result of pathogen infection, one needs to look at cross-sections of tissue. This preparation of transverse sections, however, is technically challenging to achieve due to the high percentage of water in plant tissue leading to the high risk of metal redistribution (113,114,159,160). To maintain elemental distributions as close as possible to the physiological state, the “gold standard” method is to rapidly freeze the sample to below ~-130^{o}C to prevent crystalline ice formation and form vitreous, or amorphous, ice which takes

up the same volume as liquid water (161,162). Improper freezing may lead to a phenomenon known as the “Swiss cheese effect” where crystalline ice formation causes damage to the sample via physical puncturing of the internal structure and loss of cellular contents (163,164). This cryofixation is often performed by rapidly plunging the sample in a liquid nitrogen-cooled cryogen such as isopentane (114). Using liquid nitrogen alone is not advisable due to the Leidenfrost effect, where the comparatively warm sample will form an insulating vapour layer around itself, reducing freezing efficiency.(114,162) An alternative to plunge cryofixation is high pressure freezing (HPF). As the name suggests, this method freezes samples under high pressure to promote homogenous supercooling and is typically able to efficiently freeze samples of a greater thickness than plunge cryofixation (114). However, due to the highly vacuolar nature of leaf tissue, HPF introduces the risk of structural damage (165).

Once the sample has been cryofixed, it is crucial for it to remain frozen and for any subsequent preparation steps to be carried out as quickly as possible. For example, temperatures of a cryotome typically range from -15ºC to -30ºC which is sufficient to keep the sample frozen, but the previously mentioned ice-related artefacts may form over extended periods of time (114).

While other methods of fixation and tissue preparation are available to study metal distribution, there are limitations, particularly if the aim is to quantify metal contents or to additionally study metal speciation. For example, freeze-drying is an attractive method if the beamline or facility does not have the capabilities to measure samples under cryogenic conditions as these samples once prepared can be measured at ambient temperature. Cryofixation followed by freeze-drying has successfully been used by Vogel-Mikuš et al to study metal distribution in the cadmium and zinc hyperaccumulator *Noccaea praecox* (166). However, this method risks altering the chemistry of the sample, for example via oxidation of metal complexes, which XANES is particularly sensitive to (114,167). Additionally, while

chemical fixation and freeze-substitution enable preservation of tissue ultrastructure, these techniques may result in the loss or movement of metals of interest (114,168).

Another complicating factor is that X-rays are penetrative and thus will pass through multiple cell layers. Consequently, if samples are too thick, i.e. greater than the depth of a cell, spatial resolution will be lost. Thus, samples need to be sufficiently thin in order to study cellular differences but naturally this makes them more fragile and difficult to handle (114).

In this Chapter, the development of a sample preparation and mounting pipeline for both 2D-XRF imaging and XANES spectroscopy of transverse leaf tissue will be discussed. While not the primary aim of this work, the sample preparation pipeline was developed to enable samples where metal contents could be quantified – by not using fixatives or freeze drying that could alter the chemistry or freeze substitution that could affect the concentration of metals via the physical removal of aqueous components. Thus, the resulting method is for the cryo-preparation of frozen-hydrated tissue. This method was used to study the distribution and speciation of zinc in the leaves of *N. caerulescens* and how this changes upon infection with *Pseudomonas syringae*. Additionally, complementary inductively coupled plasma mass spectrometry (ICP-MS) was used to quantify metal contents in the apoplast, providing evidence of a process leading to the release of zinc into the apoplast in infected tissue.

3.2 Results

3.2.1 Determining the pathogenicity of *Pseudomonas syringae* pv. maculicola NCPPB2038 in *Noccaea caerulescens*

As discussed in section 1.6, *Pseudomonas cannabina* pv. alisalensis could not be used in this work. Instead, two UK-native strains were used: *Pseudomonas syringae* pv. maculicola NCPPB2038 (Psm) and *Pseudomonas syringae* pv. syringae SnB11 (B11). The latter of these was found to be pathogenic to *N. caerulescens* in a previous study, with growth being limited in plants growing on the highest concentration of zinc (300 µM) (25). Pathogenicity is often determined by colony counting-based infection assays. However, this method involves the maceration of tissue which may expose the bacteria to artificially high concentrations of metal if the metal is indeed stored predominantly in epidermal vacuoles as previously indicated (7,8,169). Instead, the pathogenicity of Psm was determined using luminescence imaging with bacteria expressing *luxCDABE*. As shown in Figure 19, an increase in green colour can be seen by 4DPI indicating an increase in the proliferation of Psm.

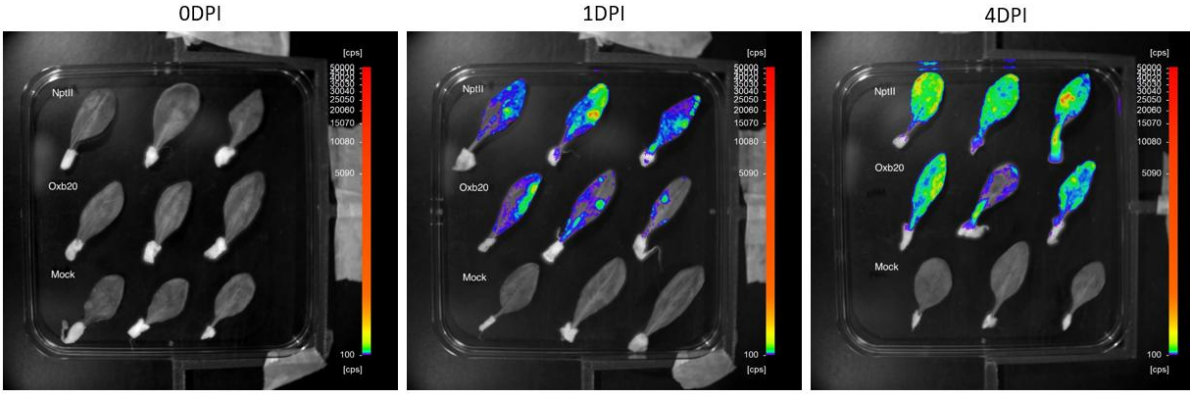


Figure 19: UK Psm is pathogenic to *Noccaea caerulescens.* Luminescence imaging of extra low zinc (10 µM) *Noccaea caerulescens* leaves infected with *P. syringae* pv maculicola expressing *luxCDABE* under the *nptII* and *OXB20* promoters. Mock inoculation was performed by infiltrating leaves with 10 mM $MgCl_2$. Leaves were surface sterilised and then incubated for 10 minutes in the dark before imaging.

Additionally, symptoms were observable in all plants at 6 days post inoculation (DPI) (Figure 20), with these increasing in severity with decreasing zinc concentration, as observed previously with other pathogenic strains.

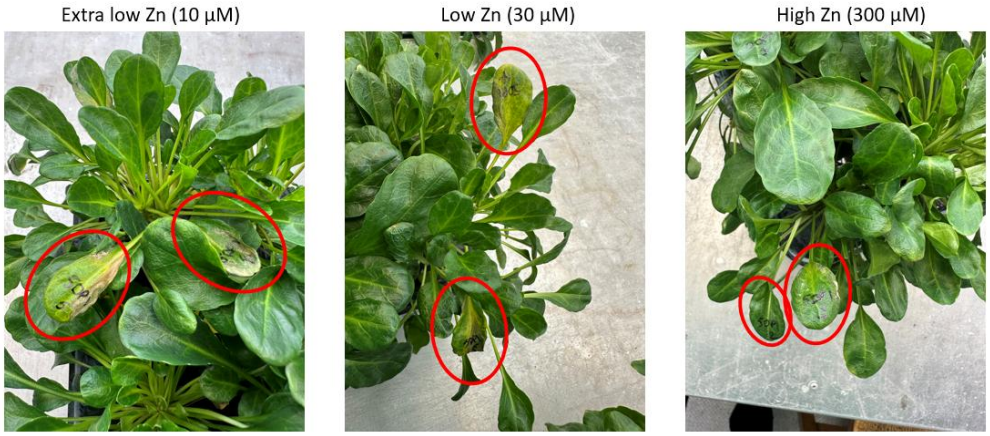


Figure 20: UK Psm is pathogenic to *Noccaea caerulescens.* Photos of symptoms taken after an experiment, at 6DPI. Plants inoculated with Psm at a density of 10^7 cfu/mL.

3.2.2 Development of a pipeline to prepare and mount transverse sections of leaf on the I18 beamline at Diamond Light Source

Prior to synchrotron-based imaging, histological study of *N. caerulescens* was performed to establish an understanding of the typical structure and morphology of the cross section of the plant's leaves. A representative result of this can be seen in Figure 21. No observable difference was found in plants grown on different concentrations of zinc. Cell sizes range between approximately 30 and 50 µm in diameter, becoming smaller with increasing distance from the midrib.

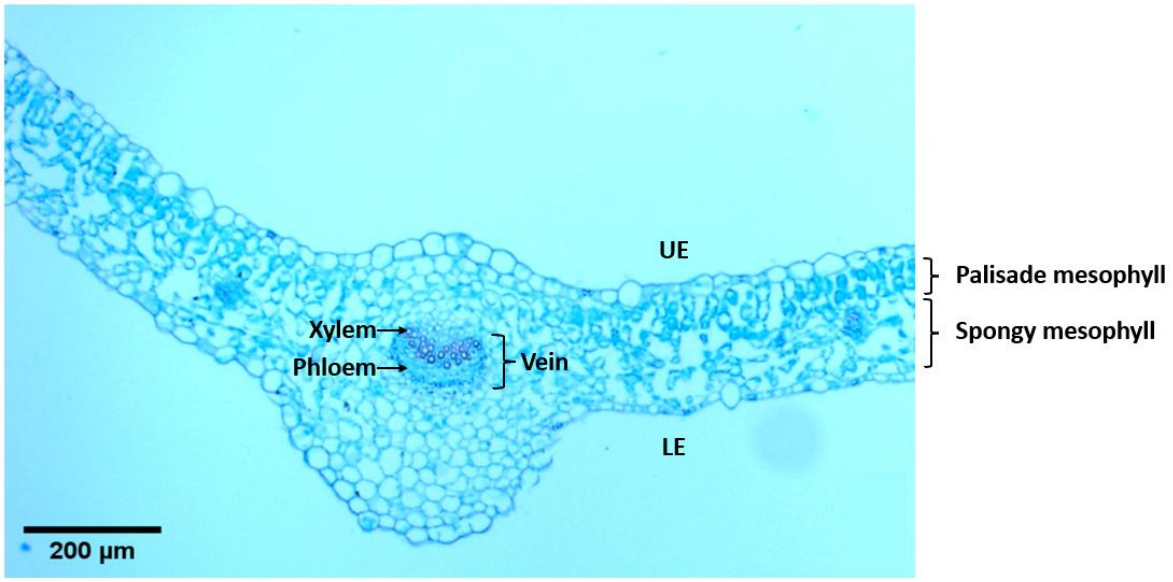


Figure 21: Structure of a transverse section of *Noccaea caerulescens* leaf, taken from the midrib region. Paraffin-embedded and stained with Safranin-O and Fast Green. 10 µm thick section and image taken with 5x magnification. UE = upper epidermis, LE = lower epidermis.

Initial cryosectioning tests followed what was commonly used in the laboratories at Diamond and Oxford at the time, typically for mammalian tissue. In this, small sections of leaf were rapidly excised from the plant using a razor blade and embedded in optimal cutting temperature compound (OCT) in a commercially available cryomold (10 x 10 x 5mm, Tissue-Tek). OCT is a gel at room temperature but freezes solid to act as a support during the subsequent cryosectioning step (170). The cryomold containing the sample and OCT were then cryofixed in isopentane cooled by dry ice (171,172). The frozen block was then affixed to the cryotome's chuck using OCT and left to freeze and equilibrate for ~30 minutes in the cryotome at -18°C (Leica CM1860 UV). Sections were cut to thicknesses of 25 µm and melted onto a room temperature sapphire disc (1 cm diameter, 1mm thick) (170). The sapphire disc was then attached to a custom 3D-printed mount and transferred to the I18 beamline at ambient temperature. The holder was then mounted on the beamline cryostat at 85K (-188°C) for measurement.

Results from this initial beamtime experiment can be seen in Figures 22-24. Figure 22A shows the zinc distribution, figure 22B the potassium distribution, and figure 22C is a composite image showing both the zinc (magenta) and potassium (grey) distributions in a high zinc sample of *N. caerulescens*. Figure 23 shows the same but in a low zinc sample. Zinc is seemingly preferentially stored towards the lower epidermis, with regular “hot spots” being apparent in what could be vasculature. Additionally, zinc seems to be most abundant in the cell walls. Being a macronutrient and the most abundant inorganic cation in plant cells, it was expected that potassium would be present throughout the tissue and in the majority (if not all) cellular compartments (173). However, this does not seem to be the case, with potassium, like zinc, being localised to the cell walls and almost overlaying with zinc in distribution.

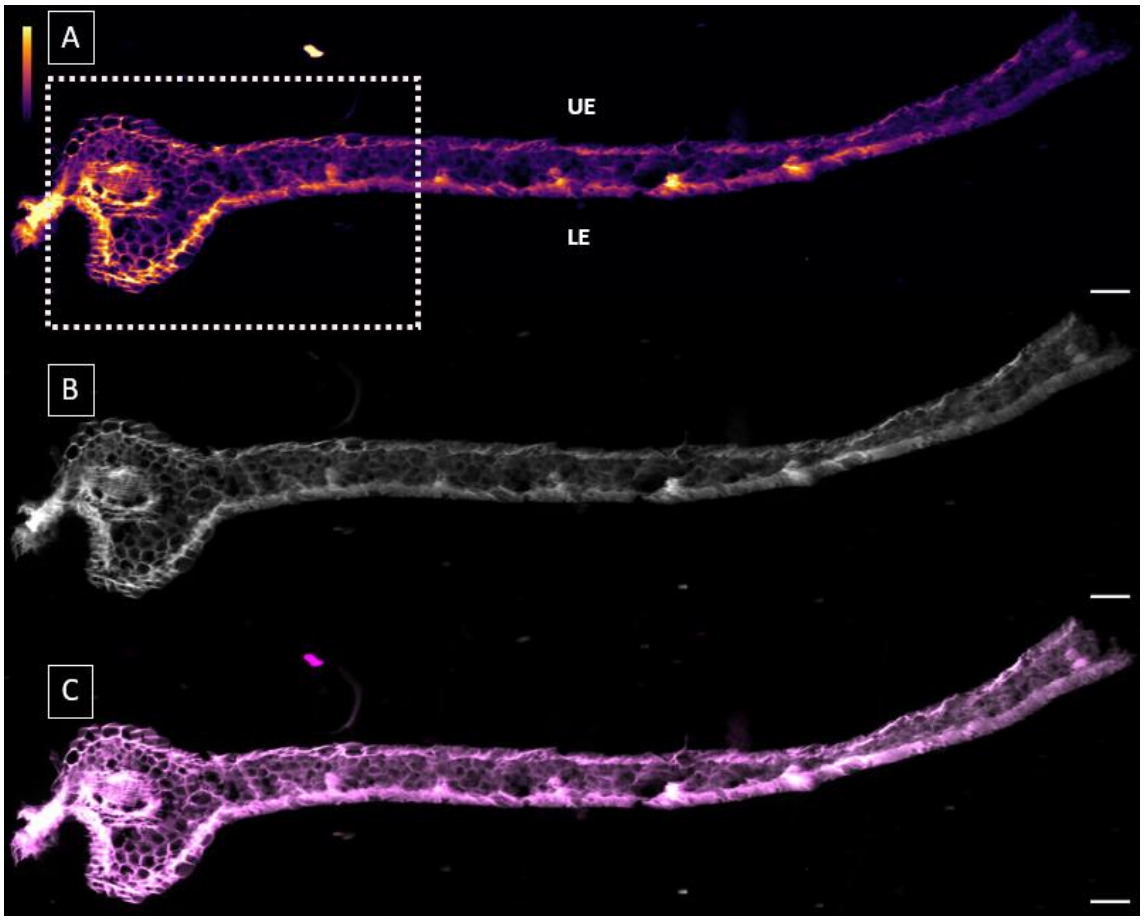


Figure 22: False colour XRF map of a transverse section of high zinc (300 µM) *Noccaea caerulescens* leaf. 2 µm spatial resolution. (A) Zinc distribution indicated by perceptually uniform colour map. (B) Potassium distribution. (C) Composite map showing the relative distribution of zinc (magenta) and potassium (grey). UE = upper epidermis, LE = lower epidermis. Dashed box indicates the approximate size of the sections shown in section 3.2.3. Scale bar indicates 100 µm.

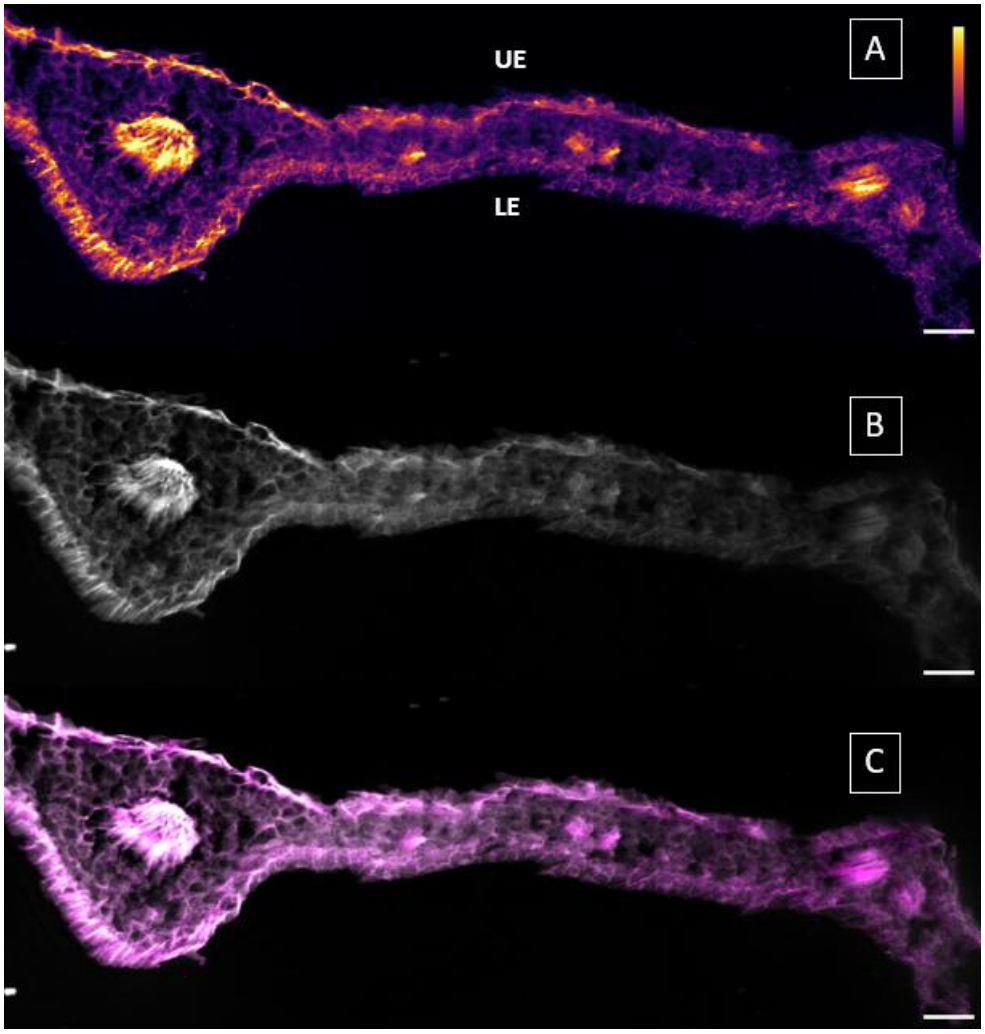


Figure 23: False colour XRF map of a transverse section of low zinc (30 µM) *Noccaea caerulescens* leaf. 2 µm spatial resolution. (A) Zinc distribution indicated by perceptually uniform colour map. (B) Potassium distribution. (C) Composite map showing the relative distribution of zinc (magenta) and potassium (grey). UE = upper epidermis, LE = lower epidermis. Scale bar indicates 100 µm.

Based on previous studies, it was expected that zinc would be stored in the epidermal vacuoles so as to not interfere with important metabolic processes (7,8). Additionally, potassium is known to be present in vacuoles throughout the leaf, and vacuoles have been noted as being the “main cellular reservoir” for the metal (174,175). It was surprising, therefore, that vacuoles seem to be devoid of both potassium and zinc. This can be seen in Figure 24.

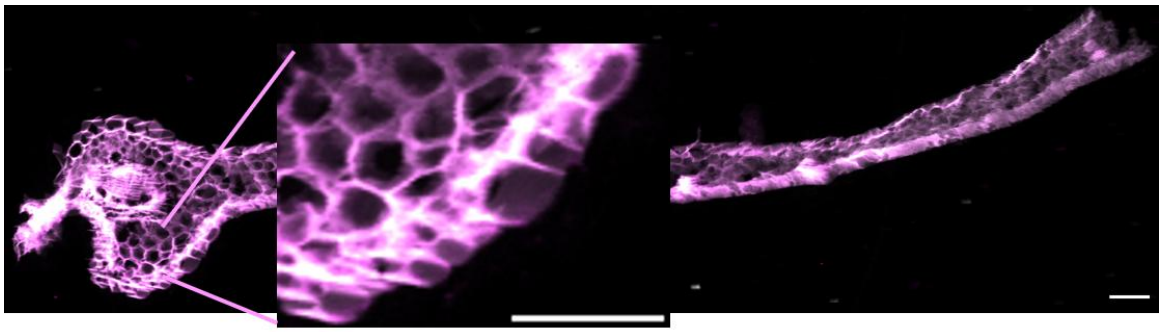


Figure 24: Highlighted region indicating the absence of vacuolar metals. Scale bar indicates 100 μm.

It thus became apparent that these results reflected limitations in sample quality. These factors are discussed in section 3.1, but the artefact most apparent is the “Swiss cheese effect” arising due to improper freezing. Various steps in the preparation of these samples could have influenced sample quality. Using dry ice in the cool bath with isopentane limits freezing to approximately -70ºC, far below the crucial -130ºC to prevent crystalline ice formation (161,162,176). Additionally, samples were not maintained in a frozen state; the substrate was used at room temperature to adhere to the sample, and transfer to the beamline was also done at ambient temperature. In combination with these factors, cells with diameters equivalent to the section thickness (25 μm) would be “open” and the contents would leak out due to improper preparation.

In a subsequent beamtime, therefore, more emphasis was placed on maintaining the sample in a frozen state. The cryofixation step was also changed from dry ice to liquid nitrogen and isopentane, which reaches approximately -160ºC (177). Using liquid nitrogen, however, led to new issues with visibility due to the vapour. This meant it was difficult to keep the cryomold flat during cryofixation. If the cryomold was not kept flat, the OCT could shift with the sample before it was frozen and would lead to the sample not being in the correct orientation to enable the production of transverse sections. To aide with this, a custom 3D-printed cradle was made for the cryomold to fit in to, which could be held in the cool bath with forceps. This can be seen in Figure 25.

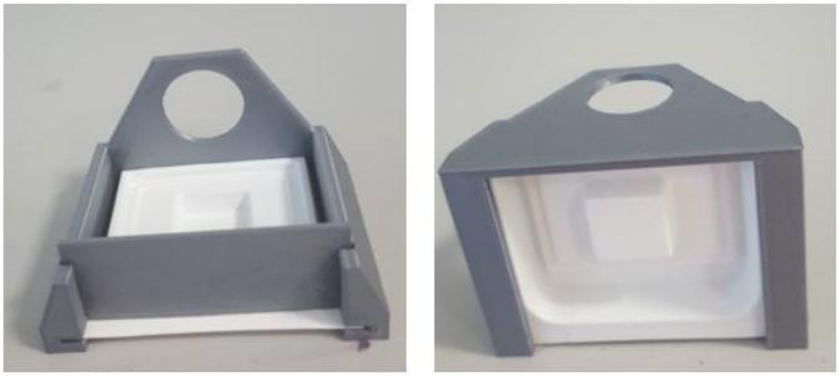


Figure 25: Commercially available cryomold (10 x 10 x 5 mm) contained in a custom 3D-printed cradle for submersion in cryogens.

Because a focus was on keeping the sample frozen, the melting method of affixing the sample to a room temperature substrate could not be used. Instead, carbon-based Leit tabs were used which are adhesive on both sides (Agar Scientific, UK). These were applied to the substrate in the cryotome, which did not reduce the adhesivity. The substrate with sample attached could then be affixed to the mount with glue as previously described and transferred to the beamline on dry ice.

Although the improvements in keeping the sample frozen were successful, it was apparent that the cryofixation step was still too slow. The block of OCT in the cryomold took 10s of seconds to freeze solid which would indicate that the sample of leaf would take at least this long to freeze.

The subsequent aim was to improve the cryofixation step. Discussion with Professor Katarina Vogel-Mikuš (University of Ljubljana, Slovenia) guided the focus to reduce the size of the cryomold to increase freezing efficiency (178). The improved protocol can be seen in Figure 26. An aluminium tube with internal diameter of 2mm was cut to be approximately an inch in length and a drop of OCT was applied to one of the ends. A small section of leaf was rapidly excised from the plant, as indicated in Figure 26A, and inserted into the tube with the OCT acting as an adhesive. In most imaging, the midrib region was chosen as the focus due to its role in metal transport and to also enable easy distinction between the upper and lower

epidermal layers. Next, the tube was inverted using a pair of tweezers and dipped into a container of OCT to form a droplet around the sample. Then using a pair of 30 cm forceps, the tube containing the leaf sample was submerged in liquid nitrogen cooled isopentane for ~20 seconds. Freezing occurs almost instantaneously, but the prolonged submersion is to ensure complete freezing. The tube with the frozen sample was inserted directly into a polystyrene box of dry ice, ensuring direct contact with the sample. This was then transferred to the cryotome and inserted into a custom chuck (Figure 26E) which could be tightened around the sample tube.

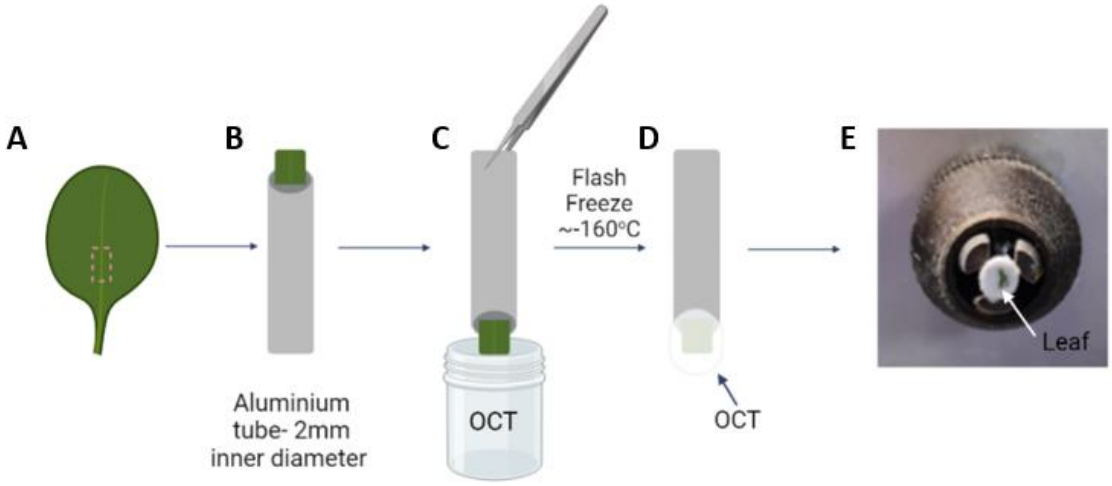


Figure 26: A) A small section of leaf is rapidly excised. B) The section of leaf is inserted into an aluminium tube with internal diameter of 2mm. C) The tube is dipped into optimal cutting temperature (OCT) compound. D) The leaf is flash frozen in isopentane cooled by liquid nitrogen. E) The tube is inserted into a custom chuck, placed in a Leica CM1860 cryotome and sectioned to thicknesses of 25 µm. Adapted from Vogel-Mikuš, K et al, 2014. Made in BioRender.

25 µm thick sections were prepared using the cryotome and affixed to the Leit tab as previously described using cooled tweezers and fine paintbrushes. As shown in Figure 27, this step could be further optimised as it is difficult to get samples to lie flat on the substrate. Because of this, multiple samples are mounted on one disc increasing the likelihood that at least one will be suitable for imaging. Subsequently, an approximately 1x1 cm piece of 4 µm

thick Ultralene® (Fisher Scientific, UK) is placed over the samples to minimise damage from the cryostat and vacuum. As described previously, while still in the cryotome, the substrate can then be glued to the custom 3D-printed mount (shown in Figure 27, indicated by the red arrow). Magnets on this mount enable easier transfer from the cryotome to the beamline, using a magnetised transfer device. For transfer, the sample is placed in a polystyrene box of dry ice, again ensuring direct contact.

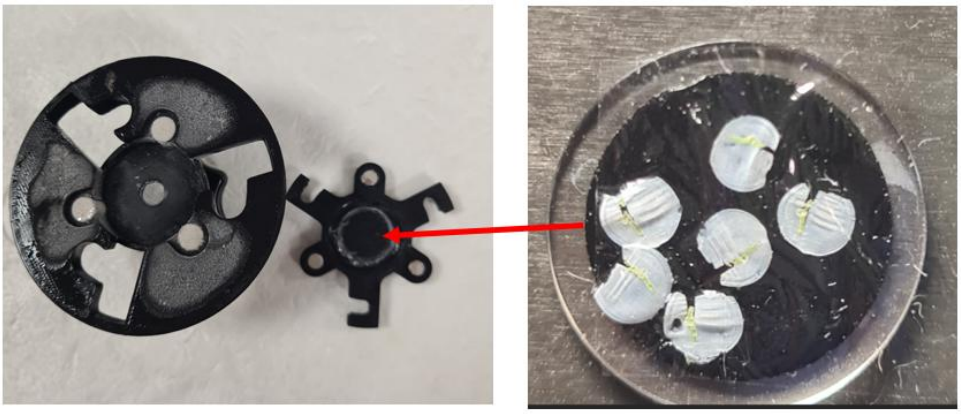


Figure 27: Leaf sections are mounted on an adhesive carbon “Leit” tab on a 1 cm diameter sapphire disc. A sheet of Ultralene® is placed over the samples to minimise damage from the cryostat and vacuum. The sapphire disc is mounted in a 3D-printed sample holder, which can then be attached via magnets to a transfer device (far left) to allow mounting on the beamline.

As previously discussed, sample thickness is likely to have an effect on the resulting spatial resolution of XRF images. Therefore, two thicknesses were tested: 25 μm and 60 μm, the former likely to be smaller than the diameter of a cell and the latter likely to be larger. Results of this test are shown in Figure 28, where it can be seen that individual cells are more easily distinguished in the 25 μm sample. Thus, although it is easier to produce thicker sections, spatial resolution is lost as X-rays are penetrative. Because of this, 25 μm thick sections are used throughout this work.

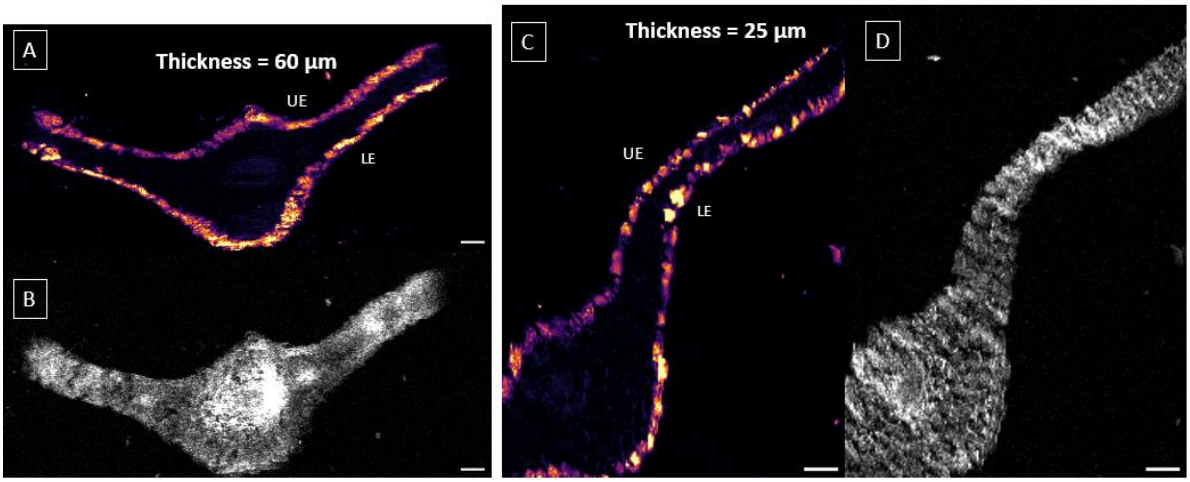


Figure 28: Image resolution is affected by sample thickness. High zinc samples of *Noccaea caerulescens* leaves sectioned to 60 µm (left) and 25 µm (right) thicknesses. Zinc distribution is shown in A and C, and potassium distribution is shown in B and D. UE = upper epidermis, LE = lower epidermis. Scale bar indicates 100 µm.

As discussed in sections 1.7 and 2.8, multiple elements are detected simultaneously in XRF. The elements that provide a signal in *N. caerulescens* leaves can be seen in Figure 29. A surprising observation is that the signal for iron is very weak, when it is well known that iron is an important micronutrient in plants and is present in the hydroponic media. The cause of this observation remains uncertain; however, interference from the substrate is a possible factor, as suggested by the more distinct background patterning.

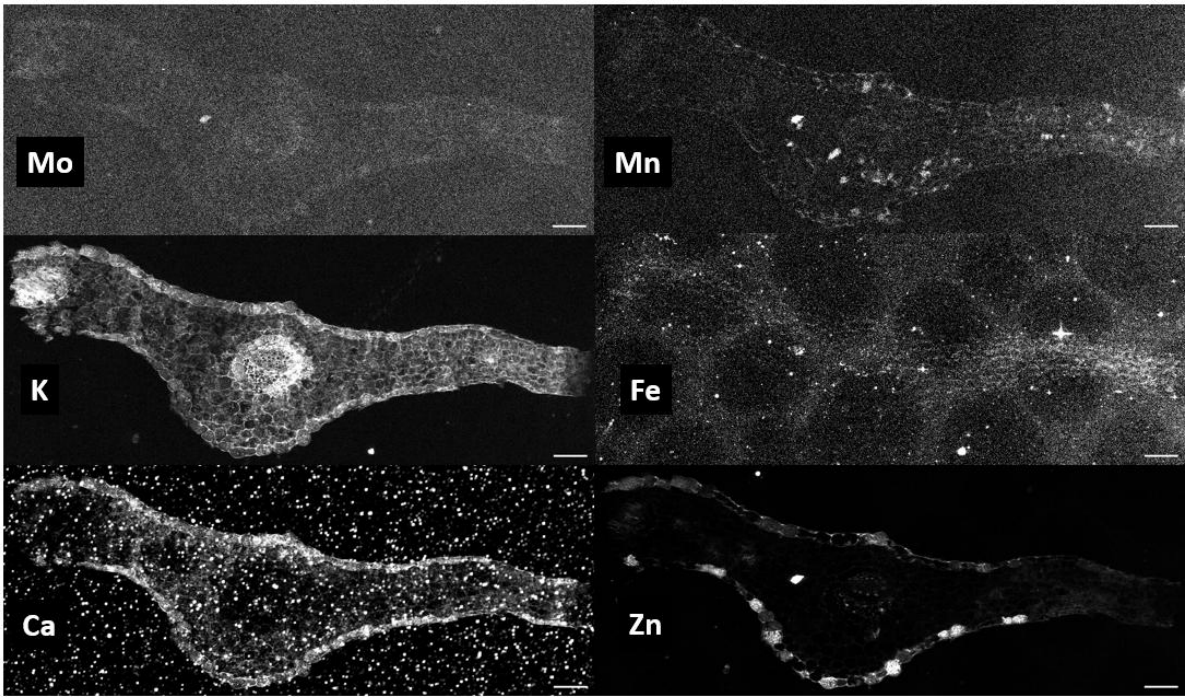


Figure 29: Signals obtained from different elements in *Noccaea caerulescens* leaf. Scale bar indicates 100 µm.

There is also a clear artefact in the calcium map, which is now understood to have arisen from the Kapton window of the cryostat. Future beamtimes will test the cryojet system typically used for tomography. Nonetheless, the distribution of calcium is similar to that of potassium with the exception of the vasculature.

The signal for potassium is strong and the metal is apparent throughout the tissue, enabling its use as a proxy for sample integrity. As discussed previously, cell leakage is likely to occur due to damage during the sample preparation steps or due to improper freezing. Therefore, if the potassium signal is present throughout the cells we can assume sample integrity.

3.2.3 XRF imaging of healthy and infected *Noccaea caerulescens*

The sample preparation pipeline discussed in section 3.2.2 was used to prepare frozen-hydrated leaf samples of *Noccaea caerulescens* grown on different concentrations of zinc. These sections were mounted on the I18 beamline at Diamond Light Source to monitor the distribution of zinc using XRF spectroscopy. Results of this can be seen in Figures 30-32. In each image A, the zinc distribution is indicated using a perceptually uniform colour map, with a more yellow colour indicating greater intensity or concentration. Counts values for each map are given on each image, but it is important to note that the maps are not normalised to each other – the primary aim is to highlight the difference in zinc distribution. Each image B shows the distribution of potassium. Each image C is a composite of the zinc distribution overlaid with that of potassium. As previously discussed, potassium is almost ubiquitous in leaf tissue and thus could be used as a guide to indicate tissue anatomy and also as a control to ensure sample integrity.

A representative, high resolution XRF map of untreated *N. caerulescens* grown on the lowest concentration of zinc (“extra low”, 10 μM) can be seen in Figure 30. Zinc distribution is localised to the epidermis, with greater intensities in the lower epidermis and in

larger cells. Particularly notable, though, is that the distribution of zinc in the epidermal layers is not uniform. Some epidermal cells do not seem to contain any zinc, while others have a relatively high intensity. To ensure this observation is not simply due to sample damage and loss of vacuolar contents, one can look at the potassium map. It can be seen that in epidermal cells devoid of zinc, potassium is still present. As expected, potassium is distributed throughout the tissue, with higher intensities observed in the vasculature.

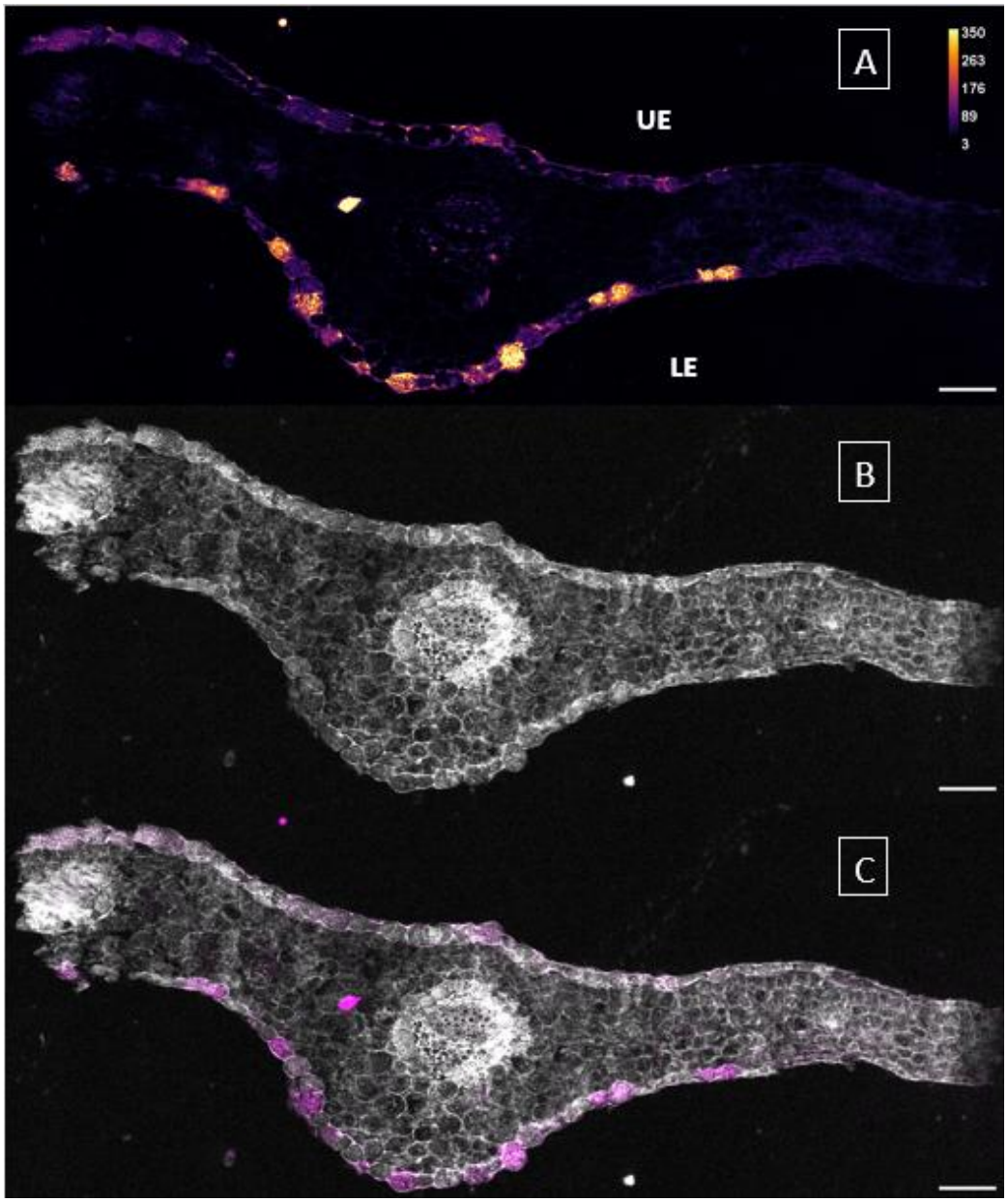


Figure 30: False colour XRF map of a transverse section of extra low zinc (10 µM) *Noccaea caerulescens* leaf. 1 µm spatial resolution. (A) Zinc distribution indicated by perceptually uniform colour map. (B) Potassium distribution. (C) Composite map showing the relative distribution of zinc (magenta) and potassium (grey). UE = upper epidermis, LE = lower epidermis. Scale bar indicates 100 µm.

Debris can be seen on Figure 30 as a high zinc intensity hotspot in the mesophyll. This likely occurred as the sample preparation, particularly the cryotome, is “open” meaning particulate matter from the laboratory can land on or otherwise interfere with the sample.

A representative, XRF map of *N. caerulescens* grown on the middle concentration of zinc (“low”, 30 µM) can be seen in Figure 31. Compared to the extra low zinc plant, more of the epidermal cells seemingly contain zinc, again more so in the lower epidermis. Particularly noticeable in the upper epidermis is that, like the extra low zinc, zinc is seemingly preferentially stored in larger cells. The distribution of potassium is consistent with the extra low zinc plant.

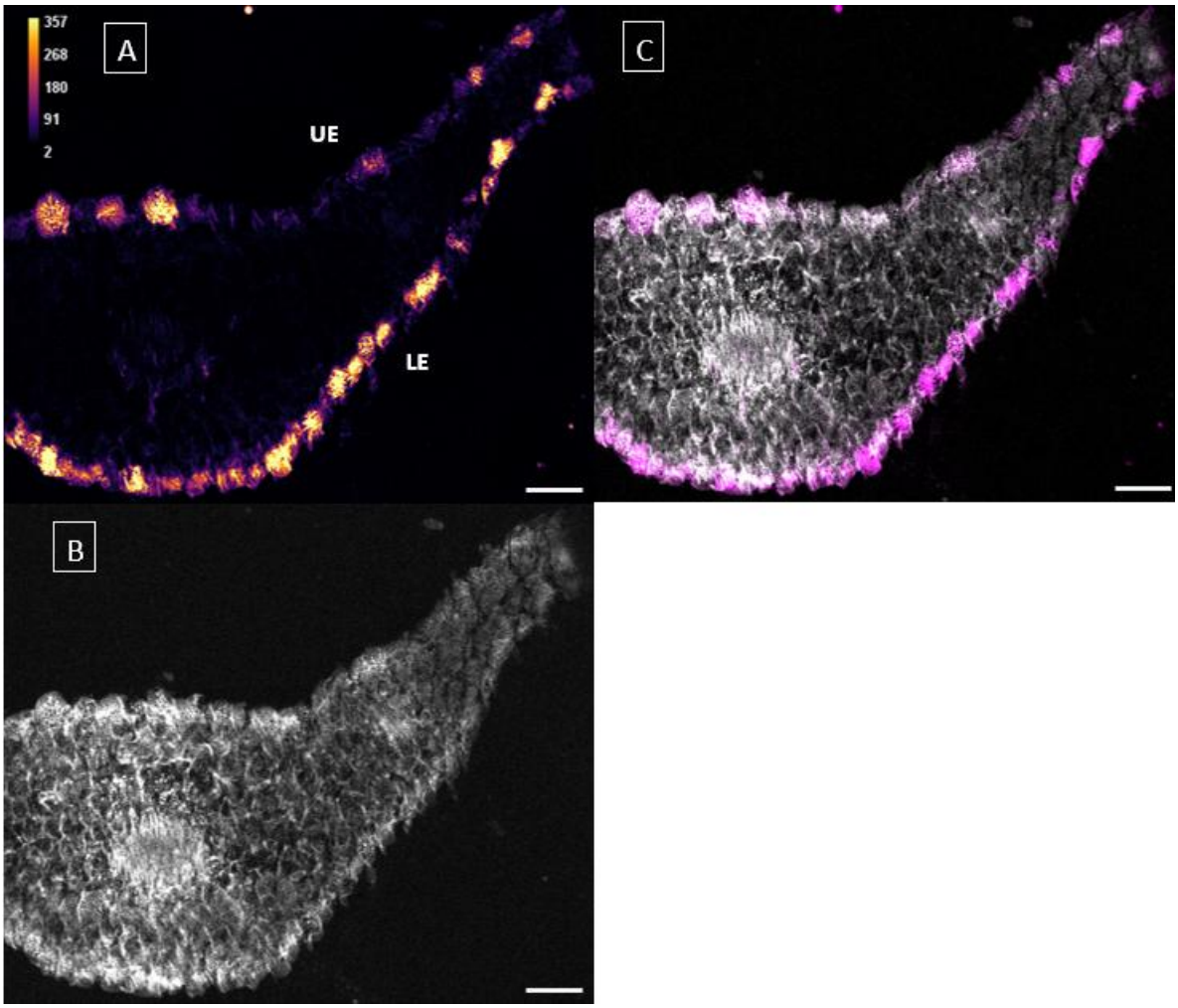


Figure 31: False colour XRF map of a transverse section of low zinc (30 µM) *Noccaea caerulescens* leaf. 2 µm spatial resolution, 25 µm thick. (A) Zinc distribution indicated by perceptually uniform colour map; colour bar shows values in counts. (B) Potassium distribution. (C) Composite map showing the relative distribution of zinc (magenta) and potassium (grey). UE = upper epidermis, LE = lower epidermis. Scale bar indicates 100 µm.

A representative, XRF map of *N. caerulescens* grown on the highest concentration of zinc (“high”, 300 µM) can be seen in Figure 32. In keeping with the trend, a greater number of the epidermal cells contain zinc. Additionally, it appears as if the distribution between the upper and lower epidermis evens out, with comparable intensities being observed. In this high zinc sample, there also appears to be lower preference for zinc storage in larger cells, particularly in the upper epidermis. The distribution of potassium is consistent with the extra low and low zinc plants, with the exception of a seemingly higher intensity area on the right-hand-side of the sample. This may have arisen due to the sample not being completely flat.

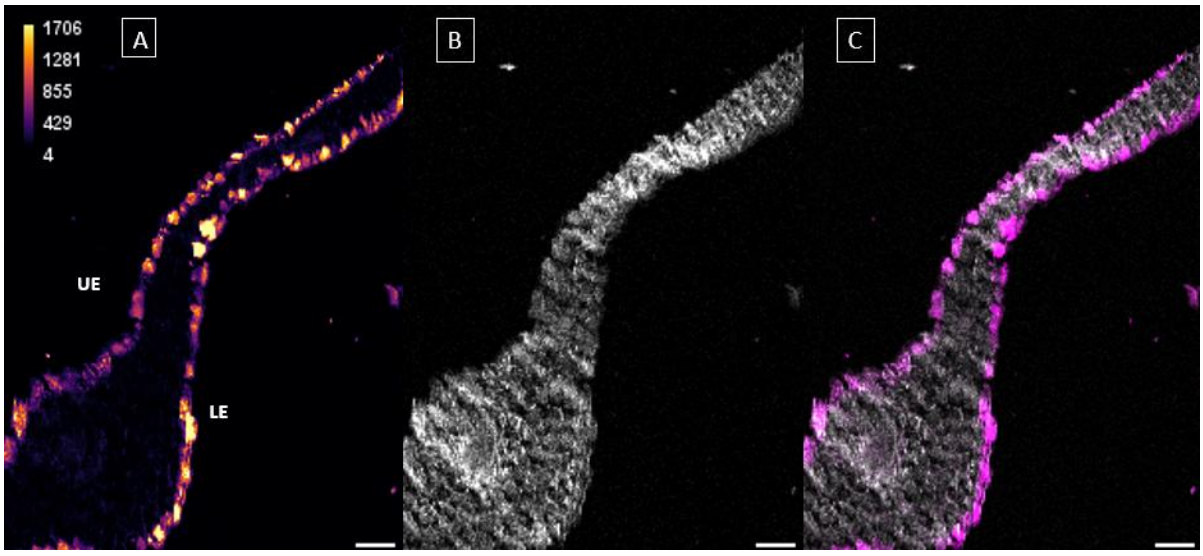


Figure 32: False colour XRF map of a transverse section of high zinc (300 µM) *Noccaea caerulescens* leaf. 5 µm spatial resolution. (A) Zinc distribution indicated by perceptually uniform colour map. (B) Potassium distribution. (C) Composite map showing the relative distribution of zinc (magenta) and potassium (grey). UE = upper epidermis, LE = lower epidermis. Scale bar indicates 100 µm.

Additional replicates taken from different plants of all three zinc treatments can be seen in the Appendix Figures 85 - 87.

To map the differences in zinc distribution and intensity observed in the epidermis as treatment concentration increases, the intensity profile was measured for the upper and lower epidermis as described in section 2.8. Cell 0 in Figure 33 refers to the first cell visible on the left-hand side, with increasing numbers moving to the right across the sample.

Because the images show different fields of view, the approximate location of the cells above or below the midrib is marked with a dashed line. As the potassium signal is consistent throughout the maps and between samples, data is plotted as the ratio of zinc to potassium intensities for each cell.

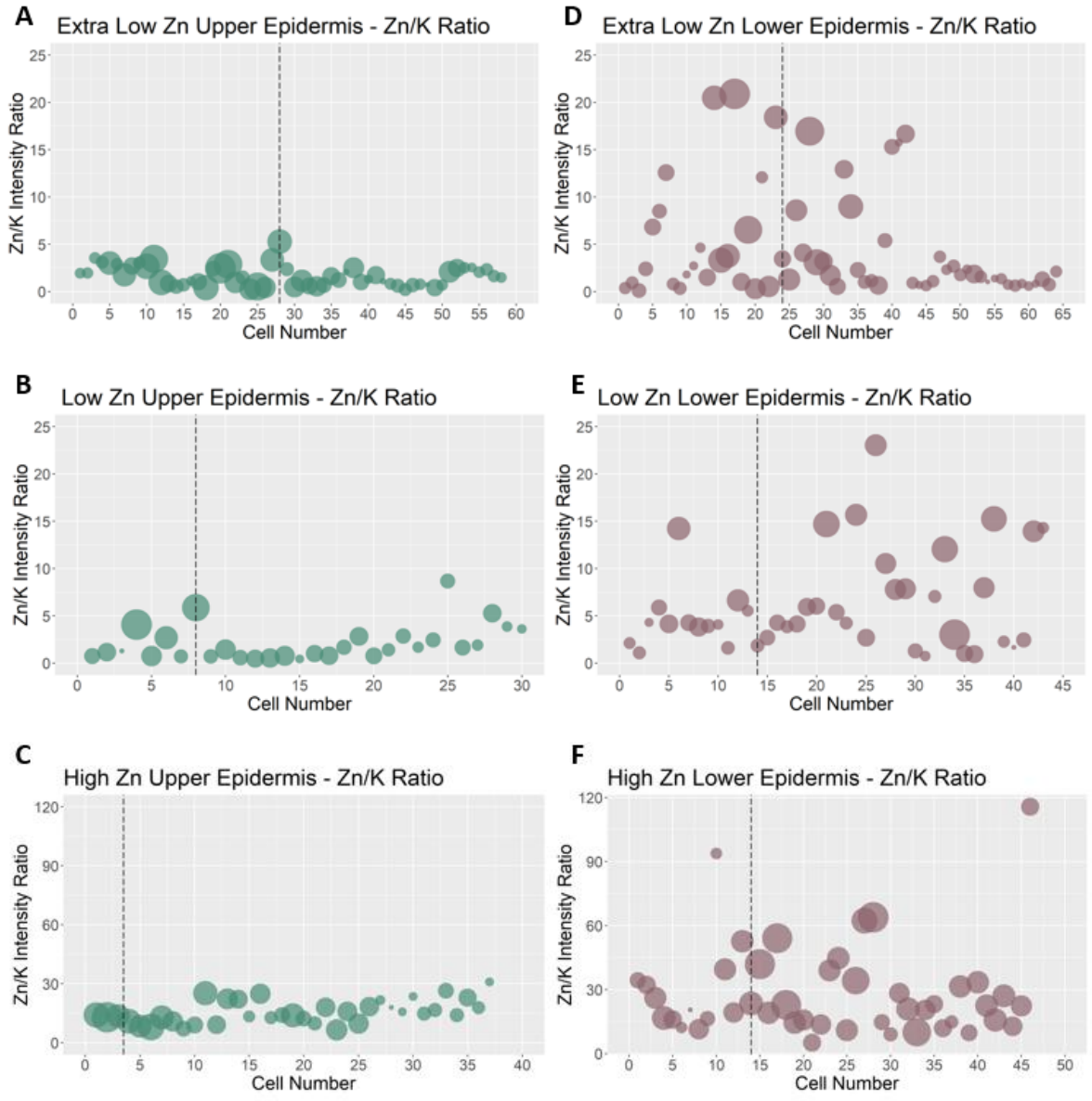


Figure 33: Graphical representation of the size and zinc content of cells in the upper and lower epidermal layers in extra low (A and D), low (B and E), and high zinc (C and F) *N. caerulescens*. Cell number 0 refers to the cell on the far left of the image, as described in section 2.8. The size of the "bubble" indicates the relative size of the epidermal cell. The dashed line indicates the approximate location of the centre point of the central vein.

A clear observation in Figure 33 is that there is a greater degree of heterogeneity in the lower epidermis, decreasing with increasing zinc treatment. In the high zinc sample, both the upper and lower epidermis show similar distribution patterns but with slightly more variation in the lower epidermis. Extra low and low zinc samples, however, show more variation between the two epidermal layers. In both samples, zinc : potassium ratio in the upper epidermis is more consistent, indicating less variability.

Another observation from Figure 33 is that there does seem to be a correlation between cell size and zinc intensity, with larger cells often containing more zinc. To confirm this observation, zinc intensity expressed in counts is directly plotted against cell size in Figure 34. There is a positive correlation in the extra low and low zinc samples but this trend is less evident in the high treatment, with a slight negative correlation in the upper epidermis. These observations perhaps suggest that there is a preference for zinc storage in larger epidermal cells when environmental zinc is limited.

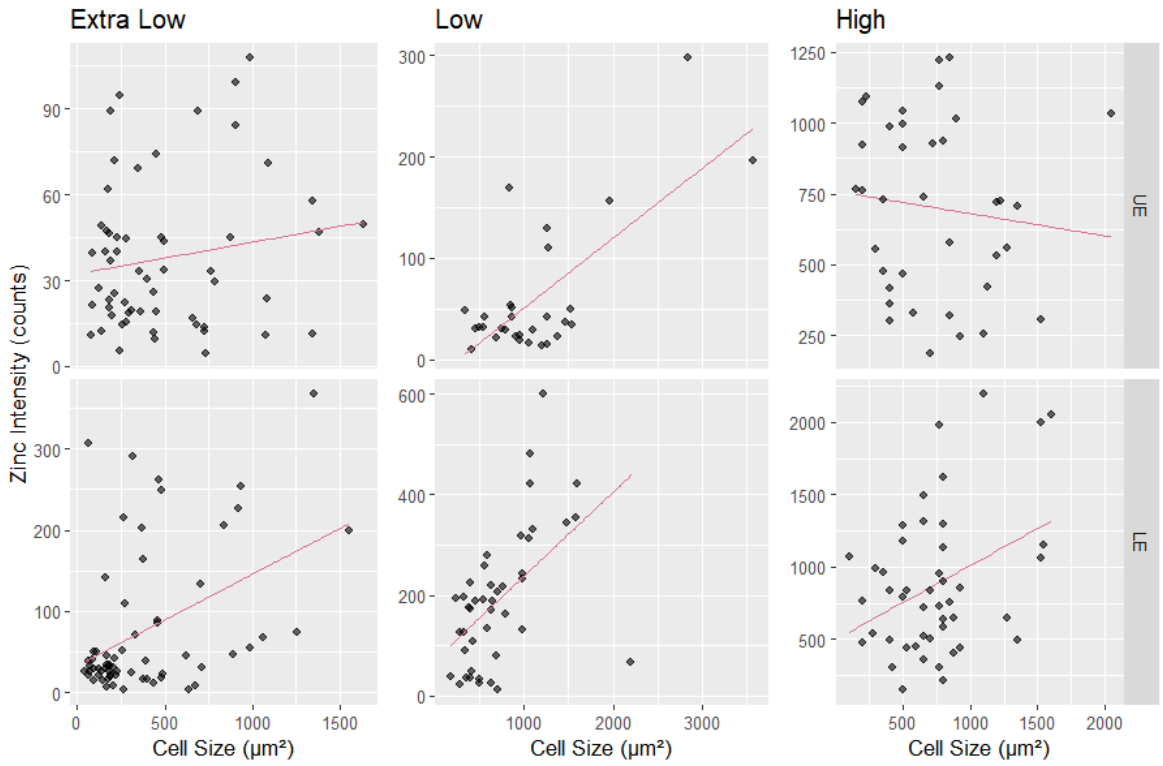


Figure 34: The correlation of zinc intensity and cell size in the epidermal layers. UE = upper epidermis, LE = lower epidermis.

The intensity of zinc in the upper and lower epidermis can be seen in Figure 35 expressed as box plots. In keeping with previous observations, the difference in zinc concentration between the two epidermises is greatest in the extra low and low zinc plants. The mean intensity values are reasonably proportional to the zinc treatment, with the highest zinc intensity observed in the high zinc sample. It should be noted, however, that as X-rays are penetrative and would pass through the entire 25 μm section, that the zinc signal could be influenced by position at which the (approximately) spherical cells are sectioned. Cells sectioned closer to their centre point would be shown as larger and potentially yield a higher zinc signal.

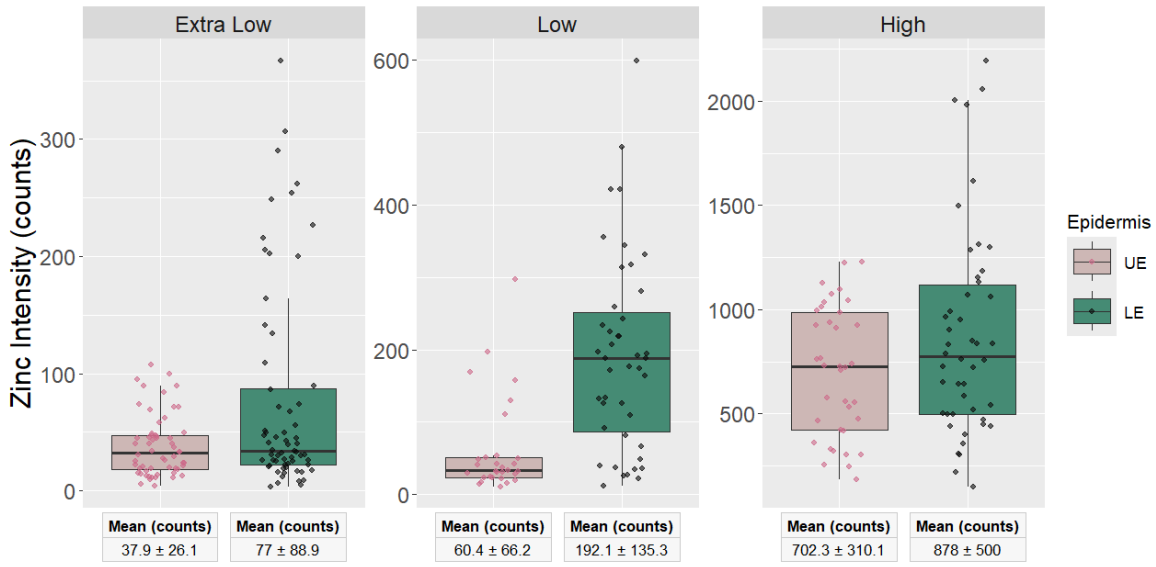


Figure 35: Comparison of zinc intensity in the upper and lower epidermis in extra low, low, and high zinc *Noccaea caerulescens*. The mean and standard deviation is expressed in counts at the bottom of the plots. Each dot represents an individual cell. Box plots display the median, interquartile range, and minimum/maximum values. Outliers are presented outside of the whiskers.

In order to study any potential changes in zinc distribution that occur as a result of *Pseudomonas syringae* infection, infected transverse sections of *N. caerulescens* were measured with XRF imaging. Two different strains with potentially varying virulence mechanisms, *P. syringae* pv. maculicola and *P.* syringae pv. syringae SnB11, were tested to see if any changes in phenotype were observable. Due to symptoms present on extra low

and low zinc plants (see Figure 20) making sectioning difficult, only high zinc samples were used. Figure 36 shows an XRF map of a high zinc section of *N. caerulescens* excised from the plant at 5 days post inoculation (DPI) with *Pseudomonas syringae* pv. maculicola (Psm). While zinc is still apparent in the epidermis, the majority appears to be in the periphery of the cells or has mobilised from the vacuoles to the apoplastic space. Additionally, compared to the untreated sample (Figure 32), there seems to be an increase of zinc in the xylem and phloem of the mid vein. Potassium, however, is still largely visible in the epidermal cell vacuoles.

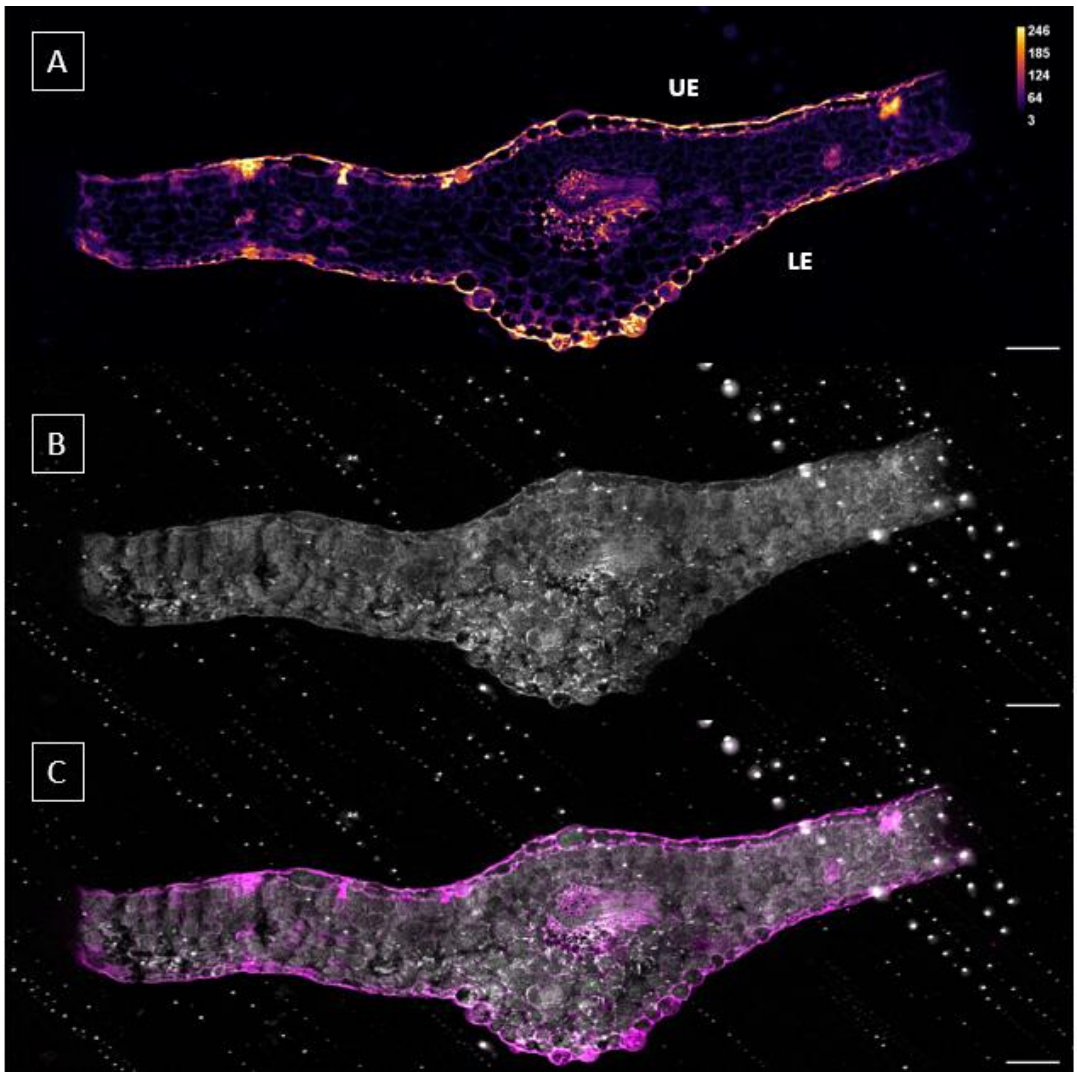


Figure 36: False colour XRF map of a transverse section of high zinc (300 µM) *Noccaea caerulescens* leaf infected with *P. syringae* pv maculicola (5 days post infection). 1 µm spatial resolution, 25 µm thickness. (A) Zinc distribution indicated by perceptually uniform colour map. (B) Potassium distribution. (C) Composite map showing the relative distribution of zinc (magenta) and potassium (grey). Artefact apparent from Kapton visible on the potassium map. UE = upper epidermis, LE = lower epidermis. Scale bar indicates 100 µm.

Figure 37 shows an enlarged section of Figure 36 to highlight the presence of zinc in the apoplastic space of the infected tissue. As shown, zinc is apparent between potassium filled cells – particularly in the mesophyll.

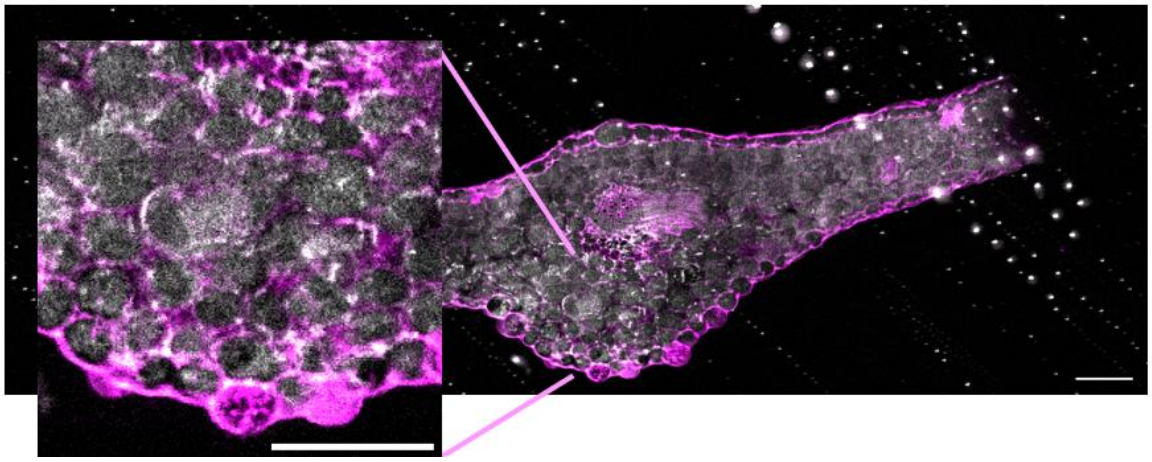


Figure 37: Highlighted area of Figure 36 indicating the presence of zinc in the apoplastic space. Scale bars indicate 100 μm.

Zinc mobilisation is also observed in tissue infected with *P. syringae* pv. syringae SnB11 (B11), as seen in Figure 38. Additionally, potassium also appears consistent with the untreated tissue. As with Psm infected tissue, more zinc is seen in the xylem and phloem of the midvein than in the untreated tissue. Figure 39 shows an enlarged section of Figure 38 to highlight the presence of zinc in the apoplastic space of the tissue infected with B11. In both the Psm and B11 maps, not every epidermal cell has mobilised zinc. Some cells, typically the larger cells, have retained the metal.

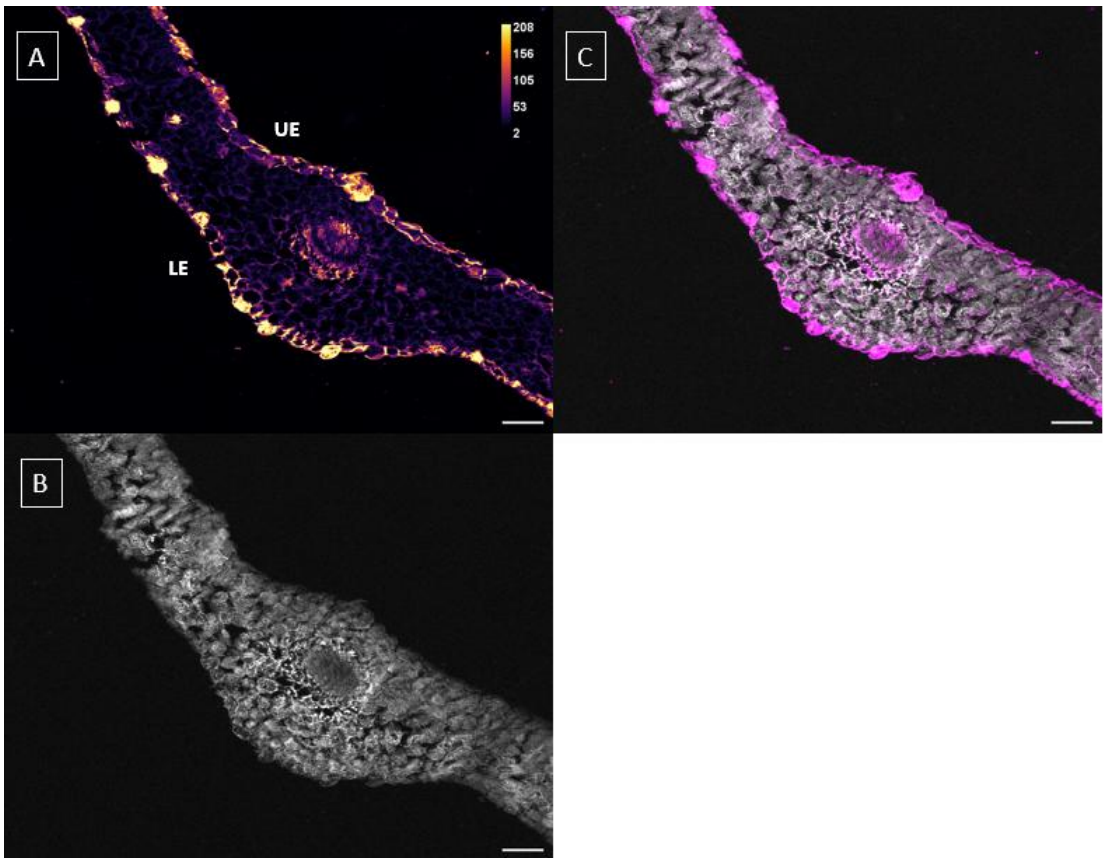


Figure 38: False colour XRF map of a transverse section of high zinc (300 µM) *Noccaea caerulescens* leaf infected with *P. syringae* pv syringae SnB11 (5 days post infection). 1 µm spatial resolution. (A) Zinc distribution indicated by perceptually uniform colour map. (B) Potassium distribution. (C) Composite map showing the relative distribution of zinc (magenta) and potassium (grey). Scale bars indicate 100 µm.

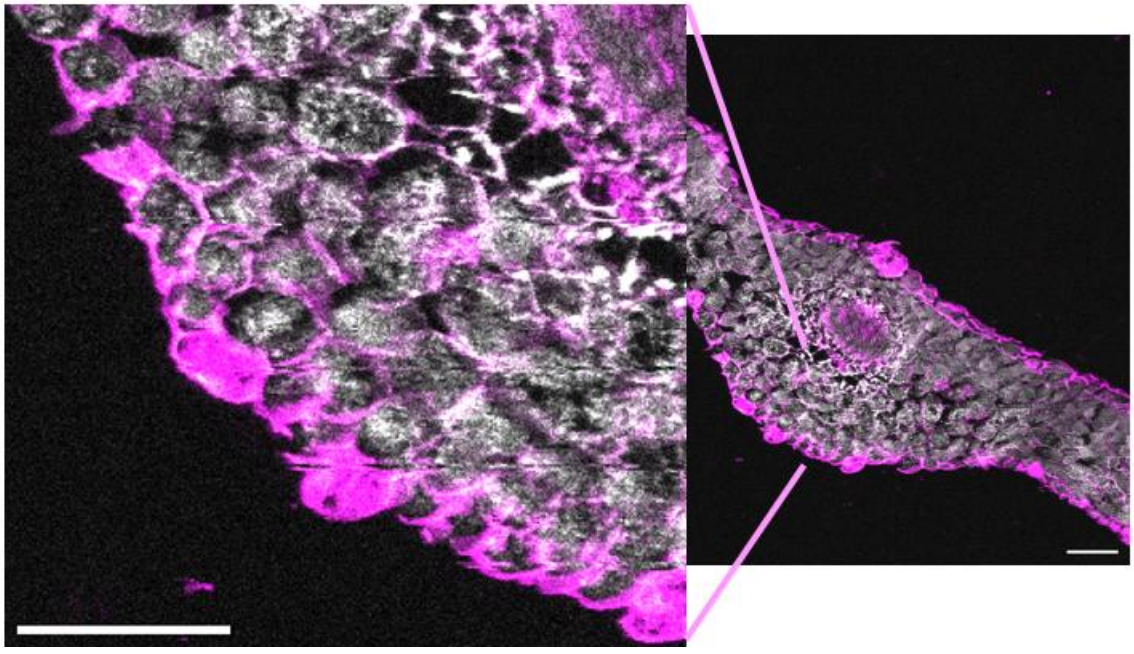


Figure 39: Highlighted area of Figure 38 indicating the presence of zinc in the apoplastic space. Scale bars indicate 100 µm.

To ensure the observation of zinc mobilising from the epidermal vacuoles to the apoplastic space is not a result of the mechanical process of infiltration, mock inoculation was performed on the tissue using magnesium chloride. As shown in Figure 40, the zinc in the mock inoculated tissue is distributed comparably to the untreated tissue.

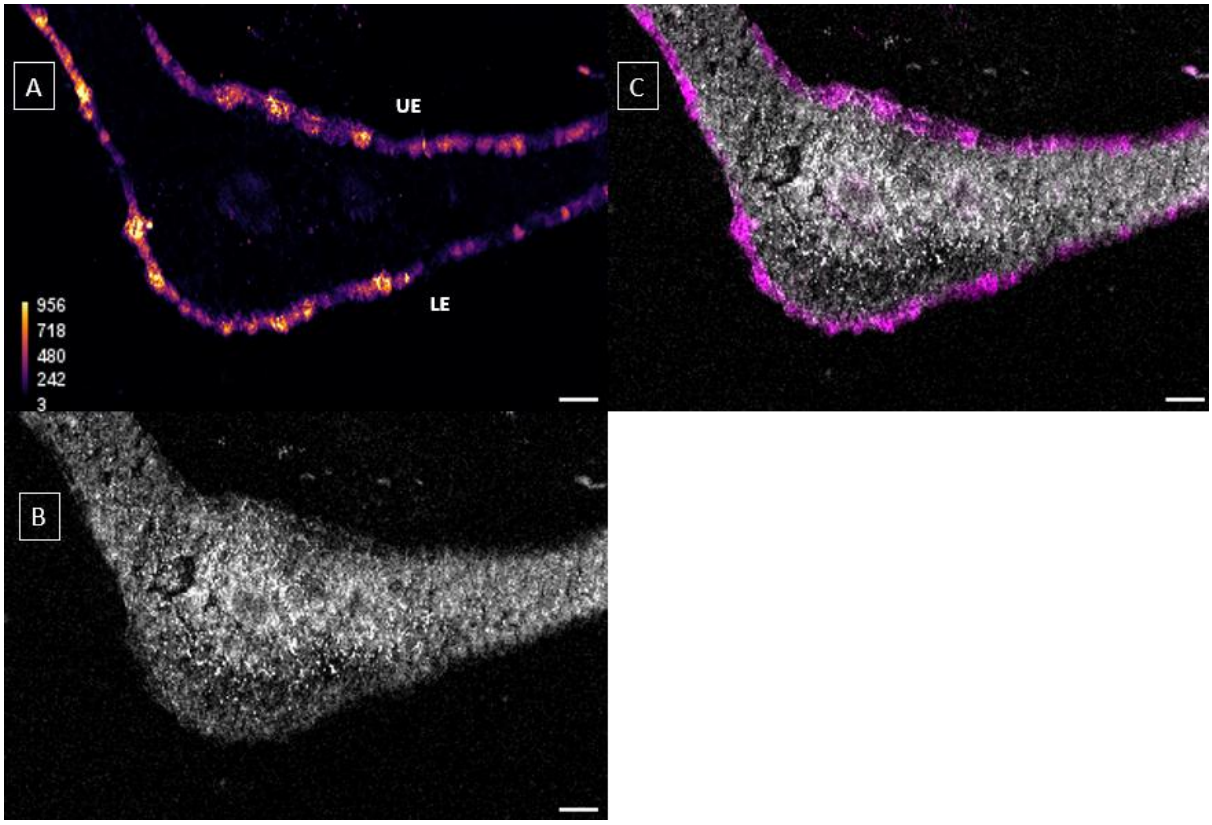


Figure 40: False colour XRF map of a transverse section of high zinc (300 µM) mock inoculated *Noccaea caerulescens* leaf. 5 µm spatial resolution. (A) Zinc distribution indicated by perceptually uniform colour map. (B) Potassium distribution. (C) Composite map showing the relative distribution of zinc (magenta) and potassium (grey). Scale bars indicate 100 µm.

In the infected maps, Figures 36 and 38, the zinc in the vein is more apparent than in the untreated and mock samples (Figures 32 and 40, respectively). However, this observation could be due to lower contrast between the different regions as the high inensity epidermal regions of the untreated and mock samples are less significant in the infected images. Figure 41 compares the zinc intensity of the cells of the upper and lower epidermis, the vein, and the extracellular space of the mesophyll tissue in the untreated, mock treated, and infected samples.

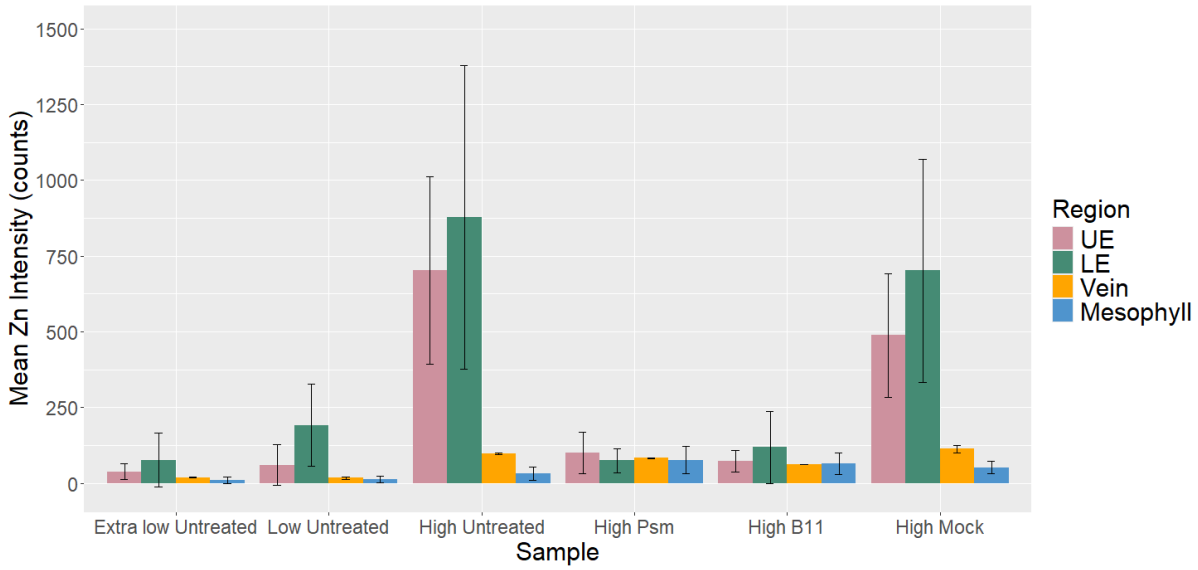


Figure 41: Zinc intensity by region in different samples of *Noccaea caerulescens* leaf tissue. Error bars indicate standard deviation. UE = upper epidermis, LE = lower epidermis. The vein refers to the xylem and phloem of the main vein (midrib). The mesophyll regions were averaged from between 30-50 single pixel points of the extracellular space.

The untreated and mock samples all show similar patterns, with greater zinc intensity in the upper and lower epidermis compared to the vein and mesophyll. Importantly, the high zinc untreated and mock samples show agreement in intensity values which supports the idea that zinc mobilisation is due to the bacterial infection rather than the mechanical process of infiltrating the tissue. A clear difference is apparent in the infected samples compared to the untreated and mock samples. The intensity is more uniform across the different regions of the tissue. This could explain why the zinc signal in the vein is more apparent in the infected samples, because the contrast is indeed lower than the untreated and mock maps.

Suprisingly, the zinc in the mesophyll of the infected tissue is not significantly higher than the untreated and mock samples. However, this could be due to the fact that obtaining ROIs in this region is limited by resolution and it is difficult to quantify the small extracellular space from images. Zinc in the extracellular space could be more clearly studied by extracting the apoplast and direclty measuring the zinc content.

3.2.4 ICP-MS analysis of healthy and infected *Noccaea caerulescens* apoplast

In section 3.2.3, zinc was seen to become mobilised from epidermal vacuoles in *N. caerulescens* upon infection with *P. syringae* pathovars maculicola and syringae SnB11. Although the zinc appeared to move into the apoplastic space, this can be confirmed by isolating apoplastic washing fluid (AWF) at different time points and quantifying zinc concentration. To do this, the highly sensitive inductively coupled plasma mass spectrometry (ICP-MS) can be used. As both pathovars tested in section 3.2.3 showed the same phenotype, only Psm was used. Additionally, zinc content was measured in untreated extra low, low, and high zinc *N. caerulescens* AWF, and compared to the related, non-accumulating *Arabidopsis thaliana.* Results of ICP-MS analysis of these untreated samples can be seen in Figure 42A. Unsurprisingly, zinc content in untreated *N. caerulescens* AWF increases with zinc treatment. In untreated *A. thaliana*, the concentration of zinc in AWF is comparable to low zinc *N. caerulescens*.

In Figures 42B-D, the zinc content in mock and infected *N. caerulescens* AWF extracted at 0, 1, and 5DPI can be seen. In all zinc treatments, the zinc concentration did not significantly change in mock inoculated samples at any time points. However, in infected samples, the zinc concentration in AWF increases at 5DPI – consistent with XRF imaging. Interestingly, the highest zinc concentration observed in infected samples was isolated from low zinc plants. Maximum zinc concentrations in infected samples reached approximately 9000 μg/L in extra low, 95,000 μg/L in low, and 40,000 μg/L in high zinc *N. caerulescens* AWF. In the extra low and low samples, the concentration of zinc increases at 5DPI by a factor of approximately 15. In the high zinc sample, this is lower – a factor of approximately 2. Figure 43 shows a photograph of AWF isolated from the three zinc treatments of infected *N. caerulescens* at 5DPI. The high zinc sample is clear and colourless, whereas the low and extra low zinc samples are brownish yellow. The low zinc sample is the darkest in colour,

which is perhaps due to release of organic compounds associated with the greater release of zinc.

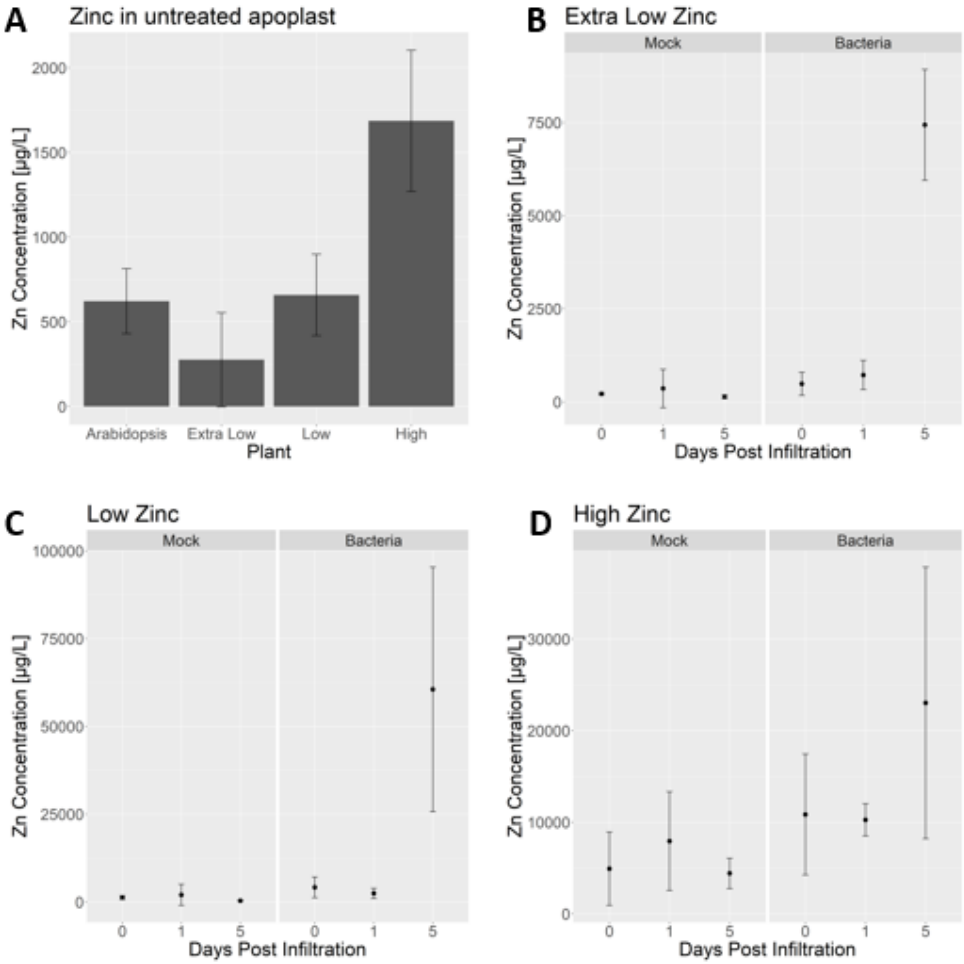


Figure 42: Zinc concentration in apoplast samples determined by inductively coupled plasma mass spectrometry. (A) Comparing the zinc content in untreated soil-grown *Arabidopsis thaliana* to hydroponically cultivated *N. caerulescens.* (B, C, D) Comparing zinc content in the apoplast of mock versus *Psm* inoculated leaves of extra low (10 µM), low (30 µM) and high zinc (300 µM) *N. caerulescens*, respectively. n=3 except for untreated high zinc and 5DPI mock infiltrated extra low zinc *N. caerulescens* where n=2. Error bars show standard deviation between samples.

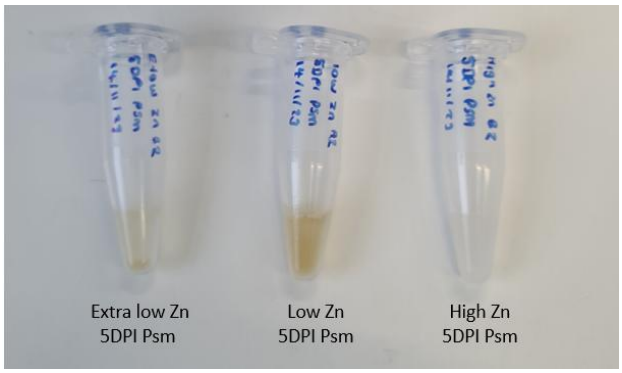


Figure 43: Apoplastic washing fluid extracted at 5DPI from *Noccaea caerulescens* infected with Psm.

In untreated plants, unlike zinc, calcium concentration was greatest in *A. thaliana* by a factor of approximately 20. However, as with zinc, calcium concentration also increases by 5DPI in infected *N. caerulescens.* Maximum calcium concentrations in infected samples reached approximately 35,000 µg/L in extra low, 100,000 µg/L in low, and 13,000 µg/L in high zinc *N. caerulescens* AWF.

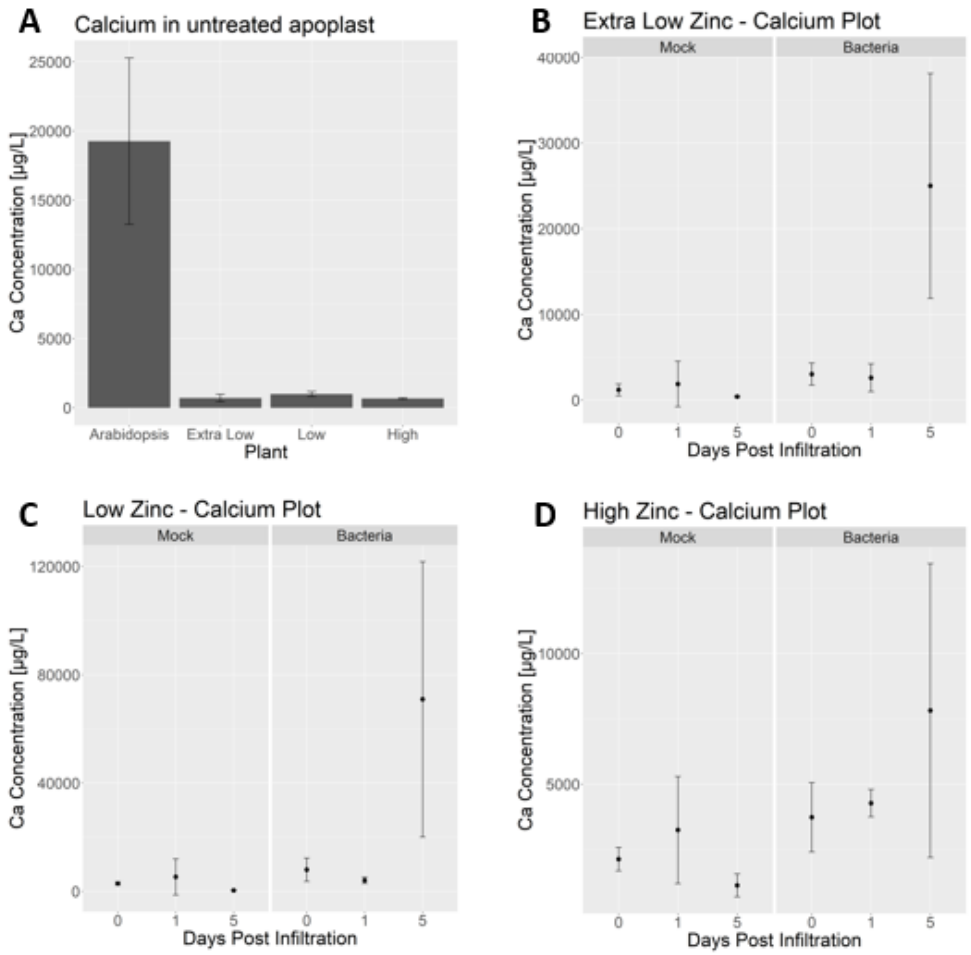


Figure 44: Calcium concentration in apoplast samples determined by inductively coupled plasma mass spectrometry. (A) Comparing the calcium content in untreated, soil-grown *Arabidopsis thaliana* to hydroponically cultivated *N. caerulescens.* (B, C, D) Comparing calcium content in the apoplast of mock versus *Psm* inoculated leaves of extra low (10 µM), low (30 µM) and high zinc (300 µM) *N. caerulescens*, respectively. n=3 apart from untreated high zinc where n=2. Error bars show standard deviation between samples.

Similarly to calcium, the concentration of magnesium is approximately 120 times greater in *A. thaliana* AWF than any of the *N. caerulescens* samples. Maximum magnesium concentrations in infected samples reached approximately 47,000 μg/L in extra low, 160,000 μg/L in low, and 25,000 μg/L in high zinc *N. caerulescens* AWF. Interestingly, the difference in magnesium concentration in the infected AWF at each time point in the high zinc samples appears to be smaller than seen with the other two plants and other metals.

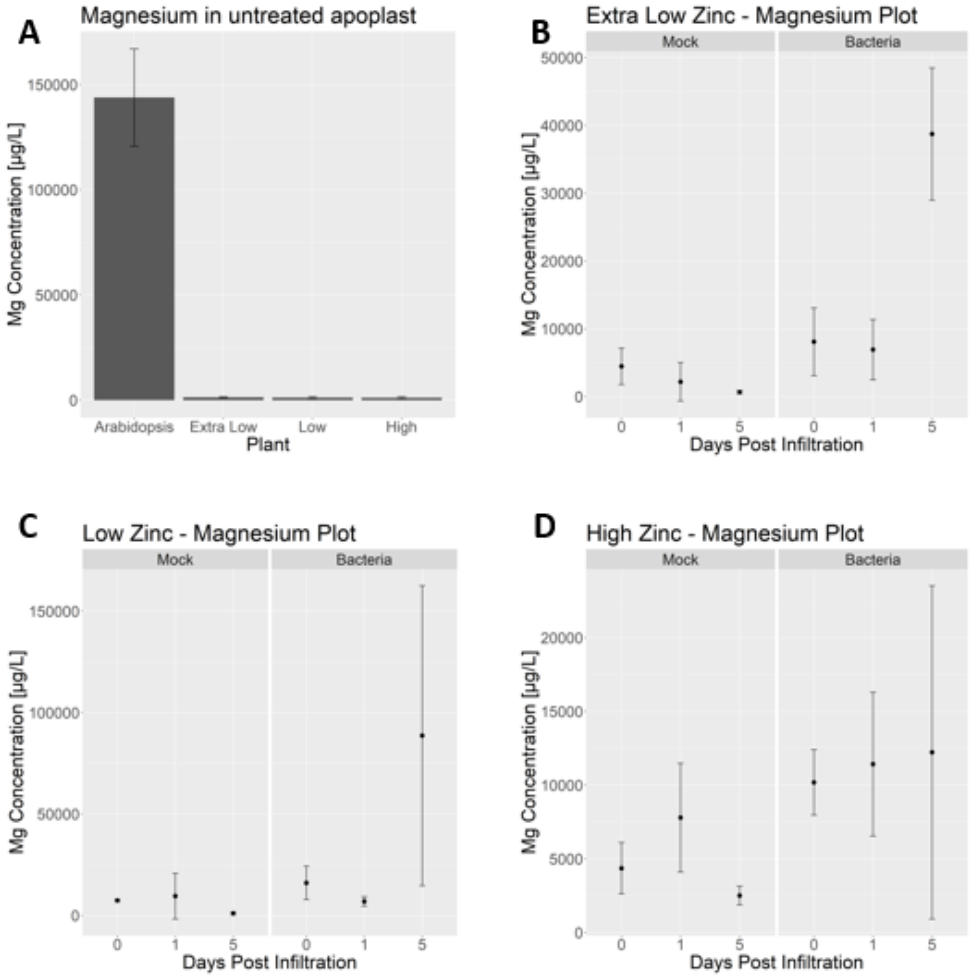


Figure 45: Magnesium concentration in apoplast samples determined by inductively coupled plasma mass spectrometry. (A) Comparing the magnesium content in untreated, soil-grown *Arabidopsis thaliana* to hydroponically cultivated *N. caerulescens.* (B, C, D) Comparing magnesium content in the apoplast of mock versus *Psm* inoculated leaves of extra low (10 μM), low (30 μM) and high zinc (300 μM) *N. caerulescens*, respectively. n=3 apart from untreated high zinc where n=2. Error bars show standard deviation between samples.

3.2.5 XANES analysis of healthy and infected *Noccaea caerulescens*

In previous sections, it has been observed that, upon infection, zinc is mobilised from epidermal vacuoles into the apoplastic space. It follows, therefore, that there may additionally be a shift in chemical form from the storage site to the form that the pathogen is exposed to in the apoplast. To study this, XANES spectroscopy can be used. For samples of tissue, sections were prepared in the same manner as for 2D-XRF and XANES mapping was utilised, resulting in a hyperspectral image where each pixel contains a XANES spectrum. From these XANES maps, individual regions of interest, for example a cell, could be averaged.

A XANES spectrum is additive, containing contributions from all zinc species present at the area of the sample being measured by the beam. Thus, in order to identify zinc species present in the sample, linear combination fitting (LCF) can be used (179). LCF requires a library of zinc reference standards to be collected which can then be used to determine approximate and relative proportions of each zinc species in the ROI of the sample. The XANES reference standards prepared and measured in this study can be seen in Figure 46. By visual inspection, XANES spectra look similar. However, the spectra contain subtle differences with the position, shape, and intensity of the absorption peak, shoulders, and secondary peaks which each arise due to differences in the chemical environment (148).

R-factor and χ^2 values are measures of closeness between the sample spectra and the fit spectra and can be seen in the Appendix, Table 10. Lower values indicate a better fit (118,180). The best fits were generally obtained when a larger ROI was averaged, with the smaller epidermal cells being more noisy and thus providing worse fits.

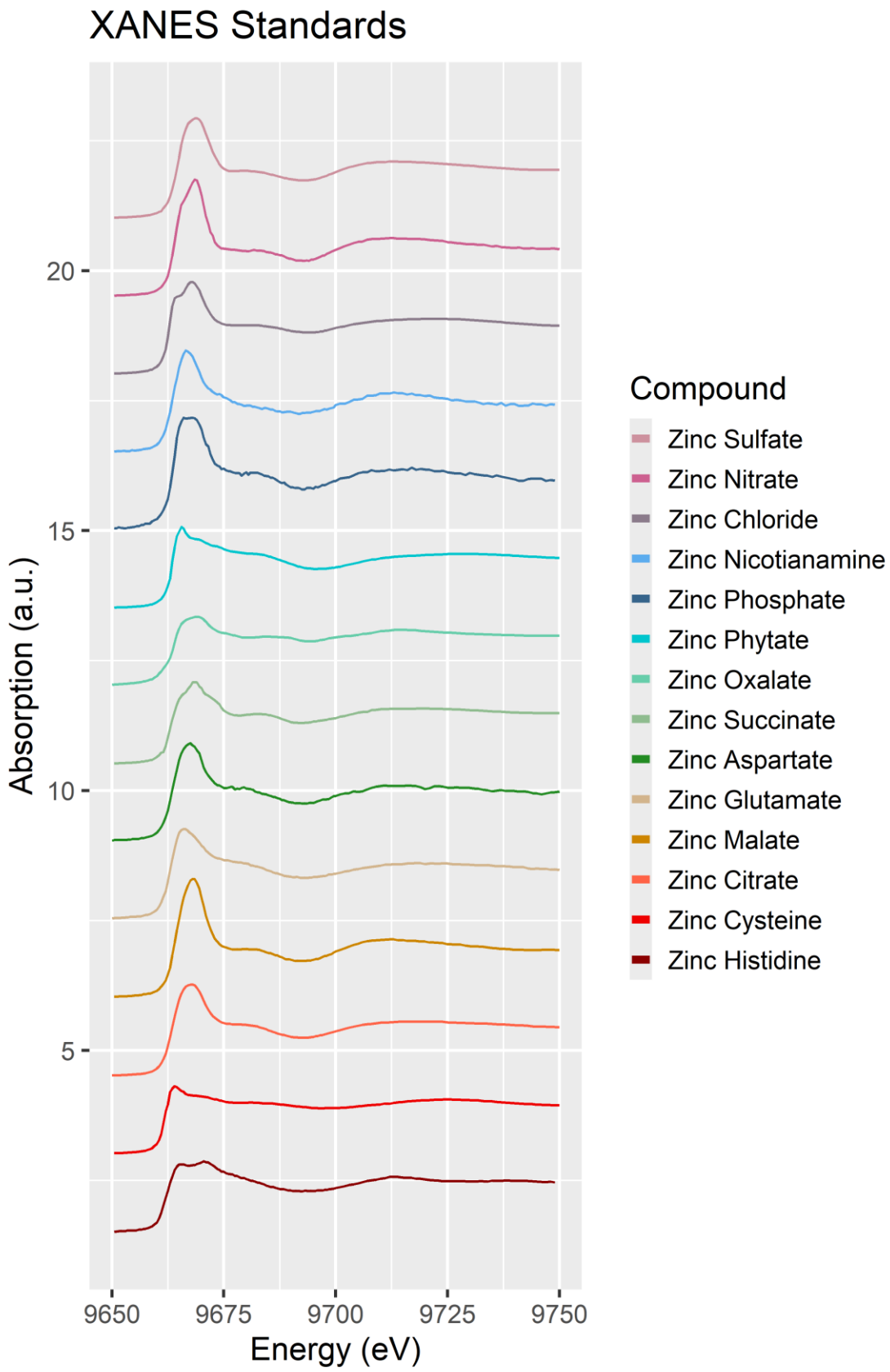


Figure 46: Zinc XANES standard spectra, plotted with an offset and cropped to show the region 9650 – 9750 eV. AU = arbitrary units.

As the second standards beamtime was undertaken in late 2024, XANES analysis is ongoing. To date, a subset of XANES maps of high zinc *N. caerulescens* have been processed and will be discussed below, with several more maps from this and the other zinc treatments to process for any resulting publication. LCF results from averaged regions from XANES maps collected from untreated, mock inoculated, and leaves taken at 1- and 4-days post inoculation with *P. syringae* pv. maculicola can be seen in Figures 46 – 49. These show the relative proportions of total zinc compounds identified, but in most cases the fits were not 100%. Figure 46 shows the LCF results averaged from individual lower epidermal cells. Replicates are different cells from the same sample map, and cells from infected tissue are those still containing zinc. Zinc citrate appears to be a major component regardless of treatment, accounting for between approximately 28 and 83% of speciation. Zinc nicotianamine also appears to be a significant chelator in the lower epidermal cells, accounting for between 14 and 56% of zinc speciation. Lower contributions were seen for zinc chloride, zinc cysteine, zinc phytate, and zinc nitrate.

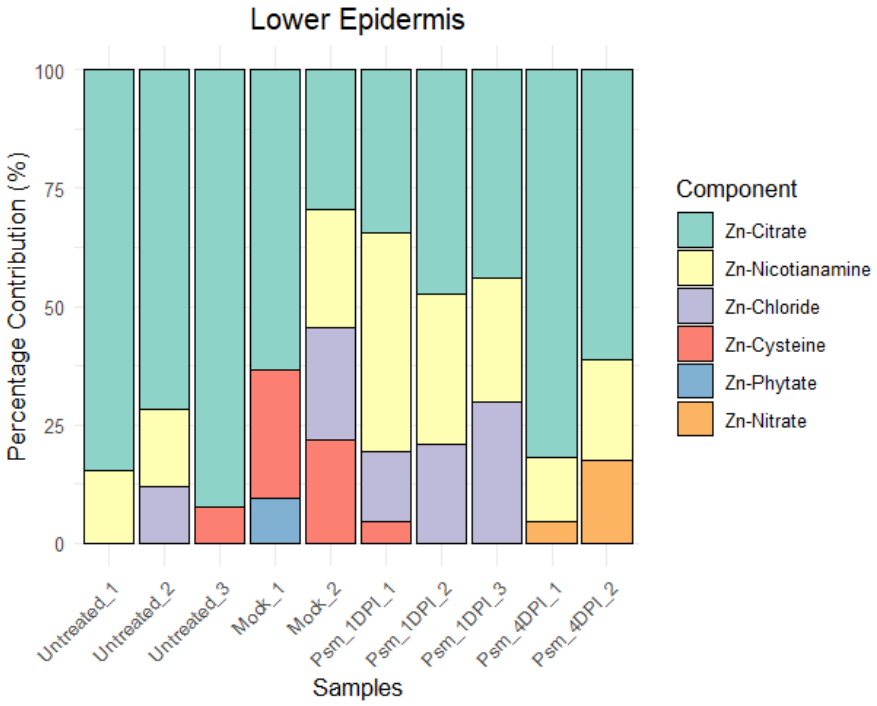


Figure 47: Linear combination fitting results showing percentage contributions of different zinc species in the lower epidermis of untreated, mock inoculated, or samples of *N. caerulescens* infected with *P. syringae* pv maculicola and measured at 1- and 4-DPI. All samples are high zinc *N.* caerulescens. Replicates shown are different cells averaged from the same map.

At this stage, it is unclear why there appears to be a significant proportion of zinc-cysteine in the mock samples and zinc-nitrate in the 4DPI infected samples in the lower epidermis. These studies would benefit from a greater number of samples to more accurately determine trends.

Similar to the lower epidermis, zinc citrate is a significant component of zinc in the upper epidermal cells. As seen in Figure 47, zinc citrate accounts for between 33 and 83% of total zinc in the upper epidermal cells measured. With the exception of zinc nitrate, the same species were found in the upper and lower epidermis.

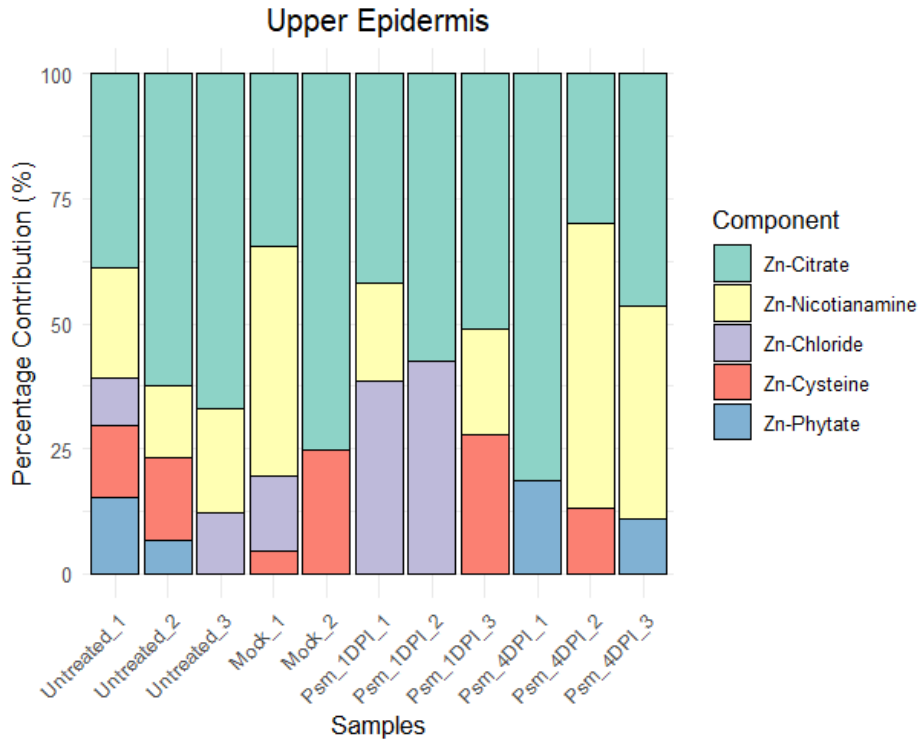


Figure 48: Linear combination fitting results showing percentage contributions of different zinc species in the upper epidermis of untreated, mock inoculated, or samples of *N. caerulescens* infected with *P. syringae* pv maculicola and measured at 1- and 4-DPI. All samples are high zinc *N.* caerulescens. Replicates shown are different cells averaged from the same map.

Because the zinc signal in the mesophyll was relatively weak compared to that in the epidermal cells, larger regions of interest covering multiple cells were averaged for the mesophyll. LCF results from these regions can be seen in Figure 48. Zinc citrate is also

present in the mesophyll, but in lower proportions than seen in the epidermis. A larger range of zinc species is also apparent, with glutamate being a significant chelator in the samples it is present in.

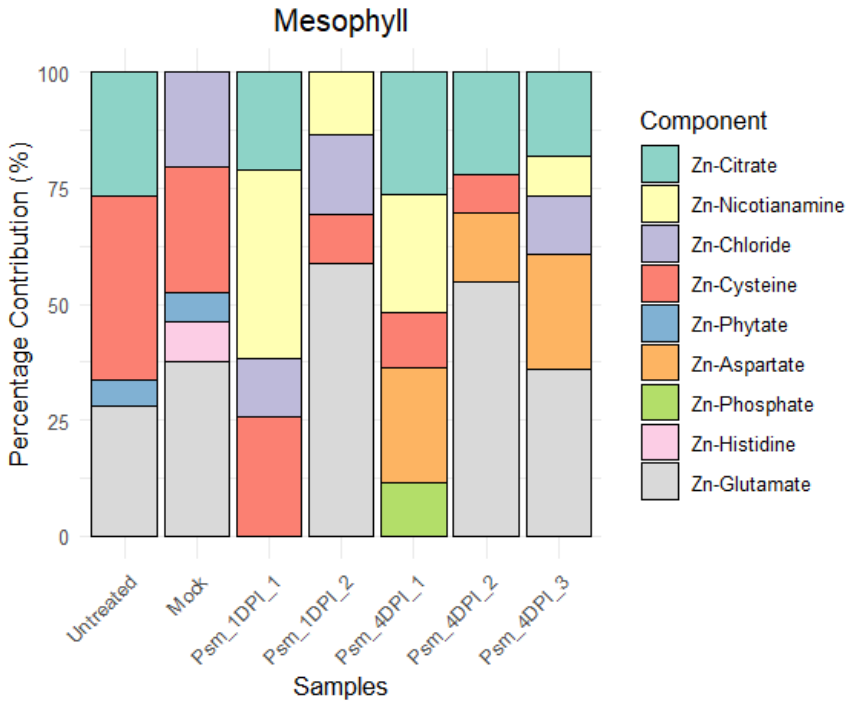


Figure 49: Linear combination fitting results showing percentage contributions of different zinc species in averaged regions of the mesophyll of untreated, mock inoculated, or samples of *N. caerulescens* infected with *P. syringae* pv maculicola and measured at 1- and 4-DPI. All samples are high zinc *N.* caerulescens. Replicates shown are different regions averaged from the same map.

In the vein, like the mesophyll, a larger range of zinc species were detected than in the epidermis. As seen in Figure 50, zinc chloride, zinc cysteine, and zinc phytate are all present in similar proportions.

A proof-of-concept analysis using a single sample of apoplastic washing fluid extracted from *N. caerulescens* infected with Psm at 5DPI was also performed. Because AWF samples are dilute, it was not certain that there would be detectable zinc. In this sample, zinc citrate was the most abundant form of zinc, accounting for approximately 94% of the total zinc detected.

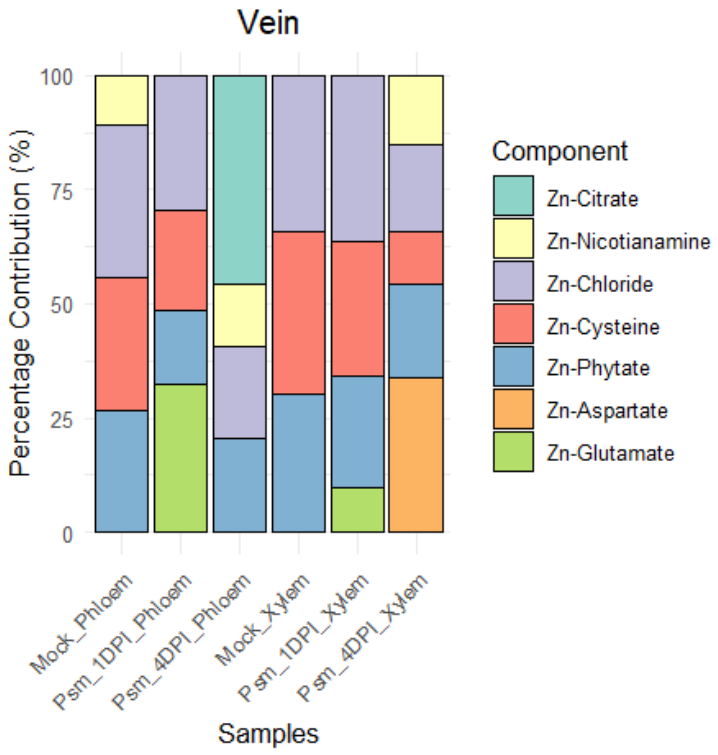


Figure 50: Linear combination fitting results showing percentage contributions of different zinc species in averaged regions of the phloem or xylem of mock inoculated, or samples of *N. caerulescens* infected with *P. syringae* pv maculicola and measured at 1- and 4-DPI. All samples are high zinc *N.* caerulescens.

As discussed with the 2D-XRF imaging and the penetrating nature of X-rays, the XANES data collected may be impacted by the position of the section across a cell. Likewise, errors such as overlapping regions may be introduced as the ROIs are determined by hand.

3.3 Discussion

In this chapter, a sample preparation and mounting pipeline was developed to facilitate the high-resolution synchrotron-based XRF and XANES mapping of transverse sections of leaf tissue. As described in earlier sections, this is not straightforward and was not successful upon first attempt. However, these initial tests proved useful as it provides a resource of what transverse sections of leaf look like with improper sample preparation or if samples become damaged. The final method, described in Figure 26, was used to image zinc distribution in healthy, untreated *Noccaea caerulescens* grown hydroponically on increasing concentrations of zinc: 10 μM, 30μM, and 300 μM.

Agreeing with previous reports, zinc is highly localised to the epidermal vacuoles of *N. caerulescens.* This has been theorised to be a strategy employed by hyperaccumulators to prevent disruption to important cellular processes like protein synthesis and photosynthesis that predominantly occur in the cytoplasm and chloroplast of mesophyll cells (7,40,57). In the highest zinc treatment, zinc appears to populate all visible epidermal vacuoles (Figure 32). Logically, we thought that perhaps with the lower zinc treatments that the distribution would follow that of the high zinc samples but with proportionally lower intensities. However, it was actually found that with lower zinc treatments there was more heterogeneity in zinc distribution throughout the epidermal vacuoles, most prevalent in the extra low zinc sample. In this lowest treatment, seen in Figure 30, many epidermal cells appear devoid of zinc, while zinc is apparent in relatively high intensities in other epidermal cells. In the cells containing no (or very little) zinc, however, there was still potassium which makes it more likely that this observation is not an artefact as the cells are intact, with “inflated vacuoles” (126). This heterogeneity when environmental zinc is limited could perhaps be a defensive strategy. It could be more beneficial to the plant to store (relatively) highly concentrated pockets of heavy metals rather than a more even distribution of metal with much lower concentration. This may be particularly successful in defence against

herbivory or with a haustoria-forming filamentous pathogen that directly penetrates individual cells.

There appears to be a preference for zinc to be stored in larger cells. In the extra low and low zinc maps, the cells that do contain zinc in the extra low plant tend to be the larger epidermal cells. This was confirmed in Figures 33 and 34 where cell size was compared to zinc intensity. This observation has been noted previously in *N. caerulescens* and with the nickel hyperaccumulator *Noccaea goesingensis* (48,57,181). This could indicate that the larger epidermal cells “fill” with zinc first. It may be metabolically favourable to initially store higher concentrations of metal in fewer, larger cells as, for example, fewer cells would need to upregulate metal transporters and vacuolar transport systems.

Another potential explanation for the observed heterogeneity in zinc distribution is that the plant may avoid storing zinc in cells adjacent to stomata until the more distant epidermal cells are “full” so as to minimise stomatal dysfunction (182). Conversely, as *Pseudomonas syringae* is known to enter plants via natural opening such as stomata, it may also make sense that zinc is stored near to these features. To confirm if either of these are true, XRF studies of the surface of the leaf could be performed to observe whether zinc is stored close to or away from stomata. To ensure this observation is not a sectioning artefact, capillary micro-sampling targeting individual cells could enable the measurement of the concentration of zinc in larger cells compared to smaller cells (183). The heterogeneity may also be linked to ancestral trichomes – a known site of metal accumulation in plants containing them (51,184). This could potentially be probed using single cell transcriptomics and comparing the gene expression profiles in the different sized cells and identifying if any are associated with trichome formation or development.

There additionally seems to be a preference for zinc storage in the lower epidermis compared to the upper epidermis, particularly in the low and extra low zinc plants. It is currently unclear about whether this is associated with structural features or perhaps a

defensive mechanism. As discussed above, *Pseudomonas syringae* is known to enter the plant through the stomata which are often predominantly located on the lower epidermis.

Another key observation from this chapter is that, upon infection with *P. syringae*, zinc is mobilised; crucially, into the apoplastic space which is the known site of *P. syringae* inhabitation. This finding could therefore explain the mechanism of defence in *N. caerulescens.* As discussed in section 1.6, a notable difference in the strains tested is that B11 produces the phytotoxin syringomycin which causes pore-formation in membranes, leading ultimately to cell lysis and thus could explain the “dumping” of zinc out of epidermal vacuoles. However, the same phenotype of zinc redistribution was observed with both strains of *P. syringae* which potentially rules this out.

The effector AvrE is part of the conserved effector locus and, as discussed in section 1.6, is known to form channels in the plant cell plasma membrane which could allow solutes, including zinc, to pass through into the apoplast. To evaluate the role of AvrE in the mobilisation of zinc, an AvrE knockout mutant could be inoculated into *N. caerulescens*. The effector could then be implicated if zinc remains in the epidermal vacuoles. Alternatively, the reverse could also be tested using a mutant bacteria capable of producing and delivering only AvrE.

Hatsugai et al described a mechanism whereby, upon infection with *Pseudomonas syringae* pv. *tomato* DC3000, vacuoles in *Arabidopsis thaliana* cells fused with the plasma membrane during programmed cell death (PCD). This fusion causes the contents of the vacuoles to become discharged into the extracellular space to attack the intercellular pathogen. It could therefore follow that, in hyperaccumulators, heavy metals are released alongside vacuolar antibacterial proteins as part of the PCD mechanism (78,185). Although not yet studied in Prayon, this “non-destructive” route of PCD maintains the integrity of the vacuolar membrane and cytoplasm and could explain what has been observed in the XRF imaging as the cells appear intact at the time of imaging (186). However, this could potentially be seen more clearly with nanoscale imaging. This could also more directly be

studied in *N. caerulescens* utilising a mass spectrometry approach to monitor apoplastic washing fluid for vacuole-specific compounds such as anthocyanins, betalain, or vacuolar proteins.

Another observation from the infected XRF images is the increase in zinc in the midvein which could indicate an upregulation of zinc transporter genes. This has been observed previously by Escudero et al using the necrotrophic fungus *Plectosphaerella cucumerina* to cause infection in *Arabidopsis thaliana.* Using XRF to measure the surface of infected leaf tissue, the authors found that zinc increased in intensity in the vasculature surrounding the infection site at 2DPI. This was implicated to an upregulation of the transporters HMA2 and HMA4 which, as discussed in section 1.3, are involved in root-to-shoot translocation. The double mutant *hma2hma4* had higher pathogen proliferation and did not cause a local increase in zinc at infection site (187). To determine whether a similar process could explain the observations in *N. caerulescens*, a gene expression study such as single-cell RNA-seq comparing mock-inoculated and infected tissue could be conducted.

The results from ICP-MS could support the non-destructive route of membrane fusion described by Hatsugai et al, as other vacuolar metals alongside zinc are seen to increase in concentration in the apoplast by 5DPI. But likewise, this could be as a result of necrosis in the later stages of infection. An interesting observation from the ICP-MS data was that low zinc plants infected with *P. syringae* had the greatest concentrations of measured metal in the apoplast. Additionally, as shown in Figure 43, the apoplast from these plants was darker in colour compared to the other zinc treatments. A possible explanation for this is that the bacteria were able to proliferate to a greater extent than in the high zinc plants and trigger a greater release of vacuolar metals. The high zinc plants have a greater baseline concentration of zinc in the apoplast, as shown in Figure 42A, which could inhibit the bacteria prior to the observed metal mobilisation from epidermal vacuoles. Another notable observation in the untreated plants is the difference in metal concentration, apart from zinc, in *A. thaliana* versus *N. caerulescens*. The former contained much higher concentrations of

potassium, calcium, magnesium, and manganese in the apoplast. To determine whether this is simply due to the fact soil-grown *A. thaliana* and hydroponically cultivated *N. caerulescens* plants were used, the experiment could be repeated using plants all grown hydroponically in the same, or similar, nutrient media. Ideally, more samples need to be measured for more robust statistical analysis but this proved difficult to achieve due to the low sample volumes obtained per plant (10s – low 100s of microlitres) and the time-sensitive nature of the experiment.

Typically, during an ICP-MS experiment a certified reference standard (CRM) with a similar matrix to the sample of interest is measured alongside samples and blanks. A CRM has known concentrations and is thus used to ensure proper instrument function and detection. A CRM of river water that was kindly gifted to us was measured but unfortunately it appeared contaminated, having response values varying from the reference values in a non-uniform manner. However, the measurements from internal and external standards matched the expected value ranges and the samples showed consistent trends. Indeed, the technician responsible for the instrument, Andrew Dodson, believes the instrument was working appropriately and as expected.

Another point worth considering regarding the ICP-MS data are the dilution factors discussed in section 2.9, Table 6. As can be seen, these dilution factors vary between plant treatments; they are similar for *A. thaliana* and the extra low zinc *N. caerulescens* with values of approximately 1.5 but increase with increasing zinc concentration. More recently, we have begun considering whether this observation is a consequence of increased ROS and zinc presence in the apoplast which effects the indigo carmine in some way. Indeed, degradation of indigo carmine in the presence of hydrogen peroxide and horseradish peroxidase has previously been reported (188). Although indigo carmine is routinely used for calculation of dilution factors resulting from the infiltration of leaves, perhaps this observation needs to be looked into further and highlights the potential need for an alternative chemical (143). Due to its large molecular weight preventing cellular entry, blue dextran has been

proposed as an alternative chemical for calculating dilution factors in plants and its application has been demonstrated in *Oryza sativa* (143,189). Additionally, it may be worthwhile repeating the analysis of the ICP-MS data using the 1.5 figure as the dilution factor.

XANES is indicative not definitive because it depends on the library of reference standards used (179). In all samples measured, there were no significant trends between untreated *N. caerulescens* leaves and leaves infected with Psm. However, it appears that in the epidermal vacuoles of both untreated and infected tissue zinc was predominantly stored chelated to citrate. Citrate is a low-molecular weight organic acid that is abundant in vacuoles and has been previously implicated in the chelation of zinc in metal hyperaccumulator plants (190). For instance, Salt et al and Monsant et al found that zinc citrate constituted 38% and 75-94%, respectively, of the total zinc in leaf tissue of *N. caerulescens* (56,179). Zinc nicotianamine, often associated with transport, was also present in relatively high proportions in the epidermis (57,146).

In the mesophyll, zinc glutamate was identified as a significant chelator. Although not commonly identified as a zinc chelator, this could perhaps simply be due to existing literature not commonly measuring the reference compound. However, the presence of zinc glutamate in the mesophyll is perhaps unsurprising as glutamate has a key role in plant metabolism and signalling and is known to be present in the cytoplasm and apoplast (191,192). Zinc chloride is also not commonly implicated as a zinc complex in hyperaccumulator plants, but its presence could be supported by the findings of Küpper et al, who identified chloride in the mesophyll and upper and lower epidermal cells of *N. caerulescens* (48). A somewhat surprising result was the low proportion of zinc histidine detected in any of the measured regions. However, zinc histidine has previously been reported to be more abundant in the roots which were not measured in this study, and is thought to have an important role in xylem loading of the metal (56,179,193).

Gas chromatography-mass spectrometry (GC-MS) has previously been used to observe an increase in citrate in the apoplast of *Phaseolus vulgaris* infected with *Pseudomonas syringae* pv. phaseolicola (194). This could therefore link to the observation of zinc citrate being the major form of zinc in apoplast extracted from *N. caerulescens* infected with Psm. However, a greater number of samples need to be measured to confirm this observation. This work would additionally benefit from complementary metabolomics study of untreated versus infected leaf samples to more directly study any changes in the metabolic profile that occur as a result of infection with *P. syringae*. Unfortunately, there was not enough time to measure the XANES standards that were initially measured at room temperature using the cryogenic pipeline. This will be done in a future beamtime and used for the analysis in resulting papers. Additionally, pH value can influence metal chelation so remeasuring standards at more physiologically relevant pH values may provide a more accurate picture of zinc speciation in *N. caerulescens* (195).

It is a well-known limitation of synchrotron-based studies that time is extremely limited and not guaranteed. Generally, we were awarded 2-3 days beamtime per experiment which meant it was difficult to collect high resolution replicates which is an unfortunate reality for synchrotron experiments (196,197). Additionally, issues with the sample preparation or once mounted on the beamline (vacuum failure, for example) sometimes resulted in artefacts which looked similar to infected tissue or the improperly prepared samples seen in Figure 22-24. However, other data collected and presented in this and future sections supports the findings discussed. For example, ICP-MS data confirmed that mock inoculation did not cause zinc release into the apoplast and thus supports the XRF images of mock tissue. Additionally, 3D-XRF tomography discussed in Chapter 4 complements the 2D-XRF data.

In this chapter, the development of a pipeline to enable the preparation of transverse sections of frozen-hydrated leaf tissue was discussed. This pipeline was used to study the distribution of zinc in untreated and infected leaves of *N. caerulescens* using XRF imaging.

In untreated tissue, zinc was highly localised to the epidermal vacuoles but exhibited a concentration-dependent heterogeneity. In infected tissue, zinc was shown to mobilise into the apoplastic space, providing a mechanism by which the metal can interact with the bacteria. This observation was supported by complementary ICP-MS analysis. XANES analysis did not detect any changes in zinc speciation that occur as a result of infection, but zinc citrate, zinc nicotianamine, and zinc glutamate were all found to be significant forms of zinc in the leaves of *N. caerulescens*.

Chapter 4: Cryo-XRF tomography of *Noccaea caerulescens*

4.1 Introduction

In Chapter 3, a sample preparation pipeline was developed to enable 2D-XRF imaging and XANES spectroscopic analysis of transverse sections of plant tissue. Although successful, the process remains complex and involves multiple steps where the sample is vulnerable to damage or to the introduction of artefacts. A potential alternative is 3D-XRF tomography, utilising virtual sectioning and a potentially simplified sample preparation. Additionally, 3D-XRF tomography enables volumetric mapping of elements potentially providing a more comprehensive view as information from entire cells and structures is obtainable (198).

Typically, 3D-XRF tomography is used for tissues elongated in one dimension compared to the other; roots or stems for example (199). Such samples enables a consistent X-ray path and simplifies alignment. This has been demonstrated by Mishra et al, studying arsenic toxicity in the leaves of *Ceratophyllum demersum*, possessing acicular (needle-shaped) morphology (200). Additionally, van der Ent et al has used 3D-XRF tomography to study arsenic distribution in various tissues of the hyperaccumulating fern species *Pteris vittata* (201). Fewer studies look at planar leaf samples.

In 3D-XRF tomography, a sample is rotated about a single axis and XRF spectra are collected at specified degree increments. Thus, it is imperative that the sample is appropriately aligned about this axis. For a single slice of the sample, all the projections measured at different rotation angles are combined into a sinogram, which encodes the elemental information as a function of both the rotation angle and detector position. This process is repeated in defined vertical increments along the sample, and sinograms are processed and reconstructed into a 2D slice, known as a tomogram, via one of several

reconstruction algorithms (202–204). Neighbouring tomograms are then stacked together to form the final 3D-XRF image.

A known drawback with 3D-XRF tomography, however, are matrix effects known as self-absorption. This phenomenon occurs primarily with lighter elements such potassium and calcium and sample thicknesses in the order of tens of microns or more. Lighter elements emit proportionally lower energy characteristic X-rays that are more easily attenuated by the sample, resulting in signal distortion (198,199,201,203).

In this chapter, a sample preparation and mounting methodology for the 3D-XRF tomography of leaf samples from *Noccaea caerulescens* will be discussed. The primary objective of this chapter is to assess whether the zinc distributions observed in 3D images align with those obtained through 2D-XRF, while also identifying the strengths and limitations of both imaging techniques. In addition, a comparison of the metal distribution within seeds of *N. caerulescens* and *Arabidopsis thaliana* will be presented.

4.2 Results

4.2.1 Mounting test with *Arabidopsis thaliana*

Initial cryo-XRF tomography mounting tests were performed using *Arabidopsis thaliana* and samples were measured at room temperature as these experiments were carried out during COVID-19 related restrictions. *A. thaliana* plants take significantly less time to reach maturity and require less extensive maintenance than *Noccaea caerulescens.* Sections were measured at room temperature as the setup is simpler and requires fewer people. The aim of this was not to generate robust data of metal distributions, but to test mounting strategies. As discussed previously, 3D-XRF tomography does not require transverse sectioning but entire leaves (with morphology akin to that of *A. thaliana* or *N. caerulescens*) are not suitable due to their size and shape. Instead, as outlined in Figure 51, small strips of leaf with widths of approximately 2 mm can be excised from the plant.

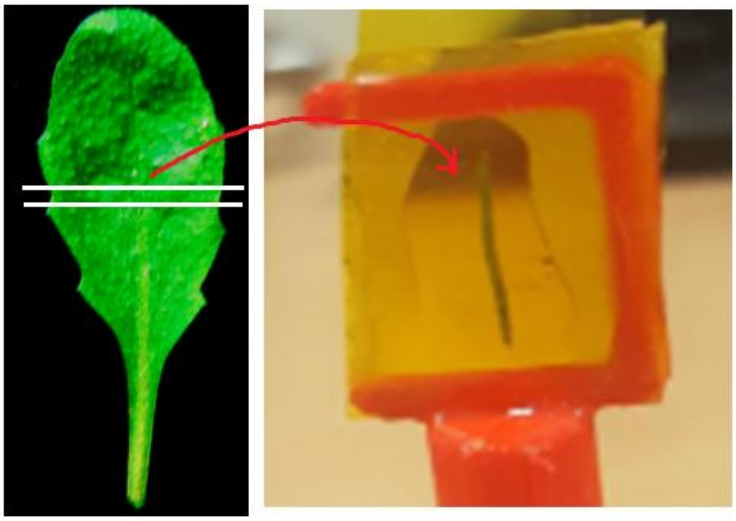


Figure 51: Initial mounting test for 3D-XRF tomography. A section of *Arabidopsis thaliana* is mounted between two sheets of Kapton and attached to a 3D-printed frame.

In the first test, a strip of leaf was rapidly excised from the plant and placed between two sheets of X-ray transparent Kapton film. This structure was secured with superglue then cut to size and affixed to a 3D-printed frame. This frame was designed to fit into the rotating sample holder used for tomography. Results from this initial test can be seen in Figure 52, showing a section of *A. thaliana*. A striking observation from this is the presence of an intact trichome which can be seen to accumulate multiple metals. Calcium is observed through the structure, manganese is located towards the base of the trichome, and zinc is localised to a ring at the base. However, the leaf structure itself is less apparent which is likely due to sample degradation and damage due to not being measured in cryogenic conditions. Potassium can be detected but only as a sheet-like structure rather than distinct cells which may, in addition to sample damage, also be due to the self-absorption artefact described in section 4.1.

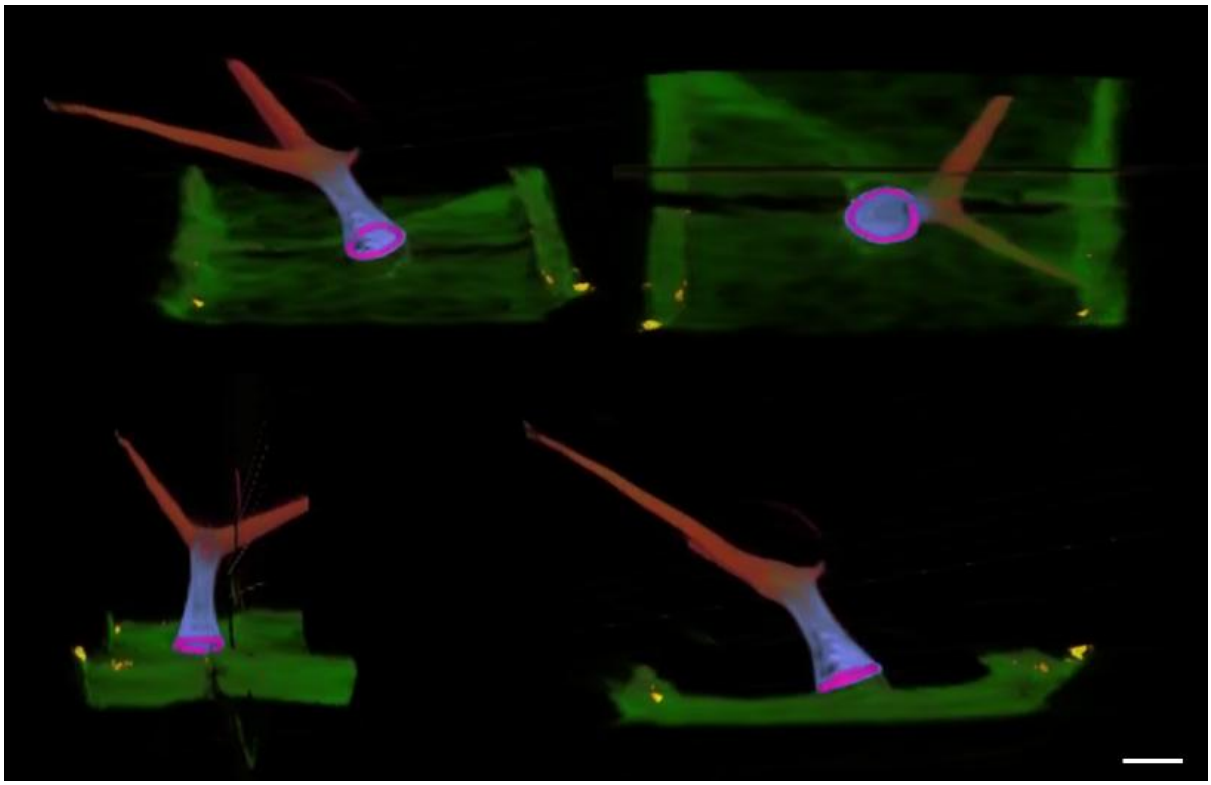


Figure 52: 3D-XRF reconstruction of a section of *A. thaliana* leaf with trichome visible. Composite image showing the relative distributions of potassium (green), calcium (red), iron (yellow), manganese (purple), and zinc (magenta) in various perspectives. Scale bar indicates 100 μm.

In addition to the apparent damage due to being measured at room temperature, the mounting method may also not be completely appropriate. The frame used to mount the sample appears to introduce an empty line within the image, bisecting the sample and visible in the top right and bottom left perspectives of Figure 52. In subsequent beamtimes, a capillary approach was used for leaf samples which has been used by other researchers and perhaps lends itself to tomography due to its shape (201,205).

4.2.2 Comparison of metal distributions in seeds of *Noccaea caerulescens* and *Arabidopsis thaliana*

As with section 4.2.1, COVID-19 restrictions in place at this point during the project limited what experiments could be performed both at Diamond and otherwise. In order to

obtain a relevant data set to practice the 3D-XRF tomography data processing and analysis workflow, seeds were used. Seeds have a relatively low water content and are sufficiently small to not require further sample preparation, so do not need to be measured at cryogenic temperatures (206). Seeds of *A. thaliana* collected from plants grown in standard growth conditions and seeds from the Prayon population of *N. caerulescens* obtained directly from plants at the former smelter site were affixed to a pin on the rotating sample mount used for tomography (207).

3D-XRF maps showing the spatial distributions of a range of metals in seeds of *A. thaliana* and *N. caerulescens* can be seen in Figure 53. Figure 54 shows composite maps of select combinations of metals. One of the clearest observations is the distribution of iron which appears to be localised to the vasculature of the cotyledons in both seeds. Calcium and potassium are localised to the seed coat, or testa. Ring-like regions are particularly noticeable in potassium and calcium maps of *N. caerulescens* and might be an artefact of the step size used. Zinc, manganese, and nickel appear to be localised to the endosperm and surround the iron in the cotyledons. In both *A. thaliana* and *N. caerulescens* seeds the distribution of zinc is quite uniform throughout the endosperm. Manganese and nickel distribution, however, differ between the two seeds. Manganese in *A. thaliana* appears to more closely surround the embryo, whereas in *N. caerulescens* the metal appears closer to the seed coat. The opposite trend is visible for nickel, and in *A. thaliana* it is more diffuse and lower intensity.

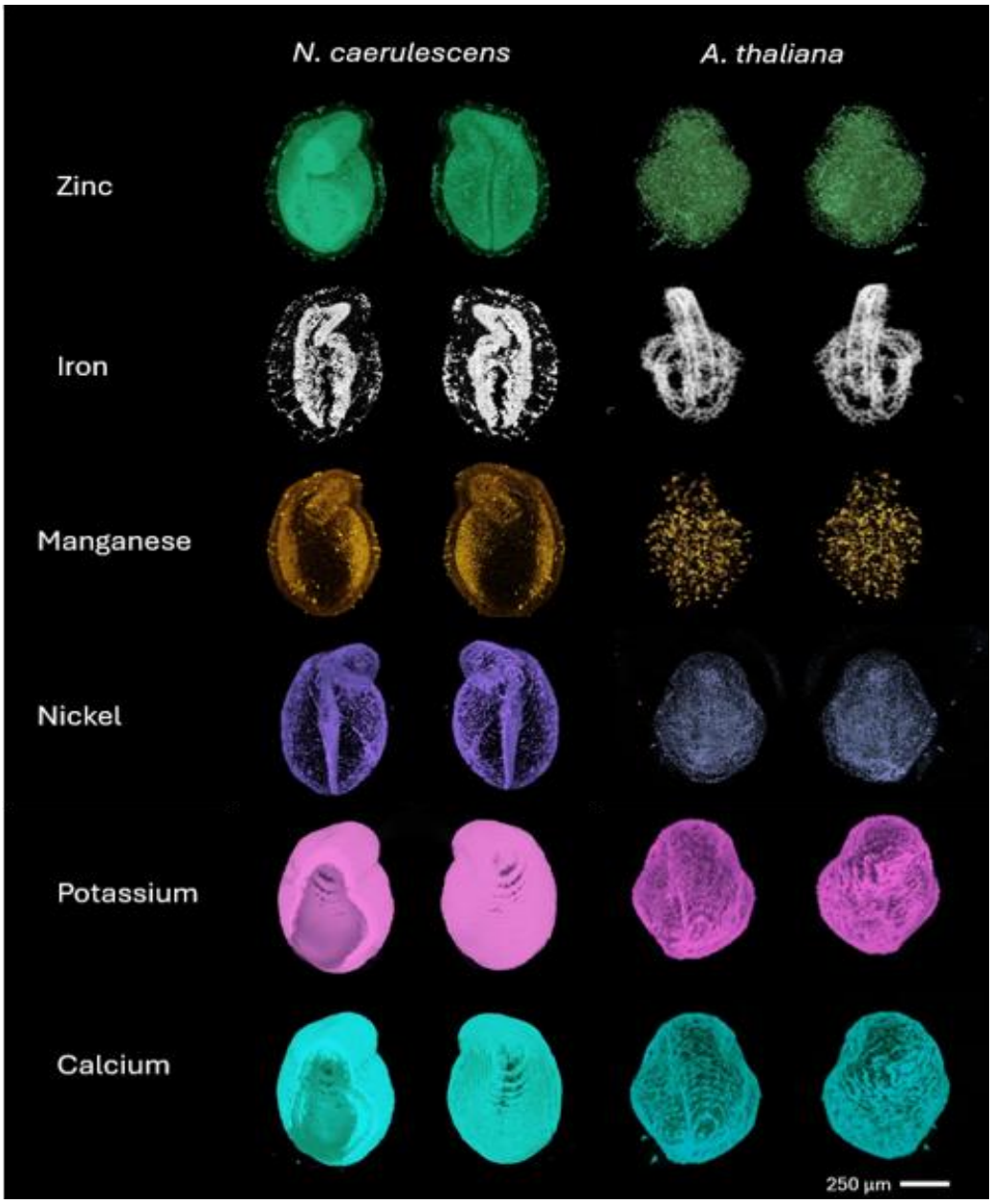


Figure 53: 3D-XRF tomography of *Noccaea caerulescens* and *Arabidopsis thaliana* seed in false colours showing various elements. Front and back perspectives of each seed are shown.

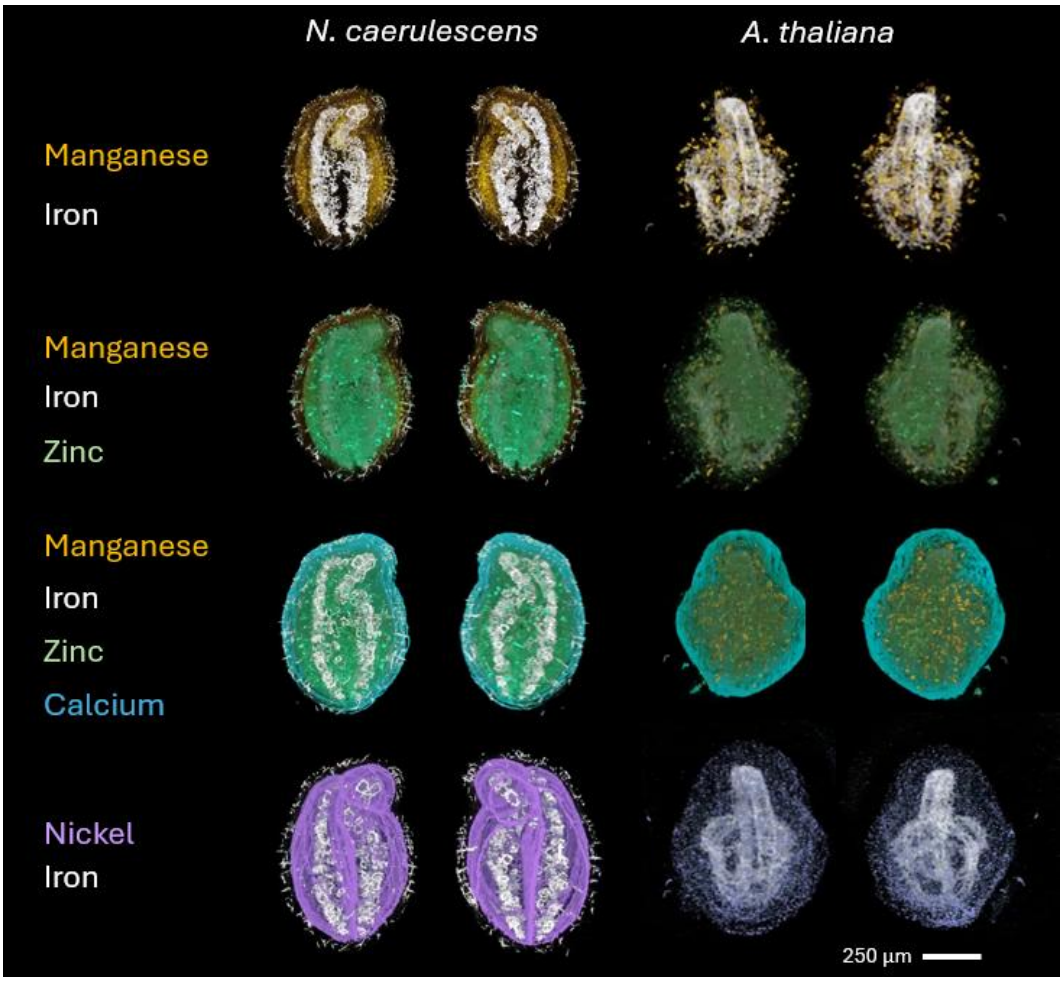


Figure 54: 3D-XRF tomography of *Noccaea caerulescens* and *Arabidopsis thaliana* seed in false colours showing select combinations of elements. Front and back perspectives of each seed are shown.

4.2.3 3D-XRF tomography of young and mature *Noccaea caerulescens* leaves

Following on from the initial tomography beamtime using *A. thaliana* and an unsuccessful method of measuring leaf tissue, the next beamtime used a capillary-based mounting system. The setup used for this can be seen in Figure 55. A small section of leaf (~ 2 x 3 mm) was rapidly excised from the plant using a razor. A small drop of optimal cutting temperature compound (OCT) was placed at the opening of the capillary (internal diameter 2mm), and the section of leaf was carefully inserted into the capillary, through the OCT. The OCT freezes solid and stabilises the leaf, preventing movement.

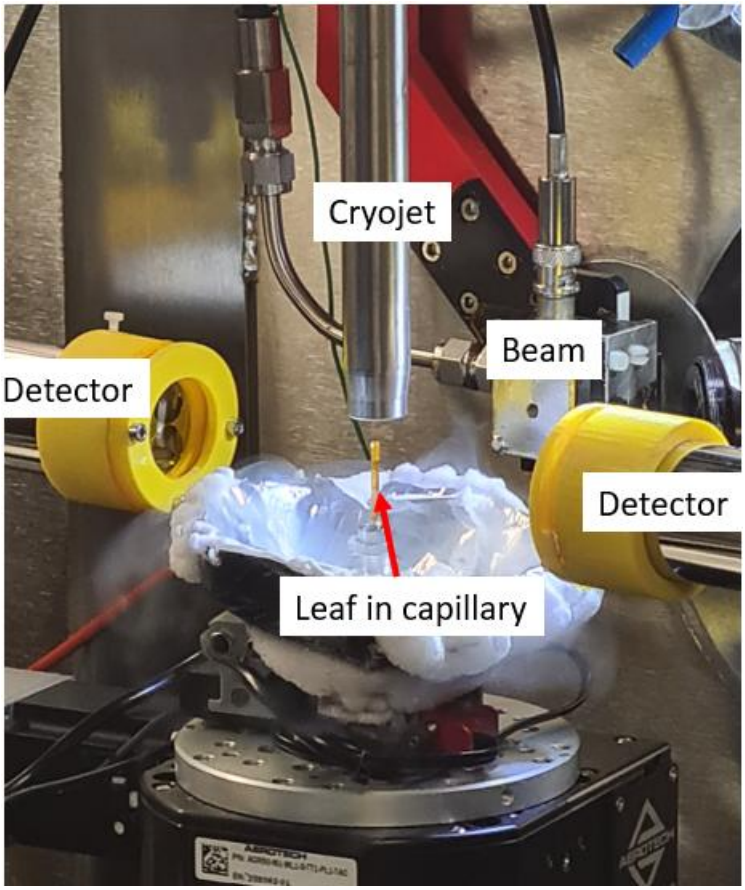


Figure 55: Sample setup for 3D-XRF tomography of leaf tissue on the I18 beamline at Diamond Light Source.

At the time of a tomography beamtime at Diamond, the mature plants that were planned to be used for measurements had to be destroyed due to the presence of insects. Instead, unaffected plants from a different growth cabinet had to be used. However, these plants were young: 4 weeks old compared to the usual ~12-week-old plants that are typically used. Nonetheless, measuring the distribution of zinc in young plants may provide useful temporal insights into how *N. caerulescens* may (or may not) redistribute the metal as they age, by comparing results to that of mature plants.

As was the case in Chapter 3, the aim here is to highlight any differences in zinc distribution so the maps are not normalised in intensity to each other. As discussed previously, lighter elements (for example potassium and calcium) are prone to self-absorption artefacts due to the lower energy fluorescent X-ray becoming aberrated by the

leaf tissue. Therefore, in the following 3D-XRF maps zinc will be the focus and the distribution will be compared to those obtained in Chapter 3. Due to time limitations, only extra low and high zinc samples were measured. Figure 56 shows a young high zinc sample of *N. caerulescens*, showing a cross section view akin to the transverse imaging in Chapter 3, and also the sample rotated 90^{o} to show the distribution on the lower epidermis of the leaf. From the transverse view, the distribution of zinc appears similar to that obtained with 2D-XRF, being localised to the majority of the epidermal vacuoles. Indeed, the vacuolar storage of zinc is very apparent in the 3D images, indicated by the red colour. There is also a clear area of lower intensity surrounding the vacuoles, likely showing zinc presence in the cell wall. Elongated cells are observed in the epidermis directly surrounding the central vein and these cells appear to be a major site for zinc accumulation.

The forthcoming images show a subset of the sample, not the entire sample, with the number of “slices” given in the figure legend. An increasing number of slices provides more information in the Z dimension as indicated by the axes in Figure 56. Additionally, as hand sectioning could introduce cell leakage, the region defined for imaging avoids the outermost portion of the sections.

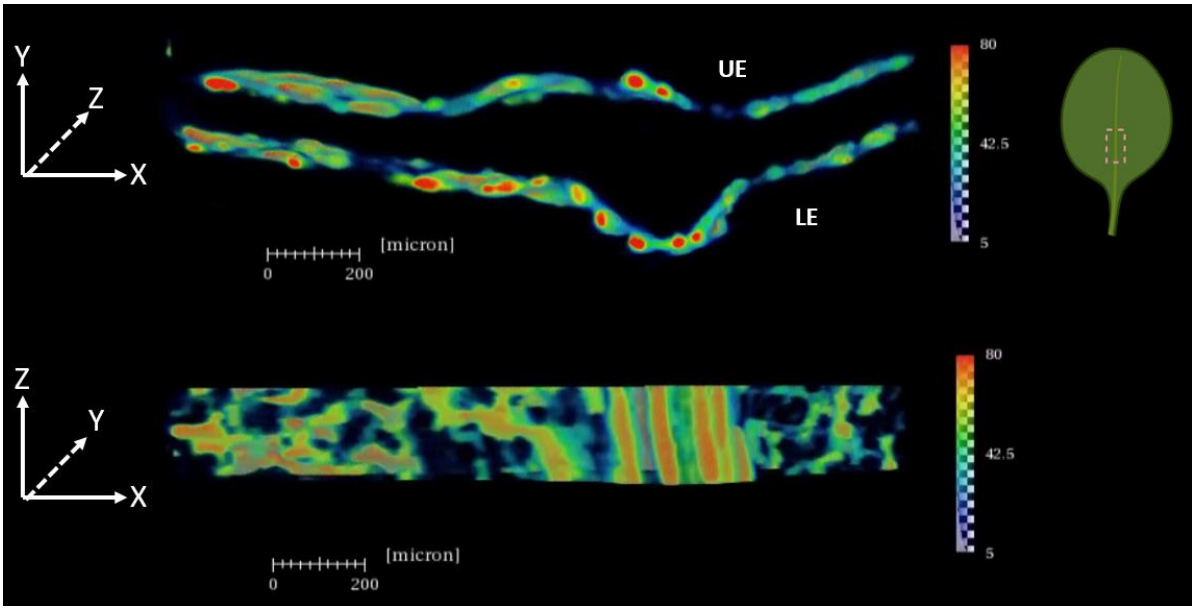


Figure 56: 3D-XRF reconstruction of a midrib section of leaf excised from a young (4-week-old), high zinc (300 µM) *N. caerulescens* plant. Transverse view (top) and abaxial view (below) showing zinc distribution. 48 slices, 5µm spatial resolution. UE = upper epidermis, LE = lower epidermis.

As with the 2D-XRF images, fewer vacuoles seem to contain zinc in the extra low *N. caerulescens* 3D-XRF map (Figure 57) compared to the high zinc sample. Although fewer slices were collected in the extra low zinc sample, the seemingly preferential storage in the elongated epidermal cells surrounding the central vein is apparent.

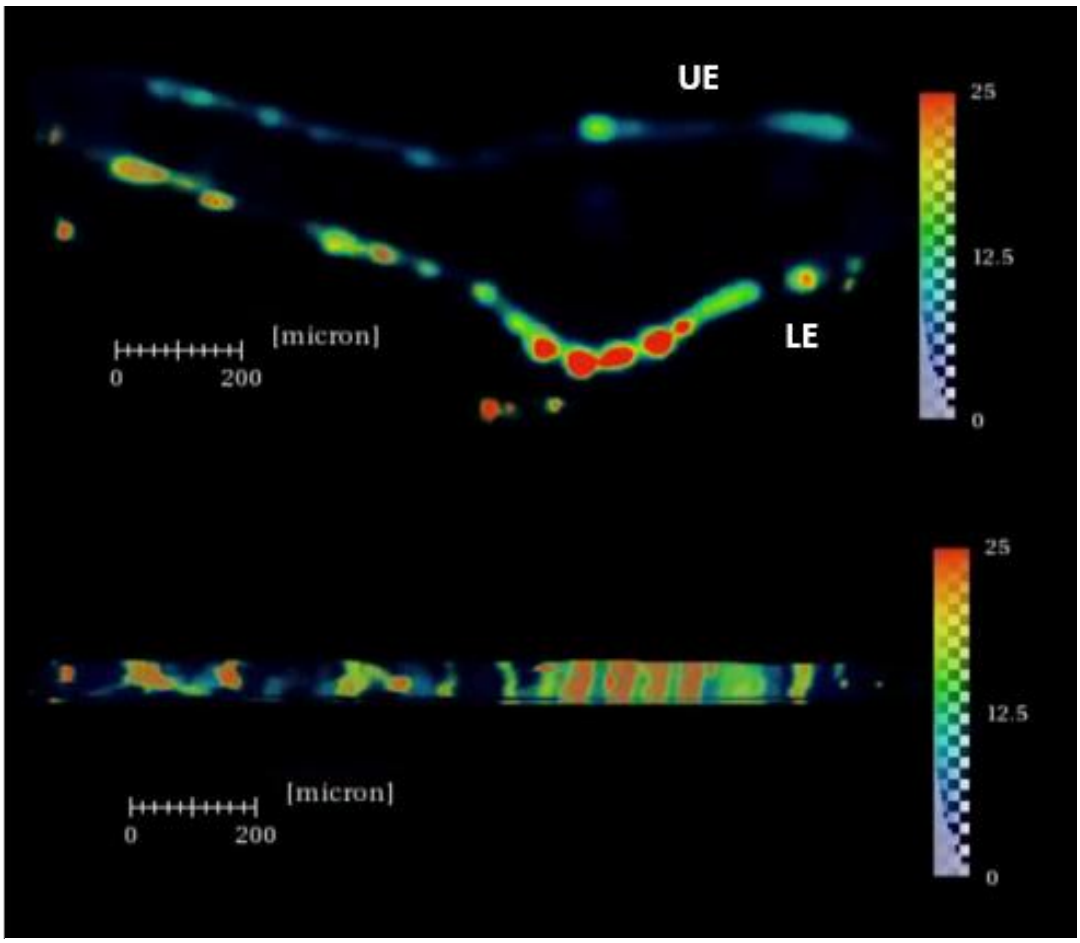


Figure 57: 3D-XRF reconstruction of a midrib section of leaf excised from a young (4-week-old), extra low zinc (10 µM) *N. caerulescens* plant. Transverse view (top) and abaxial view (below) showing zinc distribution. 18 slices, 5 µm spatial resolution. UE = upper epidermis, LE = lower epidermis.

In addition to the central leaf region that has been used for measurements up to this point, the leaf margin of young plants was also measured with 3D-XRF tomography. Figures 58 and 59 respectively show the zinc distribution in the margin of a high zinc and extra low zinc leaf. In keeping with the previous trends, zinc in the high zinc sample is distributed more evenly throughout the tissue compared to the extra low zinc sample. Interestingly, and particularly obvious in the extra low zinc sample, there is more zinc in the upper epidermis.

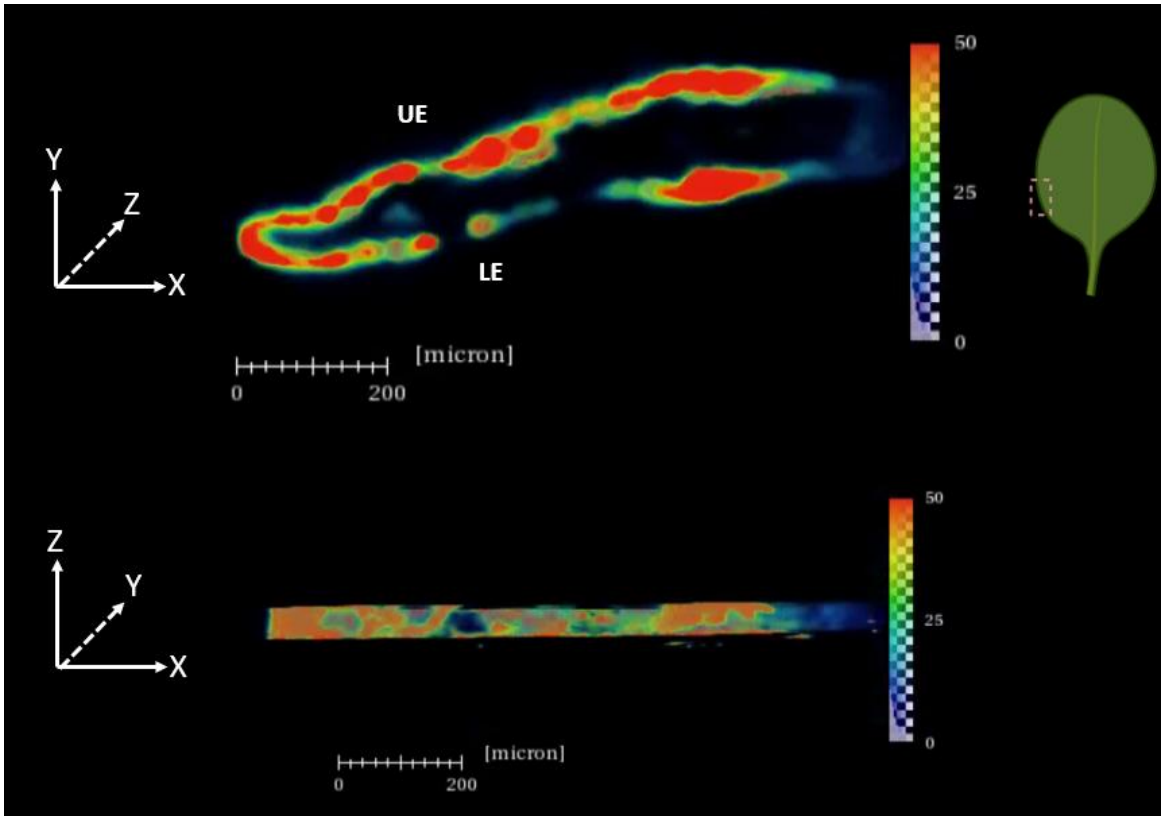


Figure 58: 3D-XRF reconstruction of a margin section of leaf excised from a young (4-week-old), high zinc (300 µM) *N. caerulescens* plant. Transverse view (top) and abaxial view (below) showing zinc distribution. 14 slices, 5 µm spatial resolution. UE = upper epidermis, LE = lower epidermis.

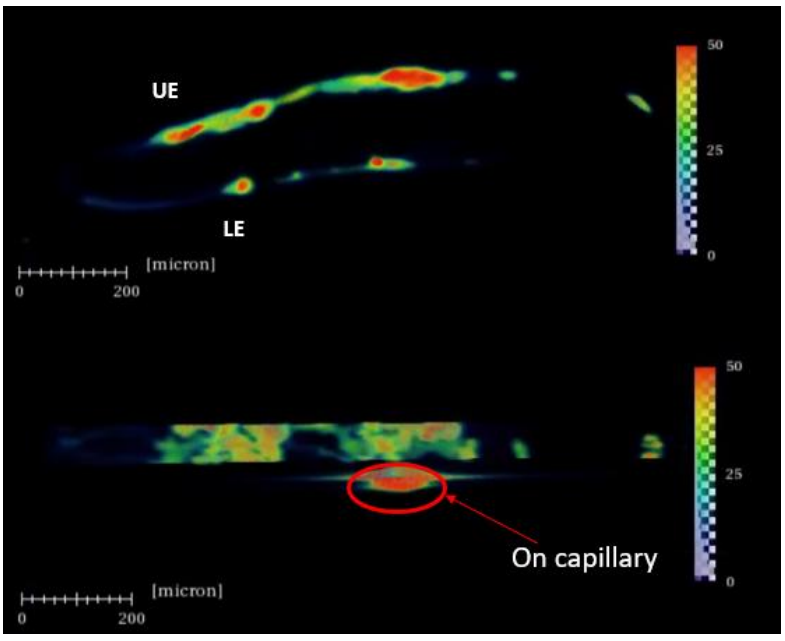


Figure 59: 3D-XRF reconstruction of a margin section of leaf excised from a young (4-week-old), extra low zinc (10 µM) *N. caerulescens* plant. Transverse view (top) and abaxial view (below) showing zinc distribution. 22 slices, 5 µm spatial resolution. UE = upper epidermis, LE = lower epidermis.

In a subsequent beamtime, mature plants were measured by 3D-XRF tomography. However, due to a lack of time, only mature plants grown on the high zinc concentration were measured. An untreated sample can be seen in Figure 60. Fewer slices were imaged in this sample, which is why it looks thinner. The distribution of zinc is consistent with both the 2D-XRF map (Figure 32) and the young high zinc sample (Figure 56) – being present in the majority of epidermal cells.

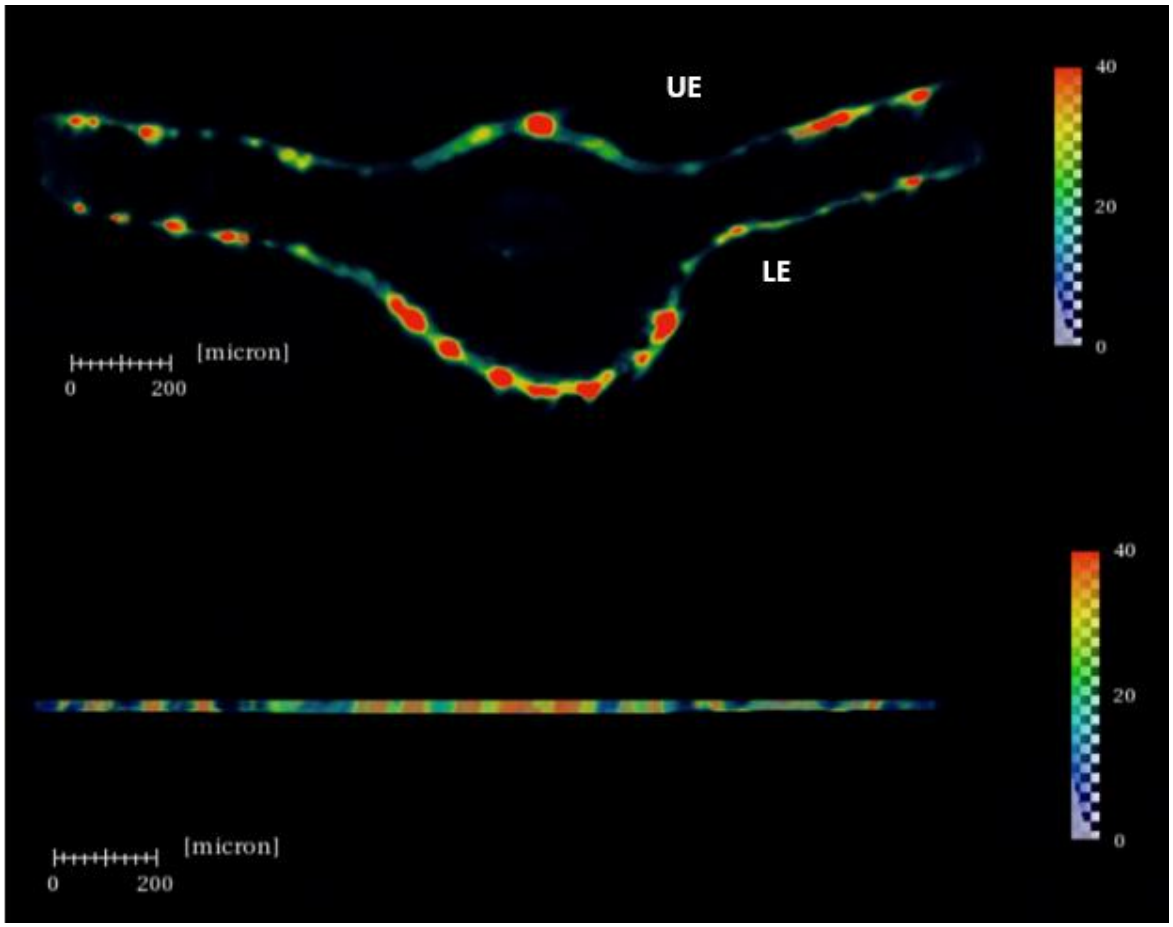


Figure 60: 3D-XRF reconstruction of a midrib section of leaf excised from an untreated mature high zinc (300 µM) *N. caerulescens* plant. Transverse view (top) and abaxial view (below) showing zinc distribution showing zinc distribution. 6 slices, 5 µm spatial resolution. UE = upper epidermis, LE = lower epidermis.

As with the 2D-XRF maps, in addition to untreated samples, mock inoculated and samples infected with *Pseudomonas syringae* were also measured with 3D-XRF tomography. As the phenotype of zinc release was the same with both strains tested in

section 3.2.3, only *Pseudomonas syringae* pv. maculicola was used. A mock inoculated sample can be seen in Figure 61. In this sample there are areas of zinc in the upper epidermis that are of lower intensity relative to the lower epidermis, but the distribution is largely the same as previously seen. As with the mock inoculated samples in section 3.2.3, zinc still remains highly localised to the epidermal cells and, as with the previous 3D-XRF samples, the vacuolar storage is particularly apparent.

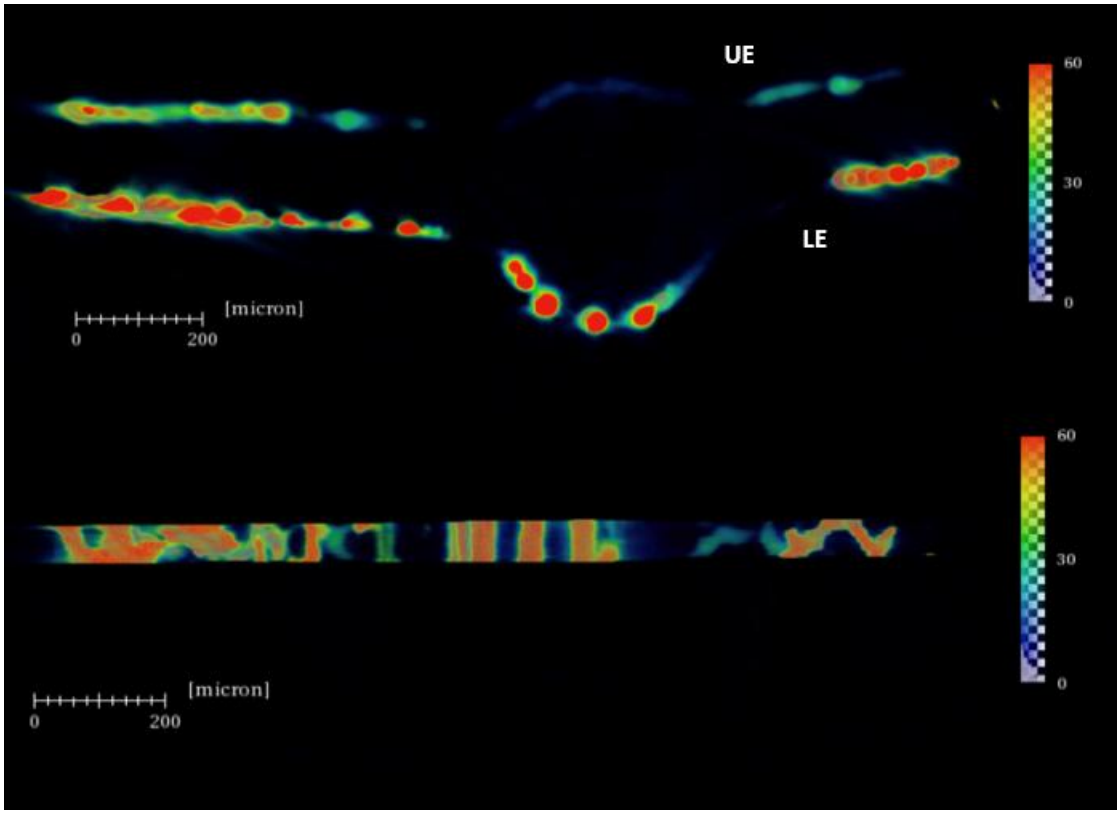


Figure 61: 3D-XRF reconstruction of a midrib section of leaf excised from a mature high zinc (300 µM) *N. caerulescens* plant. Mock infiltration, 5DPI. Transverse view (top) and abaxial view (below) showing zinc distribution. 16 slices, 5 µm spatial resolution. UE = upper epidermis, LE = lower epidermis.

Figure 62 shows a sample infected with Psm and excised from the plant at 1DPI. Most noticeable is that the previously distinct vacuolar storage of zinc now appears more diffuse. The zinc appears to be mobilising out of the vacuoles into cell walls or neighbouring epidermal cells.

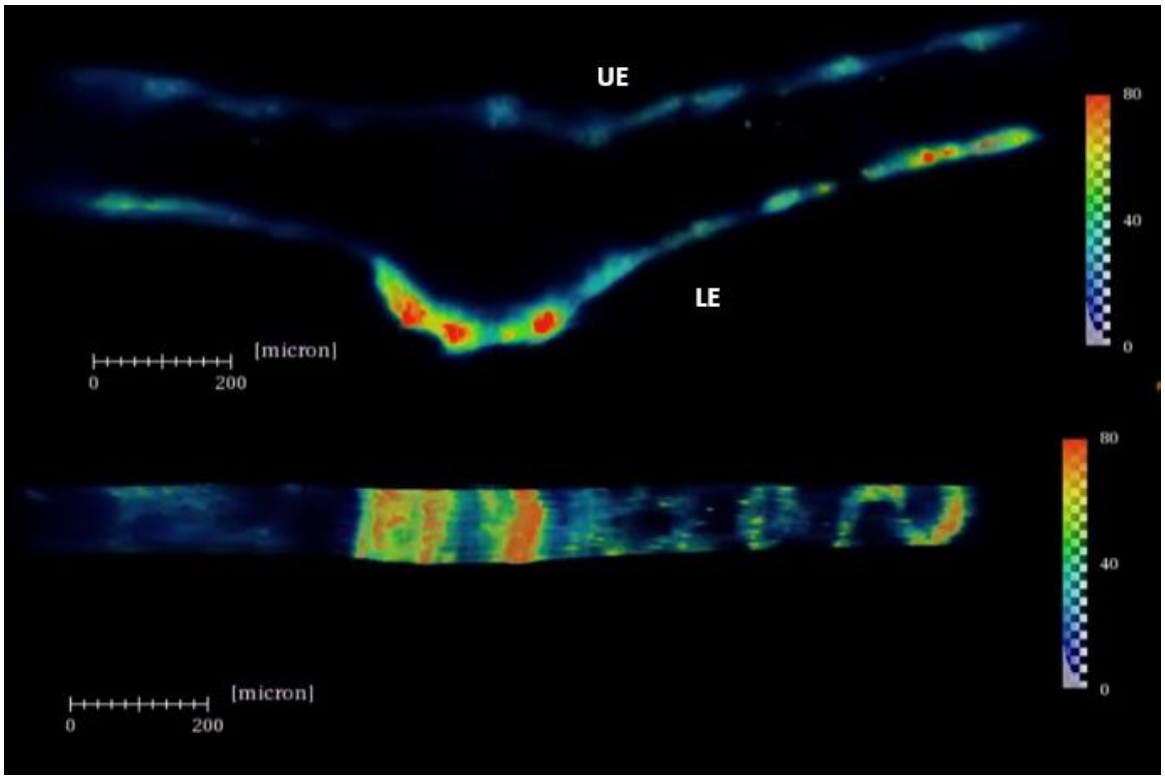


Figure 62: 3D-XRF reconstruction of a midrib section of leaf excised from a mature high zinc (300 µM) *N. caerulescens* plant infected with *P. syringae* pv maculicola. 1DPI. Transverse view (top) and abaxial view (below) showing zinc distribution. 25 slices, 5 µm spatial resolution. UE = upper epidermis, LE = lower epidermis.

Figure 63 shows a high zinc leaf infected with Psm and excised from the plant at 5DPI. The phenotype seen complements what was observed in section 3.2.3, with much of the zinc stored in epidermal cells becoming mobilised. Compared to the infected 2D-XRF samples, zinc in the apoplast and vasculature is less visible in the 3D map. However, this is more obvious in the single slice tomogram, as shown in the bottom panel of Figure 63.

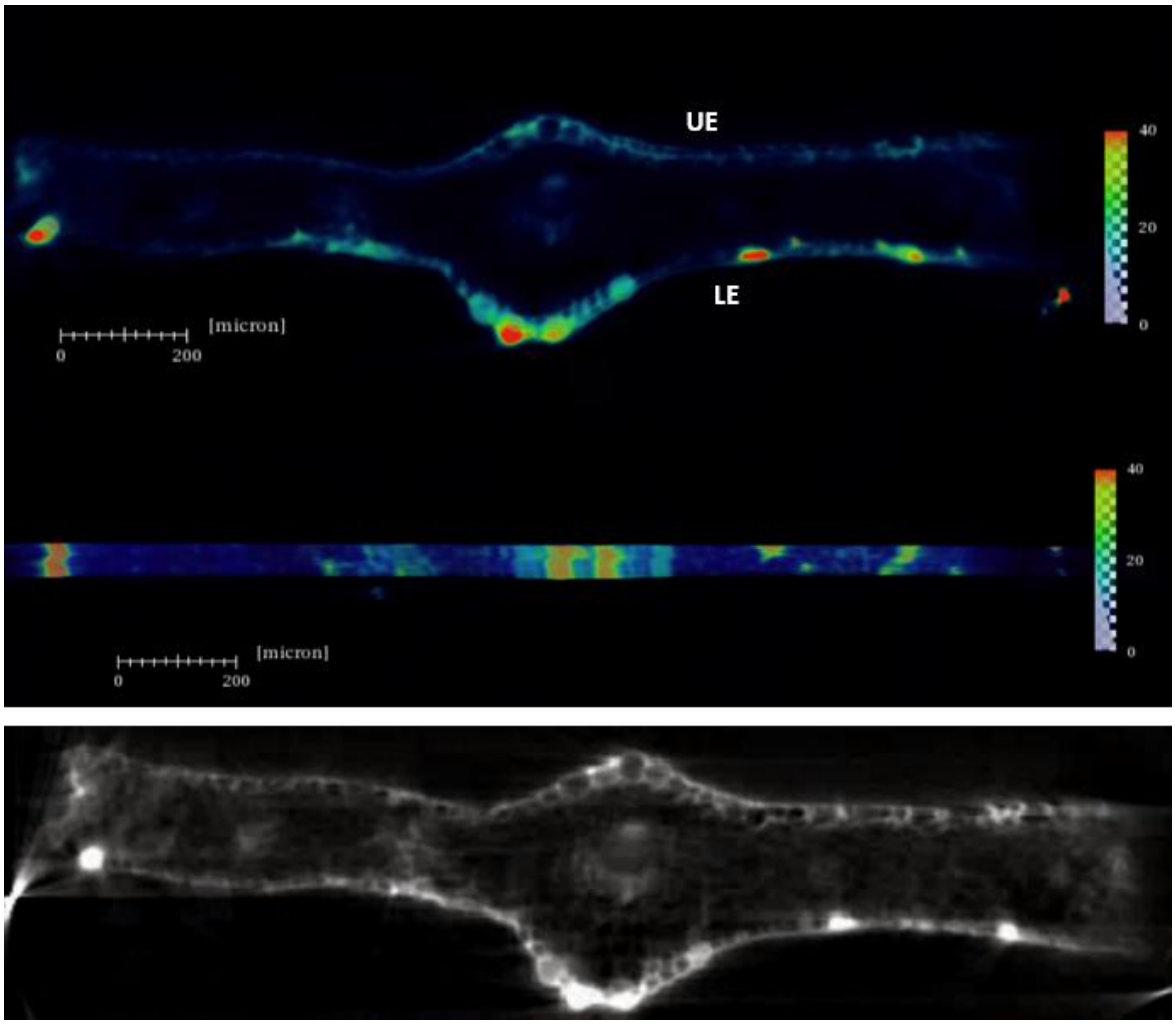


Figure 63: 3D-XRF reconstruction of a midrib section of leaf excised from a mature high zinc (300 µM) *N. caerulescens* plant infected with *P. syringae* pv maculicola. 5DPI. Transverse view (top) and abaxial view (centre). Single slice tomogram (bottom). Grey colour showing zinc distribution. 13 slices, 5 µm spatial resolution. UE = upper epidermis, LE = lower epidermis.

4.3 Discussion

The major aim of this chapter was to use 3D-XRF tomography to map the 3D distribution of zinc throughout the leaves of healthy and infected *Noccaea caerulescens* and to compare to results that were obtained with 2D-XRF in Chapter 3. The latter technique is far more involved with respect to sample preparation and there are number of ways artefacts can be introduced. The sample preparation for 3D-XRF tomography is far more simplified, using so-called virtual sectioning to probe metal distribution through sample volumes. A drawback, however, is that lighter elements are difficult to accurately measure and, due to the previously described self-absorption artefact being apparent for potassium, only the zinc distribution was studied.

Although the initial mounting test with *A. thaliana* was not successful in preserving leaf structure, surprisingly, there was an intact trichome visible. Multiple metals were observed without any self-absorption artefacts present which may indicate that 3D-XRF tomography is a suitable technique to measure metal accumulation in trichomes as less material is sampled. Agreeing with previous reports, calcium was observed throughout the structure and zinc was localised to a shallow ring around the base of the trichome (51). As with the epidermal cells in *N. caerulescens*, the base of the trichome could be a storage site for zinc in the non-accumulating *A. thaliana*. Indeed, in the cadmium and zinc hyperaccumulator *Arabidopsis halleri*, these metals were also localised to the base of the trichome (208). This initial test also highlighted the importance of measuring hydrated tissues under cryogenic conditions, as the sample measured at room temperature showed degradation. Instead of induvial cells, the potassium signal appeared as a sheet-like structure.

To the best of our knowledge, no published work has measured seeds of the Prayon population of *N. caerulescens* with 3D-XRF tomography. Here, the distribution of multiple metals were compared to seeds of the non-accumulating *A. thaliana*. Metals are required for

the health and successful germination of seeds, particularly iron and manganese (209). In both seeds, iron is seen to be highly localised to the vasculature of the cotyledons. This has been previously reported by Guo et al and Kim et al for *A. thaliana* and by van der Ent et al in *N. caerulescens* (Ganges, Vosges, and Cira populations) (206,209,210). Furthermore, Kim et al determined that this localisation of iron is crucial for seedling development as mutants lacking the vacuolar iron uptake transporter VIT1 showed disrupted iron distribution and exhibited poor growth under iron-limited conditions (206). The endosperm has been identified previously as an important storage site of nutrients for the developing seed, including zinc, which has been suggested as a mechanism to prevent toxicity in the embryo (211,212).

Higher intensities of nickel were observed in *N. caerulescens* than *A. thaliana* which may be because the former is a hyperaccumulator of this metal. The *N. caerulescens* seeds used in this study were collected from the former smelter site in Prayon (Belgium) which has elevated zinc levels in the soil (213). It may therefore be of interest to compare the 3D-XRF results from these seeds to seeds obtained from other populations or from plants cultivated hydroponically with controlled concentrations of metals in a future experiment. This would, however, first require the establishment of the conditions that promote seed production.

For leaf tissue, we found that the beamline's cryojet froze the sample sufficiently fast to maintain metal distribution and prevent ice-related artefacts from appearing. However, if future researchers planning to do 3D-XRF tomography do not have 2D-XRF maps of their sample to compare to, it would be recommended to flash freeze the sample in liquid nitrogen-cooled isopentane prior to mounting to maximise freezing efficiency.

The distribution of zinc in the untreated 3D-XRF maps largely complement what was observed in the 2D-XRF sections. Vacuolar storage of zinc was very apparent in the epidermal cells as indicated by a distinct region of much higher intensity in the centre of the cell. However, there was also zinc present in the cell wall of epidermal cells but at lower concentration than the vacuole. This distinction between the vacuole and cell wall was more

apparent in the 3D-XRF images compared to the 2D-XRF images even when the pixel size used in the latter was smaller. This may therefore be a benefit of mapping entire cell volumes. As one might expect, the most spatial information could be obtained when a greater number of tomograms were collected. However, measuring more slices requires more time which is already limited in a beamtime experiment. Also apparent in the 3D-XRF images is that cells surrounding the midrib are elongated and seem to be a site of preferential zinc storage. It is unclear at this stage what the implications of this observation are and would likely benefit from complementary confocal microscopy. Alternatively, a clearer picture of the relationship between cell type and preferential zinc storage could be seen with a composite view of potassium and zinc distribution. As seen with the 2D maps, potassium is present in all cells so can be used as a guide for leaf morphology. This, however, would require correction of the self-absorption phenomenon. Correction of self-absorption has previously been demonstrated in, for example, *Allium schoenoprasum* to enable study of the 3D distribution of light elements (214).

In both young and mature plants, the distribution of zinc appears consistent. This is in agreement with Nascimento et al, who used 2D-XRF to study metal distribution on the surface of *N. caerulescens* leaves of different ages. The authors found that the distribution was largely the same regardless of leaf age, particularly localised to areas surrounding the midrib and secondary veins, but that concentration increases with age. The authors also observed that distribution did not change when plants were grown on increasing concentrations of zinc which is in contrast to what we have found in this work. However, the authors were looking at a more macroscale view of the leaf surface compared to smaller millimetre sized sections so it is possible the finer details could have been missed (215).

As with samples in section 3.2.3, the mock inoculated map is largely consistent with the untreated sample, with zinc being localised to the epidermal vacuoles, further evidencing that the zinc mobilisation upon infection is not a mechanical effect from the infiltration. In Figure 60, in the infected sample excised from the plant at 1DPI, it appears as if zinc is

starting to be released from the epidermal vacuoles into adjacent tissue - apparent from the more diffuse appearance of the zinc in the epidermal layer than the mock and untreated samples. This observation could potentially explain why zinc concentrations were not elevated in apoplastic washing fluid at 1DPI in the ICP-MS data (section 3.2.4), but more samples and time points, both for 3D-XRF and ICP-MS, would be required to fully understand the timing and route of zinc release. As seen in the 5DPI sample (Figure 63), although zinc has clearly moved from the epidermal cells, it is difficult to see the increase in zinc in the apoplast of the mesophyll and in the vasculature in the 3D image. This is perhaps simply due to the lower spatial resolution used for tomography, which was chosen as lower resolution maps take proportionally less time to collect. The 3D maps of the infected tissue could thus be repeated at higher resolution at the expense of proportionally longer acquisition times. For example, the 2D-XRF maps where zinc was visible in the extracellular space were collected at 1 μm spatial resolution.

In this chapter, 3D-XRF tomography was used to measure the 3D zinc distribution in the leaves of *N. caerulescens.* Due to the presence of self-absorption, no “control” with potassium was analysed, but the zinc distribution is consistent with results obtained using 2D-XRF mapping and the volumetric measurements highlight the vacuolar storage of the metal. A major benefit of 3D-XRF imaging is the far more simplified sample preparation process, requiring only that the leaf is rapidly excised from the plant and razor-sectioned to an approximate size of 2 x 3 mm before being inserted into a capillary. This process avoids the artefacts that can occur during the significantly more intensive transverse sample preparation for 2D imaging and thus, as the results between the two techniques are comparable, the 3D mapping corroborates the findings in Chapter 3. Correction algorithms for self-absorption are available, but as the primary interest in this work was to compare zinc distribution between 2D and 3D-XRF imaging and this was not affected by self-absorption, correction was not attempted. However, a greater number of metals could be measured using 3D-XRF in seeds and trichomes than in leaves due to their smaller size and absence

of self-absorption artefacts. Future work would benefit from measuring a greater number of slices to get a more comprehensive view of the tissue-wide distribution of zinc. Additionally, the sample setup used for this work could be extended to 3D-XANES tomography to obtain information on zinc speciation within whole cell volumes.

Chapter 5: Understanding the effect of zinc and reactive oxygen on the viability of *Pseudomonas syringae*

5.1 Introduction

A more recent refinement to the elemental defence hypothesis of metal hyperaccumulation suggests that the presence of hyperaccumulated metal may act in synergy with existing plant defences to boost the defensive effect of both, in what is termed the “joint effects” hypothesis (70,75). In previous chapters and studies, it has been established that bacteria in *Noccaea caerulescens* are exposed to both increased zinc and reactive oxygen species (ROS) (25,86). This chapter will assess the in vitro tolerance of *Pseudomonas syringae* to zinc and ROS, both as individual stressors and in combination, with the aim of determining whether there is a synergistic, joint effect between zinc and ROS and uncovering the possible mechanisms underlying their toxicity. In this work, hydrogen peroxide is used as a representative source of ROS as, although it is labile, it is more stable than other ROS like superoxide, and thus more practical to use (216). Furthermore, superoxide is rapidly transformed into hydrogen peroxide by the action of the enzyme superoxide dismutase (SOD), making hydrogen peroxide an important product of the oxidative burst and a target of bacterial antioxidant defences (216–218).

Though not widely studied, particularly with respect to bacterial plant pathogens, joint effects have been observed when metal + metal, and metal + organic acid artificial diets were fed to *Plutella xylostella* (diamondback moth). Relatively low concentrations of metals in combination with an organic acid or another metal were sufficient to increase the effectiveness of either defence individually. The authors used commonly-hyperaccumulated metals and plant-relevant organic compounds and related their observations to the defensive strategies of hyperaccumulator plants, suggesting they may leverage similar synergistic relationships to enhance their resistance to herbivores (219). A synergistic effect has also been observed when silver ions were used in combination with antibiotics or the

organoselenium drug molecule ebselen, providing an enhanced defence against Gram-negative bacteria. The combination of the metal and drug molecules increased the oxidative stress of the bacteria by affecting glutathione and thioredoxin activity (220,221).

As established in Chapter 3, upon infection with *P. syringae*, zinc is released into the apoplastic space. Likewise, an altered ROS response has been observed in *N. caerulescens* where superoxide levels increase in response to increasing zinc, independent of the presence of *P. syringae* (25,38,87). In addition to this, *N caerulescens* has been found to display a flg-22 induced, NADPH oxidase-dependent oxidative burst in response to pathogen detection (Johnson, Bach-Pages and Preston, unpublished). Thus, *P. syringae* inhabiting the apoplastic space of *N. caerulescens* leaves must contend with the simultaneous stress of zinc exposure and ROS, prompting interest in investigating whether these stressors may act synergistically to provide the plant with a joint defensive effect.

As is the case in plants, metals are essential for the normal function of bacteria but become toxic at high levels, through the indirect formation of ROS for example (106). A key defence mechanism is through the use of antioxidant enzymes such as SOD, catalase, and peroxidase, many of which are metalloenzymes that rely on metal ions as cofactors for their catalytic activity (222,223). In addition to enzymes that work to break down ROS, glutathione is a key thiol-containing antioxidant that functions as an important redox buffer in the majority of eukaryotes (224). This function is a consequence of the “reversible interconversion” of the reduced form of glutathione (GSH) and the oxidised form glutathione disulfide (GSSG) (225). Glutaredoxins are redox enzymes that use glutathione as a cofactor to reduce oxidised proteins (via disulfide reduction) and restore their functionality after oxidative stress (226,227).

To assess the effect of ROS on *P. syringae* both as an individual stressor and when combined with zinc, as is the case in *N. caerulescens*, the biosensor redox-sensitive green fluorescent protein (roGFP) can be used. roGFP is the commonly used GFP modified with two surface-exposed cysteine residues and is used to assess the real-time intracellular

redox state of bacteria. As shown in Figure 64, upon oxidation, the two cysteine residues form a reversible disulfide bridge resulting in a shift of conformation (228). This conformational shift leads to a shift in fluorescence excitation spectra and thus ratiometric analysis between the two wavelengths enables quantitative measurement of the redox state within the bacterial cells. By utilising ratiometric measurements, variability stemming from biosensor concentration or expression levels is minimised (228,229). Various roGFPs exist varying in, for example, the position of cysteine residues, and can be targeted to a specific bacterial (or indeed plant) compartment (230,231). This work utilises roGFP2 which has previously been used to monitor oxidative stress under hydrogen peroxide challenge (229–231). However, roGFP2 primarily reports on cellular glutathione redox potential (232). Mediated by glutaredoxins, roGFP2 reacts with GSH and GSSG to undergo the previously mentioned reversible disulfide bond formation (232). This functionality allows roGFP to report on the ratio of cellular GSH:GSSG (228,233,234). A potential limitation of roGFP2, however, is its reliance on endogenous glutaredoxins for efficient equilibrium with the GSH:GSSG couple, which can limit its responsiveness in reporting redox kinetics. To address this, the fusion construct Grx1-roGFP2 was developed which enhances the probe's sensitivity and kinetics by facilitating a faster and more specific interaction with the glutathione system (230,235).

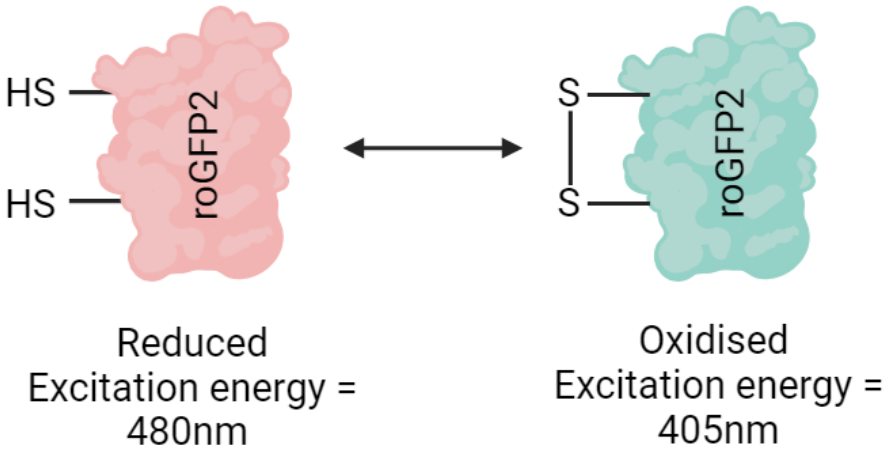


Figure 64: Cartoon showing the simplified structure of the roGFP2 protein and the disulfide bridge formation that occurs due to oxidation. Made in BioRender.

While tolerance assays and roGFP experiments can shed light on how zinc and ROS affect the respective growth and redox state of the bacteria, neither technique provides insights into how these stressors affect the overall molecular composition of a bacterium. Raman microspectroscopy is an analytical technique that enables (bio)chemical fingerprinting of a sample at the single-cell level and can identify potential biomarkers of stress (236). For example, Verma et al identified differences in the nucleic acid to protein, and nucleic acid to lipid Raman peak ratios depending on the antibiotic *Escherichia coli* were exposed to (237).

Interaction with monochromatic light causes a molecule to vibrate and, most commonly, the incident light is elastically scattered – leaving with the same energy. However, a much lower proportion of the incident photons can be scattered inelastically. In this situation, the incident light excites electrons to a short-lived virtual state existing between energy levels and when these electrons relax, it is to either a higher (Stokes) or lower (Anti-Stokes) energy state. This is Raman scattering and is outlined in Figure 65. Raman spectroscopy measures the change in incident and scattered light, called the Raman shift, depicted in wavenumbers (cm^{-1}) (238). The vibration of different functional groups within a compound will appear in the Raman spectrum at characteristic Raman shifts, following the relationship seen in Equation 2.

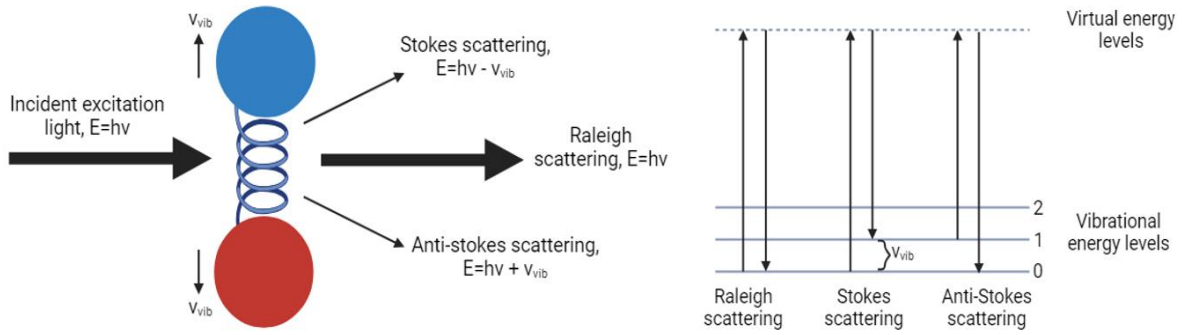


Figure 65: Schematics outlining the principles of Raman spectroscopy. Raleigh, Stokes, and Anti-Stokes scattering after incident light interacts with a molecule of interest. The difference in energy between incident and scattered light is referred to as Raman shift, presented here as v_{vib}. Made in BioRender.

While Raman spectroscopy is an inherently label-free technique, stable isotope labelling can be used to monitor metabolic activity. In metabolically active cells, the incorporation of an isotope with a different mass will be expressed as a distinct peak in the Raman spectrum, due to the relationship described in Equation 2. This has been demonstrated by Song et al who used Raman deuterium stable isotope probing to identify and distinguish antimicrobial-resistant and susceptible bacteria from the river Thames (239).

Equation 2: Hooke's law for a harmonic oscillator where $\tilde{\nu}$ is wavenumber (cm^{-1}), k is the force constant (Nm^{-1}), and μ is the reduced mass (kg).

$$\tilde{\nu} = \frac{1}{2\pi}\sqrt{\frac{k}{\mu}}$$

In this chapter, various in vitro assays and techniques will be used to assess the tolerance of *Pseudomonas syringae* to challenge by zinc and hydrogen peroxide. These stressors will be applied individually and in combination to explore a potential joint, synergistic effect.

5.2 Results

5.2.1 Investigating the zinc and ROS tolerance of *Pseudomonas syringae*

As discussed in Chapter 1, there are a multitude of plant defences alongside elemental defences and ROS that may affect pathogen viability in the plant environment. Therefore, in order to assess the direct effect of increasing zinc and ROS on *Pseudomonas syringae* pv. maculicola and *Pseudomonas syringae* pv syringae SnB11, both separately and in combination with one another, a series of in vitro assays were performed. Optical density at 600 nm (OD_{600}) is used as a measure of cell density and thus plotting OD_{600} over

time provides an indication of bacterial growth and can be used to assess the effects of stressors on bacterial viability.

The growth of Psm under zinc challenges of 0-1.4 mM can be seen in Figure 66A. Increasing zinc concentration caused stepwise inhibition of bacterial growth until complete inhibition at concentrations greater than 1 mM. Increasing the concentration of zinc above 0.6 mM also increased the lag phase, that is, the time prior to the observed exponential growth. Increasing concentrations of ROS, in the form of hydrogen peroxide (H_2O_2), did not cause the gradual inhibition observed with zinc. As seen in Figure 66B, Psm is tolerant to hydrogen peroxide up to 30 mM and completely inhibited at the concentrations tested above this. However, the presence of sublethal levels of zinc appears to increase the sensitivity of Psm to ROS. As shown in Figure 65C, challenge with both 0.4 mM zinc and hydrogen peroxide reduces the tolerance of Psm to 20 mM. Likewise, in Figure 66D, including 0.8 mM zinc reduces the tolerance further. Both sublethal zinc concentrations also reduce the maximum OD measured, from approximately 0.8 to relative ODs of approximately 0.6 and 0.5. The reduction in maximum OD values is likely due to the cessation or slowing of bacterial proliferation.

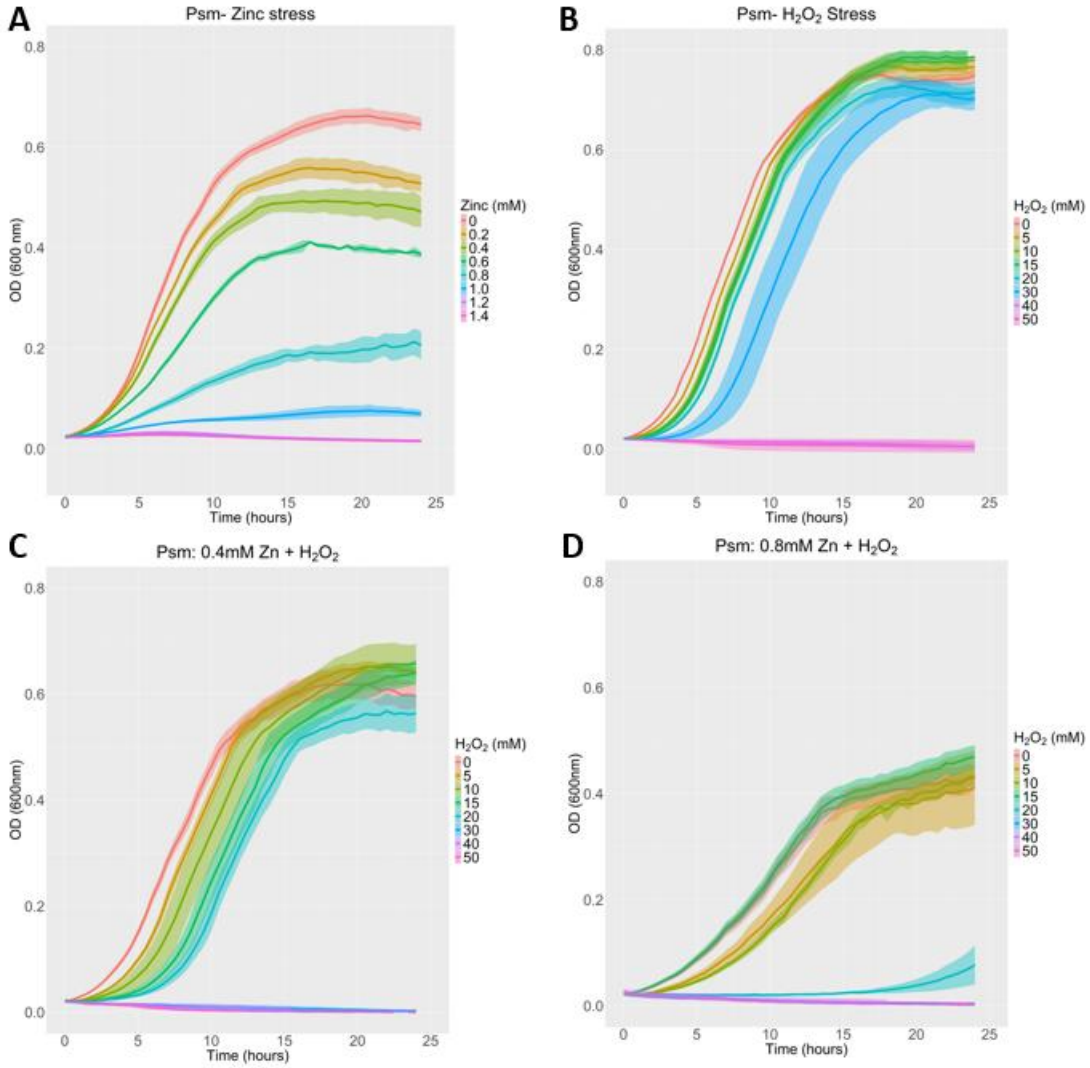


Figure 66: Growth of Psm in LB media stressed with zinc (A), hydrogen peroxide (B), or a combination of hydrogen peroxide and non-lethal concentrations of zinc (C - 0.4 mM and D – 0.8 mM). Both stressors added simultaneously. Lines indicate mean values and ribbons indicate standard deviation between replicate wells. Plots are representative examples of each assay, each repeated at least three times.

To more directly see the combined effect of zinc and ROS on Psm, single concentrations of hydrogen peroxide are plotted for the two zinc treatments (0.4, and 0.8 mM) and compared to the zero-zinc scenario in Figure 67. Zinc had similar effects in the 5- and 10-mM hydrogen peroxide plots; 0.8 mM causing the greatest inhibition. Psm was completely inhibited at any treatment with 40 mM hydrogen peroxide.

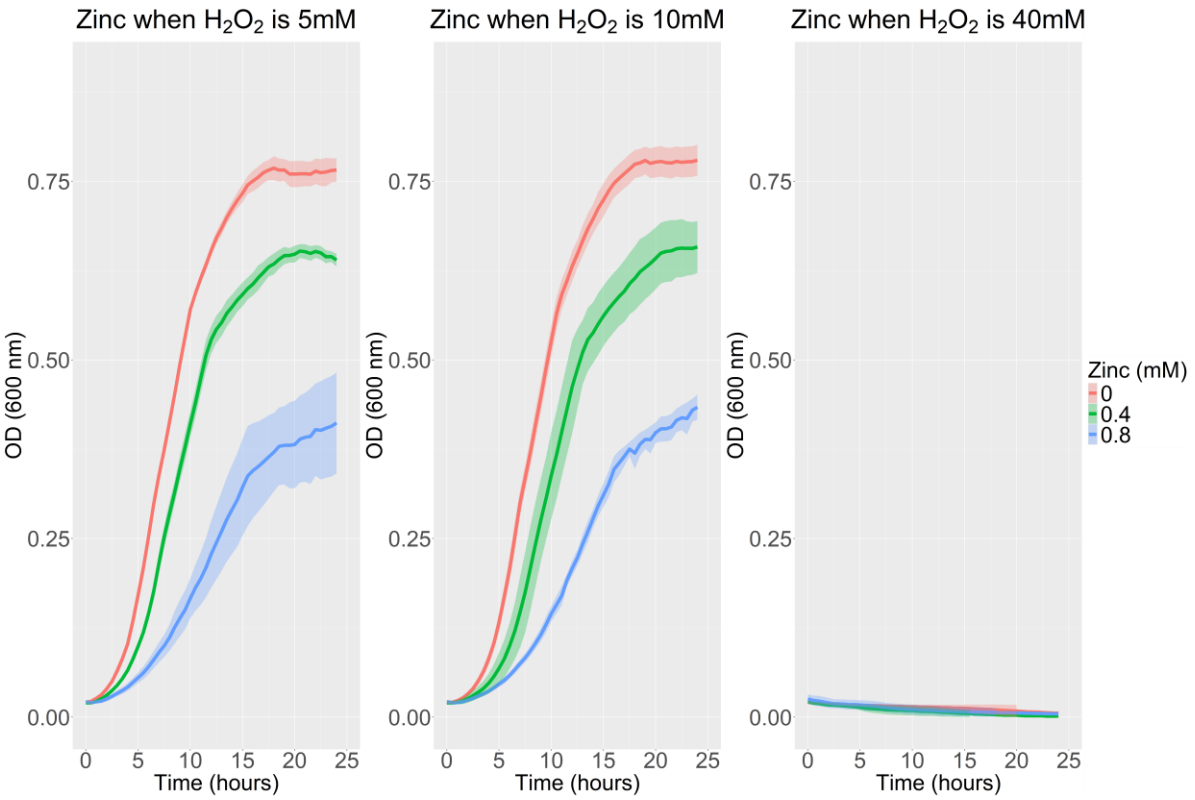


Figure 67: Growth of Psm in LB media stressed with zinc and different concentrations of hydrogen peroxide. Both stressors added simultaneously. Lines indicate mean values and ribbons indicate standard deviation between replicate wells. Data extracted from the plots shown in Figure 66.

The growth of B11 under zinc challenges of 0-1.4 mM can be seen in Figure 68A. As with Psm, increasing zinc concentration caused a stepwise inhibition of bacterial growth until complete inhibition at concentrations greater than 1 mM. However, B11 was found to be much more tolerant to hydrogen peroxide than Psm and so a different range of concentrations were used, 0-150 mM. As with Psm, though, the tolerance of B11 to hydrogen peroxide is not stepwise, it is tolerant up to 125 mM but completely inhibited by the next concentration tested. Upon addition of 0.4 or 0.8 mM of zinc, the sensitivity of B11 to hydrogen peroxide again increases. In all assays shown in Figure 68, increasing stressor concentration increases the lag phase.

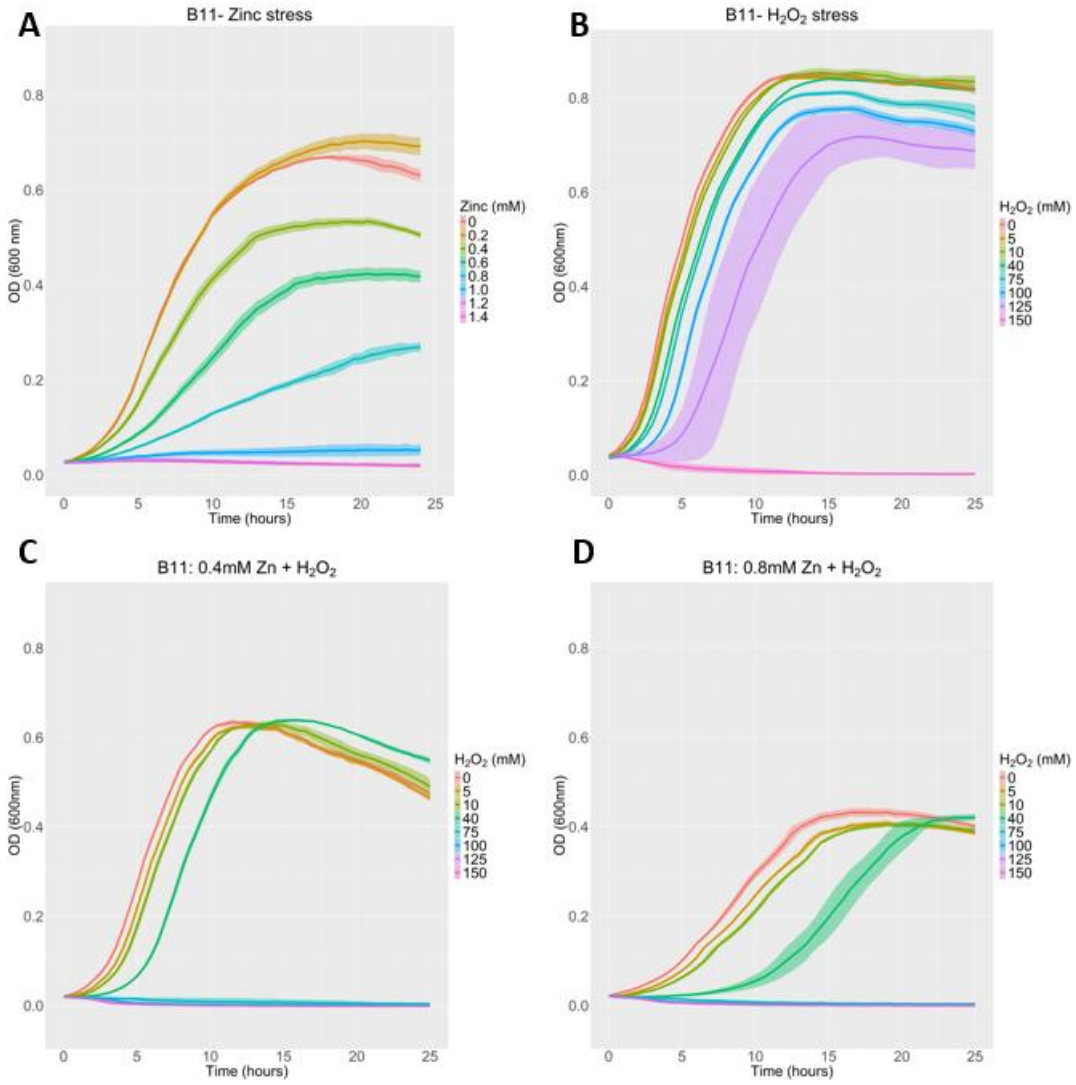


Figure 68: Growth of B11 in LB media stressed with zinc (A), hydrogen peroxide (B), or a combination of hydrogen peroxide and non-lethal concentrations of zinc (C - 0.4 mM and D – 0.8 mM). Both stressors added simultaneously. Lines indicate mean values and ribbons indicate standard deviation between replicate wells. Plots are representative examples of each assay, each repeated at least three times.

To more directly see the combined effect of zinc and ROS on B11, single concentrations of hydrogen peroxide are plotted for the two zinc treatments (0.4, and 0.8 mM) and compared to the zero-zinc scenario in Figure 69. Zinc had similar effects in the 5- and 10-mM hydrogen peroxide plots; 0.8 mM causing the greatest inhibition. Unlike Psm, B11 is tolerant to all zinc combinations with 40 mM hydrogen peroxide. However, an increase in lag phase is observed in the 0.4- and 0.8-mM zinc plots at 40 mM hydrogen peroxide compared to the 5 mM and 10 mM hydrogen peroxide plots.

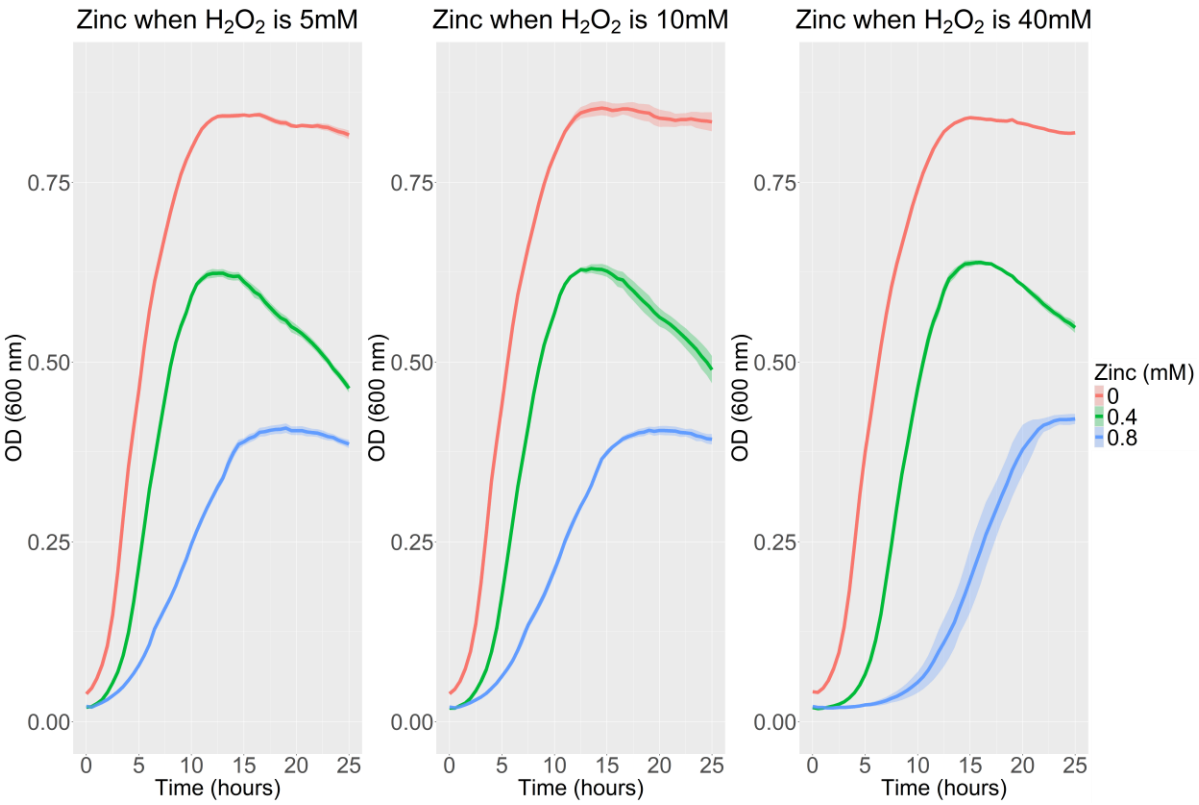


Figure 69: Growth of B11 in LB media stressed with zinc and different concentrations of hydrogen peroxide. Both stressors added simultaneously. Lines indicate mean values and ribbons indicate standard deviation between replicate wells. Data extracted from the plots shown in Figure 68.

Since the order in which bacteria encounter zinc and ROS in the plant environment is unclear, tolerance assays were conducted in which one stressor was applied an hour prior to the other. Additionally, this approach may also allow for the study of a potential priming effect, whereby pre-exposure to either stressor may provide enhanced resistance. Here, assays testing this potential effect were all measured in one 96-well plate, so fewer concentrations of zinc were used than previously. Additionally, a higher concentration of zinc was used in case there was a priming effect.

Adding hydrogen peroxide at +1hr as the sole stressor had a surprising effect of reducing the tolerance of B11. Compared to Figure 68B where B11 is tolerant up to 125 mM, in Figure 70B, when hydrogen peroxide is added to the 96-well plate after an hour of untreated bacterial growth, the tolerance drops to 75 mM.

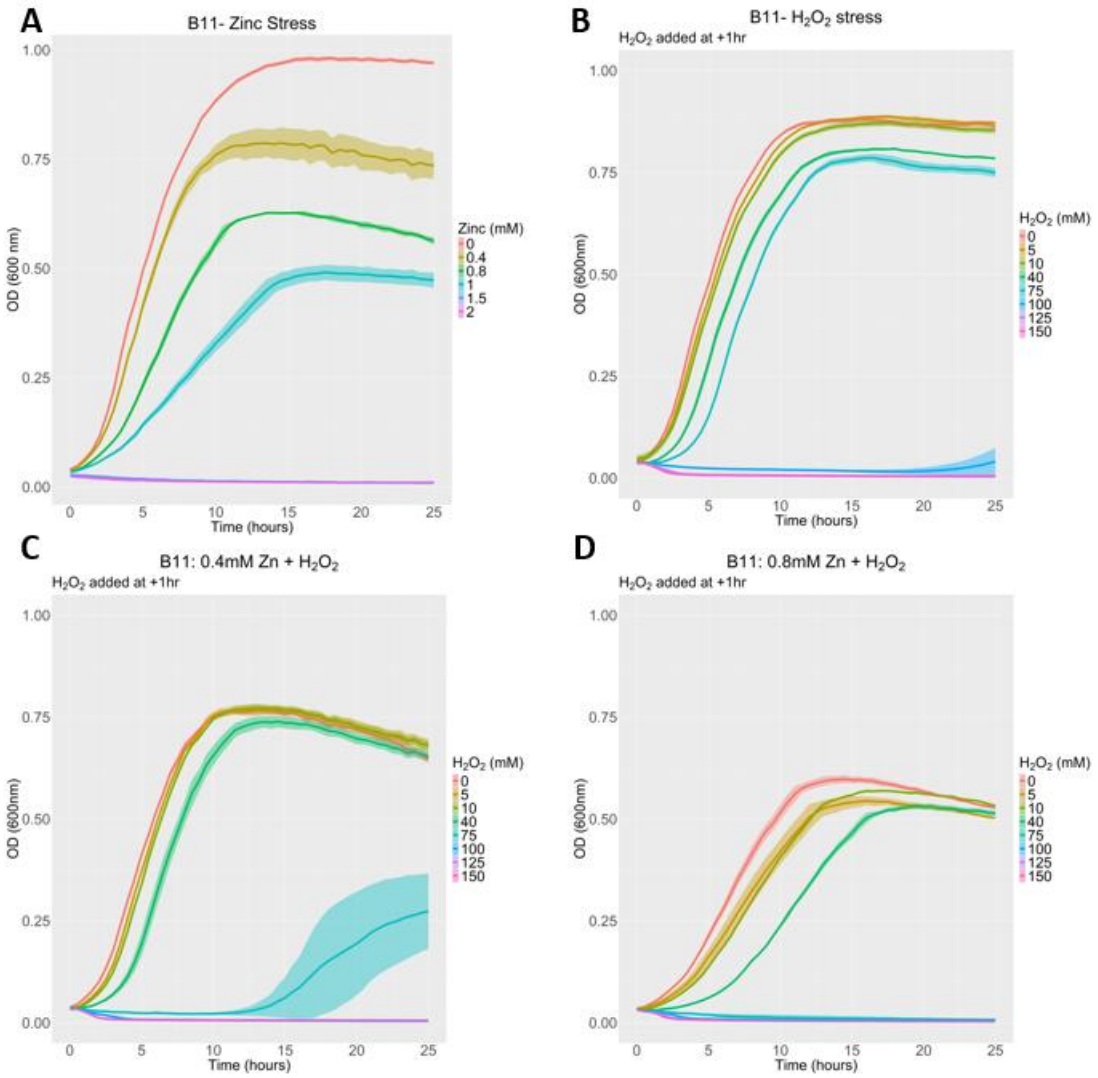


Figure 70: Growth of B11 in LB media stressed with zinc (A), hydrogen peroxide (B), or a combination of hydrogen peroxide and non-lethal concentrations of zinc (C - 0.4 mM and D – 0.8 mM). Zinc added at time 0 and hydrogen peroxide added at +1 hour. Lines indicate mean values and ribbons indicate standard deviation between replicate wells. Plots are representative examples of each assay, each repeated at least three times.

The B11 growth curves for combined zinc and hydrogen peroxide stressors appear visually similar whether the stressors are added concurrently (Figure 68C and D) or with hydrogen peroxide introduced 1 hour later (Figure 70C and D). However, the concentration of hydrogen peroxide required to cause half-maximal inhibition in the latter scenario suggests slightly reduced tolerance when bacteria are exposed to zinc prior to ROS: 54 ± 3.61 mM compared to 72 ± 20.66 mM. Concentrations causing half-maximal inhibition (IC_{50}) are often used as a measure of potency of a given antagonist (240). The IC_{50} values for each stressor, and combination of stressors, are given in Table 8. These values were calculated for the 10-hour time point, chosen due to it being mid-exponential phase where the greatest concentration effect was observed. The dose response curves used to calculate IC_{50} values can be seen in the Appendix. It is important to note that, for example, B11 zinc in the second and third column are treated separately because the latter was measured concurrently with the other treatments in the same column and the former was not.

Unlike hydrogen peroxide, when zinc is added at time +1hr as the sole stressor there does not appear to be a noticeable effect on bacterial growth. A slight increase in tolerance is observed when 0.8 mM zinc is added an hour after the introduction of hydrogen peroxide: 39 ± 15.1 mM compared to 58.7 ± 16.8 mM hydrogen peroxide.

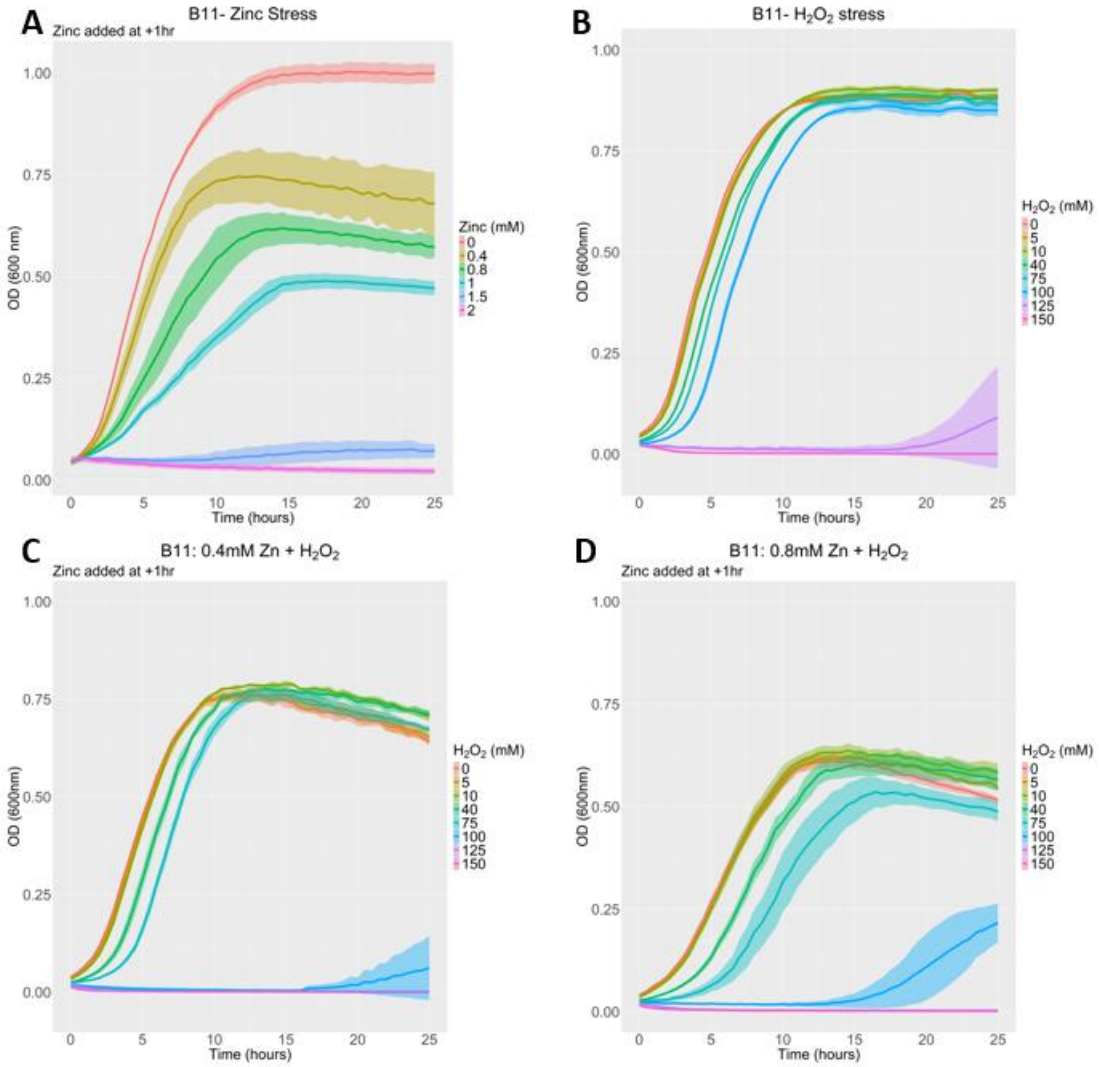


Figure 71: Growth of B11 in LB media stressed with zinc (A), hydrogen peroxide (B), or a combination of hydrogen peroxide and non-lethal concentrations of zinc (C - 0.4 mM and D – 0.8 mM). Hydrogen peroxide added at time 0 and zinc added at +1 hour. Lines indicate mean values and ribbons indicate standard deviation between replicate wells. Plots are representative examples of each assay, each repeated at least three times.

Table 8: Average IC_{50} values calculated from at least 3 independent experiments, error shown is standard deviation. Time = 10 hours. The final two columns show that one of the stressors was added at time zero and one was added an hour later to test for a potential priming effect.

	IC_{50} (mM)			
Treatment	**Psm**	**B11**	**B11 – H_2O_2 added at +1hr**	**B11 - Zn added at +1hr**
Zn	0.67 ± 0.14 (n = 7)	0.77 ± 0.14 (n = 6)	0.76 ± 0.19 (n = 3)	0.86 ± 0.0058 (n = 3)
H_2O_2	25.5 ± 6.1 (n = 4)	118.33 ± 20.21 (n = 3)	78 ± 10.44 (n = 3)	91.67 ± 16.07 (n = 3)
H_2O_2 + 0.4mM Zn	18.5 ± 5.4 (n = 4)	72 ± 20.66 (n = 3)	54 ± 3.61 (n = 3)	63.67 ± 16.74 (n = 3)
H_2O_2 + 0.8mM Zn	11 ± 4.6 (n = 4)	39 ± 15.1 (n = 3)	24.67 ± 14.47 (n = 3)	58.67 ± 16.77 (n = 3)

5.2.2 Investigating the cellular redox state of zinc and ROS stressed *Pseudomonas syringae*

In order to study the real-time intracellular redox state of *Pseudomonas syringae* stressed with ROS and zinc, the biosensor roGFP2 was used. Here only the results for *P. syringae* pv. syringae SnB11 are presented but the same trends were also observed for *P. syringae* pv. maculicola. Firstly, the effect of just hydrogen peroxide was tested as it is a known oxidising agent. In the following plots, the first ~30 minutes show the baseline oxidative state of the bacteria and the arrow indicates the time at which the ROS was applied. Almost immediate oxidation was observed when concentrations above 50 mM were used, indicated by a sharp peak in Figure 72. This rapid reaction may indicate that there is sufficient endogenous glutaredoxin present to catalyse the equilibrium between roGFP2 and the GSH : GSSH redox couple (224,230). A few minute delay was observed with the lowest concentration tested, 5 mM. As expected, the water control did not cause oxidation.

It took longer for the bacteria to recover from oxidative stress at increasing concentrations, indicated by the peak width. While the 5 mM-stressed bacteria recovered to their baseline oxidative state in approximately 10 minutes, it took the 100 mM-stressed bacteria approximately 30 minutes. At 150 and 500 mM, B11 does not recover from oxidative stress, indicated by the horizontal line. This makes sense, as in Figure 68B it was established that B11 would survive in concentrations of hydrogen peroxide up to 125 mM. We can therefore assume that these bacteria are likely dead.

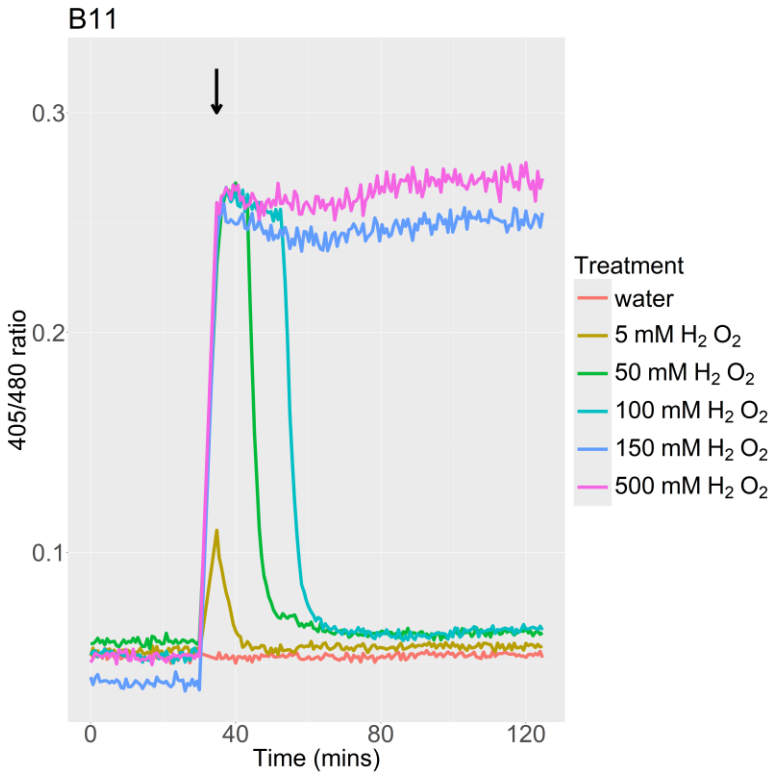


Figure 72: Real-time analysis of the intracellular redox state of roGFP-transformed *P. syringae* pv. syringae B11 stressed with hydrogen peroxide. Arrow indicates the time of hydrogen peroxide addition. A sharp peak above the baseline indicates oxidation. Plot shown is a representative example.

The next experiment was to test the effect of adding the sublethal concentrations of zinc used in the previous section in combination with hydrogen peroxide. A representative result of this can be seen in Figure 73, A and B showing the respective addition of 0.4- and 0.8-mM zinc. Whereas previously, when just stressed with ROS, the bacteria could recover up to the previously established tolerance concentration. However, in combination with zinc, the bacteria become oxidised and remain in that state for the duration of the experiment, regardless of the concentration of hydrogen peroxide. At this stage it is unknown whether these bacteria or alive or dead. To determine this, and any degree of heterogeneity, live/dead staining combined with flow cytometry could be used.

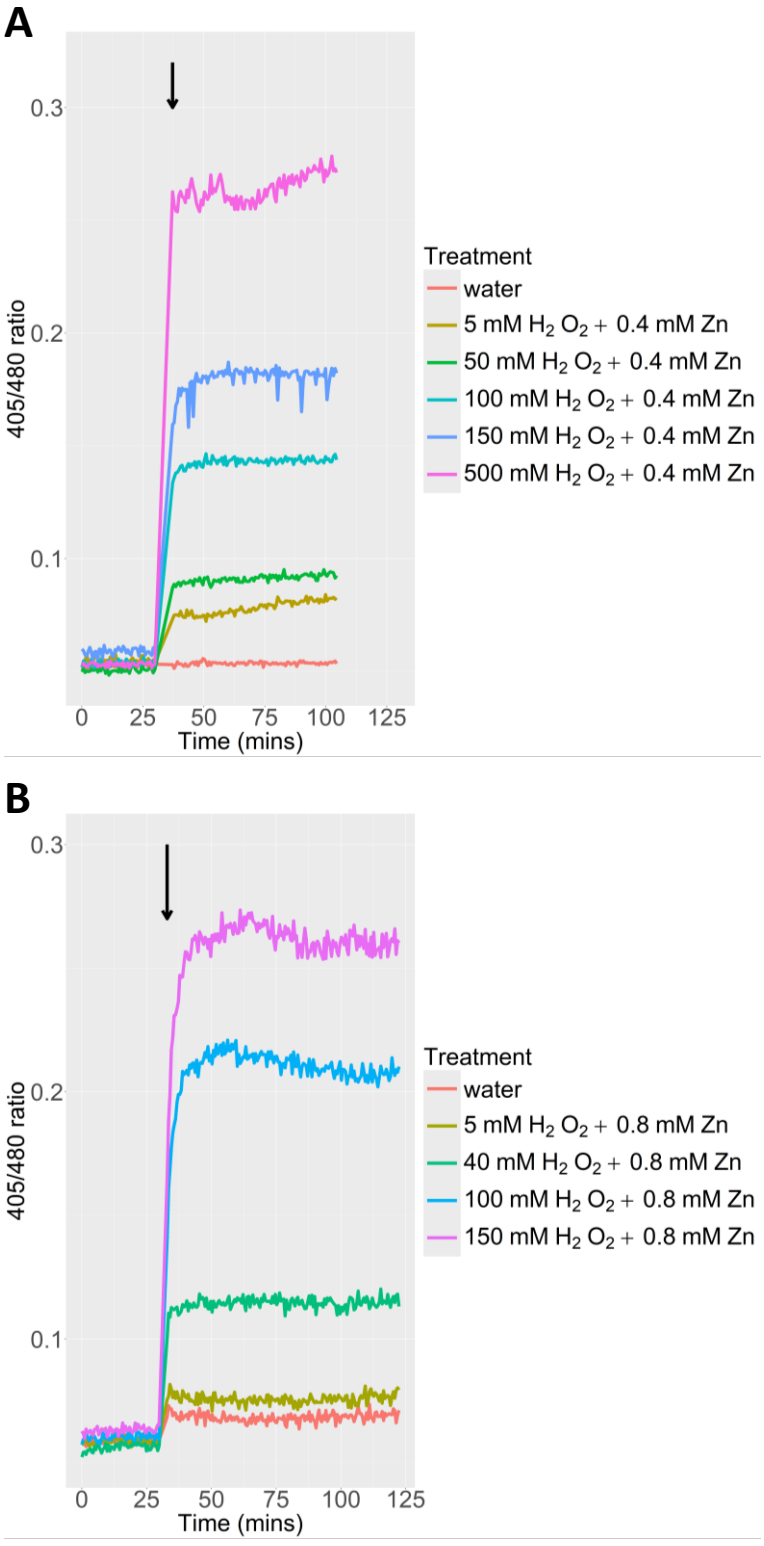


Figure 73: Real-time analysis of the intracellular redox state of roGFP-transformed *P. syringae* pv. syringae B11 stressed with hydrogen peroxide in combination with 0.4 mM zinc (A) and hydrogen peroxide in combination with 0.8 mM zinc (B). Arrow indicates the time of hydrogen peroxide addition. A sharp peak above the baseline indicates oxidation. Plots shown are representative examples.

To understand if the results observed in Figure 73 were specific to zinc or occurred with other metals, the experiment was repeated using nickel. B11 exhibits a similar tolerance to nickel as to zinc so the same 0.4- and 0.8-mM concentrations were used. As seen in Figure 74, the presence of sub-lethal nickel does not cause the sustained oxidation that was observed with zinc. However, the bacteria do take slightly longer to recover from oxidative stress than when just stressed with hydrogen peroxide. Additionally, and particularly when 0.8 mM nickel was used, the bacteria do not return to their baseline redox state when concentrations of 100 mM hydrogen peroxide and above were used.

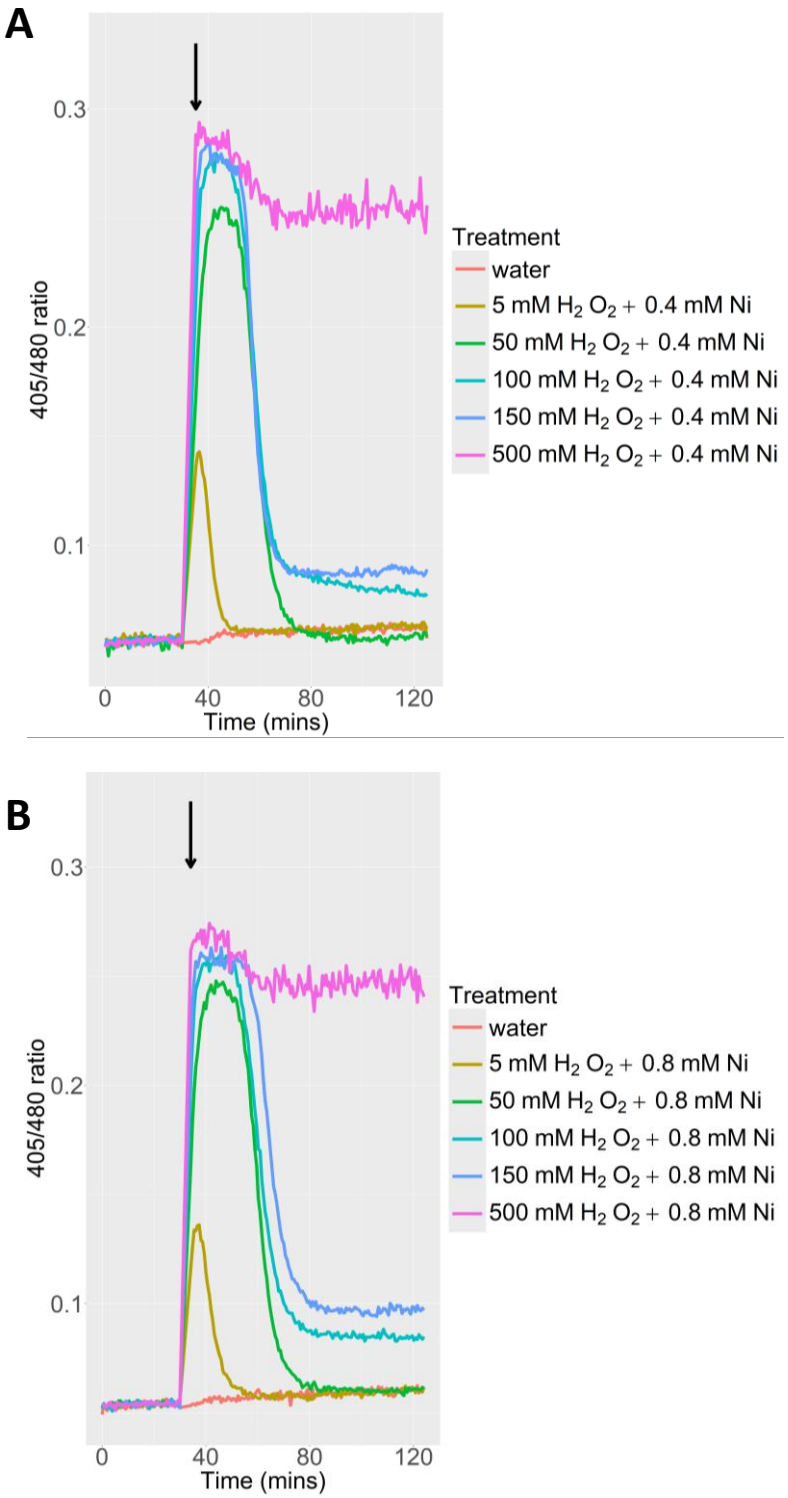


Figure 74: Real-time analysis of the intracellular redox state of roGFP-transformed *P. syringae* pv. syringae B11 stressed with hydrogen peroxide in combination with 0.4 mM nickel sulfate (A) and hydrogen peroxide in combination with 0.8 mM nickel sulfate (B). Arrow indicates the time of hydrogen peroxide addition. A sharp peak above the baseline indicates oxidation. Plots shown are representative examples.

5.2.3 In vitro Raman microspectroscopy of zinc stressed *Pseudomonas syringae*

As discussed in section 5.1, Raman spectroscopy is an analytical technique that can provide a “phenotypic profile” of individual bacterium (239). A representative Raman spectrum of untreated *Pseudomonas syringae* pv. syringae SnB11 can be seen in Figure 75. The region approximately covering 500 – 1800 cm^{-1} is often referred to as the “fingerprint” region and includes signals from biomolecules such as amino acids, nucleic acids, and lipids. The region spanning ~1800 – 2700 cm^{-1} is referred to as the “silent region”, where very few biomolecular signals occur. Finally, the typically largest peak in the Raman spectrum covering ~2800 – 3100 cm^{-1} is associated with stretching vibrations of C-H groups (241). The smaller CH peak at the higher wavenumber is likely associated with unsaturated or aromatic systems.

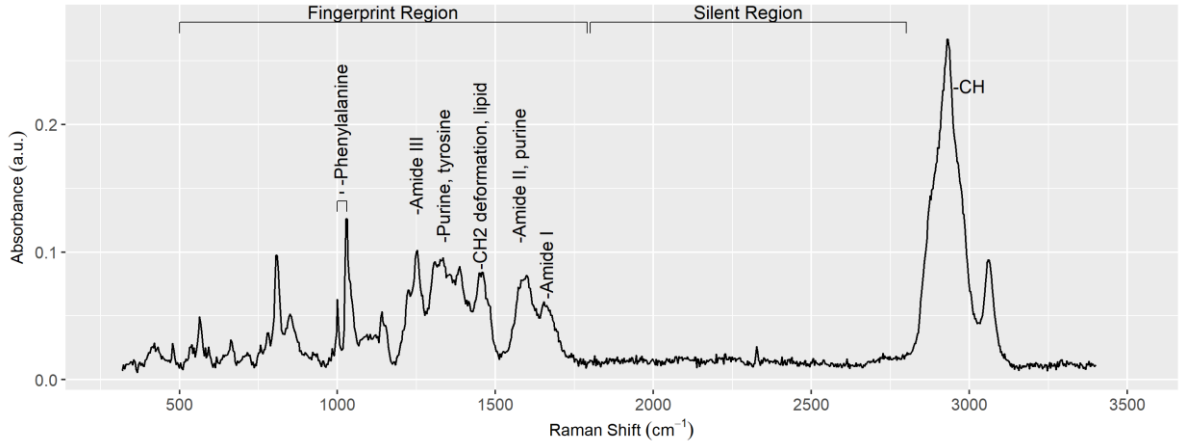


Figure 75: Mean Raman spectrum of *Pseudomonas syringae* pv. syringae SnB11 averaged from 18 cells. Cells grown in LB medium and fixed with 4% formaldehyde in PBS. Not all peaks are assigned. A.U. = arbitrary units.

The aim of this initial section of Raman work was to assess whether zinc stress induces a characteristic biomarker in the fingerprint region which could potentially then provide information on the mechanism of zinc toxicity or the effect of zinc on hydrogen peroxide tolerance. A zero-zinc control, a concentration of zinc causing sub-lethal inhibition

(0.8 mM), and a lethal dose (2 mM) of zinc were chosen for this work. The rationale behind this was to see if there was a characteristic difference in the Raman spectrum between untreated, zinc stressed and completely inhibited bacteria. Furthermore, bacteria were isolated at four time points over six hours to monitor any changes that become apparent due to zinc stress. The results of this can be seen in Figure 76, the title label “hydrogenated” refers to the fact that the bacteria were grown in normal, as opposed to deuterated, media.

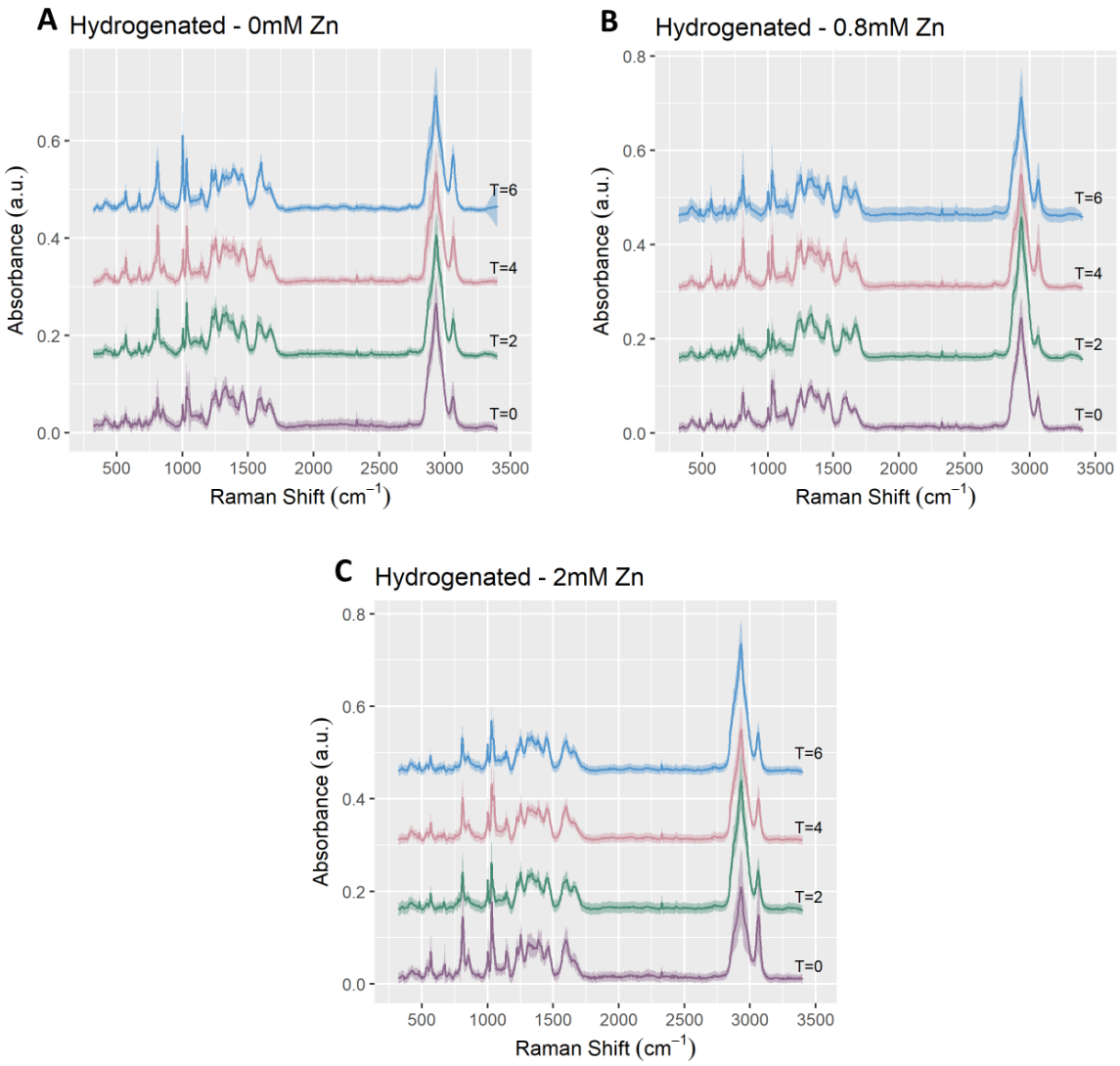


Figure 76: Zinc stress does not induce a characteristic response in the Raman spectrum of *Pseudomonas syringae* pv. syringae SnB11. Raman spectra from cells stressed with no zinc, with sub-lethal concentrations of zinc, or with lethal concentrations of zinc over 4 time points shown with offset baselines (A-C). Mean spectra are plotted with standard deviation shown as the shaded region around the line. 63, 58, 42, 44 cells averaged for time points 0, 2, 4, and 6 hour, respectively (A). 43, 88, 68, 91 cells averaged for time points 0, 2, 4, and 6 hour, respectively (B). 34, 109, 104, 73 cells averaged for time points 0, 2, 4, and 6 hour, respectively (C). A.U. = arbitrary units.

Upon visual inspection, there are not any significant changes in the spectra of zinc-stressed bacteria compared to the control at any time point. However, because changes may be subtle in the complex spectra, principal component analysis (PCA) can be used identify whether there is variance in the data set. Ideally, though, the first ~4 principal components should account for about 80% of the variation in order to perform PCA without losing information (242). For this, Scree plots can be used which describe the percentage of variance in each dimension, or component. Scree plots separating the data by time point and thus comparing the effect of zinc concentration on the Raman spectra can be seen in Figure 77. As can be seen, the first four dimensions do not describe >80% of the variance.

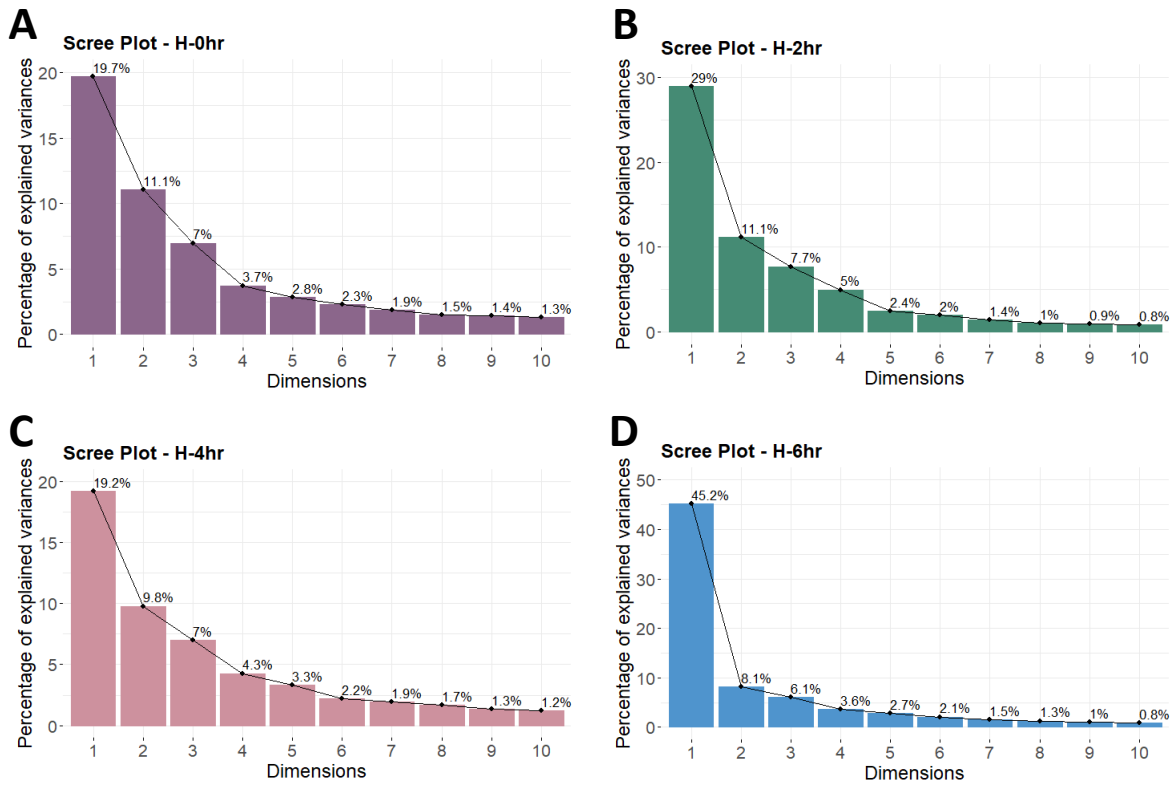


Figure 77: Scree plots outlining the proportion of the variance that can be described by each principal component. For clarity, only the first 10 principal components are shown. Scree plot showing the variance in the Raman dataset containing all zinc concentrations at the 0-hour time point (A). Scree plot showing the variance in the Raman dataset containing all zinc concentrations at the 2-hour time point (B). Scree plot showing the variance in the Raman dataset containing all zinc concentrations at the 4-hour time point (C). Scree plot showing the variance in the Raman dataset containing all zinc concentrations at the 6-hour time point (D).

The resulting PCA plots can be seen in Figure 78 and indicate that there are not significant differences in the Raman spectra due to zinc stress. The first two components which are plotted here only account for between 29 and 53% of the variance.

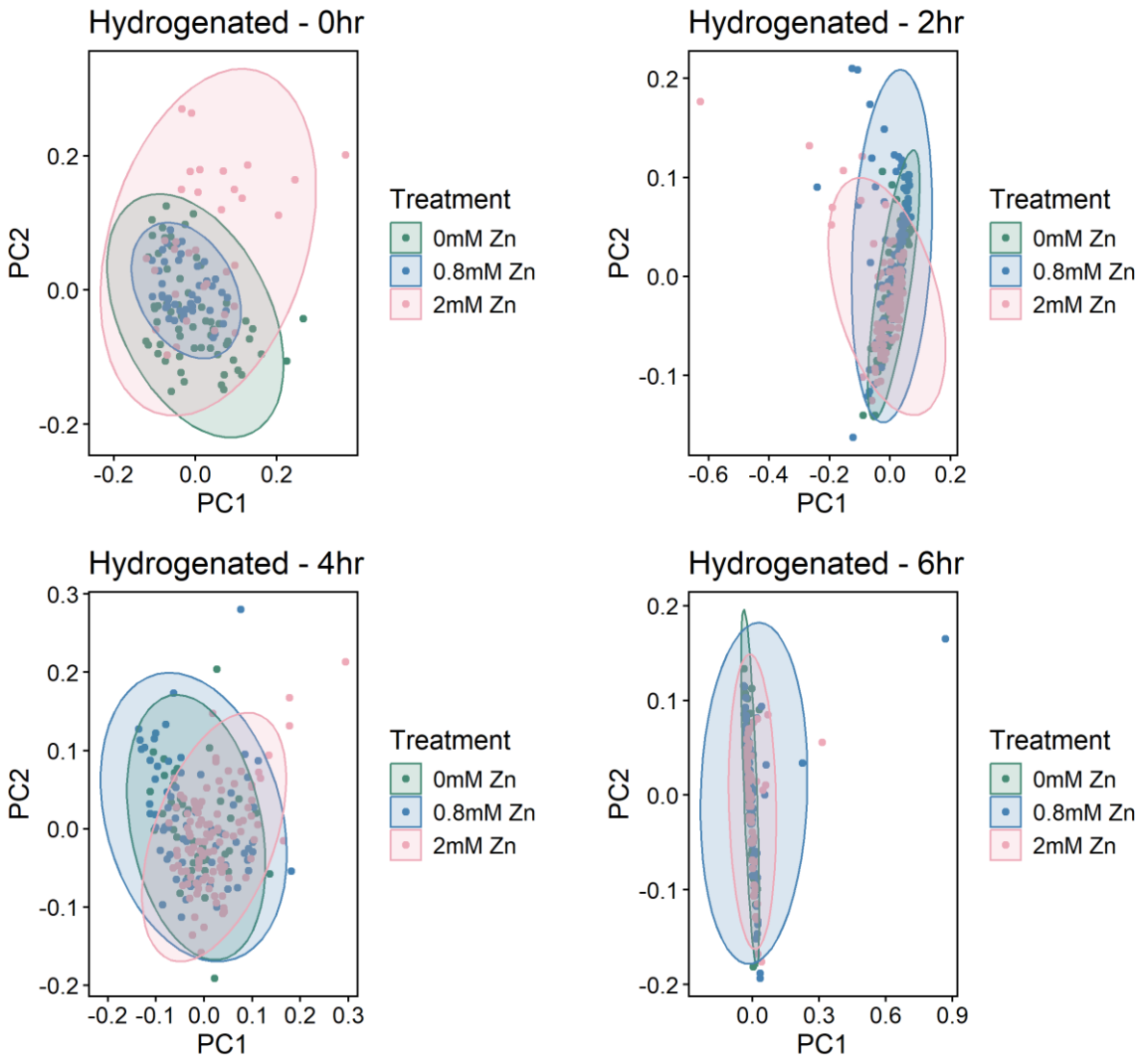


Figure 78: The Raman spectra of *Pseudomonas syringae* pv. syringae SnB11 are not significantly different under zinc stress. Principal component analysis score plots of the first two principal components for 0, 2, 4, and 6-hour time points (A-D respectively). Each dot represents an individual bacterium. The shaded regions represent a 95% confidence interval.

To determine whether increasing time had a greater effect on the Raman spectra, the above process was repeated but this time separating the data by zinc concentration. The resulting Scree plots and PCA can be seen in Figures 79 and 80, respectively. There is not a significant difference in the PCA but, again, the first two components only account for between 28.6 and 49.4% of the variance.

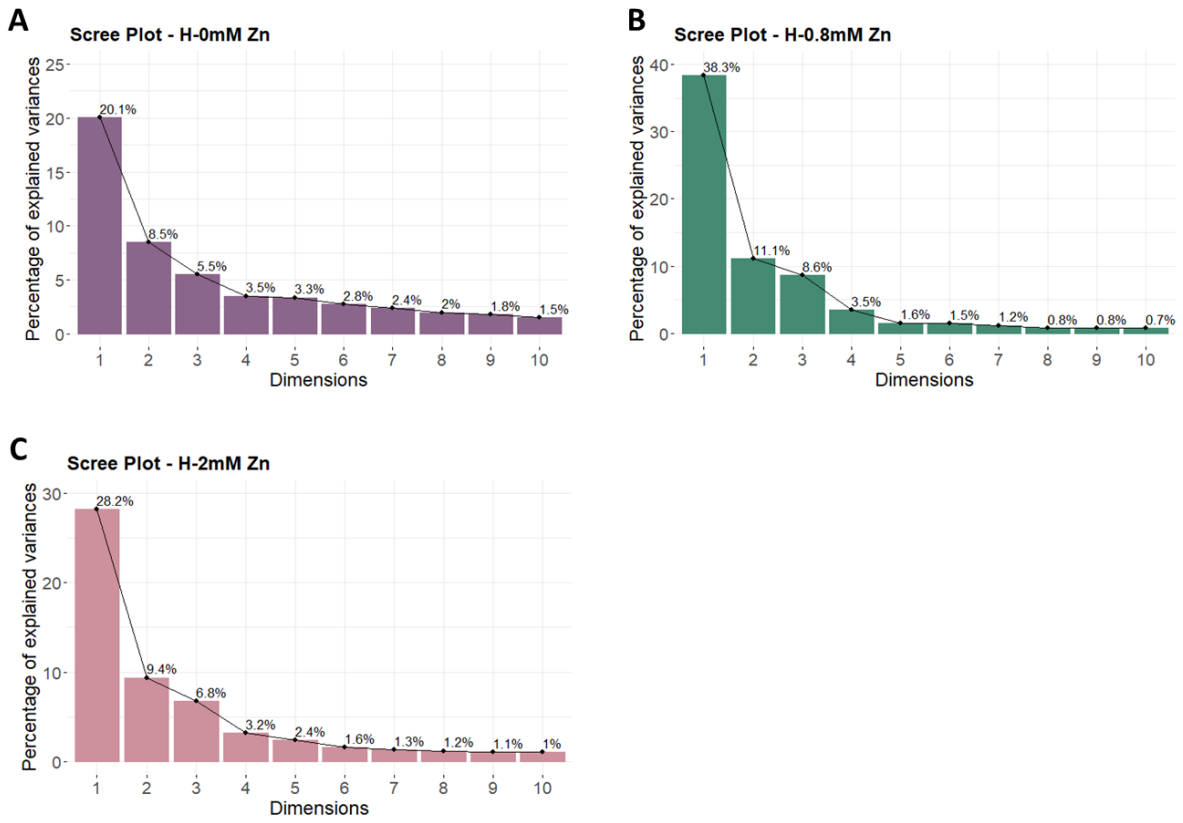


Figure 79: Scree plots outlining the proportion of the variance that can be described by each principal component. For clarity, only the first 10 principal components are shown. Scree plot showing the variance in the Raman dataset containing 0mM zinc at all time points (A). Scree plot showing the variance in the Raman dataset containing 0.8mM zinc at all time points (B). Scree plot showing the variance in the Raman dataset containing 2mM zinc at all time points (C).

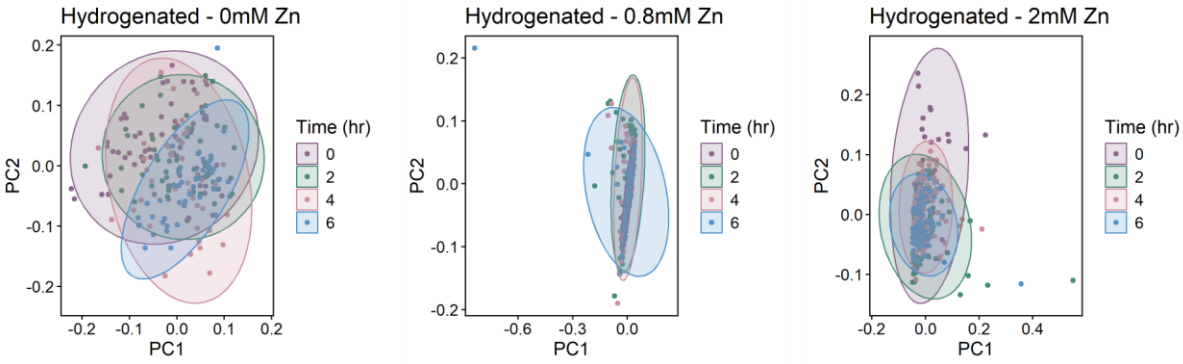


Figure 80: The Raman spectra of *Pseudomonas syringae* pv. syringae SnB11 are not significantly different under zinc stress. Principal component analysis score plots of the first two principal components for 0, 0.8, and 2mM zinc (A-C respectively). Each dot represents an individual bacterium. The shaded regions represent a 95% confidence interval.

The region of the Raman spectrum spanning ~1800 – 2700 cm^{-1} is typically referred to as the "silent region" due to the lack of biomolecular signals that occur (241). However, usefully, the carbon-deuterium bond does appear in this region; meaning that stable isotope labelling with deuterium can be used to monitor metabolic activity through either labelling or unlabelling. This is because in actively growing cells, the deuterium can be replaced by hydrogen (or vice versa) depending on the media used (239). The relative positions of CD and CH peaks are outlined in Figure 81.

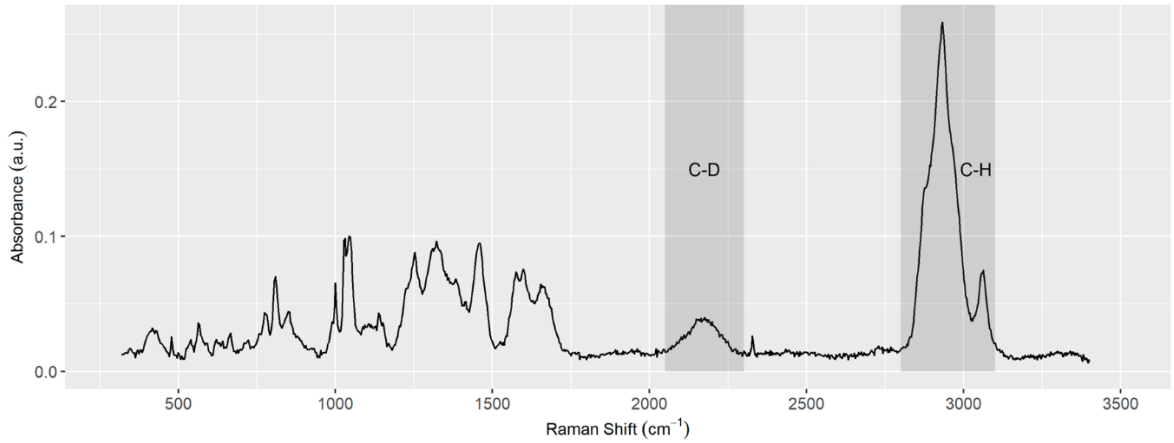


Figure 81: Mean Raman spectrum of *Pseudomonas syringae* pv. syringae SnB11 averaged from 48 cells. Cells grown in LB medium with 50% D_2O and fixed with 4% formaldehyde in PBS. Highlighted regions indicate the positions of the C-D peak (2050 - 2300 cm^{-1}) and C-H peaks (2800 - 3100 cm^{-1}). A.U. = arbitrary units.

Here, deuterium unlabelling was used to identify the effect of increasing zinc concentration on the metabolic activity of B11. Thus, it was expected that in the non-stressed control that the deuterium peak would disappear over time, as metabolically active cells could replace the deuterium with hydrogen. This was indeed what was observed, as seen in Figure 82A. Likewise in cells stressed with 0.8 mM zinc, the deuterium peak is also shown to disappear by the 4-hour time point, shown in Figure 82B. However, at 2 mM zinc, the deuterium peak remains at the same intensity. As shown in Figure 81C, this indicates that the bacteria are no longer metabolically active. In Figure 82, the title label “deuterated” refers to the fact that the bacteria were initially grown in deuterated media.

The ratio of C-D/(C-H + C-D) has previously been used to quantify the dynamics of isotope unlabelling (154,239). This can be seen in Figure 84. At 0- and 0.8-mM zinc, the ratio of C-D/(C-H + C-D) decreases over time. However, the ratio remains stable at 2 mM zinc.

An observation from Figures 82 and 83 is that the deuterium peak at time 0 in the untreated control is of lower intensity than the corresponding 0.8 mM peak. This is likely due to the fact that unlabelling was already occurring prior to untreated bacteria being fixed with paraformaldehyde as these cells were metabolising at a faster rate.

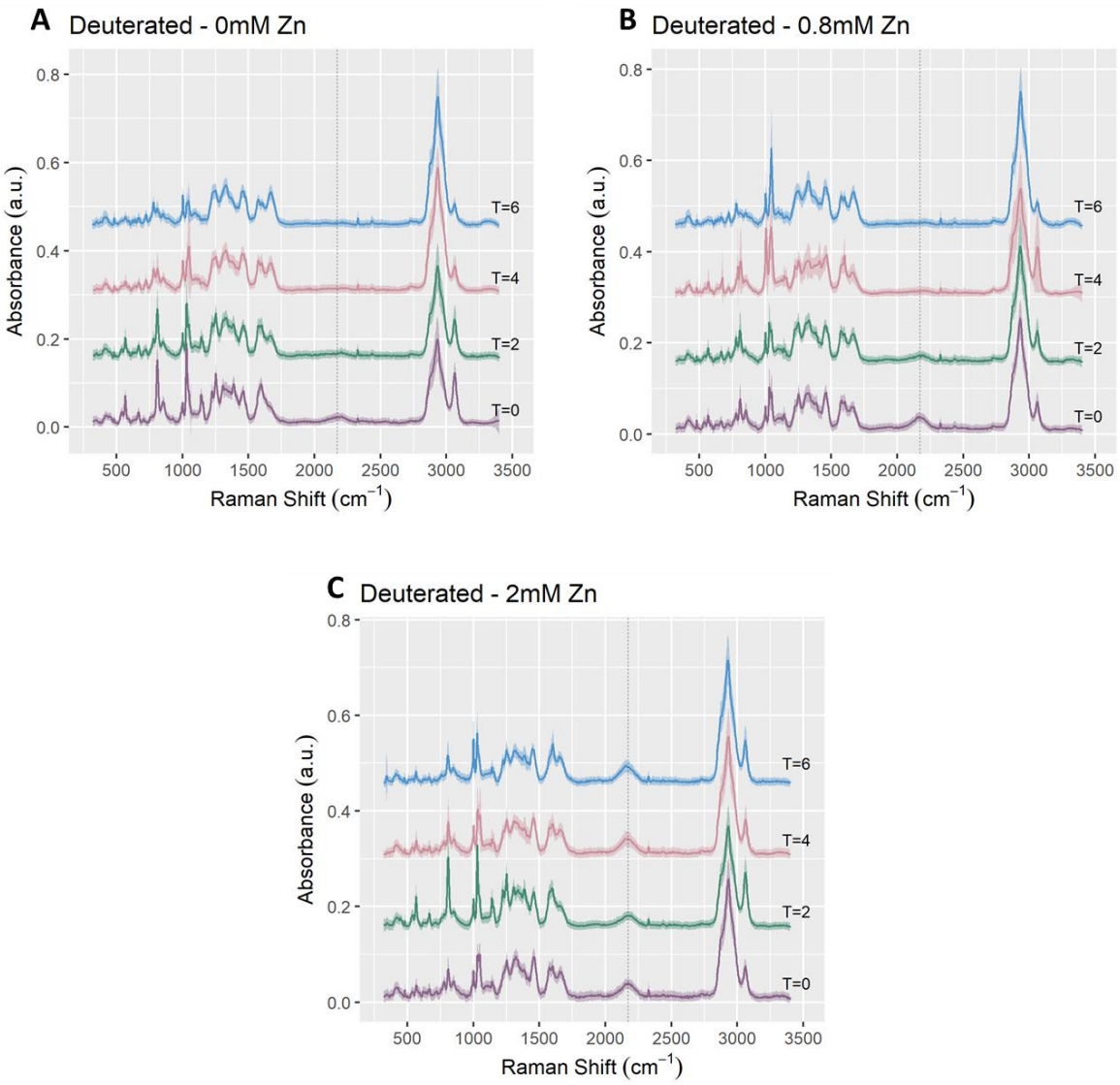


Figure 82: Deuterium can be replaced with hydrogen in metabolically active *Pseudomonas syringae* pv. syringae SnB11. Raman spectra from cells stressed with no zinc, with sub-lethal concentrations of zinc, or with lethal concentrations of zinc over 4 time points shown with offset baselines (A-C). Mean spectra are plotted with standard deviation shown as the shaded region around the line. 80, 70, 90, 101 cells averaged for time points 0, 2, 4, and 6 hour, respectively (A). 100, 67, 75, 82 cells averaged for time points 0, 2, 4, and 6 hour, respectively (B). 48, 102, 83, 57 cells averaged for time points 0, 2, 4, and 6 hour, respectively (C). Dotted line indicates the position of the C-D peak. A.U. = arbitrary units.

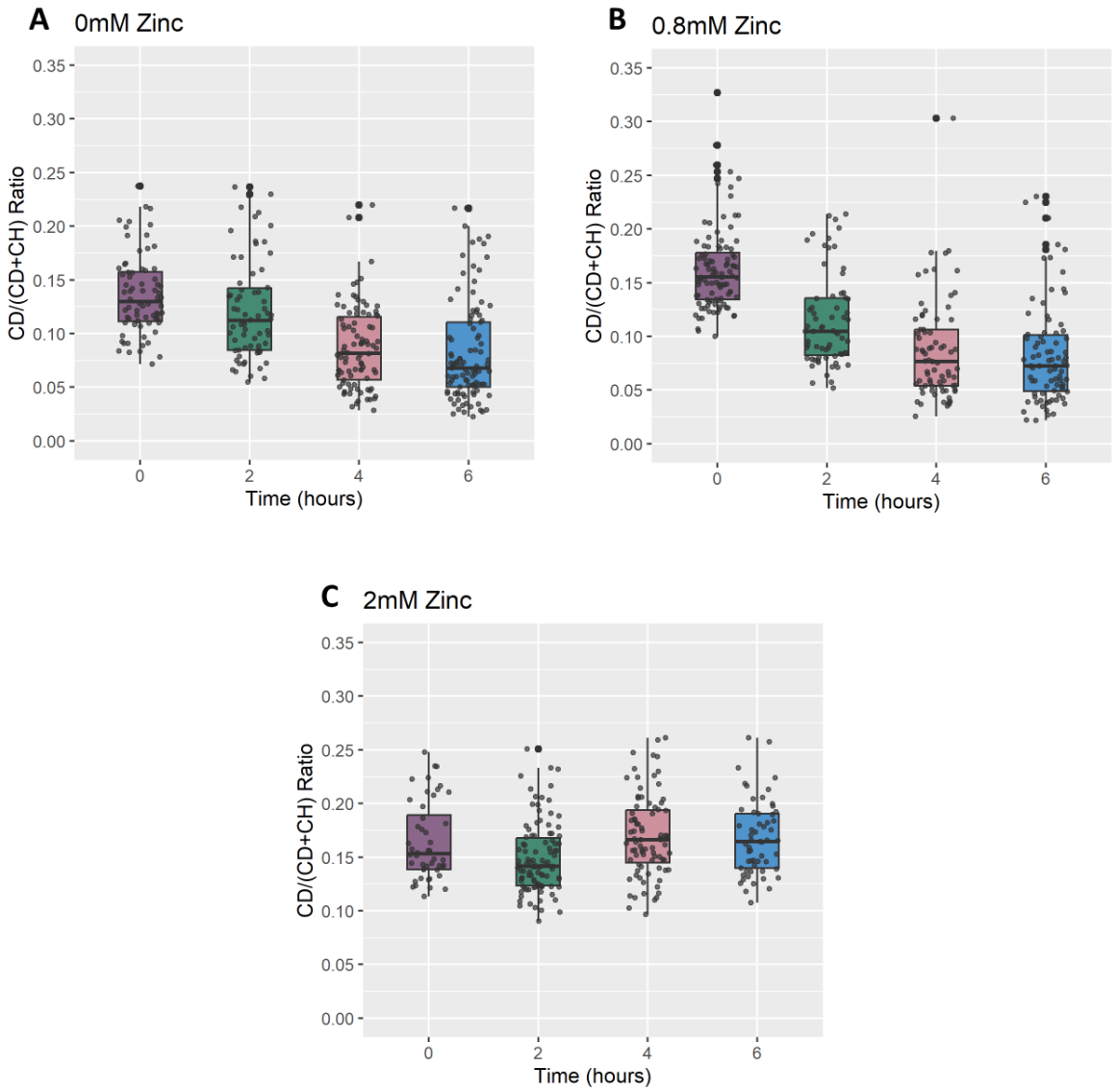


Figure 83: Stable isotope labelling decreases over time in metabolically active cells but not in those inhibited by zinc. Quantification of deuterium un-labelling indicated by the reduction in CD/(CD+CH) peak ratio over time for cells stressed with 0, 0.8, and 2mM zinc (A-C respectively). Each dot represents a single bacterium. Box plots display the median, interquartile range, and minimum/maximum values. Outliers are presented outside of the whiskers.

5.3 Discussion

The aim of this chapter was to explore routes of toxicity in *Pseudomonas* syringae and whether zinc and reactive oxygen species (ROS) may act synergistically to limit pathogen growth. Growth curves were performed to understand the direct effect of increasing zinc and ROS concentrations on the viability of *P. syringae.* The intracellular redox state of *P. syringae* exposed to zinc and ROS was studied using the biosensor roGFP. Finally, Raman spectroscopy was used to examine the metabolic activity of zinc-stressed bacteria, and whether their "chemical fingerprint" undergoes any characteristic changes.

All assays (with the exception of roGFP) were performed using LB media as other media tested formed precipitates upon the addition of zinc, which would skew data depending on optical density measurements. It should thus be considered that, as LB is favourable to pathogen growth, the tolerances reported are over estimations. However, this should not affect the trends observed.

Pseudomonas syringae pv syringae SnB11 was far more tolerant to ROS than the other strain tested in this study, *Pseudomonas syringae* pv maculicola. This is perhaps a consequence of the former being originally isolated from *Noccaea caerulescens* plants growing at a former mining site in Snowdonia. As discussed in section 1.5 (Figure 8) constitutively higher levels of ROS were identified in *N. caerulescens* compared to the non-accumulating *A. thaliana.* However, the zinc tolerance of the two strains was similar. With both strains, zinc tolerance decreased incrementally with increasing concentration of the metal. Conversely, with hydrogen peroxide, there was complete inhibition when a threshold value was met. This is likely due to the latter being a transient stress and the former not. Bacteria that survive the initial stress by hydrogen peroxide can go on to establish themselves as the ROS is labile and would degrade over time. Introducing sublethal concentrations of zinc, 0.4- or 0.8 mM, increased the sensitivity of *P. syringae* to hydrogen

peroxide; lowering the maximum growth and increasing the lag phase – indicating a longer time was required for the bacteria to adjust to their environment.

It has previously been established that pre-exposing bacteria to sublethal levels of hydrogen peroxide had a priming effect where these bacteria were able to detoxify the ROS faster and survive higher subsequent concentrations than naïve bacteria (229,243). This has been shown to be due to the upregulation of many of the genes under the control of the OxyR regulon and the priming response lasts multiple generations (243). Priming with hydrogen peroxide and subsequently stressing B11 with 0.8 mM zinc did seem to increase its tolerance to ROS. This priming effect was not observed with the lower concentration of zinc tested, however. A decrease in tolerance was observed when hydrogen peroxide, as a sole stressor, was introduced to the bacteria an hour after experiment initiation. This was not observed when zinc was added at +1hr as the sole stressor.

As opposed to a protective priming effect, a slight reduction in tolerance was observed when bacteria was primed with zinc prior to stress with hydrogen peroxide. This observation may indicate that zinc affects the bacteria's ability to scavenge ROS, for example by replacing the native metal cofactor in catalase or peroxidase enzymes. As a result, the subsequent addition of hydrogen peroxide is not broken down as efficiently. Zinc forms very strong complexes, second only to copper, irrespective of the ligand (244). As discussed in section 5.1, many ROS scavenging enzymes are metalloenzymes, relying on metal ions as cofactors for their catalytic activity (222,223). The strong binding efficiency effectively means zinc can outcompete the native cofactor and thus lead to cofactor competition or mismetallation. This may result in the inactivation or reduced efficiency of enzymes. Mismetallation by zinc has been observed in *Escherichia coli,* causing a 95% drop in efficiency of the iron-metalloenzyme ribulose-3-phosphate 5-epimerase (245). Additionally, zinc acetate but not cadmium acetate was found to reduce efficiency of the ROS scavenging enzyme catalase, highlighting zinc's ability to outcompete native cofactors (246). Conversely, relatively low micromolar concentrations of zinc were also found

to slightly increase catalase activity (247). This uncertainty would therefore prompt a future experiment looking at ROS scavenging enzyme activity under the concentrations of zinc used in and relevant to this work. Additionally, knockout mutants lacking enzymes such as catalases could be used to determine whether the level of synergy is reduced.

Although the mechanism is unclear, zinc has also been implicated in the inactivation of glutathione reductase, required to maintain cellular levels of the antioxidant glutathione by catalysing the reduction of GSSG back to GSH (248–250). Though not explored in the plant context, it is thus possible that the observed synergy between ROS and zinc could potentially result from, or be further influenced by, the disruption of glutathione metabolism.

A significant lag phase such that bacteria began to grow after the 10-hour time point, as seen in Figure 70C, should be considered when analysing the IC_{50} values reported in Table 8. An additional time point, for example 20 hours, could also be used to generate dose-response plots to obtain a clearer picture of any trends.

Further supporting the idea that zinc imparts toxicity by limiting the bacteria's ability to scavenge ROS, was the observation that zinc caused sustained oxidation of the redox biosensor roGFP. In the time measured, *P. syringae* did not recover from oxidative stress when any concentration of hydrogen peroxide was applied in combination with zinc. When nickel was applied, however, the bacteria could recover but this process took longer than when just ROS was applied. Nickel may therefore have an additive effect in combination with ROS and has previously been speculated to catalyse disulfide bond formation (229).

Raman spectroscopy has previously been used to determine biomarkers of traumatic brain injury and has identified changes in the nucleic acid peaks as a result of heat stress in bacteria, for example (251,252). However, no significant changes in the Raman spectrum of B11 over time or as a result of increasing zinc concentration were observed. However, longer time periods could be measured. Additionally, other methods to reduce the dimensionality of the data to try and identify differences such as t-Distributed Stochastic Neighbour Embedding (t-SNE) could be tried. Alternatively, recent advancements in

machine learning have facilitated the development of a convolutional neural network (CNN) which has been shown to outperform PCA in data classification (253).

Stable isotope labelling with deuterium showed that B11 remains metabolically active when stressed with 0.8 mM zinc, the concentration that was previously observed to cause growth inhibition. However, at 2 mM zinc the deuterium peak did not disappear, indicating that these cells are no longer metabolically active. This also indicates that Raman spectroscopy may be suitable to assess the metabolic activity of bacteria *in planta*. Previous unpublished work has successfully isolated and used Raman to measure the relative deuteration of *P. syringae* cells after infection in *Nicotiana benthamiana* plants (154). This could allow us to gain direct insights into how the previously described high zinc and ROS environment of *N. caerulescens* affects bacterial viability.

In this chapter, a synergistic effect of zinc and ROS was observed using in vitro methods. Applying zinc increased the sensitivity of *P. syringae* to ROS. Additionally, zinc was found to cause sustained oxidation of B11 when applied with hydrogen peroxide which could indicate a route of toxicity. Finally, Raman spectroscopy was used to show that increasing zinc affects the metabolic activity of *P. syringae*. A clear next step from this chapter is to study the direct effect of relevant concentrations of zinc on ROS scavenging enzymes through enzyme activity assays. Additionally, using a technique such as live-dead staining with flow cytometry would enable an understanding of whether the zinc and ROS stressed bacteria are alive but inhibited or dead.

We have seen in Chapter 3 that, upon infection, zinc is mobilised from intracellular, vacuolar storage to the extracellular space where *Pseudomonas syringae* inhabits. Additionally, as discussed in section 1.5, *N. caerulescens* exhibits an altered ROS response to pathogen invasion, possessing only the nicotinamide adenine dinucleotide phosphate (NADPH) oxidase-dependent ROS burst. Importantly, the NADPH-oxidase enzyme is located in the plant cell plasma membrane and generates apoplastic superoxide which, through the action of superoxide dismutase (SOD), is rapidly broken down to hydrogen

peroxide (254,255). Likewise, it has previously been established that there is constitutively higher levels of ROS present in aerial tissue of *N. caerulescens* with increasing zinc treatment (87). All these factors mean that apoplastic-dwelling *P. syringae* are faced with a dual zinc/ROS challenge. We propose a synergistic mechanism of toxicity where increasing zinc causes mismetallation of bacterial ROS scavenging enzymes and/or inhibits glutathione metabolism leading to prolonged oxidative stress. Even in plants without apparent constitutively high levels of ROS, the joint effect of zinc with ROS released through the oxidative burst may still provide this defensive effect.

Chapter 6: General discussion and conclusions

The overarching aim of this thesis has been to determine the mechanisms underlying the previously observed defensive effects of accumulated zinc in the metal hyperaccumulator plant *Noccaea caerulescens* against the common bacterial pathogen *Pseudomonas syringae* (6,25). To do this, synchrotron-based X-ray spectroscopic techniques were used in which sample preparation and mounting pipelines were developed. These methods enabled the study of frozen-hydrated tissue, the preparation of which is notoriously difficult due to the high-water content which could cause the introduction of artefacts or lead to metal redistribution if not done properly (114). These methods could be applied to other biological systems, furthering the imaging capabilities at Diamond Light Source.

In Chapter 3, the development of a method to prepare transverse sections of leaf tissue for the study of 2D metal distribution (XRF) and zinc speciation (XANES) was discussed. In agreement with previous reports, zinc distribution in untreated tissue was found to be highly localised to the epidermis, theorised to be a strategy employed by hyperaccumulators to avoid zinc toxicity affecting important metabolic processes. However, the epidermal distribution itself exhibited heterogeneity depending on the concentration of zinc the plant was grown on. In plants growing on the highest zinc concentration tested, 300 μM, there was a fairly uniform distribution, with zinc present in the majority of epidermal vacuoles. The plants grown on the lowest concentration of zinc, 10 μM, however did not follow this pattern. Instead, some epidermal cells were devoid of the metal while others had a relatively high concentration, with an apparent preference for larger cells.

The observation of *N. caerulescens* seemingly altering the epidermal distribution of zinc when access to the metal is limited could perhaps be a defensive strategy. Having areas of higher concentration of zinc may be more beneficial to the plant in defence against a haustoria-forming pathogen where cells are penetrated. This could be tested by repeating

the experiments discussed in Chapter 3 with a pathogen such as *Erysiphe cruciferarum* (256). Additionally, this observed heterogeneity may be true of other plant defences which could support the trade-off in defences discussed in section 1.5. The distribution of vacuolar antimicrobial compounds, for example, could be studied using an imaging metabolomics approach such as matrix-assisted laser desorption ionisation mass spectrometry imaging (MALDI-MSI). This approach has previously been applied to study the spatial distribution of phytoalexins during the infection of grapevine leaves with the fungal pathogen *Botrytis cinerea* (257,258).

As zinc distribution in untreated tissue was highly localised to the epidermal vacuoles, the question still remained regarding how the metal provides a defence against the apoplastic space-inhabiting pathogen. In samples infected with *P. syringae* pv. maculicola or *P. syringae* pv. syringae SnB11, zinc mobilisation from the epidermal vacuoles to the apoplastic space was observed. This is a key finding from this work, as the apoplastic space is the known site of inhabitation for *P. syringae*. Further evidence for this zinc release to the apoplast was confirmed using complementary ICP-MS analyses, comparing the concentrations of zinc in the apoplast between untreated, mock inoculated, and samples infected with *P. syringae*. At the latest time point tested, 5DPI, zinc was seen to increase in concentration in the infected samples but not the mock inoculated samples. This observation, alongside XRF data, confirmed that the zinc release was not due to the mechanical effect of the inoculation, but rather was a result of the infection.

Additionally, while the observation of zinc release into the apoplastic space provides a mechanism for how *N. caerulescens* defends itself against bacterial disease by *P. syringae*, it is currently unknown whether this is a plant-mediated immune response or a consequence of the bacterial infection itself, for example, due to effectors and/or phytotoxins or simply as a result of necrosis. ICP-MS data indicates that zinc release occurs between 1 and 5DPI which perhaps supports the latter as plant immune responses typically occur earlier. However, finer time points of both XRF imaging and ICP-MS are needed to fully

understand the temporal dynamics of the zinc release. Likewise, XRF study of zinc distribution after the application of elicitors such as flg22 or chitin would enable an understanding of whether the zinc-release phenomenon is an immune response. To understand whether this observation is a result of effectors or toxins produced by the bacteria, these experiments could be repeated with bacterial mutants.

As the zinc release was observed with both of the *P. syringae* strains tested, Psm and B11, a good starting point for this would be focussing on effectors present in the conserved effector locus (CEL) as discussed in section 1.6 and seen in Table 2. AvrE seems to be a good potential candidate for this as it functions as a channel in the plant cell plasma membrane, allowing water and solutes, potentially including zinc complexes, to pass through into the apoplast (99). Preparing and testing knockout mutants could implicate AvrE if the zinc mobilisation does not occur. Likewise, a mutant strain only capable of producing AvrE could be prepared and tested to see if zinc mobilisation does occur. To determine whether the zinc mobilisation is a plant response, a single-cell transcriptomics approach could be used on epidermal cells. An upregulation of zinc transporters such as HMA4 could support this (187,259).

Future work leading from the observations in Chapter 3 could include correlative imaging with neighbouring sections of infected leaf tissue being imaged with 2D-XRF and cryo-fluorescence microscopy. During this project, yellow fluorescent protein (YFP) tagged strains of B11 and Psm were prepared. Correlative imaging at different time points using these tagged strains, in conjunction with cell viability assays, could enable an in planta view of the consequence of zinc release on the bacteria by studying the relative localisation of zinc and the bacteria. Additionally, work to date has focussed on imaging the zinc distribution near to the infection site. To determine whether this is a localised response, areas further away from the infection site could be imaged. Spray or dip inoculations could also be performed to assess a more natural infection route.

Chapter 4 used 3D-XRF tomography to confirm the observations discussed in Chapter 3. However, the sample preparation and mounting procedures were far simplified in comparison to that required for 2D imaging of transverse sections of tissue. This is a significant benefit as it would allow untrained users on beamlines to obtain data more easily, especially useful if samples are particularly precious. Additionally, while it was not attempted in this work, the simplified sample preparation may enable imaging of samples with more significant disease symptoms that were difficult to prepare for 2D sectioning, for example infected extra low and low zinc treated *N. caerulescens*. Although the distribution for zinc is comparable between the 2D and 3D imaging techniques, a slight drawback with the latter is the inability to measure lighter elements (without correction) due to self-absorption artefacts. Future work may benefit from imaging at higher resolutions to more clearly observe the zinc mobilisation into the apoplastic space. Likewise, a focus on generating 3D images of larger sections by imaging a greater number of slices would be beneficial to obtain a clearer picture of zinc distribution.

In Chapter 3, the observation of bacterial infection with *P.* syringae initiating flooding of the apoplast with zinc forces the interaction between the metal and the bacteria. Additionally, it has previously been established that there are high levels of ROS in *N. caerulescens*, increasing with increasing zinc concentration and immune-induced upon flg22 recognition (87). In Chapter 5, the implications of this increased zinc and ROS environment on *P. syringae* was studied using a series of in vitro experiments. As assessed by Raman microspectroscopy, toxicity of zinc against *P. syringae* appears to be unlikely to be due to the metal causing harmful biomolecular changes in the bacteria. No significant differences in the spectra were observed at any concentration or time point tested. However, it was established using Raman spectroscopy and stable isotope labelling that zinc does affect the bacteria's metabolic activity.

Zinc toxicity is also unlikely to be due to disruption to the bacterial membrane. The outer leaflet of bacterial membranes predominantly consist of lipopolysaccharides (LPS)

stabilised by magnesium and calcium cations.(260) As discussed, zinc is particularly strong at outcompeting natively bound metals and thus we hypothesised that zinc could displace magnesium and/or calcium in the bacterial LPS, destabilising the membrane. This was studied using neutron reflectivity at ISIS neutron and muon source (261). Analysis for this is ongoing but it does not appear that zinc disrupts the outer leaflet of *P. syringae* (Bourdon, Menon, Harper, Clifton, and Preston, data not shown).

However, a synergistic relationship between zinc and ROS was observed, potentially providing evidence for the joint effects hypothesis of metal hyperaccumulation. In a series of growth assays, zinc was found to increase sensitivity to ROS. Additionally, using the cellular redox biosensor roGFP, sublethal concentrations of zinc were found to cause sustained oxidation of *P. syringae*. We hypothesise that this could be due to zinc interfering with ROS scavenging mechanisms: glutathione metabolism and/or enzymes such as catalases and peroxidases. To confirm this, enzyme activity assays could be performed using the concentrations of zinc relevant to this work. Likewise, to better understand how the plant environment directly influences the bacteria's redox response, roGFP analysis could be conducted in planta. Though not widely attempted, N-ethylmaleimide (NEM) has been used to "freeze" the oxidation state of nodule bacteria to enable roGFP measurements in the dynamic plant environment (262). roGFP2 tagged bacteria could be inoculated into leaves of *N. caerulescens* and at relevant time points leaves could be removed and sections submerged into NEM solution. A confocal microscope equipped with a cryo-stage would enable imaging of transverse sections of leaf tissue, prepared using the technique discussed in Chapter 3, theoretically allowing for in planta measurement of the redox state of the bacteria.

In addition to in planta roGFP experiments, in planta Raman microspectroscopy combined with deuterium stable isotope labelling could enable an understanding of how the high zinc and ROS environment of the plant directly affects the metabolic activity of *P. syringae*. This has been tested in non-published work studying the interaction of *Nicotiana*

benthamiana infected with *P. syringae* pv. DC3000 grown in deuterated media (154). At different time points post inoculation, apoplastic washing fluid containing the bacteria was extracted from the plant using a method similar to the one described in section 2.9. However, here, bacteria were extracted into 4% paraformaldehyde to fix the bacteria in a state as close as possible to how they were in the plant.

To conclude, this thesis has provided insight into the mechanisms by which hyperaccumulated metal provides a defence against the bacterial pathogen *Pseudomonas syringae.* Evidence has also been presented in support of the joint effects hypothesis of metal hyperaccumulation, where zinc and ROS were found to act synergistically to inhibit bacterial growth. While this study has focussed on zinc, *N. caerulescens* also hyperaccumulates nickel and cadmium, both of which were previously found to exhibit a defensive effect against *P. syringae* (6,25). Thus, this work could be expanded to investigate whether the mechanisms observed with zinc also occur for these other metals. Likewise, *N. caerulescens* has been demonstrated to display population-dependent differences in its hyperaccumulation ability and defence strategies which could also be studied using the methods used in this work. Furthermore, testing other hyperaccumulating species and pathogens with different virulence mechanisms could provide insights into whether the defence mechanisms observed in the *N. caerulescens* – *P. syringae* model system are specific to this system or shared among hyperaccumulator plants.

Bibliography

1. Reeves RD, Baker AJM, Jaffré T, Erskine PD, Echevarria G, van der Ent A. A global database for plants that hyperaccumulate metal and metalloid trace elements. New Phytol. 2018;218(2):407–11.

2. Rascio N, Navari-Izzo F. Heavy metal hyperaccumulating plants: How and why do they do it? And what makes them so interesting? Plant Sci [Internet]. 2011;180(2):169–81. Available from: http://www.sciencedirect.com/science/article/pii/S0168945210002402

3. Verbruggen N, Hermans C, Schat H. Molecular mechanisms of metal hyperaccumulation in plants. New Phytol. 2009;181(4):759–76.

4. Poschenrieder C, Tolrà R, Barceló J. Can metals defend plants against biotic stress? Trends Plant Sci. 2006;11(6):288–95.

5. Boyd RS, Martens SN. Nickel hyperaccumulated by Thlaspi montanum var. montanum is acutely toxic to an insect herbivore. Oikos. 1994;70(1):21–5.

6. Fones H, Davis CAR, Rico A, Fang F, Smith JAC, Preston GM. Metal hyperaccumulation armors plants against disease. PLoS Pathog. 2010;6(9):e1001093.

7. Balafrej H, Bogusz D, Triqui Z-EA, Guedira A, Bendaou N, Smouni A, et al. Zinc hyperaccumulation in plants: A review. Plants. 2020;9(5):562.

8. Chardonnens AN, ten Bookum WM, Vellinga S, Schat H, Verkleij JAC, Ernst WHO. Allocation patterns of zinc and cadmium in heavy metal tolerant and sensitive Silene vulgaris. J Plant Physiol. 1999;155(6):778–87.

9. Fones H, Preston GM. The impact of transition metals on bacterial plant disease. FEMS Microbiol Rev. 2013;37(4):495–519.

10. Kalaivanan D, Ganeshamurthy AN. Mechanisms of Heavy Metal Toxicity in Plants. In: Rao NKS, Shivashankara KS, Laxman RH, editors. Abiotic Stress Physiology of Horticultural Crops [Internet]. New Delhi: Springer India; 2016. p. 85–102. Available from: https://doi.org/10.1007/978-81-322-2725-0_5

11. Chrysargyris A, Höfte M, Tzortzakis N, Petropoulos SA, Di Gioia F. Micronutrients: The borderline between their beneficial role and toxicity in plants. Front Plant Sci. 2022;13:840624.

12. Nies DH, Brown NL. Two-component systems in the regulation of heavy metal resistance. In: Metal Ions in Gene Regulation. Springer; 1998. p. 77–103.

13. Hänsch R, Mendel RR. Physiological functions of mineral micronutrients (Cu, Zn, Mn, Fe, Ni, Mo, B, Cl). Curr Opin Plant Biol [Internet]. 2009;12(3):259–66. Available from: http://www.sciencedirect.com/science/article/pii/S1369526609000429

14. Miller GW, Huang IJ, Welkie GW, Pushnik JC. Function of iron in plants with special emphasis on chloroplasts and photosynthetic activity. In: Iron Nutrition in Soils and Plants. Springer; 1995. p. 19–28.

15. Balk J, Schaedler TA. Iron Cofactor Assembly in Plants. Annu Rev Plant Biol [Internet]. 2014 Apr 29;65(1):125–53. Available from: https://doi.org/10.1146/annurev-arplant-050213-035759

16. Balk J, Lobréaux S. Biogenesis of iron–sulfur proteins in plants. Trends Plant Sci [Internet]. 2005;10(7):324–31. Available from: http://www.sciencedirect.com/science/article/pii/S1360138505001202

17. McCall KA, Huang C, Fierke CA. Function and Mechanism of Zinc Metalloenzymes. J Nutr [Internet]. 2000 May 1;130(5):1437S-1446S. Available from: https://doi.org/10.1093/jn/130.5.1437S

18. Broadley MR, White PJ, Hammond JP, Zelko I, Lux A. Zinc in plants. New Phytol. 2007;173(4):677–702.

19. Hafeez B, Khanif YM, Saleem M. Role of zinc in plant nutrition-a review. Am J Exp Agric. 2013;3(2):374.

20. Haghighizadeh A, Rajabi O, Nezarat A, Hajyani Z, Haghmohammadi M, Hedayatikhah S, et al. Comprehensive analysis of heavy metal soil contamination in mining Environments: Impacts, monitoring Techniques, and remediation strategies. Arab J Chem. 2024;105777.

21. Stohs SJ, Bagchi D. Oxidative mechanisms in the toxicity of metal ions. Free Radic Biol Med. 1995;18(2):321–36.

22. Hassan KA, Pederick VG, Elbourne LDH, Paulsen IT, Paton JC, McDevitt CA, et al. Zinc stress induces copper depletion in Acinetobacter baumannii. BMC Microbiol. 2017;17:1–15.

23. Eijkelkamp BA, Morey JR, Ween MP, Ong CY, McEwan AG, Paton JC, et al. Extracellular zinc competitively inhibits manganese uptake and compromises oxidative stress management in Streptococcus pneumoniae. PLoS One. 2014;9(2):e89427.

24. Yadav SK. Heavy metals toxicity in plants: an overview on the role of glutathione and phytochelatins in heavy metal stress tolerance of plants. South African J Bot. 2010;76(2):167–79.

25. Fones H. The Ecological and Evolutionary Significance of Disease Resistance in Metal Hyperaccumulating Plants. University of Oxford; 2010.

26. Shahid M, Pourrut B, Dumat C, Nadeem M, Aslam M, Pinelli E. Heavy-Metal-Induced Reactive Oxygen Species: Phytotoxicity and Physicochemical Changes in Plants BT - Reviews of Environmental Contamination and Toxicology Volume 232. In: Whitacre DM, editor. Reviews of Environmental Contamination and Toxicology [Internet]. Cham: Springer International Publishing; 2014. p. 1–44. Available from: https://doi.org/10.1007/978-3-319-06746-9_1

27. Jalmi SK, Bhagat PK, Verma D, Noryang S, Tayyeba S, Singh K, et al. Traversing the Links between Heavy Metal Stress and Plant Signaling. Front Plant Sci [Internet]. 2018;9:12. Available from: https://www.frontiersin.org/article/10.3389/fpls.2018.00012

28. Brooks RR, Lee J, Reeves RD, Jaffré T. Detection of nickeliferous rocks by analysis of herbarium specimens of indicator plants. J Geochemical Explor. 1977;7:49–57.

29. Assunção AGL, Schat H, Aarts MGM. Thlaspi caerulescens, an Attractive Model Species to Study Heavy Metal Hyperaccumulation in Plants. New Phytol [Internet]. 2003;159(2):351–60. Available from: http://www.jstor.org/stable/1514231

30. Guillot S, Hattori K. Serpentinites: essential roles in geodynamics, arc volcanism, sustainable development, and the origin of life. Elements. 2013;9(2):95–8.

31. van Der Ent A, Baker AJM, Reeves RD, Chaney RL, Anderson CWN, Meech JA, et al. Agromining: farming for metals in the future? Environ Sci Technol. 2015;49(8):1–8.

32. Rigola D, Fiers M, Vurro E, Aarts MGM. The heavy metal hyperaccumulator Thlaspi caerulescens expresses many species-specific genes, as identified by comparative expressed sequence tag analysis. New Phytol. 2006;170(4):753–66.

33. Reeves RD, Schwartz C, Morel JL, Edmondson J. Distribution and metal-accumulating behavior of Thlaspi caerulescens and associated metallophytes in France. Int J Phytoremediation. 2001;3(2):145–72.

34. Gonneau C, Genevois N, Frérot H, Sirguey C, Sterckeman T. Variation of trace metal accumulation, major nutrient uptake and growth parameters and their correlations in 22 populations of Noccaea caerulescens. Plant Soil. 2014;384(1–2):271–87.

35. Sterckeman T, Cazes Y, Gonneau C, Sirguey C. Phenotyping 60 populations of Noccaea caerulescens provides a broader knowledge of variation in traits of interest for phytoextraction. Plant Soil [Internet]. 2017;418(1):523–40. Available from: https://doi.org/10.1007/s11104-017-3311-0

36. Visioli G, Gullì M, Marmiroli N. Noccaea caerulescens populations adapted to grow in metalliferous and non-metalliferous soils: Ni tolerance, accumulation and expression analysis of genes involved in metal homeostasis. Environ Exp Bot. 2014;105:10–7.

37. Assunção AGL, Bookum WM, Nelissen HJM, Vooijs R, Schat H, Ernst WHO. Differential metal-specific tolerance and accumulation patterns among Thlaspi caerulescens populations originating from different soil types. New Phytol [Internet]. 2003 Aug 1;159(2):411–9. Available from: https://doi.org/10.1046/j.1469-8137.2003.00819.x

38. Fones HN, Preston GM, Smith JAC. Variation in defence strategies in the metal hyperaccumulator plant Noccaea caerulescens is indicative of synergies and trade-offs between forms of defence. R Soc open Sci [Internet]. 2019 Jan 23;6(1):172418. Available from: https://pubmed.ncbi.nlm.nih.gov/30800336

39. Escarré J, Lefèbvre C, Frérot H, Mahieu S, Noret N. Metal concentration and metal mass of metallicolous, non metallicolous and serpentine Noccaea caerulescens populations, cultivated in different growth media. Plant Soil. 2013;370:197–221.

40. Kozhevnikova AD, Seregin I V, Gosti F, Schat H. Zinc accumulation and distribution over tissues in Noccaea caerulescens in nature and in hydroponics: a comparison. Plant Soil. 2017;411:5–16.

41. Baker AJM. Accumulators and excluders-strategies in the response of plants to heavy metals. J Plant Nutr. 1981;3(1–4):643–54.

42. Assunção AGL, Martins PDC, De Folter S, Vooijs R, Schat H, Aarts MGM. Elevated expression of metal transporter genes in three accessions of the metal hyperaccumulator Thlaspi caerulescens. Plant Cell Environ. 2001;24(2):217–26.

43. Papoyan A, Kochian L V. Identification of Thlaspi caerulescens genes that may be involved in heavy metal hyperaccumulation and tolerance. Characterization of a novel heavy metal transporting ATPase. Plant Physiol. 2004;136(3):3814–23.

44. Lasat MM, Baker AJM, Kochian L V. Physiological characterization of root Zn2+ absorption and translocation to shoots in Zn hyperaccumulator and nonaccumulator species of Thlaspi. Plant Physiol. 1996;112(4):1715–22.

45. Hammond JP, Bowen HC, White PJ, Mills V, Pyke KA, Baker AJM, et al. A comparison of the Thlaspi caerulescens and Thlaspi arvense shoot transcriptomes. New Phytol. 2006;170(2):239–60.

46. Lasat MM, Pence NS, Garvin DF, Ebbs SD, Kochian L V. Molecular physiology of zinc transport in the Zn hyperaccumulator Thlaspi caerulescens. J Exp Bot [Internet]. 2000 Jan 1;51(342):71–9. Available from: https://doi.org/10.1093/jexbot/51.342.71

47. Bert V, Macnair MR, De Laguerie P, Saumitou-Laprade P, Petit D. Zinc tolerance and accumulation in metallicolous and nonmetallicolous populations of Arabidopsis halleri (Brassicaceae). New Phytol. 2000;146(2):225–33.

48. Küpper H, Zhao FJ, McGrath SP. Cellular compartmentation of zinc in leaves of the hyperaccumulator Thlaspi caerulescens. Plant Physiol. 1999;119(1):305–12.

49. Frey B, Keller C, Zierold K. Distribution of Zn in functionally different leaf epidermal cells of the hyperaccumulator Thlaspi caerulescens. Plant Cell Environ. 2000;23(7):675–87.

50. Monsant AC, Wang Y, Tang C. Nitrate nutrition enhances zinc hyperaccumulation in Noccaea caerulescens (Prayon). Plant Soil. 2010;336(1–2):391–404.

51. Ricachenevsky FK, Punshon T, Salt DE, Fett JP, Guerinot M Lou. Arabidopsis thaliana zinc accumulation in leaf trichomes is correlated with zinc concentration in leaves. Sci Rep. 2021;11(1):5278.

52. Krämer U, Grime GW, Smith JAC, Hawes CR, Baker AJM. Micro-PIXE as a technique for studying nickel localization in leaves of the hyperaccumulator plant Alyssum lesbiacum. Nucl Instruments Methods Phys Res Sect B Beam Interact with Mater Atoms. 1997;130(1–4):346–50.

53. Tewes LJ, Stolpe C, Kerim A, Krämer U, Müller C. Metal hyperaccumulation in the Brassicaceae species Arabidopsis halleri reduces camalexin induction after fungal pathogen attack. Environ Exp Bot. 2018;153:120–6.

54. Bothe H. Plants in heavy metal soils. In: Detoxification of heavy metals. Springer; 2011. p. 35–57.

55. Sarret G, Saumitou-Laprade P, Bert V, Proux O, Hazemann J-L, Traverse A, et al. Forms of zinc accumulated in the hyperaccumulatorArabidopsis halleri. Plant Physiol. 2002;130(4):1815–26.

56. Salt DE, Prince RC, Baker AJM, Raskin I, Pickering IJ. Zinc Ligands in the Metal Hyperaccumulator Thlaspi caerulescens As Determined Using X-ray Absorption Spectroscopy. Environ Sci Technol [Internet]. 1999 Mar 1;33(5):713–7. Available from: https://doi.org/10.1021/es980825x

57. Leitenmaier B, Küpper H. Compartmentation and complexation of metals in hyperaccumulator plants. Front Plant Sci. 2013;4:374.

58. Callahan DL, Baker AJM, Kolev SD, Wedd AG. Metal ion ligands in hyperaccumulating plants. JBIC J Biol Inorg Chem. 2006;11(1):2–12.

59. Zhang Z, Chen B, Qiu B. Phytochelatin synthesis plays a similar role in shoots of the cadmium hyperaccumulator Sedum alfredii as in non-resistant plants. Plant Cell Environ. 2010;33(8):1248–55.

60. Freeman JL, Persans MW, Nieman K, Albrecht C, Peer W, Pickering IJ, et al. Increased glutathione biosynthesis plays a role in nickel tolerance in Thlaspi nickel hyperaccumulators. Plant Cell. 2004;16(8):2176–91.

61. Colangelo EP, Guerinot M Lou. Put the metal to the petal: metal uptake and transport throughout plants. Curr Opin Plant Biol [Internet]. 2006;9(3):322–30. Available from: http://www.sciencedirect.com/science/article/pii/S1369526606000549

62. Boyd RS, Martens SN. The raison d'être for metal hyperaccumulation by plants. Intercept, Andover, UK; 1992 p. 279–89.

63. Boyd RS. Ecology of metal hyperaccumulation. New Phytol. 2004;162(3):563–7.

64. Macnair MR, Bert V, Huitson SB, Saumitou-Laprade P, Petit D. Zinc tolerance and hyperaccumulation are genetically independent characters. Proc R Soc London Ser B Biol Sci. 1999;266(1434):2175–9.

65. Manara A, Fasani E, Furini A, DalCorso G. Evolution of the Metal Hyperaccumulation and Hypertolerance Traits. Plant Cell Environ. 2020;43(12):2969–86.

66. Jaffe BD, Ketterer ME, Shuster SM. Elemental allelopathy by an arsenic hyperaccumulating fern, Pteris vittata L. J Plant Ecol. 2018;11(4):553–9.

67. El Mehdawi AF, Quinn CF, Pilon-Smits EAH. Effects of selenium hyperaccumulation on plant–plant interactions: evidence for elemental allelopathy? New Phytol [Internet]. 2011 Jul 1;191(1):120–31. Available from: https://doi.org/10.1111/j.1469-8137.2011.03670.x

68. Cappa JJ, Pilon-Smits EAH. Evolutionary aspects of elemental hyperaccumulation. Planta. 2014;239(2):267–75.

69. Statwick JM, Williams AK, Sher AA. Lack of evidence for the drought tolerance hypothesis of hyperaccumulation in Astragalus species. Int J Plant Sci. 2017;178(6):478–84.

70. Boyd RS. The defense hypothesis of elemental hyperaccumulation: status, challenges and new directions. Plant Soil. 2007;293:153–76.

71. Hörger AC, Fones HN, Preston GM. The current status of the elemental defense hypothesis in relation to pathogens. Front Plant Sci. 2013;4:395.

72. Martens SN, Boyd RS. The ecological significance of nickel hyperaccumulation: a plant chemical defense. Acta Oecol. 1994;98:379–84.

73. Stolpe C, Krämer U, Müller C. Heavy metal (hyper) accumulation in leaves of Arabidopsis halleri is accompanied by a reduced performance of herbivores and shifts in leaf glucosinolate and element concentrations. Environ Exp Bot. 2017;133:78–86.

74. Hanson B, Lindblom SD, Loeffler ML, Pilon-Smits EAH. Selenium protects plants from phloem-feeding aphids due to both deterrence and toxicity. New Phytol. 2004;162(3):655–62.

75. Boyd RS. Plant defense using toxic inorganic ions: conceptual models of the defensive enhancement and joint effects hypotheses. Plant Sci. 2012;195:88–95.

76. Cheruiyot DJ, Boyd RS, Moar W. Testing the joint effects hypothesis of elemental defense using Spodoptera exigua. J Chem Ecol. 2015;41:168–77.

77. Dodds PN, Rathjen JP. Plant immunity: towards an integrated view of plant–pathogen interactions. Nat Rev Genet. 2010;11(8):539–48.

78. Muthamilarasan M, Prasad M. Plant innate immunity: an updated insight into defense mechanism. J Biosci. 2013;38:433–49.

79. Wang Y, Pruitt RN, Nuernberger T, Wang Y. Evasion of plant immunity by microbial pathogens. Nat Rev Microbiol. 2022;20(8):449–64.

80. Herrera-Vásquez A, Salinas P, Holuigue L. Salicylic acid and reactive oxygen species interplay in the transcriptional control of defense genes expression. Front Plant Sci [Internet]. 2015 Mar 19;6:171. Available from: https://pubmed.ncbi.nlm.nih.gov/25852720

81. Boller T, He SY. Innate immunity in plants: an arms race between pattern recognition receptors in plants and effectors in microbial pathogens. Science (80-). 2009;324(5928):742–4.

82. Hückelhoven R. The effective papilla hypothesis. New Phytol. 2014;204(3):438–40.

83. Lukan T, Coll A. Intertwined roles of reactive oxygen species and salicylic acid

signaling are crucial for the plant response to biotic stress. Int J Mol Sci. 2022;23(10):5568.

84. Tierens KF-J, Thomma BPHJ, Brouwer M, Schmidt J, Kistner K, Porzel A, et al. Study of the role of antimicrobial glucosinolate-derived isothiocyanates in resistance of Arabidopsis to microbial pathogens. Plant Physiol. 2001;125(4):1688–99.

85. Clay NK, Adio AM, Denoux C, Jander G, Ausubel FM. Glucosinolate metabolites required for an Arabidopsis innate immune response. Science (80-). 2009;323(5910):95–101.

86. Fones HN, Preston GM. Trade-offs between metal hyperaccumulation and induced disease resistance in metal hyperaccumulator plants. Plant Pathol [Internet]. 2013 Dec 1;62(S1):63–71. Available from: https://doi.org/10.1111/ppa.12171

87. Fones HN, Eyles CJ, Bennett MH, Smith JAC, Preston GM. Uncoupling of reactive oxygen species accumulation and defence signalling in the metal hyperaccumulator plant N occaea caerulescens. New Phytol. 2013;199(4):916–24.

88. Bothe H, Słomka A. Divergent biology of facultative heavy metal plants. J Plant Physiol. 2017;219:45–61.

89. Pollard AJ, Reeves RD, Baker AJM. Facultative hyperaccumulation of heavy metals and metalloids. Plant Sci [Internet]. 2014;217–218:8–17. Available from: http://www.sciencedirect.com/science/article/pii/S0168945213002574

90. Xin X-F, Kvitko B, He SY. Pseudomonas syringae: what it takes to be a pathogen. Nat Rev Microbiol [Internet]. 2018 Feb 26;16:316. Available from: https://doi.org/10.1038/nrmicro.2018.17

91. Arnold DL, Preston GM. Pseudomonas syringae: enterprising epiphyte and stealthy parasite. Microbiology. 2018;165(3):251–3.

92. Zeng W, Brutus A, Kremer JM, Withers JC, Gao X, Jones AD, et al. A Genetic Screen

Reveals Arabidopsis Stomatal and/or Apoplastic Defenses against Pseudomonas syringae pv. tomato DC3000. PLOS Pathog [Internet]. 2011 Oct 6;7(10):e1002291. Available from: https://doi.org/10.1371/journal.ppat.1002291

93. Emms DM, Kelly S. OrthoFinder: solving fundamental biases in whole genome comparisons dramatically improves orthogroup inference accuracy. Genome Biol. 2015;16:1–14.

94. Herold L, Choi S, He SY, Zipfel C. The conserved AvrE family of bacterial effectors: functions and targets during pathogenesis. Trends in Microbiology. Elsevier; 2024.

95. Degrave A, Siamer S, Boureau T, Barny M. The AvrE superfamily: ancestral type III effectors involved in suppression of pathogen-associated molecular pattern-triggered immunity. Mol Plant Pathol. 2015;16(8):899–905.

96. Chen H, Chen J, Zhao Y, Liu F, Fu ZQ. Pseudomonas syringae pathovars. Trends Microbiol. 2022;30(9):912–3.

97. Jayaraman J, Yoon M, Applegate ER, Stroud EA, Templeton MD. AvrE1 and HopR1 from Pseudomonas syringae pv. actinidiae are additively required for full virulence on kiwifruit. Mol Plant Pathol. 2020;21(11):1467–80.

98. Munkvold KR, Russell AB, Kvitko BH, Collmer A. Pseudomonas syringae pv. tomato DC3000 type III effector HopAA1-1 functions redundantly with chlorosis-promoting factor PSPTO4723 to produce bacterial speck lesions in host tomato. Mol plant-microbe Interact. 2009;22(11):1341–55.

99. Nomura K, Andreazza F, Cheng J, Dong K, Zhou P, He SY. Bacterial pathogens deliver water-and solute-permeable channels to plant cells. Nature. 2023;621(7979):586–91.

100. Lozano-Durán R, Bourdais G, He SY, Robatzek S. The bacterial effector HopM1 suppresses PAMP-triggered oxidative burst and stomatal immunity. New Phytol. 2014;202(1):259–69.

101. Badel JL, Shimizu R, Oh H-S, Collmer A. A Pseudomonas syringae pv. tomato avrE1/hopM1 mutant is severely reduced in growth and lesion formation in tomato. Mol plant-microbe Interact. 2006;19(2):99–111.

102. DebRoy S, Thilmony R, Kwack Y-B, Nomura K, He SY. A family of conserved bacterial effectors inhibits salicylic acid-mediated basal immunity and promotes disease necrosis in plants. Proc Natl Acad Sci. 2004;101(26):9927–32.

103. Bender CL, Alarcón-Chaidez F, Gross DC. Pseudomonas syringae phytotoxins: mode of action, regulation, and biosynthesis by peptide and polyketide synthetases. Microbiol Mol Biol Rev. 1999;63(2):266–92.

104. Zheng X, Spivey NW, Zeng W, Liu P-P, Fu ZQ, Klessig DF, et al. Coronatine promotes Pseudomonas syringae virulence in plants by activating a signaling cascade that inhibits salicylic acid accumulation. Cell Host Microbe. 2012;11(6):587–96.

105. Geng X, Jin L, Shimada M, Kim MG, Mackey D. The phytotoxin coronatine is a multifunctional component of the virulence armament of Pseudomonas syringae. Planta. 2014;240(6):1149–65.

106. Fones H, Preston GM. Reactive oxygen and oxidative stress tolerance in plant pathogenic Pseudomonas. FEMS Microbiol Lett. 2012;327(1):1–8.

107. Girard L, Höfte M, Mot R De. Lipopeptide families at the interface between pathogenic and beneficial Pseudomonas-plant interactions. Crit Rev Microbiol. 2020;46(4):397–419.

108. Dinsley JM, Davies HS, Gomez-Gonzalez MA, Robinson CH, Pittman JK. The value of synchrotron radiation X-ray techniques to explore microscale chemistry for ecology and evolution research. Ecosphere. 2022;13(12):e4312.

109. Welz B, Sperling M. Atomic absorption spectrometry. John Wiley & Sons; 2008.

110. Tyler G, Yvon J. ICP-OES, ICP-MS and AAS Techniques Compared. ICP Opt Emiss

Spectrosc Tech Note 5. 1995;1–11.

111. Adesina KE, Burgos CJ, Grier TR, Sayam ASM, Specht AJ. Ways to Measure Metals: From ICP-MS to XRF. Curr Environ Heal Reports. 2025;12(1):7.

112. Petrelli M, Laeger K, Perugini D. High spatial resolution trace element determination of geological samples by laser ablation quadrupole plasma mass spectrometry: implications for glass analysis in volcanic products. Geosci J. 2016;20:851–63.

113. Moore KL, Lombi E, Zhao F-J, Grovenor CRM. Elemental imaging at the nanoscale: NanoSIMS and complementary techniques for element localisation in plants. Anal Bioanal Chem. 2012;402:3263–73.

114. van der Ent A, Przybyłowicz WJ, de Jonge MD, Harris HH, Ryan CG, Tylko G, et al. X-ray elemental mapping techniques for elucidating the ecophysiology of hyperaccumulator plants. New Phytol. 2018;218(2):432–52.

115. Pushie MJ, Pickering IJ, Korbas M, Hackett MJ, George GN. Elemental and chemically specific X-ray fluorescence imaging of biological systems. Chem Rev. 2014;114(17):8499–541.

116. Kowalska J, DeBeer S. The role of X-ray spectroscopy in understanding the geometric and electronic structure of nitrogenase. Biochim Biophys Acta (BBA)-Molecular Cell Res. 2015;1853(6):1406–15.

117. D'Acapito F. X-ray Absorption Spectroscopy Studies on Materials Obtained by the Sol-Gel Route. In: Klein L, Aparicio M, Jitianu A, editors. Handbook of Sol-Gel Science and Technology [Internet]. Cham: Springer International Publishing; 2018. p. 1231–55. Available from: https://doi.org/10.1007/978-3-319-32101-1_31

118. Calvin S. XAFS for Everyone. CRC press; 2013.

119. Iglesias-Juez A, Chiarello GL, Patience GS, Guerrero-Pérez MO. Experimental methods in chemical engineering: X-ray absorption spectroscopy—XAS, XANES,

EXAFS. Can J Chem Eng. 2022;100(1):3–22.

120. Parsons JG, Aldrich M V, Gardea-Torresdey JL. Environmental and biological applications of extended X-ray absorption fine structure (EXAFS) and X-ray absorption near edge structure (XANES) spectroscopies. Appl Spectrosc Rev. 2002;37(2):187–222.

121. Ortega R, Carmona A, Llorens I, Solari PL. X-ray absorption spectroscopy of biological samples. A tutorial. J Anal At Spectrom. 2012;27(12):2054–65.

122. Cramer SP. X-ray spectroscopy with synchrotron radiation. Bernard S. Gerstman, Department of Physics FIU, Miami, FL U, editors. Biological and Medical Physics, Biomedical Engineering. Springer; 2020.

123. Materlik G, Rayment T, Stuart DI. Diamond Light Source: status and perspectives. Philos Trans R Soc A Math Phys Eng Sci. 2015;373(2036):1–16.

124. Kopittke PM, Punshon T, Paterson DJ, Tappero R V, Wang P, Blamey FPC, et al. Synchrotron-based X-ray fluorescence microscopy as a technique for imaging of elements in plants. Plant Physiol. 2018;178(2):507–23.

125. Li C, Wang P, Lombi E, Wu J, Blamey FPC, Fernández V, et al. Absorption of foliar applied Zn is decreased in Zn deficient sunflower (Helianthus annuus) due to changes in leaf properties. Plant Soil. 2018;433:309–22.

126. van der Ent A, Spiers KM, Brueckner D, Echevarria G, Aarts MGM, Montargès-Pelletier E. Spatially-resolved localization and chemical speciation of nickel and zinc in Noccaea tymphaea and Bornmuellera emarginata. Metallomics. 2019;11(12):2052–65.

127. Dinh NT, Vu DT, Mulligan D, Nguyen A V. Accumulation and distribution of zinc in the leaves and roots of the hyperaccumulator Noccaea caerulescens. Environ Exp Bot. 2015;110:85–95.

128. Roosens N, Verbruggen N, Meerts P, Ximenez-Embun P, Smith JAC. Natural variation in cadmium tolerance and its relationship to metal hyperaccumulation for seven populations of Thlaspi caerulescens from western Europe. Plant Cell Environ. 2003;26(10):1657–72.

129. Hoagland DR, Arnon DI. The water-culture method for growing plants without soil. Circ. 347. Berkeley, CA Calif Agric Exp Stn. 1950;31.

130. Miller JH. Experiments in Molecular Genetics. Cold Spring Harbor Laboratory Press, Cold Spring Harbor, NY; 1972. 466 p.

131. Soldan R, Sanguankiattichai N, Bach-Pages M, Bervoets I, Huang WE, Preston GM. From Macro to Micro: a combined bioluminescence-fluorescence approach to monitor bacterial localization. Environ Microbiol. 2021;23(4):2070–85.

132. Figurski DH, Helinski DR. Replication of an origin-containing derivative of plasmid RK2 dependent on a plasmid function provided in trans. Proc Natl Acad Sci. 1979;76(4):1648–52.

133. Miller VL, Mekalanos JJ. A novel suicide vector and its use in construction of insertion mutations: osmoregulation of outer membrane proteins and virulence determinants in Vibrio cholerae requires toxR. J Bacteriol. 1988;170(6):2575–83.

134. Solmi L, Rossi FR, Romero FM, Bach-Pages M, Preston GM, Ruiz OA, et al. Polyamine-mediated mechanisms contribute to oxidative stress tolerance in Pseudomonas syringae. Sci Rep. 2023;13(1):4279.

135. Keen NT, Tamaki S, Kobayashi D, Trollinger D. Improved broad-host-range plasmids for DNA cloning in gram-negative bacteria. Gene. 1988;70(1):191–7.

136. Dong X, Mindrinos M, Davis KR, Ausubel FM. Induction of Arabidopsis defense genes by virulent and avirulent Pseudomonas syringae strains and by a cloned avirulence gene. Plant Cell. 1991;3(1):61–72.

137. Hughes TE, Sedelnikova O V, Wu H, Becraft PW, Langdale JA. Redundant SCARECROW genes pattern distinct cell layers in roots and leaves of maize. Development. 2019;146(14):dev177543.

138. Mosselmans JFW, Quinn PD, Dent AJ, Cavill SA, Moreno SD, Peach A, et al. I18–the microfocus spectroscopy beamline at the Diamond Light Source. J Synchrotron Radiat. 2009;16(6):818–24.

139. Solé VA, Papillon E, Cotte M, Walter P, Susini J. A multiplatform code for the analysis of energy-dispersive X-ray fluorescence spectra. Spectrochim Acta Part B At Spectrosc. 2007;62(1):63–8.

140. Schindelin J, Arganda-Carreras I, Frise E, Kaynig V, Longair M, Pietzsch T, et al. Fiji: an open-source platform for biological-image analysis. Nat Methods. 2012;9(7):676–82.

141. Crameri F, Shephard GE, Heron PJ. The misuse of colour in science communication. Nat Commun. 2020;11(1):5444.

142. Wickham H. ggplot2: Elegant Graphics for Data Analysis. 2nd ed. New York: Springer; 2016.

143. O'Leary BM, Rico A, McCraw S, Fones HN, Preston GM. The infiltration-centrifugation technique for extraction of apoplastic fluid from plant leaves using Phaseolus vulgaris as an example. J Vis Exp. 2014;94(94):e52113.

144. Chen A, He B, Jin H. Isolation of extracellular vesicles from Arabidopsis. Curr Protoc. 2022;2(1):e352.

145. Hollings AL, Lam V, Takechi R, Mamo JCL, Reinhardt J, de Jonge MD, et al. Revealing differences in the chemical form of zinc in brain tissue using K-edge X-ray absorption near-edge structure spectroscopy. Metallomics. 2020;12(12):2134–44.

146. Mijovilovich A, Mishra A, Brückner D, Spiers K, Andresen E, Garrevoet J, et al.

MicroX-ray absorption near edge structure tomography reveals cell-specific changes of Zn ligands in leaves of turnip yellow mosaic virus infected plants. Spectrochim Acta Part B At Spectrosc. 2019;157:53–62.

147. Doolette CL, Read TL, Li C, Scheckel KG, Donner E, Kopittke PM, et al. Foliar application of zinc sulphate and zinc EDTA to wheat leaves: differences in mobility, distribution, and speciation. J Exp Bot [Internet]. 2018 Aug 14;69(18):4469–81. Available from: https://pubmed.ncbi.nlm.nih.gov/29931117

148. Mishra B, McDonald LM, Roy M, Lanzirotti A, Myneni SCB. Uptake and speciation of zinc in edible plants grown in smelter contaminated soils. PLoS One. 2020;15(4):e0226180.

149. Montarges-Pelletier E, Chardot V, Echevarria G, Michot LJ, Bauer A, Morel J-L. Identification of nickel chelators in three hyperaccumulating plants: an X-ray spectroscopic study. Phytochemistry. 2008;69(8):1695–709.

150. Toplak M, Read ST, Sandt C, Borondics F. Quasar: easy machine learning for biospectroscopy. Cells. 2021;10(9):2300.

151. Newville M. Larch: an analysis package for XAFS and related spectroscopies. In: Journal of Physics: Conference Series. IOP Publishing; 2013. p. 12007.

152. R: A language and environment for statistical computing [Internet]. 2022. Available from: https://www.r-project.org/

153. van der Heijden J, Finlay BB. In vitro real-time measurement of the intra-bacterial redox potential. Bio-protocol. 2015;5(17):e1579–e1579.

154. Sanguankiattichai N. Using Raman microspectroscopy to monitor metabolic activity of Pseudomonas syringae. 2017.

155. Kassambara A, Mundt F. Factoextra: extract and visualize the results of multivariate data analyses, R package version 1.0. 7. 2020. Prepr. 2021;

156. Tang Y, Horikoshi M, Li W. ggfortify: unified interface to visualize statistical results of popular R packages. R J. 2016;8(2):474.

157. Naim F, Khambatta K, Sanglard LMVP, Sauzier G, Reinhardt J, Paterson DJ, et al. Synchrotron X-ray fluorescence microscopy-enabled elemental mapping illuminates the 'battle for nutrients' between plant and pathogen. J Exp Bot. 2021;72(7):2757–68.

158. Brouwer SM, Lindqvist-Reis P, Persson DP, Marttila S, Grenville-Briggs LJ, Andreasson E. Visualising the ionome in resistant and susceptible plant–pathogen interactions. Plant J. 2021;108(3):870–85.

159. Sarkar P, Bosneaga E, Yap Jr EG, Das J, Tsai W-T, Cabal A, et al. Electron tomography of cryo-immobilized plant tissue: a novel approach to studying 3D macromolecular architecture of mature plant cell walls in situ. PLoS One. 2014;9(9):e106928.

160. Zhang Z, Niu L, Chen X, Xu X, Ru Z. Improvement of plant cryosection. Front Biol (Beijing). 2012;7:374–7.

161. Laporte MH, Klena N, Hamel V, Guichard P. Visualizing the native cellular organization by coupling cryofixation with expansion microscopy (Cryo-ExM). Nat Methods. 2022;19(2):216–22.

162. Wightman R. An overview of cryo-scanning electron microscopy techniques for plant imaging. Plants. 2022;11(9):1113.

163. Jarošová R, Ondráčková P, Patočka Z, Sládek Z. Comparison of cryoprotective methods for histological examination of rat and porcine lung tissue. Acta Vet Brno. 2021;90(2):225–31.

164. Taqi SA, Sami SA, Sami LB, Zaki SA. A review of artifacts in histopathology. J oral Maxillofac Pathol. 2018;22(2):279.

165. Austin JR. High-pressure freezing and freeze substitution of Arabidopsis for electron

microscopy. Arab Protoc. 2014;473–86.

166. Vogel-Mikuš K, Simčič J, Pelicon P, Budnar M, Kump P, Nečemer M, et al. Comparison of essential and non-essential element distribution in leaves of the Cd/Zn hyperaccumulator Thlaspi praecox as revealed by micro-PIXE. Plant Cell Environ. 2008;31(10):1484–96.

167. Hjorth T. Effects of freeze-drying on partitioning patterns of major elements and trace metals in lake sediments. Anal Chim Acta. 2004;526(1):95–102.

168. Budka D, Mesjasz-Przybyłowicz J, Przybyłowicz WJ. Micro-PIXE analysis: importance of biological sample preparation techniques. Radiat Phys Chem. 2004;71(3–4):785–6.

169. Matsumoto A, Schlüter T, Melkonian K, Takeda A, Nakagami H, Mine A. A versatile Tn7 transposon-based bioluminescence tagging tool for quantitative and spatial detection of bacteria in plants. Plant Commun. 2022;3(1).

170. Fischer AH, Jacobson KA, Rose J, Zeller R. Cryosectioning tissues. CSH Protoc. 2008;8(8):prot4991.

171. Amrutkar M, Chursa U, Kern M, Nuñez-Durán E, Ståhlman M, Sütt S, et al. STK25 is a critical determinant in nonalcoholic steatohepatitis. FASEB J. 2016;30(10):3628–43.

172. Cameron DA, Easter SS. Cone photoreceptor regeneration in adult fish retina: phenotypic determination and mosaic pattern formation. J Neurosci. 1995;15(3):2255–71.

173. Ragel P, Raddatz N, Leidi EO, Quintero FJ, Pardo JM. Regulation of K+ nutrition in plants. Front Plant Sci. 2019;10:281.

174. Shabala S. Regulation of potassium transport in leaves: from molecular to tissue level. Ann Bot. 2003;92(5):627–34.

175. Barragan V, Leidi EO, Andres Z, Rubio L, De Luca A, Fernandez JA, et al. Ion exchangers NHX1 and NHX2 mediate active potassium uptake into vacuoles to

regulate cell turgor and stomatal function in Arabidopsis. Plant Cell. 2012;24(3):1127–42.

176. Kumarasami R, Pandidurai S, Karthik S, Sivaprakasam M, Joseph J. Optimization of Freezing Method to Facilitate Cryosectioning of Large Brain Tissues. In: 2024 IEEE International Symposium on Medical Measurements and Applications (MeMeA). IEEE; 2024. p. 1–6.

177. Rondeau RE. Slush baths. J Chem Eng Data. 1966;11(1):124.

178. Vogel-Mikuš K, Pongrac P, Pelicon P. Micro-PIXE elemental mapping for ionome studies of crop plants. Int J PIXE. 2014;24(03n04):217–33.

179. Monsant AC, Kappen P, Wang Y, Pigram PJ, Baker AJM, Tang C. In vivo speciation of zinc in Noccaea caerulescens in response to nitrogen form and zinc exposure. Plant Soil. 2011;348(1–2):167.

180. Gaur A, Shrivastava BD, Joshi SK. Copper K-edge XANES of Cu (I) and Cu (II) oxide mixtures. In: Journal of Physics: Conference Series. IOP Publishing; 2009. p. 12084.

181. Küpper H, Lombi E, Zhao F, Wieshammer G, McGrath SP. Cellular compartmentation of nickel in the hyperaccumulators Alyssum lesbiacum, Alyssum bertolonii and Thlaspi goesingense. J Exp Bot. 2001;52(365):2291–300.

182. Guo Z, Gao Y, Yuan X, Yuan M, Huang L, Wang S, et al. Effects of heavy metals on stomata in plants: A review. Int J Mol Sci. 2023;24(11):9302.

183. Zhang L, Foreman DP, Grant PA, Shrestha B, Moody SA, Villiers F, et al. In situ metabolic analysis of single plant cells by capillary microsampling and electrospray ionization mass spectrometry with ion mobility separation. Analyst. 2014;139(20):5079–85.

184. Gao W, Guo C, Hu J, Dong J, Zhou LH. Mature trichome is the earliest sequestration site of Cd ions in Arabidopsis thaliana leaves. Heliyon. 2021;7(7):e07501.

185. Hatsugai N, Iwasaki S, Tamura K, Kondo M, Fuji K, Ogasawara K, et al. A novel membrane fusion-mediated plant immunity against bacterial pathogens. Genes Dev. 2009;23(21):2496–506.

186. Hara-Nishimura I, Hatsugai N. The role of vacuole in plant cell death. Cell Death Differ. 2011;18(8):1298–304.

187. Escudero V, Ferreira Sánchez D, Abreu I, Sopeña-Torres S, Makarovsky-Saavedra N, Bernal M, et al. Arabidopsis thaliana Zn2+-efflux ATPases HMA2 and HMA4 are required for resistance to the necrotrophic fungus Plectosphaerella cucumerina BMM. J Exp Bot. 2022;73(1):339–50.

188. Terres J, Battisti R, Andreaus J, de Jesus PC. Decolorization and degradation of Indigo Carmine dye from aqueous solution catalyzed by horseradish peroxidase. Biocatal Biotransformation. 2014;32(1):64–73.

189. Nouchi I, Hayashi K, Hiradate S, Ishikawa S, Fukuoka M, Chen CP, et al. Overcoming the difficulties in collecting apoplastic fluid from rice leaves by the infiltration–centrifugation method. Plant cell Physiol. 2012;53(9):1659–68.

190. Sarret G, Saumitou-Laprade P, Bert V, Proux O, Hazemann J-L, Traverse A, et al. Forms of zinc accumulated in the hyperaccumulator Arabidopsis halleri. Plant Physiol. 2002;130(4):1815–26.

191. Forde BG, Lea PJ. Glutamate in plants: metabolism, regulation, and signalling. J Exp Bot. 2007;58(9):2339–58.

192. Liao H-S, Chung Y-H, Hsieh M-H. Glutamate: A multifunctional amino acid in plants. Plant Sci. 2022;318:111238.

193. Kozhevnikova AD, Seregin I V, Erlikh NT, Shevyreva TA, Andreev IM, Verweij R, et al. Histidine-mediated xylem loading of zinc is a species-wide character in N occaea caerulescens. New Phytol. 2014;203(2):508–19.

194. O'Leary BM, Neale HC, Geilfus C, Jackson RW, Arnold DL, Preston GM. Early changes in apoplast composition associated with defence and disease in interactions between Phaseolus vulgaris and the halo blight pathogen Pseudomonas syringae pv. phaseolicola. Plant Cell Environ. 2016;39(10):2172–84.

195. Kutrowska A, Szelag M. Low-molecular weight organic acids and peptides involved in the long-distance transport of trace metals. Acta Physiol Plant. 2014;36:1957–68.

196. Limmer MA, Webb SM, Seyfferth AL. Evaluation of quantitative synchrotron radiation micro-X-ray fluorescence in rice grain. J Synchrotron Radiat. 2023;30(2):407–16.

197. Notley S V, Chen Y, Thacker NA, Lee PD, Panoutsos G. Synchrotron imaging derived relationship between process parameters and build quality for directed energy deposition additively manufactured in718. Addit Manuf Lett. 2023;6:100137.

198. Hare DJ, New EJ, de Jonge MD, McColl G. Imaging metals in biology: balancing sensitivity, selectivity and spatial resolution. Chem Soc Rev. 2015;44(17):5941–58.

199. Spiers KM, Brueckner D, Garrevoet J, Falkenberg G, Van Der Ent A. Synchrotron XFM tomography for elucidating metals and metalloids in hyperaccumulator plants. Metallomics. 2022;14(11):mfac069.

200. Mishra S, Alfeld M, Sobotka R, Andresen E, Falkenberg G, Küpper H. Analysis of sublethal arsenic toxicity to Ceratophyllum demersum: subcellular distribution of arsenic and inhibition of chlorophyll biosynthesis. J Exp Bot. 2016;67(15):4639–46.

201. van Der Ent A, De Jonge MD, Spiers KM, Brueckner D, Montargès-Pelletier E, Echevarria G, et al. Confocal volumetric μXRF and fluorescence computed μ-tomography reveals arsenic three-dimensional distribution within intact Pteris vittata fronds. Environ Sci Technol. 2019;54(2):745–57.

202. Laforce B, Vermeulen B, Garrevoet J, Vekemans B, Hoorebeke L Van, Janssen C, et al. Laboratory scale X-ray fluorescence tomography: instrument characterization and application in earth and environmental science. Anal Chem. 2016;88(6):3386–91.

203. De Jonge MD, Vogt S. Hard X-ray fluorescence tomography—an emerging tool for structural visualization. Curr Opin Struct Biol. 2010;20(5):606–14.

204. Pereira GR, Anjos MJ, Rocha HS, Faria P, Perez CA, Lopes RT. Computed tomography and X-ray fluorescence CT of biological samples. Nucl Instruments Methods Phys Res Sect A Accel Spectrometers, Detect Assoc Equip. 2007;580(2):951–4.

205. Kopittke PM, Menzies NW, de Jonge MD, McKenna BA, Donner E, Webb RI, et al. In situ distribution and speciation of toxic copper, nickel, and zinc in hydrated roots of cowpea. Plant Physiol. 2011;156(2):663–73.

206. Kim SA, Punshon T, Lanzirotti A, Li L, Alonso JM, Ecker JR, et al. Localization of iron in Arabidopsis seed requires the vacuolar membrane transporter VIT1. Science (80-). 2006;314(5803):1295–8.

207. Rivero L, Scholl R, Holomuzki N, Crist D, Grotewold E, Brkljacic J. Handling Arabidopsis plants: growth, preservation of seeds, transformation, and genetic crosses. In: Arabidopsis protocols. Springer; 2014. p. 3–25.

208. Fukuda N, Hokura A, Kitajima N, Terada Y, Saito H, Abe T, et al. Micro X-ray fluorescence imaging and micro X-ray absorption spectroscopy of cadmium hyper-accumulating plant, Arabidopsis halleri ssp. gemmifera, using high-energy synchrotron radiation. J Anal At Spectrom. 2008;23(8):1068–75.

209. Guo R, Somogyi A, Bazin D, Bouderlique E, Letavernier E, Curie C, et al. Towards routine 3D characterization of intact mesoscale samples by multi-scale and multimodal scanning X-ray tomography. Sci Rep. 2022;12(1):16924.

210. van der Ent A, de Jonge MD, Echevarria G, Aarts MGM, Mesjasz-Przybyłowicz J, Przybyłowicz WJ, et al. Multimodal synchrotron X-ray fluorescence imaging reveals elemental distribution in seeds and seedlings of the Zn–Cd–Ni hyperaccumulator Noccaea caerulescens. Metallomics. 2022;14(5):mfac026.

211. Babst-Kostecka A, Przybyłowicz WJ, Seget B, Mesjasz-Przybyłowicz J. Zinc allocation to and within Arabidopsis halleri seeds: Different strategies of metal homeostasis in accessions under divergent selection pressure. Plant-Environment Interact. 2020;1(3):207–20.

212. Babst-Kostecka A, Przybyłowicz WJ, van Der Ent A, Ryan C, Dietrich CC, Mesjasz-Przybyłowicz J. Endosperm prevents toxic amounts of Zn from accumulating in the seed embryo–an adaptation to metalliferous sites in metal-tolerant Biscutella laevigata. Metallomics. 2020;12(1):42–53.

213. Bertrand AR, Detry E, Nouet C, Hanikenne M, Baurain D. The rhizosphere microbiota of the zinc and cadmium hyperaccumulators Arabidopsis halleri and Noccaea caerulescens is highly convergent in Prayon (Belgium). 2021.

214. Gräfenstein A, Brückner D, Rumancev C, Garrevoet J, Galbierz V, Schroeder WH, et al. Single-Slice XRF Mapping of Light Elements in Frozen-Hydrated Allium schoenoprasum via a Self-Absorption-Corrected Hyperspectral Tomographic Reconstruction Approach. Anal Chem. 2023;95(27):10186–95.

215. do Nascimento CWA, Hesterberg D, Tappero R. Imaging Zn and Ni distributions in leaves of different ages of the hyperaccumulator Noccaea caerulescens by synchrotron-based X-ray fluorescence. J Hazard Mater. 2021;408:124813.

216. Juan CA, Pérez de la Lastra JM, Plou FJ, Pérez-Lebeña E. The chemistry of reactive oxygen species (ROS) revisited: outlining their role in biological macromolecules (DNA, lipids and proteins) and induced pathologies. Int J Mol Sci. 2021;22(9):4642.

217. Mishra S, Imlay J. Why do bacteria use so many enzymes to scavenge hydrogen peroxide? Arch Biochem Biophys. 2012;525(2):145–60.

218. De Gara L, de Pinto MC, Tommasi F. The antioxidant systems vis-à-vis reactive oxygen species during plant–pathogen interaction. Plant Physiol Biochem. 2003;41(10):863–70.

219. Jhee EM, Boyd RS, Eubanks MD. Effectiveness of metal–metal and metal–organic compound combinations against Plutella xylostella: implications for plant elemental defense. J Chem Ecol. 2006;32:239–59.

220. Zou L, Lu J, Wang J, Ren X, Zhang L, Gao Y, et al. Synergistic antibacterial effect of silver and ebselen against multidrug-resistant Gram-negative bacterial infections. EMBO Mol Med. 2017;9(8):1165–78.

221. Zou L, Wang J, Gao Y, Ren X, Rottenberg ME, Lu J, et al. Synergistic antibacterial activity of silver with antibiotics correlating with the upregulation of the ROS production. Sci Rep. 2018;8(1):11131.

222. Johnson LA, Hug LA. Distribution of reactive oxygen species defense mechanisms across domain bacteria. Free Radic Biol Med. 2019;140:93–102.

223. Yuan F, Yin S, Xu Y, Xiang L, Wang H, Li Z, et al. The richness and diversity of catalases in bacteria. Front Microbiol. 2021;12:645477.

224. Schwarzländer M, Fricker MD, Müller C, Marty L, Brach T, Novak J, et al. Confocal imaging of glutathione redox potential in living plant cells. J Microsc. 2008;231(2):299–316.

225. Aller I, Rouhier N, Meyer AJ. Development of roGFP2-derived redox probes for measurement of the glutathione redox potential in the cytosol of severely glutathione-deficient rml1 seedlings. Front Plant Sci. 2013;4:506.

226. Saninjuk K, Romsang A, Duang-Nkern J, Wongsaroj L, Leesukon P, Dubbs JM, et al. Monothiol Glutaredoxin Is Essential for Oxidative Stress Protection and Virulence in Pseudomonas aeruginosa. Appl Environ Microbiol. 2023;89(1):e01714-22.

227. Lillig CH, Berndt C, Holmgren A. Glutaredoxin systems. Biochim Biophys Acta (BBA)-General Subj. 2008;1780(11):1304–17.

228. Hanson GT, Aggeler R, Oglesbee D, Cannon M, Capaldi RA, Tsien RY, et al.

Investigating mitochondrial redox potential with redox-sensitive green fluorescent protein indicators. J Biol Chem. 2004;279(13):13044–53.

229. van Der Heijden J, Vogt SL, Reynolds LA, Peña-Díaz J, Tupin A, Aussel L, et al. Exploring the redox balance inside gram-negative bacteria with redox-sensitive GFP. Free Radic Biol Med. 2016;91:34–44.

230. Morgan B, Sobotta MC, Dick TP. Measuring EGSH and H2O2 with roGFP2-based redox probes. Free Radic Biol Med. 2011;51(11):1943–51.

231. Nietzel T, Elsässer M, Ruberti C, Steinbeck J, Ugalde JM, Fuchs P, et al. The fluorescent protein sensor ro GFP 2-Orp1 monitors in vivo H2O2 and thiol redox integration and elucidates intracellular H2O2 dynamics during elicitor-induced oxidative burst in Arabidopsis. New Phytol. 2019;221(3):1649–64.

232. Meyer AJ, Brach T, Marty L, Kreye S, Rouhier N, Jacquot J, et al. Redox-sensitive GFP in Arabidopsis thaliana is a quantitative biosensor for the redox potential of the cellular glutathione redox buffer. Plant J. 2007;52(5):973–86.

233. Geissel F, Lang L, Husemann B, Morgan B, Deponte M. Deciphering the mechanism of glutaredoxin-catalyzed roGFP2 redox sensing reveals a ternary complex with glutathione for protein disulfide reduction. Nat Commun. 2024;15(1):1733.

234. Meyer AJ, Dick TP. Fluorescent protein-based redox probes. Antioxid Redox Signal. 2010;13(5):621–50.

235. Albrecht SC, Sobotta MC, Bausewein D, Aller I, Hell R, Dick TP, et al. Redesign of genetically encoded biosensors for monitoring mitochondrial redox status in a broad range of model eukaryotes. J Biomol Screen. 2014;19(3):379–86.

236. Mukherjee R, Verma T, Nandi D, Umapathy S. Understanding the effects of culture conditions in bacterial growth: A biochemical perspective using Raman microscopy. J Biophotonics. 2020;13(1):e201900233.

237. Verma T, Annappa H, Singh S, Umapathy S, Nandi D. Profiling antibiotic resistance in Escherichia coli strains displaying differential antibiotic susceptibilities using Raman spectroscopy. J Biophotonics. 2021;14(1):e202000231.

238. Smith E, Dent G. Modern Raman spectroscopy: a practical approach. 2nd ed. John Wiley & Sons; 2019.

239. Song Y, Cui L, López JÁS, Xu J, Zhu Y-G, Thompson IP, et al. Raman-Deuterium Isotope Probing for in-situ identification of antimicrobial resistant bacteria in Thames River. Sci Rep. 2017;7(1):16648.

240. Beck B, Chen Y-F, Dere W, Devanarayan V, Eastwood BJ, Farmen MW, et al. Assay operations for SAR support [Internet]. Eli Lilly & Company and the National Center for Advancing Translational Sciences. 2017. Available from: https://www.ncbi.nlm.nih.gov/books/NBK91994/

241. Xu J, Yu T, Zois CE, Cheng J-X, Tang Y, Harris AL, et al. Unveiling cancer metabolism through spontaneous and coherent Raman spectroscopy and stable isotope probing. Cancers (Basel). 2021;13(7):1718.

242. Hasan H, Tahir NM. Feature selection of breast cancer based on principal component analysis. In: 2010 6th International Colloquium on Signal Processing & its Applications. IEEE; 2010. p. 1–4.

243. Rodríguez-Rojas A, Kim JJ, Johnston PR, Makarova O, Eravci M, Weise C, et al. Non-lethal exposure to H2O2 boosts bacterial survival and evolvability against oxidative stress. PLoS Genet. 2020;16(3):e1008649.

244. Irving H, Williams Rjp. The stability of transition-metal complexes. J Chem Soc. 1953;3192–210.

245. Imlay JA. The mismetallation of enzymes during oxidative stress. J Biol Chem. 2014;289(41):28121–8.

246. Murali A, Patel S. The effect of different heavy metal acetate solutions on the inhibition of catalase enzyme. J South Carolina Acad Sci. 2017;15(2):13.

247. Qi Y, Li X, Guo S, He F, Liu R. Insights into the potential toxicity of Zn (II) to catalase and their binding mechanisms. J Mol Liq. 2024;394:123760.

248. Bishop GM, Dringen R, Robinson SR. Zinc stimulates the production of toxic reactive oxygen species (ROS) and inhibits glutathione reductase in astrocytes. Free Radic Biol Med. 2007;42(8):1222–30.

249. Trevisan R, Flesch S, Mattos JJ, Milani MR, Bainy ACD, Dafre AL. Zinc causes acute impairment of glutathione metabolism followed by coordinated antioxidant defenses amplification in gills of brown mussels Perna perna. Comp Biochem Physiol Part C Toxicol Pharmacol. 2014;159:22–30.

250. Wilhelm B, Walther U, Fichtl B. Effects of zinc chloride on glutathione and glutathione synthesis rates in various lung cell lines. Arch Toxicol. 2001;75(7):388–94.

251. Harris G, Stickland CA, Lim M, Goldberg Oppenheimer P. Raman Spectroscopy Spectral Fingerprints of Biomarkers of Traumatic Brain Injury. Cells. 2023;12(22):2589.

252. Wang W, Rahman A, Huang Q, Vikesland PJ. Surface-enhanced Raman spectroscopy enabled evaluation of bacterial inactivation. Water Res. 2022;220:118668.

253. Ibtehaz N, Chowdhury MEH, Khandakar A, Kiranyaz S, Rahman MS, Zughaier SM. RamanNet: a generalized neural network architecture for Raman spectrum analysis. Neural Comput Appl. 2023;35(25):18719–35.

254. Podgórska A, Burian M, Szal B. Extra-cellular but extra-ordinarily important for cells: Apoplastic reactive oxygen species metabolism. Front Plant Sci. 2017;8:1353.

255. Goto Y, Maki N, Sklenar J, Derbyshire P, Menke FLH, Zipfel C, et al. The

phagocytosis oxidase/Bem1p domain-containing protein PB1CP negatively regulates the NADPH oxidase RBOHD in plant immunity. New Phytol. 2024;241(4):1763–79.

256. Galanti D, Jung JH, Müller C, Bossdorf O. Discarded sequencing reads uncover natural variation in pest resistance in Thlaspi arvense. Elife. 2024;13:RP95510.

257. Maia M, Aziz A, Jeandet P, Carré V. Profiling and Localization of Stilbene Phytoalexins Revealed by MALDI-MSI during the Grapevine–Botrytis cinerea Interaction. J Agric Food Chem. 2023;71(42):15569–81.

258. Maia M, Carré V, Aziz A, Jeandet P. Molecular localization of phytoalexins at the micron scale: toward a better understanding of plant-phytoalexin-pathogen dynamics. J Agric Food Chem. 2022;70(30):9243–5.

259. Hanikenne M, Talke IN, Haydon MJ, Lanz C, Nolte A, Motte P, et al. Evolution of metal hyperaccumulation required cis-regulatory changes and triplication of HMA4. Nature. 2008;453(7193):391–5.

260. Clifton LA, Skoda MWA, Le Brun AP, Ciesielski F, Kuzmenko I, Holt SA, et al. Effect of divalent cation removal on the structure of gram-negative bacterial outer membrane models. Langmuir. 2015;31(1):404–12.

261. Webster J, Holt S, Dalgliesh R. INTER the chemical interfaces reflectometer on target station 2 at ISIS. Phys B Condens Matter. 2006;385:1164–6.

262. Pacoud M, Mandon K, Cazareth J, Pierre O, Frendo P, Alloing G. Redox-sensitive fluorescent biosensors detect Sinorhizobium meliloti intracellular redox changes under free-living and symbiotic lifestyles. Free Radic Biol Med. 2022;184:185–95.

Appendix

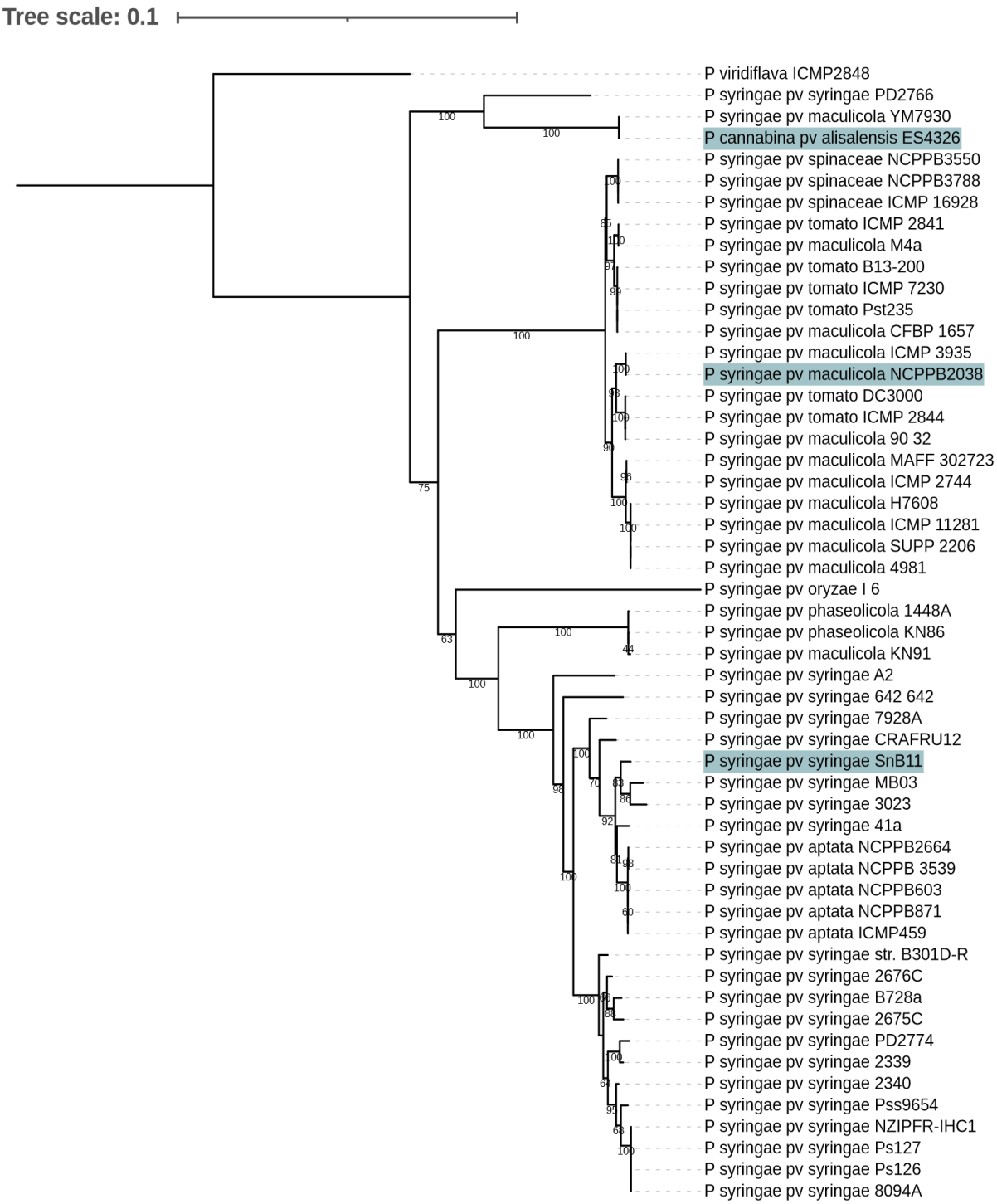


Figure 84: Phylogenetic tree of *Pseudomonas syringae* strains of interest. The highlighted strains indicate those used in this work. The numbers shown on branches are bootstrap values given as a percentage. Made by Chloe Harper using IQTREE.

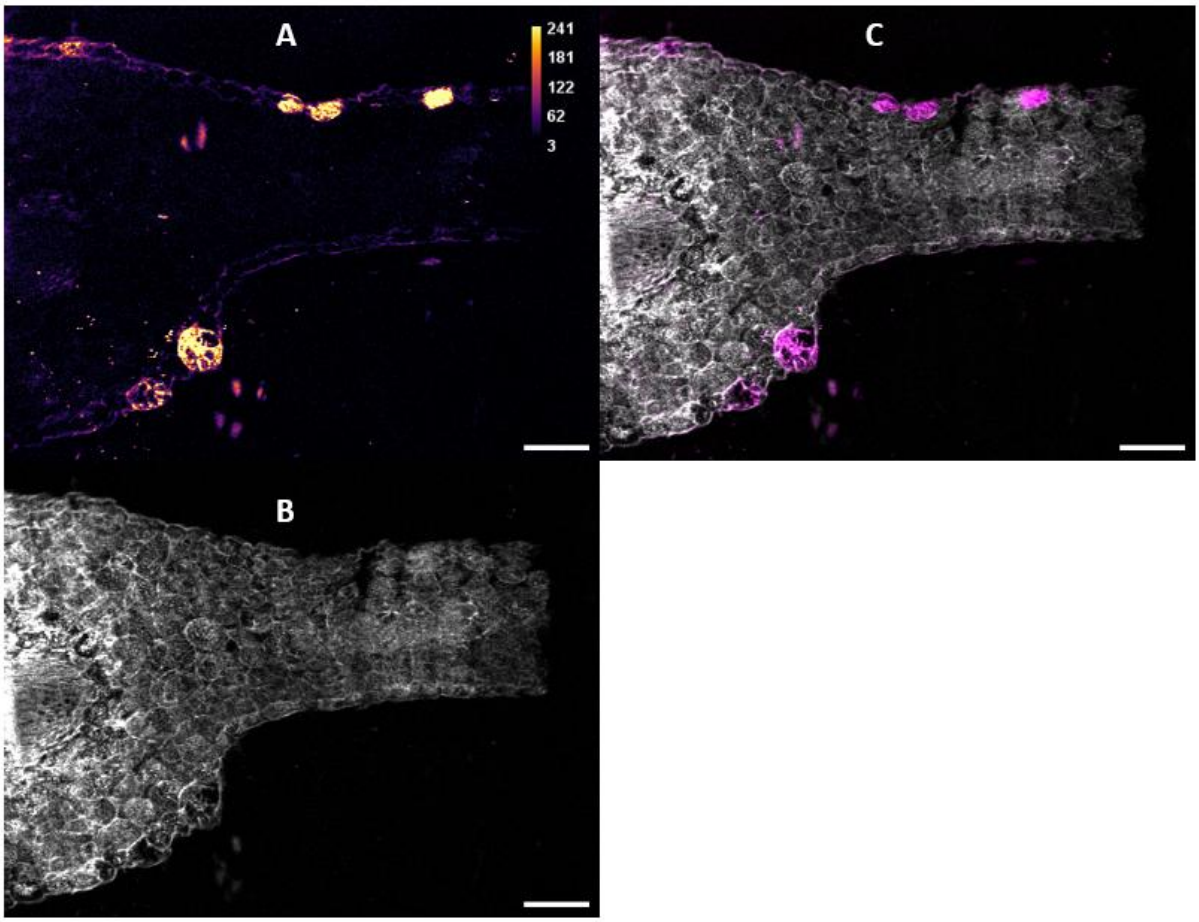


Figure 85: False colour XRF map of a transverse section of extra low zinc (10 µM) *Noccaea caerulescens* leaf. 2 µm spatial resolution, 25 µm thick. (A) Zinc distribution. (B) Potassium distribution. (C) Composite map showing the relative distribution of zinc (magenta) and potassium (grey). Scale bar indicates 100 µm.

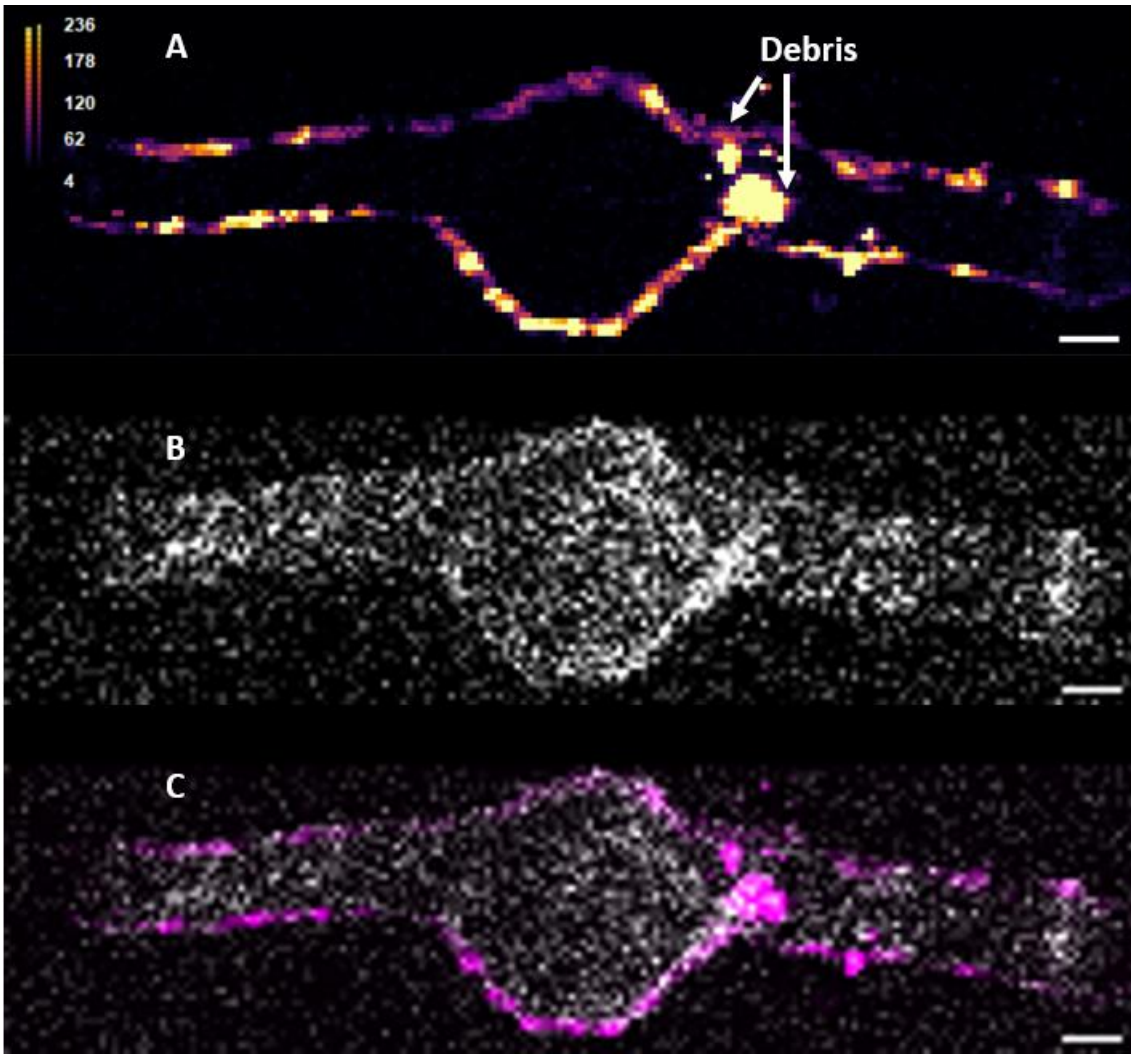


Figure 86: False colour XRF map of a transverse section of low zinc (30 µM) *Noccaea caerulescens* leaf. 10 µm spatial resolution, 25 µm thick. (A) Zinc distribution. (B) Potassium distribution. (C) Composite map showing the relative distribution of zinc (magenta) and potassium (grey). Scale bar indicates 100 µm.

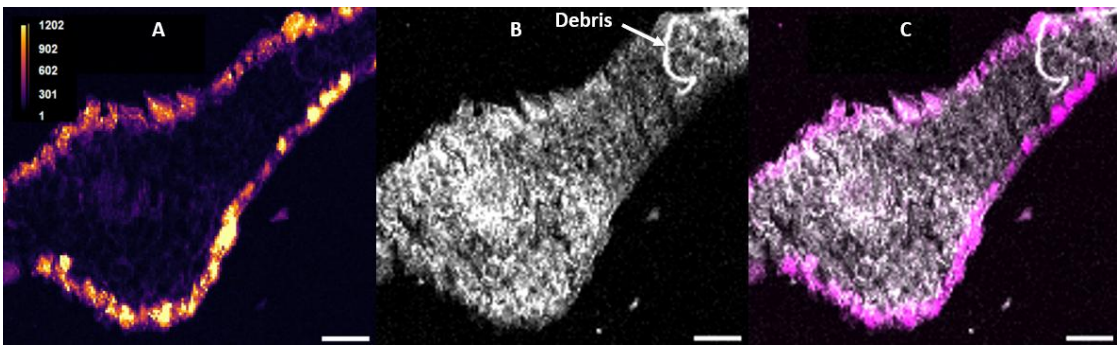


Figure 87: False colour XRF map of a transverse section of high zinc (300 µM) *Noccaea caerulescens* leaf. 5 µm spatial resolution, 25 µm thick. (A) Zinc distribution. (B) Potassium distribution. (C) Composite map showing the relative distribution of zinc (magenta) and potassium (grey). Scale bar indicates 100 µm.

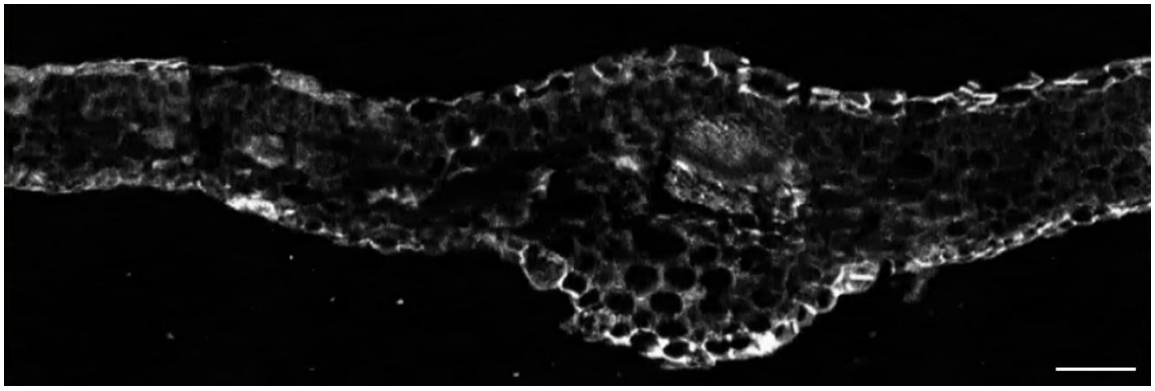


Figure 88: False colour XRF map of a transverse section of high zinc (300 µM) *Noccaea caerulescens* leaf infected with *Pseudomonas syringae* pv. maculicola. 4DPI. 1 µm spatial resolution, 25 µm thick. Zinc distribution indicated by grey colour. Scale bar indicates 100 µm.

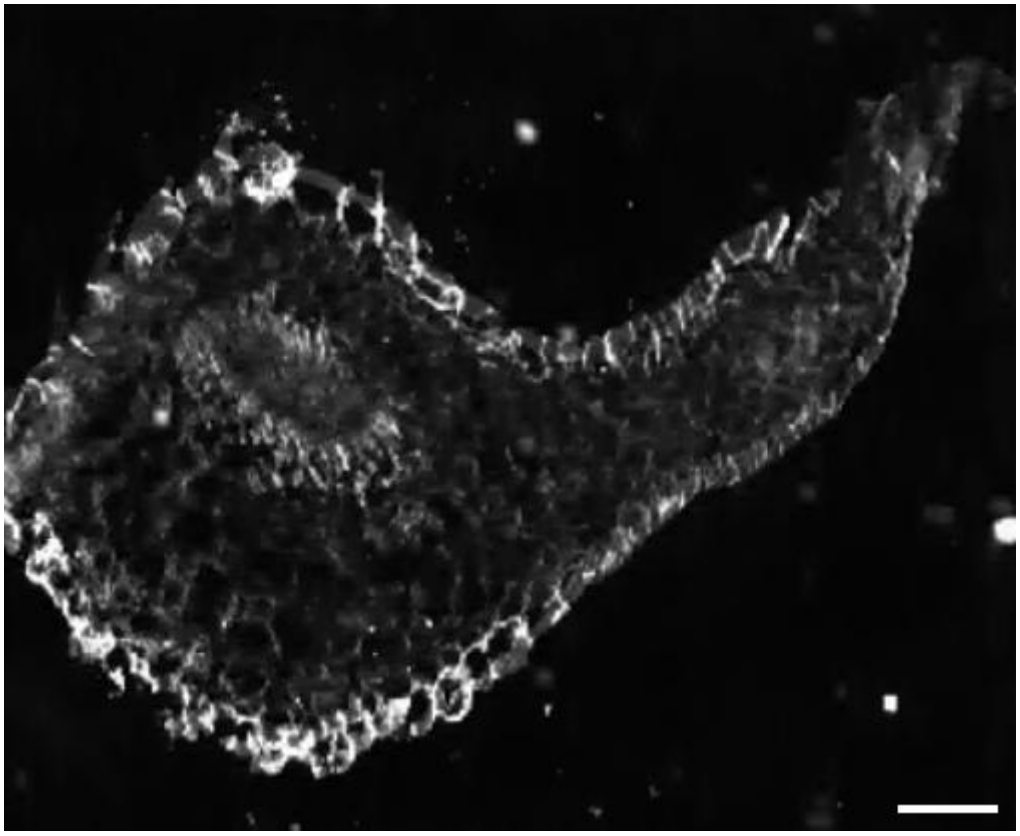


Figure 89: False colour XRF map of a transverse section of high zinc (300 µM) *Noccaea caerulescens* leaf infected with *Pseudomonas syringae* pv. syringae SnB11. 5DPI. 2 µm spatial resolution, 25 µm thick. Zinc distribution indicated by grey colour. Scale bar indicates 100 µm.

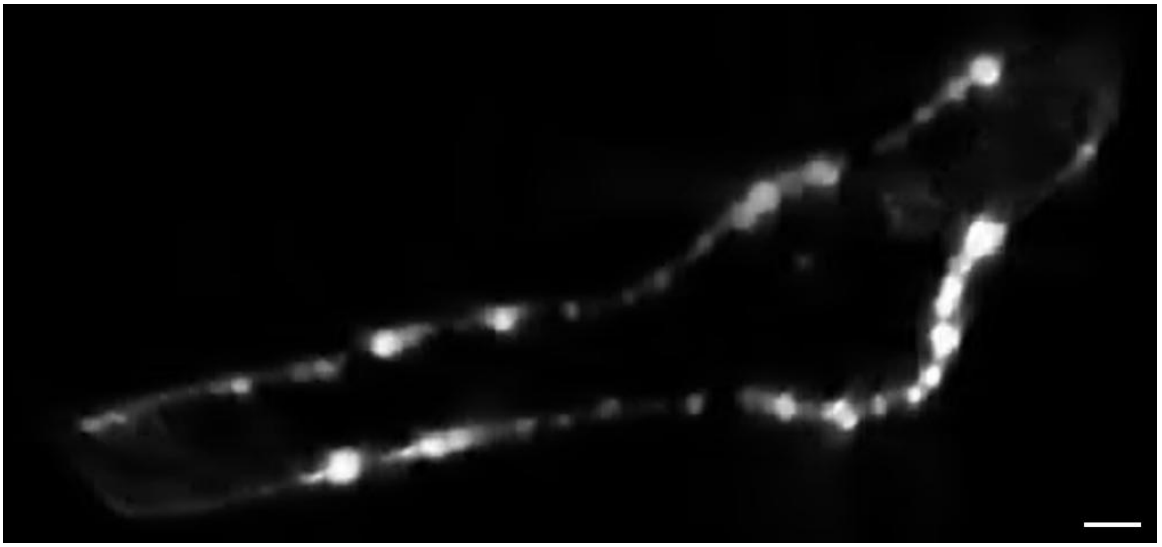


Figure 90: Single slice tomogram of an untreated high zinc (300 μM) *Noccaea caerulescens*. 5 μm spatial resolution. Zinc distribution indicated by grey colour. Scale bar indicates 100 μm.

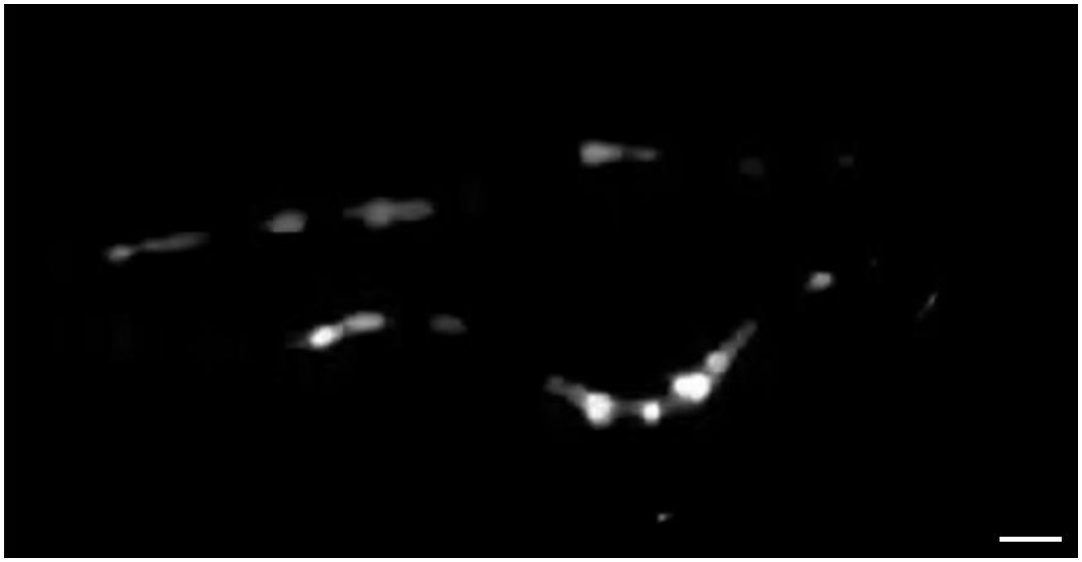


Figure 91: Single slice tomogram of an untreated extra low zinc (10 μM) *Noccaea caerulescens*. 5 μm spatial resolution. Zinc distribution indicated by grey colour. Scale bar indicates 100 μm.

Table 9: R-factors and χ^2 values indicating the closeness of fit between the sample and fit XANES spectra. UE = upper epidermis, LE = lower epidermis, DPI = days post infection with *Pseudomonas syringae* pv maculicola.

Sample	Region	R factor	χ^2
Untreated	Mesophyll	7.37E-04	0.049
Untreated	UE 1	9.96E-04	0.066
Untreated	UE 2	0.0011	0.077
Untreated	UE 3	9.30E-04	0.06
Untreated	LE 1	5.60E-03	0.39
Untreated	LE 2	2.60E-03	0.2
Untreated	LE 3	5.00E-03	0.39
Mock	Mesophyll	1.00E-02	0.09
Mock	Xylem	3.00E-03	0.31
Mock	Phloem	2.00E-03	0.22
Mock	UE 1	1.00E-03	0.18
Mock	UE 2	3.00E-03	0.14
Mock	LE 1	2.00E-03	0.22
Mock	LE 2	1.00E-03	0.09
1DPI	Mesophyll 1	1.50E-03	0.15
1DPI	Mesophyll 2	1.30E-03	0.13
1DPI	Xylem	2.60E-03	0.23
1DPI	Phloem	2.60E-03	0.26
1DPI	UE 1	2.60E-03	0.26
1DPI	UE 2	5.10E-03	0.46
1DPI	UE 3	5.90E-03	0.56
1DPI	LE 1	1.90E-03	0.19
1DPI	LE 2	5.50E-03	0.67
1DPI	LE 3	4.90E-03	0.47
4DPI	Mesophyll 1	5.29E-04	0.036
4DPI	Mesophyll 2	2.97E-04	0.026
4DPI	Mesophyll 3	3.18E-04	0.028
4DPI	Xylem	2.99E-04	0.026
4DPI	Phloem	6.20E-04	0.047
4DPI	UE 1	2.70E-03	0.19
4DPI	UE 2	2.70E-03	0.21
4DPI	UE 3	4.30E-03	0.3
4DPI	LE 1	6.46E-04	0.04
4DPI	LE 2	1.10E-03	0.083

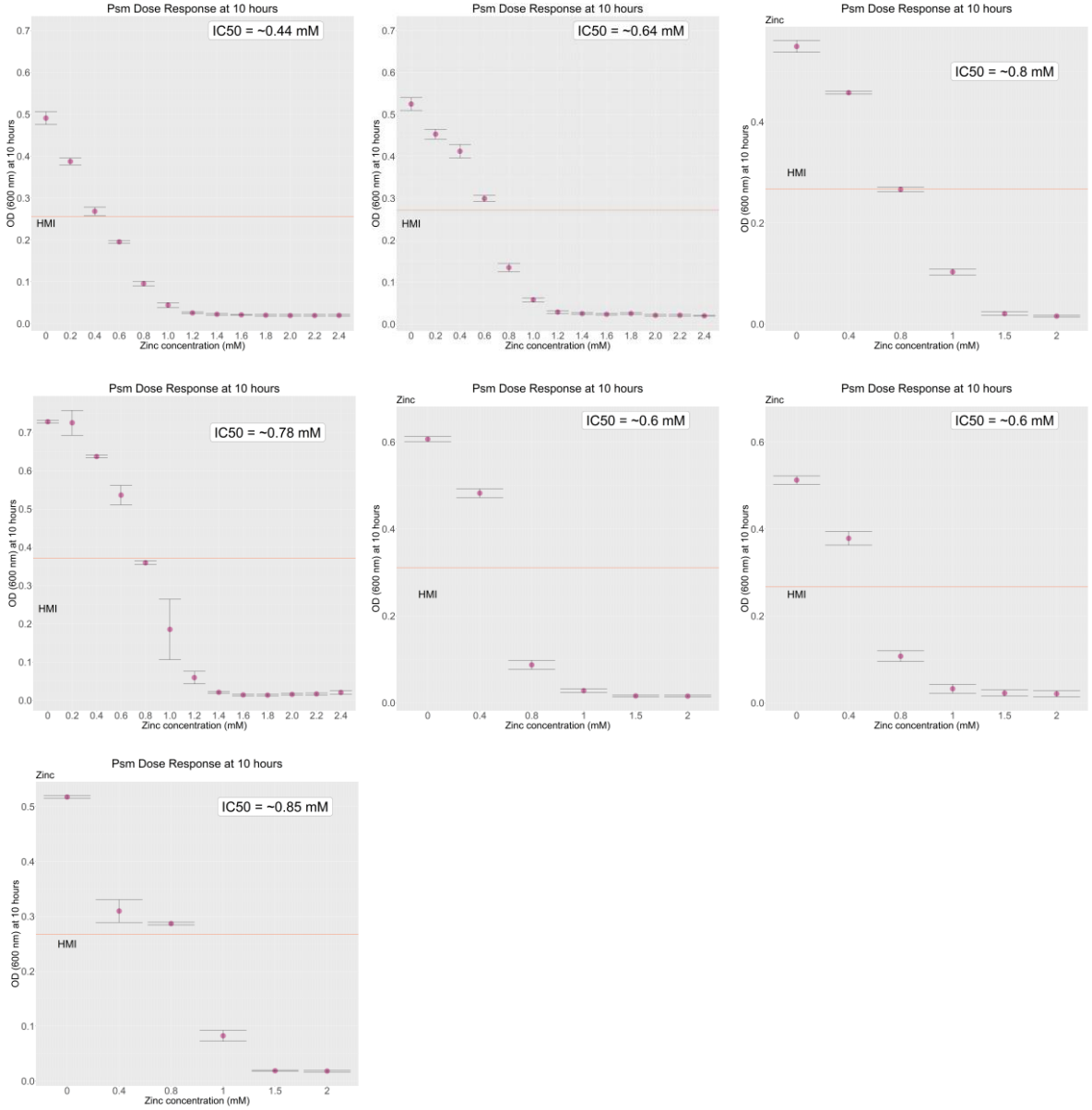


Figure 92: *Pseudomonas* syringae pv. maculicola zinc dose response plots at 10 hours.

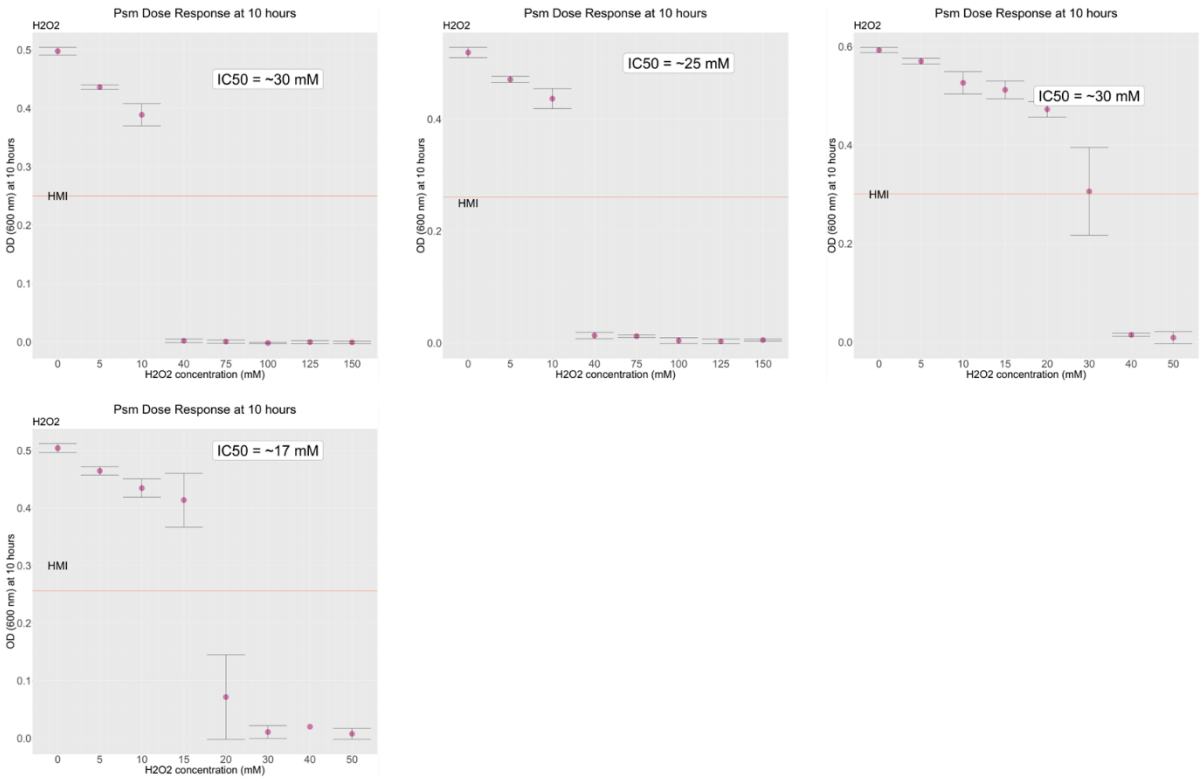


Figure 93: *Pseudomonas* syringae pv. maculicola hydrogen peroxide dose response plots at 10 hours.

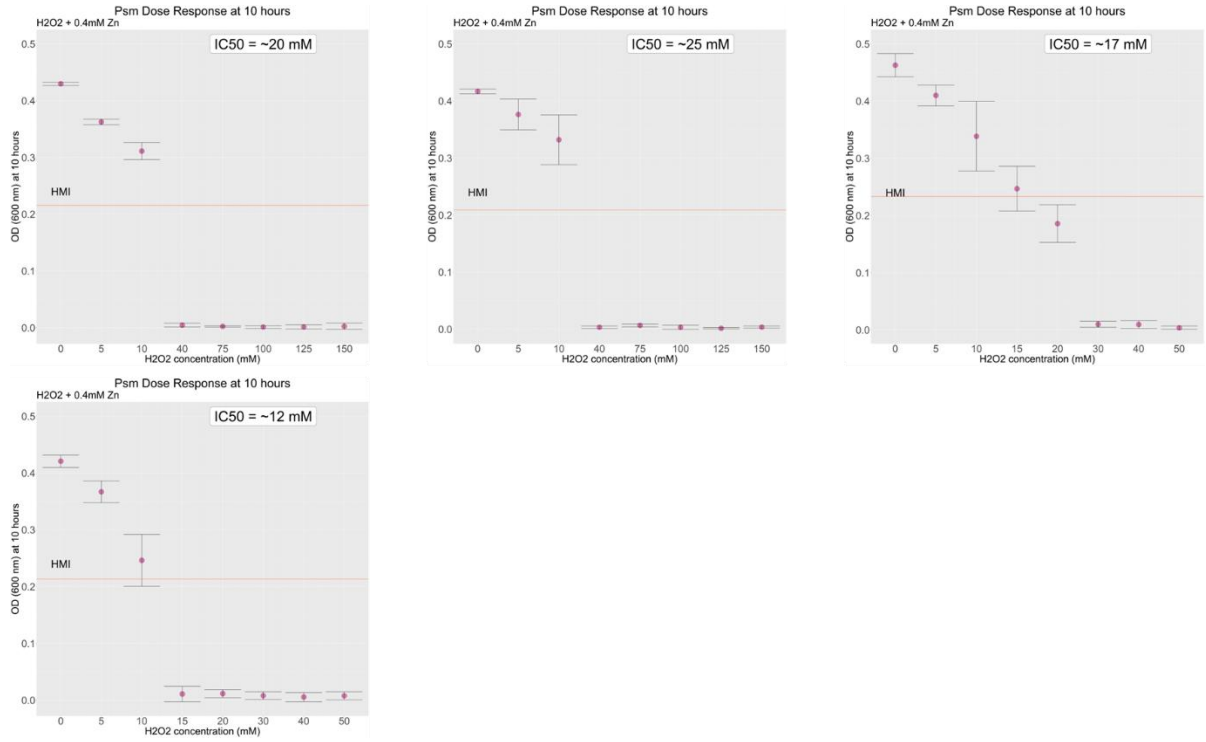


Figure 94: *Pseudomonas* syringae pv. maculicola hydrogen peroxide and 0.4 mM zinc dose response plots at 10 hours.

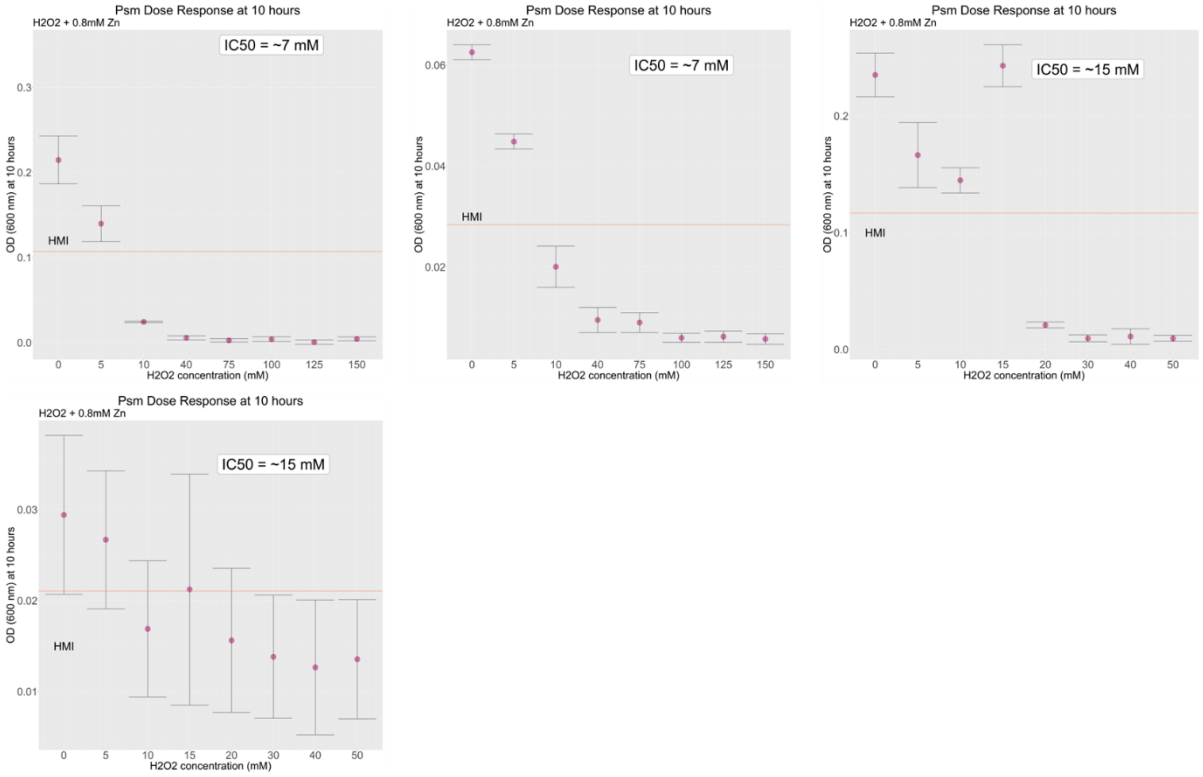


Figure 95: *Pseudomonas* syringae pv. maculicola hydrogen peroxide and 0.8 mM zinc dose response plots at 10 hours.

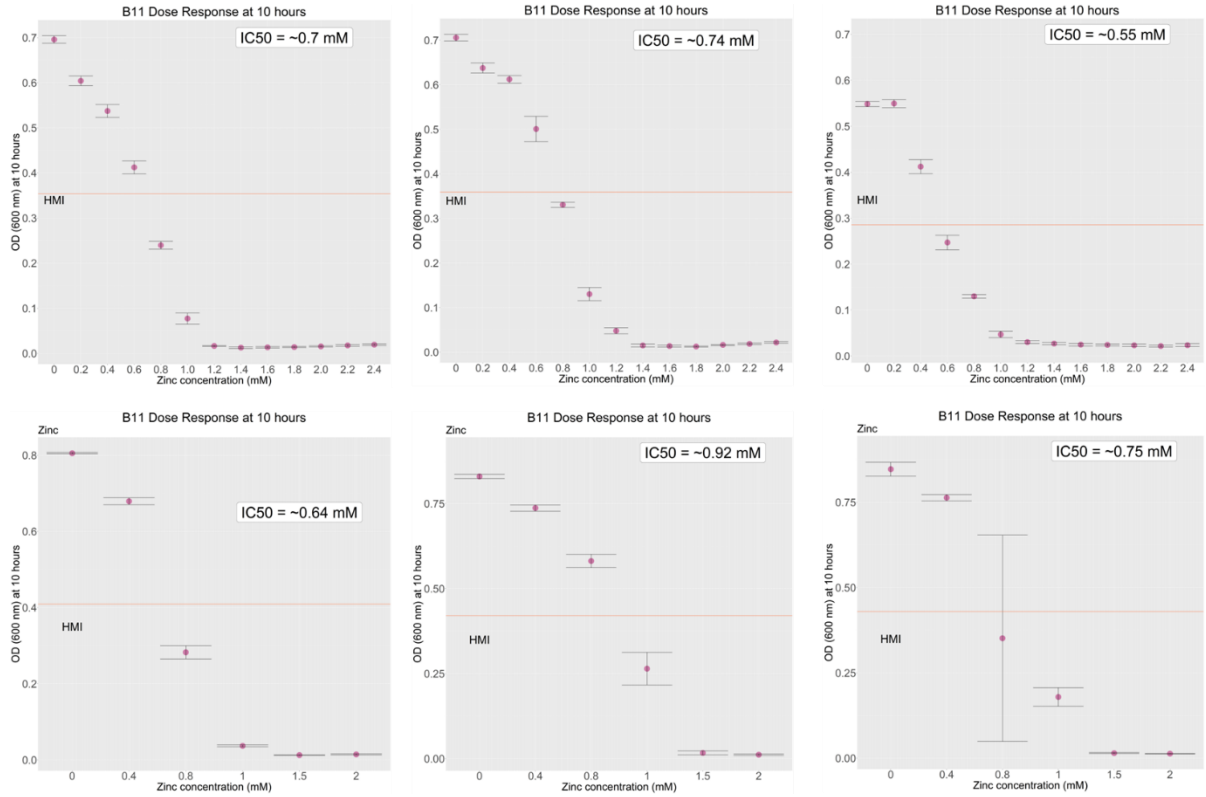


Figure 96: *Pseudomonas* syringae pv. syringae SnB11 zinc dose response plots at 10 hours.

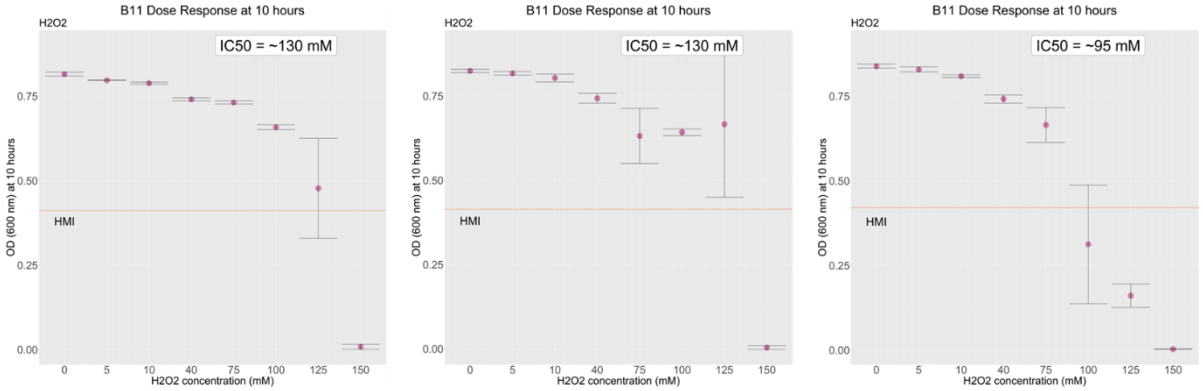


Figure 97: *Pseudomonas* syringae pv. syringae SnB11 hydrogen peroxide dose response plots at 10 hours

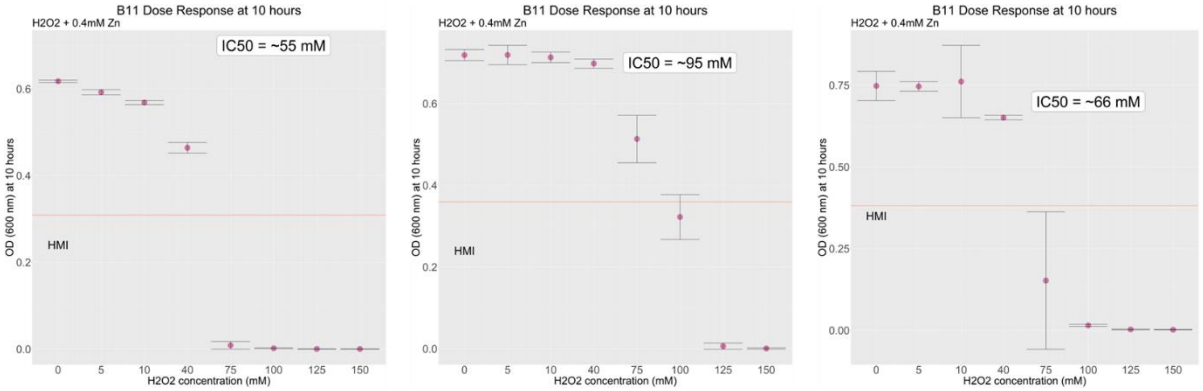


Figure 98: *Pseudomonas* syringae pv. syringae SnB11 0.4 mM zinc and hydrogen peroxide dose response plots at 10 hours

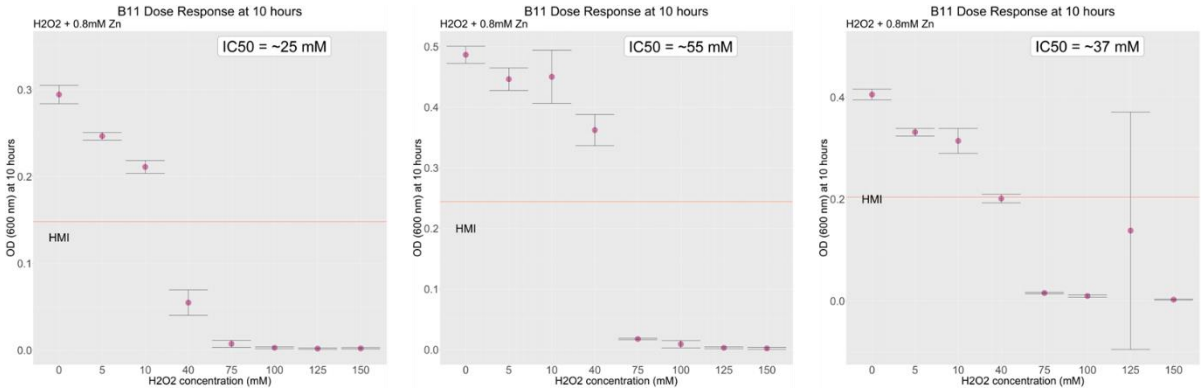


Figure 99: *Pseudomonas* syringae pv. syringae SnB11 0.8 mM zinc and hydrogen peroxide dose response plots at 10 hours

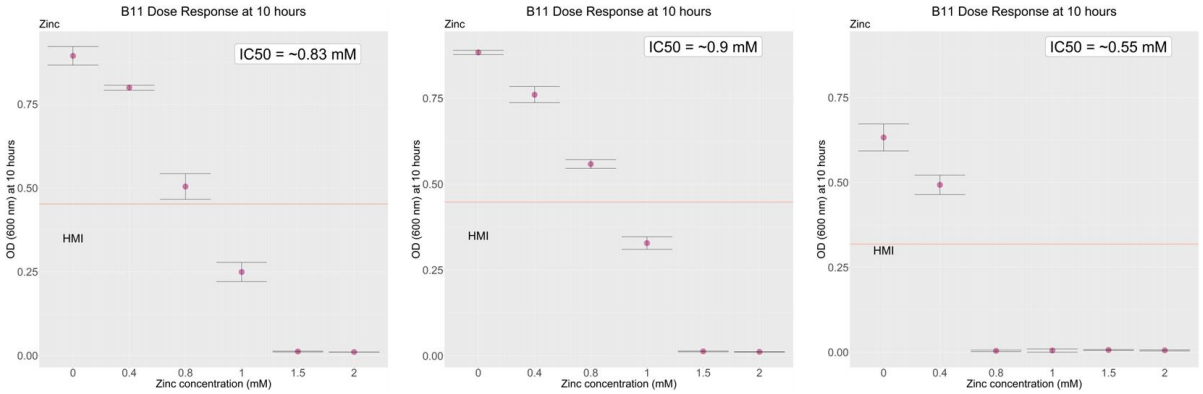


Figure 100: *Pseudomonas* syringae pv. syringae SnB11 zinc dose response plots at 10 hours. Measured concurrently with plots below and are relevant to Figure 70.

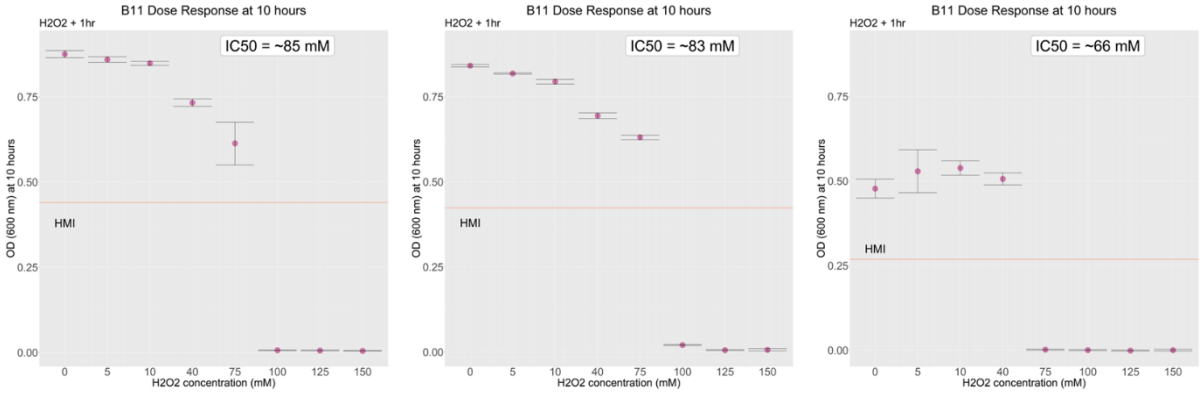


Figure 101: *Pseudomonas* syringae pv. syringae SnB11 hydrogen peroxide dose response plots at 10 hours, when hydrogen peroxide was added at +1hr.

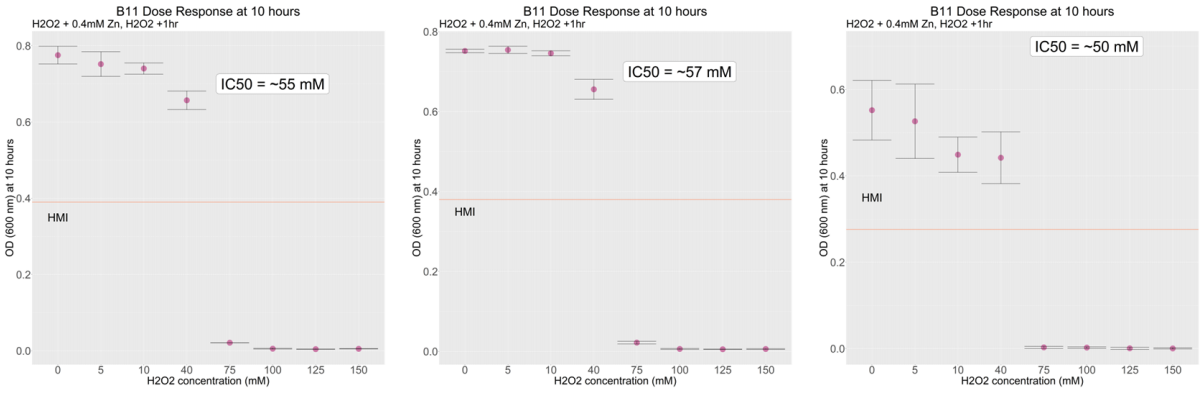


Figure 102: *Pseudomonas* syringae pv. syringae SnB11 0.4 mM zinc plus hydrogen peroxide dose response plots at 10 hours, when hydrogen peroxide was added at +1hr.

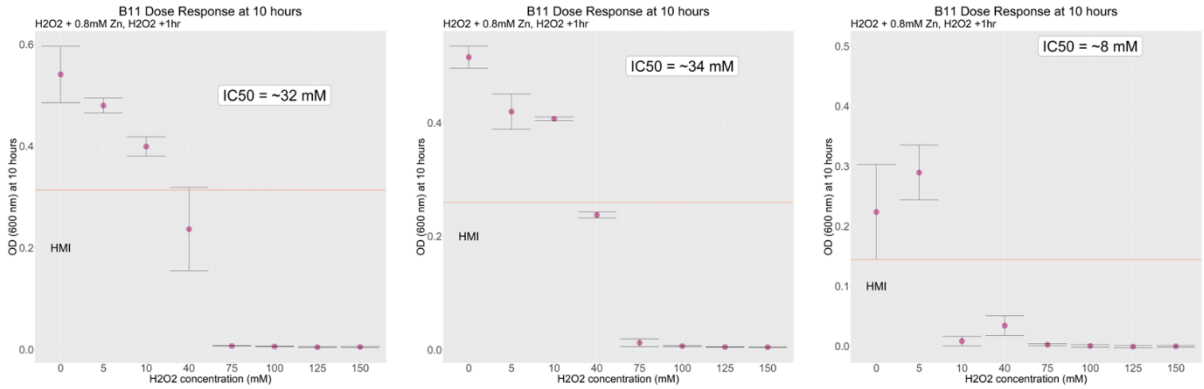


Figure 103: *Pseudomonas* syringae pv. syringae SnB11 0.8 mM zinc plus hydrogen peroxide dose response plots at 10 hours, when hydrogen peroxide was added at +1hr.

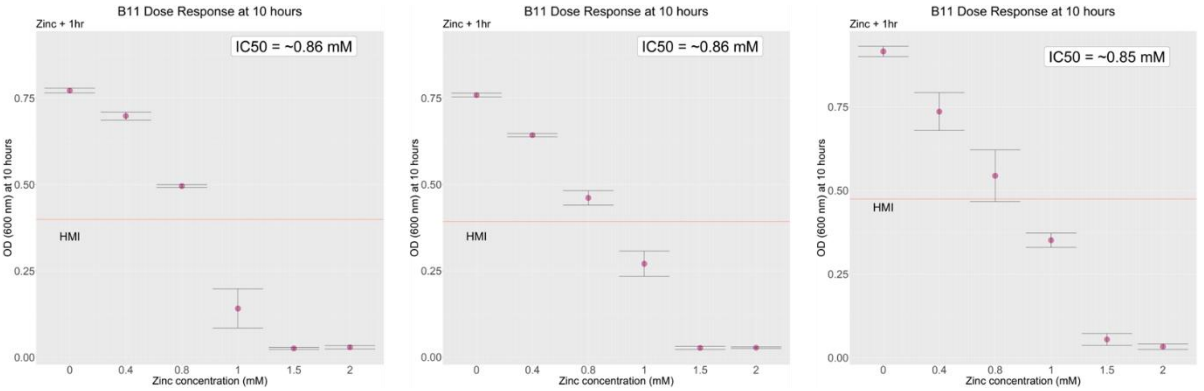


Figure 105: *Pseudomonas* syringae pv. syringae SnB11 zinc dose response plots at 10 hours, when zinc was added at +1hr.

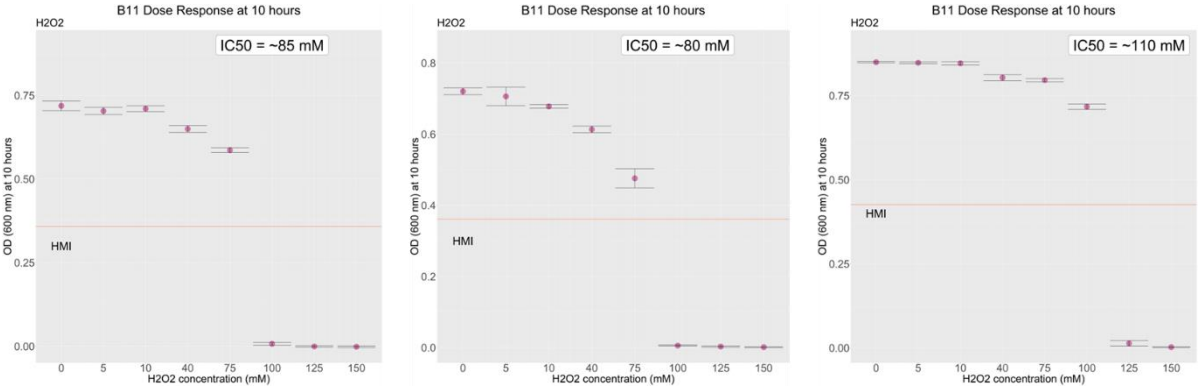


Figure 104: *Pseudomonas* syringae pv. syringae SnB11 hydrogen peroxide dose response plots at 10 hours. Measured concurrently with plots below and are relevant to Figure 71.

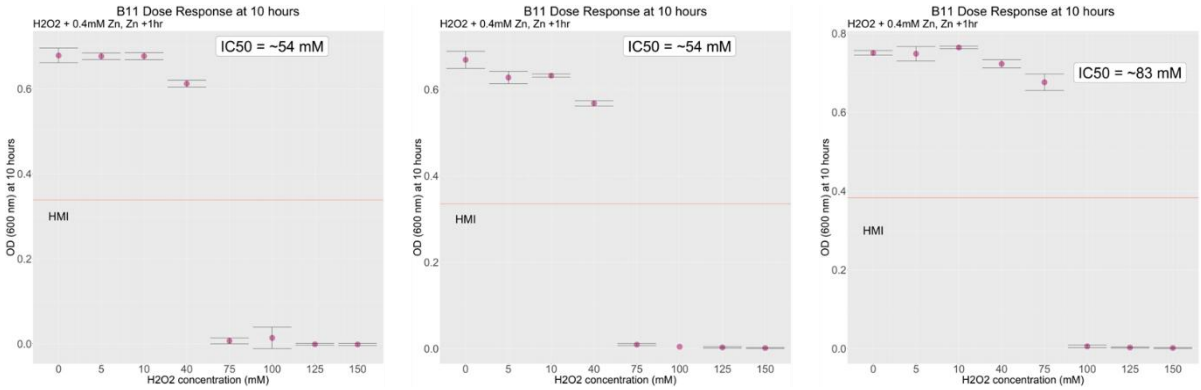


Figure 106: *Pseudomonas* syringae pv. syringae SnB11 0.4 mM zinc plus hydrogen peroxide dose response plots at 10 hours, when zinc was added at +1hr.

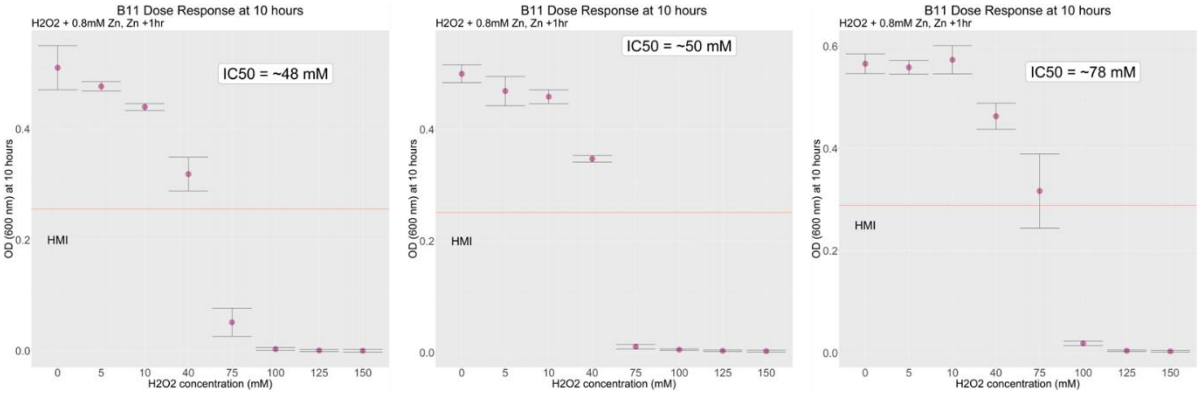


Figure 107: *Pseudomonas* syringae pv. syringae SnB11 0.8 mM zinc plus hydrogen peroxide dose response plots at 10 hours, when zinc was added at +1hr.